

Spring 2005

# Hyperpolarized xenon-129 production and applications

Iulian C. Ruset

*University of New Hampshire, Durham*

Follow this and additional works at: <https://scholars.unh.edu/dissertation>

---

## Recommended Citation

Ruset, Iulian C., "Hyperpolarized xenon-129 production and applications" (2005). *Doctoral Dissertations*. 282.  
<https://scholars.unh.edu/dissertation/282>

This Dissertation is brought to you for free and open access by the Student Scholarship at University of New Hampshire Scholars' Repository. It has been accepted for inclusion in Doctoral Dissertations by an authorized administrator of University of New Hampshire Scholars' Repository. For more information, please contact [nicole.hentz@unh.edu](mailto:nicole.hentz@unh.edu).

HYPERPOLARIZED  $^{129}\text{Xe}$  PRODUCTION AND APPLICATIONS

BY

Iulian C. Ruset

B.S., University of Bucharest, 1999

DISSERTATION

Submitted to the University of New Hampshire  
in partial fulfillment of  
the requirements for the degree of

Doctor of Philosophy

in

Physics

May 2005

UMI Number: 3176547

### INFORMATION TO USERS

The quality of this reproduction is dependent upon the quality of the copy submitted. Broken or indistinct print, colored or poor quality illustrations and photographs, print bleed-through, substandard margins, and improper alignment can adversely affect reproduction.

In the unlikely event that the author did not send a complete manuscript and there are missing pages, these will be noted. Also, if unauthorized copyright material had to be removed, a note will indicate the deletion.

**UMI**<sup>®</sup>

---

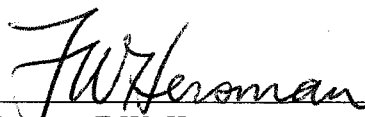
UMI Microform 3176547

Copyright 2005 by ProQuest Information and Learning Company.

All rights reserved. This microform edition is protected against unauthorized copying under Title 17, United States Code.

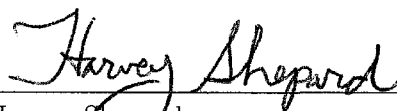
ProQuest Information and Learning Company  
300 North Zeeb Road  
P.O. Box 1346  
Ann Arbor, MI 48106-1346

This dissertation has been examined and approved.



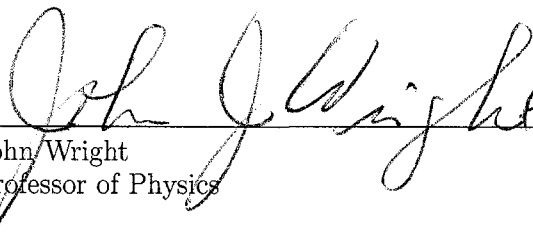
---

Director, F.W. Hersman  
Professor of Physics



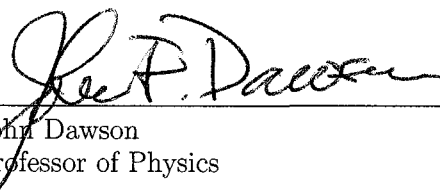
---

Harvey Shepard  
Professor of Physics



---

John Wright  
Professor of Physics



---

John Dawson  
Professor of Physics



---

Samuel Patz  
Associate Professor of Radiology, Harvard Medical  
School

5-2-2005

---

Date

# Dedication

With love, to my wife, Diana.

# Acknowledgments

A PhD dissertation is far from being a one person work, although finally it comes to a single name on the cover. There are so many people I am thankful to for getting this far.

I would like to start with Professor Bill Hersman, my adviser for the last four years, and probably the most influential person on my future career. His knowledge, scientific curiosity, and belief in new ideas will always be an inspiration to me. I thank him for all these years of re-formation and I look forward to many and successful collaborations with him.

I officially thank all the xenonites from the Hersman group. Many results presented in this thesis are backed up with so much work by these wonderful colleagues. Stephen Ketel has put a lot of effort in the first generation of the polarizer, and his skills with LabView were essential to the project. I am grateful to our group post-docs: Tong Lee, Hongguo Zhu and Silviu Covrig. They shared with me hard gained knowledge and experience. Hongguo and Tong gave credit on projects where my involvement was not as much as I wished. Jim Williams is our man in the shadow in which many of the project amps and "wonder"-boxes should see their creator. Iga Muradian is my grad colleague who is trying to cover my graduate studies expenses by finding a purpose for the polarized xenon. I thank Korac

MacArthur for his 3D drawings and his machining skills in producing unique and fine hardware equipment. And to the undergraduate students to whom I owe a great deal of saved time; they were the ones, and maybe only, who never comment on my ideas: Brendan Crowley, Mike Rayno, Steve Hersman, Mike Mason, Sean Every, Brian Whitmore, Adam Straub, Christina Johnson, Amy Cooper, Liz Hersman, Rob Morse, and Mike Farrar.

My introduction to the MRI field was done by Sam Patz and Mirko Hrovat, and I am deeply grateful to them for their precious time. Many of my lab skills were "stolen" from them during our collaboration on the low field imager. I am looking forward to future collaborations.

I am ashamed of my lab notes written before I met Ross Mair. From him I learned that small steps and hard work can do more than a lucky run. I thank also the other members of the Harvard team: Matt, Leo, John, and Ron, who were essential for finding a beginning and a finality to the low field human imaging project.

I surely couldn't be here without my dear physics professors from Romania: Andrei Medar, Mihai Vilceanu, Gheorghe Vladuca, Octavian Sima, etc. I thank you all.

Thanks to the local Romanian community gathered around Cristian Cochei (a.k.a. Mommy) for all the good times spent together. Finally, I would like to thank my home family for being so patient and for understanding the importance of my work, which might excuse a bit my absence all these years. And to my wife, Diana: I dare to hope that I will be able to repay all the sacrifices you made. Thank you!

This work was financially supported by the National Institute of Health under grants RR14297, R15HL67784, R01HL073632, and EB002553. The low field imaging work was funded by NASA under grants NAG9-1166 & NAG9-1489 and by National Institute of Health under grant HL67784.

# Contents

Dedication . . . . .	iii
Acknowledgments . . . . .	iv
Contents . . . . .	vi
List of Tables . . . . .	xi
List of Figures . . . . .	xii
ABSTRACT . . . . .	xxv
<b>1 INTRODUCTION</b>	<b>1</b>
1.1 Optical Pumping . . . . .	1
1.2 $^{129}\text{Xe}$ and $^3\text{He}$ : Properties and Applications . . . . .	3
1.3 Polarizing Helium . . . . .	10
1.4 Polarizing Xenon . . . . .	11
1.4.1 The "batch" method . . . . .	12
1.4.2 The continuous flow method . . . . .	13
1.5 Thesis Summary . . . . .	16
<b>2 THEORETICAL BACKGROUND</b>	<b>18</b>
2.1 Rubidium Optical Pumping and Polarization . . . . .	18



2.1.1	Rubidium for Optical Pumping . . . . .	18
2.1.2	Optical Pumping Equations . . . . .	21
2.1.3	Nuclear Spin Effect and Slowing-Down Factor . . . . .	25
2.1.4	Buffer Gases in Optical Pumping . . . . .	29
2.1.5	Laser Light Absorption and Optical Pumping Rate . . . . .	31
2.1.6	Skew Light Effects . . . . .	35
2.1.7	Light Absorption Heating Effects . . . . .	36
2.2	Rubidium Spin-Destruction Rate . . . . .	38
2.2.1	Rb Atom Interactions . . . . .	38
2.2.2	Rb-Rb Spin-Destruction . . . . .	43
2.2.3	Buffer-Gases Spin-Destruction . . . . .	46
2.3	Rubidium-Xenon Spin-Exchange and Spin-Destruction . . . . .	47
2.3.1	Spin-Exchange Equations . . . . .	48
2.3.2	Rb-Xe Interactions . . . . .	50
2.3.3	Rb-Xe Binary Collisions . . . . .	53
2.3.4	Rb-Xe van der Waals Molecules . . . . .	54
2.3.5	Rb-Xe Molecular Spin-Exchange Rate . . . . .	56
2.3.6	Rb Molecular Spin-Destruction Rate . . . . .	57
2.4	UNH Polarizer Concept . . . . .	59
2.5	Theoretical Modeling and Simulations . . . . .	66
2.5.1	Modeling . . . . .	66
2.5.2	Simulation Results and Discussions . . . . .	69

<b>3</b>	<b>LASERS AND OPTICS</b>	<b>78</b>
3.1	Multi-FAP Laser Beam Optimization . . . . .	79
3.2	External-Cavity Narrowing of High Power LDA Stack . . . . .	86
3.2.1	External Cavities . . . . .	86
3.2.2	UNH External-Cavity Five-Bar Stack Setup . . . . .	90
3.2.3	Stepped-Mirror and Collimator Innovations . . . . .	93
3.2.4	Laser Narrowing . . . . .	94
3.2.5	Output Power Optimization . . . . .	96
3.2.6	Laser Tuning . . . . .	98
3.2.7	Beam Shaping . . . . .	99
<b>4</b>	<b>UNH XENON POLARIZER</b>	<b>100</b>
4.1	Polarizer Implementation . . . . .	100
4.1.1	$B_0$ Magnetic Field . . . . .	100
4.1.2	Lasers and Optics . . . . .	102
4.1.3	Gas Flow System . . . . .	103
4.1.4	Polarizing Column . . . . .	104
4.2	Polarization Measurement . . . . .	109
4.2.1	NMR Hardware . . . . .	109
4.2.2	Polarization Calculation . . . . .	111
4.2.3	NMR Signal Analysis . . . . .	114
4.2.4	Error Calculation . . . . .	117

<b>5</b>	<b><math>^{129}\text{Xe}</math> POLARIZATION: RESULTS AND DISCUSSIONS</b>	<b>119</b>
5.1	General Results . . . . .	119
5.2	Polarizer Performance . . . . .	121
5.3	Temperature Dependence . . . . .	122
5.4	Nitrogen Dependence . . . . .	124
5.5	Flow Velocity Dependence . . . . .	127
5.6	Broad Laser versus Narrow Laser . . . . .	128
5.7	Laser Power Dependence . . . . .	130
5.8	Enriched versus Natural Xenon . . . . .	133
5.9	Overall Results of the UNH Polarizer . . . . .	135
<b>6</b>	<b>ACCUMULATION AND DELIVERY OF POLARIZED XENON</b>	<b>137</b>
6.1	Accumulation and Recovery of Hyperpolarized Xenon . . . . .	137
6.1.1	Frozen Xenon Relaxation Mechanisms . . . . .	138
6.1.2	Xenon Accumulation . . . . .	140
6.1.3	Single Freeze-Thaw Polarization Recovery Ratio . . . . .	143
6.1.4	Multiple Freeze-Thaw Recovery Ratio . . . . .	144
6.1.5	T1 Measurement in Frozen State . . . . .	146
6.2	Optimum Production Rates . . . . .	147
6.3	Frozen State Deliveries . . . . .	150
6.4	Xenon Gas State Relaxation Studies . . . . .	152
6.4.1	Gas Relaxation Mechanisms . . . . .	152
6.4.2	T1 Measurements in Gas State . . . . .	156
6.5	Gas State Deliveries . . . . .	159

6.6	Hyperpolarized Xenon MRI at BWH . . . . .	161
6.6.1	Xenon Dissolved-State Imaging . . . . .	164
6.6.2	<i>In vitro</i> Rabbit Lung Imaging . . . . .	166
<b>7</b>	<b>ORIENTATIONAL LOW FIELD MRI</b>	<b>169</b>
7.1	Low Field MRI . . . . .	169
7.2	UNH Imager Description . . . . .	171
7.2.1	The Magnet . . . . .	171
7.2.2	Electronics . . . . .	176
7.2.3	Gas polarization and delivery . . . . .	179
7.2.4	MRI Techniques . . . . .	182
7.2.5	Human Imaging Protocols . . . . .	185
7.3	Results . . . . .	186
<b>8</b>	<b>CONCLUSIONS</b>	<b>192</b>
 <b>Appendices</b>		
<b>A</b>	<b>IRB HUMAN PROTOCOL APPROVAL</b>	<b>195</b>
<b>B</b>	<b>IACUC ANIMAL PROTOCOL APPROVAL</b>	<b>197</b>
	<b>Bibliography</b>	<b>199</b>

# List of Tables

1.1	MRI and NMR important physical properties of noble-gases $^{129}\text{Xe}$ and $^3\text{He}$ . Adapted from [9] . . . . .	5
1.2	$^{129}\text{Xe}$ reported polarization values obtained by other research groups. . . . .	15
2.1	Pressure broadening and shifting of the D1 line induced by optical pumping gases. Values reported by [61]. . . . .	31
2.2	Optimum running parameters of the polarizer for maximizing different values of interest regarding output polarization and production rate. . . . .	70
3.1	Comparison of stimulated and feedback power in the cavity with high and low modulation gratings at 20 A laser current. . . . .	97
6.1	Polarization recovery ratios after a freeze-thaw cycle using the spiral freeze-out.	144

# List of Figures

1-1	Simple optical pumping setup. 1) $B_0$ coils - for generating a uniform magnetic field; 2) Temperature controlled heating oven; 3) Pumped cell; 4) Laser; 5) Lens; 6) Polarizing-cube-splitter; 7) Quarter-wave-plate. . . . .	2
1-2	First human lungs image acquired with hyperpolarized xenon: a) Proton MRI images showing no signal over the lung space; b) Hyperpolarized $^{129}\text{Xe}$ MRI image showing excellent resolution over the lung space filled with gas; c) The first two images superposed. Adapted from [12]. . . . .	5
1-3	Dissolve-state images of brain, chest, and kidney in an anesthetized rat (left). On the right side are different proton MRI slices to help in locating the organs. Adapted from [14]. . . . .	6
1-4	a) Wash-out dynamics in a rat lungs after the xenon inhalation is stopped. The central peak corresponds to the gas phase xenon in the lungs and the three peaks at 191, 199, and 213 ppm correspond to xenon in dissolved phase. Adapted from [15]. b) Human brain xenon dissolved-state 2D CSI spectra superposed over a brain proton image. Adapted from [16]. . . . .	7

1-5	a) Chemical shift of hyperpolarized xenon signal absorbed in graphitized carbon (top), showing a shift of 10 ppm, and Na-Y zeolite, with a shift of 59 ppm. Adapted from [19]. b) Proton signal enhancement in deuterated benzene solution containing dissolved hyperpolarized xenon. Adapted from [20]. . . . .	8
2-1	$^{87}\text{Rb}$ energy levels when considering spin-orbit interaction, hyperfine interaction, and, finally, Zeeman splitting when placed into a weak magnetic field (not drawn to scale). . . . .	20
2-2	Rb optical pumping schematic for incident positive helicity circularly polarized light. . . . .	22
2-3	Simplified schematic of optical pumping for polarizing the valence electron of an alkali atom. In this schematic the spin of the Rb nucleus is neglected.	23
2-4	Rb-Rb spin-exchange: a) An example of interaction between two $^{87}\text{Rb}$ atoms and the probabilities for the final state after the collision; b) Spin distribution on the hyperfine levels for a spin temperature $\beta = \ln 2$ . Adapted from [55].	27
2-5	Nuclear spin effect on the electron polarization: a) Electron spin average for two different nuclear spins, $I=1/2$ and $I=7/2$ , as a function of the atom position from the wall. Adapted from [55].; b) Slowing-down factor as a function of electron polarization. Adapted from [30]. . . . .	28

2-6	a) Temperature in the center of the cell as function of the pumping laser power. The diamond points show the temperature reading of a thermocouple on the cell surface. b) Temperature distribution inside the cell for 2.9 W laser power. c) Temperature distribution inside the cell for 15 W laser power; the solid curve shows the curve resulted by scaling b) with the laser power. Figures are adapted from [66]. . . . .	37
2-7	a) Nitrogen pressure dependence for two different field values. b) Rb-Rb spin relaxation rate showing a linear dependence for both, low field and high field limits, with the Rb density. c) Rb relaxation mapping at low field as a function of N <sub>2</sub> pressure, defining different relaxation regions; the red cross shows the running parameters of UNH polarizer. Graphs a) & b) taken from [75] and c) from [71]. . . . .	44
2-8	Xe-Rb angular momentums schematic. . . . .	50
2-9	Spin-exchange schematic for: a) Xe-Rb van der Waals molecule formation after a third body collision; b) Xe-Rb binary collision. . . . .	52
2-10	Molecular lifetime regimes as a function of the buffer gas pressure. Adapted from [67]. . . . .	55
2-11	Laser absorption cross-section for different total pressure of the system considering an average D1 line broadening of 18 GHz/atm. . . . .	59



2-12 UNH polarizer concept. The Rb pre-saturator spiral saturates the gas mixture with Rb vapor before entering the optical pumping region. The very long high-temperature OP region assure an efficient absorption of the laser. Finally, the Rb is extracted from the gas mixture when is still illuminated by the laser and fully polarized, hence no Xe polarization is lost by spin-exchange with unpolarized Rb. . . . . 61

2-13 UNH polarizer logistic showing advantages (green) and disadvantages (red) of the main characteristics of our design. Most of the disadvantages are corrected by other implementations in the system. Low xenon production rate required to obtain high polarization output can be increased because of the low pressure regime and Rb pre-saturator. Lower laser absorption because of lower total pressure used is corrected by a long optical pumping cell. Rb density runaways from equilibrium in the optical pumping region because of the laser heating effects is greatly reduced by the pre-saturator. . . . . 64

2-14 Logistic of the high-pressure regime polarizers showing limited advantages (green) compared with the multiple disadvantages (red), largest handicap being the limitation for the total flow rates and, implicitly, Xe production rate. 65

2-15 Simulation geometry: 4 cm diameter, 180 cm long cylinder, presenting a "hot" OP region and a Rb trapping cooling region. . . . . 66

2-16 Polarization build-up for Xe and Rb as it travels from right to left inside the polarizer. The laser beam propagates from the left in the picture. Narrow laser is attenuated faster and Rb polarization is initially smaller than with the broad laser. Higher polarization is predicted for Xe with the narrow laser. Laser power is 100 W, flow conditions are "standard". Temperature is normalized to its maximum value of 160°C. . . . .	72
2-17 Output polarization as a function of high-temperature optical pumping region length. Our system has a 95 cm long optical pumping region, which should be sufficient for saturating Xe polarization. Shorter columns are predicted with the same performances. Flow conditions: "standard". . . . .	72
2-18 Broad Laser: flux attenuation as the laser travels through the column. After 85 cm the laser enters the "hot" 160°C optical pumping region. Laser power is 100 W, FWHM=1.5 nm. Flow conditions: "standard". . . . .	73
2-19 Narrow Laser: flux attenuation as the laser travels through the column. After 85 cm the laser enters the "hot" 160°C optical pumping region. Laser power is 100 W, FWHM=0.5 nm. Flow conditions: "standard". . . . .	73
2-20 Broad Laser: total laser flux attenuation as a function of oven temperature. At 200°C most of the broad laser is absorbed. Laser power is 100 W, FWHM=1.5 nm. Flow conditions: 10:350:1000 sccm Xe:N2:He, 500 T total pressure. . . . .	74
2-21 Narrow Laser: total laser flux attenuation as a function of oven temperature. At 160°C most of the broad laser is absorbed. Laser power is 100 W, FWHM=0.5 nm. Flow conditions: 10:350:1000 sccm Xe:N2:He, 500 T total pressure. . . . .	74

2-22	Skew light effect on the output polarization for the same 100 W laser power, but different spectrum widths. The effect is stronger on the narrower spectrum lasers. Flow conditions: "standard". . . . .	75
2-23	Laser power dependence for polarization: saturation is predicted for low Xe flow rates at very large laser powers. Numbers specify the Xe flow rate, "b" stands for broad laser, "n" stands for narrow laser. Flow conditions: "standard". . . . .	75
2-24	Temperature dependence for polarization showing a slight saturation at 150-160°C. The temperature dependence for the spin-destruction and spin-exchange rates are not included in the calculations and best estimate should be at 140-160°C. Flow conditions are 10:350:1000 sccm Xe:N2:He, 500 T total pressure.	76
2-25	Total pressure dependence of the polarization. A maximum platform is predicted for 300-700 T with the broad laser. The narrow laser shows a peak at 400 T. Flow conditions: 3.7 T Xe (10 sccm), 130 T N2 (350 sccm), He varied, 160°C, constant gas velocity. . . . .	76
2-26	Total flow dependence of polarization shows a peak at ~500 sccm, dropping fast for low flow rates. Flow conditions: 10 sccm Xe, 130 T N2 (flow rate varied), He buffer (varied), 500 T total pressure, 160°C. . . . .	77
2-27	Map of the polarization as a function of Xe flow rate for optimum theoretical parameters (500 sccm total flow) and optimum experimental parameters (1360 sccm). Flow conditions: Xe flow varied, 130 T N2, He counterbalanced Xe flow, total flow rate constant, 500 T total pressure, 160°C. . . . .	77
3-1	The UNH 7 FAP lasers setup (only 5 connected). . . . .	80

3-2	Multi-FAPs combined spectrum at 30 A and 25°C. . . . .	81
3-3	Typical optical setup for circular polarizing a fiber-coupled LDA: 1.fiber output; 2.collimating lens; 3.polarizing beam splitter cube; 4&4'.quarter-wave plates; 5.mirror. . . . .	82
3-4	Novel optical setup for fiber coupled high-power lasers: 1) half-circle fiber output; 2) collimating lens; 3) polarizing beam splitter cube; 4&4') quarter-wave plates; 5&5') plano-convex lenses; 6&7&8) dielectric mirrors; 9) mirror at the focal point for beam combination; 10) biconcave lens; 11) dielectric-mirror in kinematic mount; 12) final 3" plano-convex lens. . . . .	83
3-5	a) Fiber output configuration with only five FAPs connected.; b) Magnified image of the combined halves. c) Optics setup and the beam at one meter away. . . . .	84
3-6	Laser power measurements done for the 5 FAP system at different points. .	85
3-7	External cavities used in LDA frequency narrowing: a) Littrow cavity; b) Littman-Metcalf cavity. . . . .	87
3-8	Single bar laser diode array schematic. . . . .	88
3-9	Schematic of a Littrow cavity showing LDA, telescope with magnification M, and grating. Adapted from [97]. . . . .	89
3-10	Picture of the commercial Nuvonyx 5 bar stack laser. . . . .	91
3-11	Schematic of the UNH external Littrow cavity for the 5 bars stack. . . . .	92
3-12	Comparison between free running and spectrally narrowed external cavity laser linewidth. . . . .	94
3-13	Spectral linewidth for each array and all five arrays combined. . . . .	95
3-14	Image of the 5 LDA bars confirming the middle bar with the largest "smile".	95

3-15	External cavity tuning range and the spectral power of the narrowed laser beam. . . . .	98
4-1	UNH polarizer schematic. Main components are pointed in the figure. . . .	101
4-2	Gas flow panels schematic. Input panel: MFC-mass flow controller; 1-connection to calibration volume; 2-purifier; 3-bypass loop; 4-pressure Baratron gauge; 5-secondary vacuum pump; 6-Pirani gauge. Output panel: PC-pressure controller; 7-Pirani gauge; 8-ballast nitrogen input; 9-exhaust vacuum pump. Polarizer components: 10-polarizer; 11-down-tube; 12-freeze-out. A $\otimes$ refers to a valve. System not drawn to scale. . . . .	103
4-3	a) Lower half of the main column inside the oven (not insulated at the moment). The spiral Rb saturator is visible with the optical pumping straight inner tube. b) Top half of the main column (left) and the down-tube (right). The laser is turned on and the optics box is visible over the top of the column. The NMR coils are placed in position around the down-tube. . . . .	106
4-4	1-aluminum enclosure Faraday cage; 2-drive coil; 3-receive coil. The setup can be halfway open for easy access (as shown). . . . .	109
4-5	Flip angle calibration for: a) proton, b) xenon; obtained by amplitude increase in small steps. Proton $90^\circ$ is reached at 30% on power level 1 and at 30% on power level 2 for xenon, respectively. . . . .	113
4-6	Example of NMR signal from a proton calibration file shows SNR=30, FWHM=19.3 Hz, and $T_2^*=45$ ms. File was acquired with $90^\circ$ flip angle, 1024 averages, and TR=15 s. . . . .	116

4-7	Example of NMR signal from the hyperpolarized xenon shows SNR=104, FWHM=7.3 Hz, and $T_2^*=120$ ms. File was acquired with 90° flip angle, 4 averages, TR=20 s, and polarizer flow conditions of: 10:350:1000 sccm Xe:N2:He, total pressure 500 T. . . . .	117
5-1	$^{129}\text{Xe}$ polarization at optimum found running conditions. For comparison the theoretical numbers corresponding to the same flowing conditions and for 90 W broad laser power are also plotted. . . . .	121
5-2	Polarization dependence on xenon flow rate at different oven temperatures showing an optimum at 160°C. Flow conditions: total flow rate constant at 1360 sccm, total pressure constant at 500 T, N2 flow rate 350 sccm. . . . .	123
5-3	Polarization dependence on nitrogen partial pressure: saturation is obtained above 125 torr. Flow conditions: Xe flow rate constant at 20 sccm, total flow rate constant at 1070 sccm, total pressure constant at 500 T, temperature 160°C. . . . .	126
5-4	Nitrogen quenching probability, reported by Wagshul <i>et al.</i> [57], plotted together with the normalized Xe polarization numbers from Fig. 5-3 show that for our system saturation with N2 appears at a higher value than 60-100 T, considered sufficient in previous reports. . . . .	126
5-5	Polarization dependence on the xenon flow rate for three different total flow rates. Flow conditions: total flow rate constant for each set of data, total pressure constant at 500 T, N2 partial pressure ~130 T, 160°C temperature.	128

5-6	Polarization map using the frequency-narrowed LDA stack and two set of polarization numbers obtained with the broad laser for comparison. Flowing conditions are the optimum found for the broad laser with 1360 sccm total flow, 500 T total pressure, 130 T N <sub>2</sub> , and 160°C temperature. . . . .	129
5-7	Polarization dependence on the broad laser power for three different Xe flow rates. No saturation is observed for the 10 and 20 sccm Xe flow rates. For 50 sccm Xe flow rate is difficult to conclude. The flow conditions are: 10:350:1000 sccm Xe:N <sub>2</sub> :He for the 10 sccm Xe set, 20:350:1000 for the 20 sccm Xe set, respectively 50:960:350 for the 50 sccm Xe set. Total pressure was constant at 500 T total pressure, 155°C temperature. . . . .	132
5-8	Polarization dependence on the narrowed laser power showing a fast saturation at 52.5 A, a value much lower than expected. The flow conditions are: 30:350:1000 sccm Xe:N <sub>2</sub> :He, 500 T total pressure, 160°C temperature. . . .	132
5-9	Enriched 86%- <sup>129</sup> Xe polarization map plotted together with the highest obtained polarization number for natural xenon. Flow conditions: 1360 sccm total flow rate, 500 T total pressure, 130 T N <sub>2</sub> pressure, and 160°C temperature. Xe flow was counterbalanced with He. . . . .	134
5-10	Xenon magnetization (flow x polarization) - comparison between 86% enriched Xe and natural. The enriched xenon shows a much higher magnetization. . . . .	134
5-11	Overall comparison of the UNH polarizer performance with reported results of other research groups around the world. . . . .	135
6-1	Xenon phase diagram. Adapted from [103]. . . . .	138

6-2	Natural xenon relaxation rates in frozen state as a function of temperature and magnetic field. Adapted from [39]. . . . .	139
6-3	a) Typical design of a "cold-finger" or straight-tube xenon trap. b) Photo. . . . .	140
6-4	a) Novel design of spiral freeze-out xenon trap. The dewar is kept filled with liquid nitrogen, and can be easily lifted such the freeze-out is gradually inserted in the liquid nitrogen. b) Photo. . . . .	141
6-5	Multiple freeze-thaw cycles decay of the signal and recovery ratio measurement.	146
6-6	Frozen state relaxation and $T_1$ measurement. . . . .	147
6-7	Empirical exponential fit for the highest xenon polarization numbers as a function of its flow rate. . . . .	148
6-8	Polarized xenon production map considering a relaxation time in frozen state of 2.5 hours and a known initial xenon polarization dependence on its flow rate. Optimum xenon flow rate can be found for a final accumulated volume and final wanted polarization. . . . .	149
6-9	a) Frozen xenon delivery system: large cryogenic dewar, permanent magnet box, and the freeze-out ready for delivery. b) First hyperpolarized xenon image of the spiral freeze-out acquired at BWH after a frozen state delivery.	151
6-10	$T_1$ signal decay data points and fitted curve. . . . .	157
6-11	Xenon relaxation time overview measurements in the down-tube. . . . .	158
6-12	a) Gas delivery system with the transporting case, metal box enclosing the coil, and the delivery cell. b) Delivery cell inside the coil at 0.2 T magnet at BWH. . . . .	159



6-13	Separation of xenon in gas state and xenon dissolved in oil images. Bottom cell contains only xenon. The top cell is half filled with oil and half with xenon. Cells physical positioning are indicated by the dotted drawings. By taking two consecutive scans with TE values such in the first scan the gas and dissolved states are in phase (both have 0° phase) and in the second scan there is a difference of 180° between them (gas has 0° phase and dissolved has 180° phase), we can separate the images for the gas and dissolved states: a) image of the gas phase only; b) image of the dissolve in oil xenon only (lower half of the top cell). Imaging parameters: 128x64, FOV=20 cm, SW=16.6 kHz, TR=25 ms, TE=6.36 and 7.41 ms. . . . .	165
6-14	<i>In vitro</i> rabbit lungs images at 0.2 T obtained with hyperpolarized xenon: a) 55 cc xenon injected; b) 75 cc xenon injected. We used a gradient-echo centric pulse sequence, 128x64 overfilled to 256x256, FOV=20 cm, TR=8.7 ms, TE=40 ms. . . . .	167
6-15	T <sub>1</sub> measurement in rabbit lungs: first four data points correspond to the injection of the xenon inside the lungs, followed by the exponential decay of the signal. . . . .	167
7-1	Photographs of the system showing the B <sub>0</sub> coils: a) Large Coils: D=2m, ΔH=0.74m; b) Small Coils: d=0.86m, Δh=1.2m; Human subject is shown in imaging position. . . . .	172
7-2	Measured B <sub>0</sub> field deviation map (ppm). The plot was generated by moving a small water phantom along a 1 inch grid and recording the NMR frequency at each point. . . . .	173

7-3	a) $x,y$ -axis planar gradient conductor pattern; b) $z$ -axis planar gradient conductor pattern. . . . .	174
7-4	Gradient linearity plots for the $y$ and $z$ gradients, showing linearity for 50 cm along the central $y$ and $z$ axes, respectively. The gradient deviates no more than 0.4% from the linear fit showing slopes of $1.342(6) \times 10^{-3}$ and $4.824(7) \times 10^{-3}$ G/A/cm for $y$ (same as $x$ ) and $z$ , respectively. . . . .	175
7-5	Schematic of the low field imager. . . . .	176
7-6	Receive and transmit coil circuitry. . . . .	176
7-7	Photograph of the excite and receive coils: the large Helmholtz $B_1$ coil was bolted into the table and the receive coil was attached to it using foam spacers and plastic bolts. . . . .	178
7-8	a) Photograph of $^3\text{He}$ polarizer; b) Gas handling schematic (not drawn to scale). A $\otimes$ refers to a valve. . . . .	180
7-9	Single scan spectrum of a water sample showing a SNR of 30. . . . .	186
7-10	a) Images of $^3\text{He}$ cells; b) Longitudinal projection of a large water sample at 30 G. . . . .	187
7-11	Slice selection test at low field: a) no slice gradient over the two $^3\text{He}$ cells resulting in a 2D projection; b) with slice gradient on the lower cell is eliminated. . . . .	189
7-12	Coil response corrections for cell and lung images: a) and d) raw images; b) and e) coil resonance response obtained from the raw data without signal; c) and f) coil-response corrected images. . . . .	190
7-13	Human lungs image at 39 Gauss: FOV=50cm, SW=16.67 kHz, $T_E/T_R=10/100$ ms, data scans 128x64 overfilled to 256x256: a) horizontal (supine) orientation, b) vertical orientation. . . . .	191

# ABSTRACT

## HYPERPOLARIZED $^{129}\text{Xe}$ PRODUCTION AND APPLICATIONS

by

Iulian C. Ruset  
University of New Hampshire, May, 2005

Hyperpolarized  $^3\text{He}$  and  $^{129}\text{Xe}$  were initially developed and used in the nuclear physics community. Lately they are primarily used in Medical Resonance Imaging (MRI). Although first MRI polarized gas images were acquired using  $^{129}\text{Xe}$ , the research community has focused mostly on  $^3\text{He}$ , due to the well-known polarizing methods and higher polarization numbers achieved.

The main purpose of this thesis is to present a novel design of a large-scale SEOP polarizer for producing large quantities of highly polarized  $^{129}\text{Xe}$ . High Rb-Xe spin-exchange rates through long-lived van de Waals molecules at low total pressure, implemented in a novel counterflow polarizer design, resulted in xenon polarization as high as 50% for 1.2 liters/hour, with a maximum of 64% for 0.3 l/h. We characterized and improved the polarization process by finding the optimum operating parameters of the polarizer.

Two new methods to efficiently use high-power diode lasers are described: a new optical arrangement for a better beam shaping of fiber coupled lasers and the first external-cavity spectrum narrowing of a stack of laser diode arrays.

A new accumulation technique for the hyperpolarized xenon was developed and full recovery of polarization after a freeze-thaw cycle was demonstrated for the first time.

Two approaches for xenon delivery, frozen and gas states, were developed. Hyperpolarized xenon transportation to Brigham and Women's Hospital was successfully accomplished

for collaborative research. First MRI images using hyperpolarized xenon acquired at BWH are presented.

Final chapter is focused on describing a low field human MRI scanner using hyperpolarized  $^3\text{He}$ . We built a human scale imager with open access for orientational studies of the lung functionality. Horizontal and vertical human lung images were acquired as a first stage of this project.

# Chapter 1

## INTRODUCTION

### 1.1 Optical Pumping

The optical pumping (OP) of the alkali atoms was first predicted in 1950 and experimentally two years later by A. Kastler [1]. This earned him the Nobel Prize for Physics in 1966. Thereafter Bouchiat et al. [2] observed the enhancement for the nuclear spin polarization of the noble-gases when used as buffer gases in the alkali OP experiments.

By the term of "hyperpolarized gas" one should understand a non-zero nuclear spin gas in which nuclei spins are artificially aligned along the quantization axis defined by a uniform magnetic field. The most popular method for doing this is through the absorption of circularly polarized laser light. Typically the transfer of the angular momentum from the polarized laser photons to the noble-gas nuclei is intermediated by an alkali metal vapor. The method is called Spin Exchange via Optical Pumping (SEOP). It is based on polarizing the valence electron of the alkali by resonant absorption of the laser light (optical pumping or optical "depopulation"), enhancing a single state of the ground level.

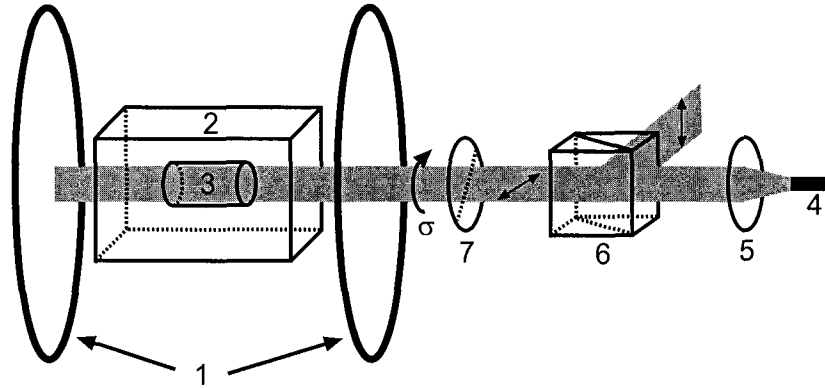


Figure 1-1: Simple optical pumping setup. 1)  $B_0$  coils - for generating a uniform magnetic field; 2) Temperature controlled heating oven; 3) Pumped cell; 4) Laser; 5) Lens; 6) Polarizing-cube-splitter; 7) Quarter-wave-plate.

Figure 1-1 shows a common optical pumping system. A spin exchange optical pumping cell is filled with a small amount of alkali metal and a mixture of gases: noble-gas to be polarized, nitrogen with the purpose of radiation quenching, and a buffer gas for pressure broadening of the alkali absorption line. The cell is placed inside a uniform low magnetic field for Zeeman splitting the Rb atom energy levels. Heating of the cell to 100-200°C is required in order to generate an optically-thick alkali vapor. The optical components have the purpose of shaping the laser beam and to transform it into circularly polarized light. The polarizing cube splitter divides the beam into two linearly-polarized halves with orthogonal polarization planes (as shown in the picture). Finally, the quarter-wave-plate transforms the linear polarized light into circular polarized light.

The vapor is illuminated by the continuous laser beam tuned to the alkali D1 absorption line. Because the incoming laser light is circular polarized, the angular momentum of the photons excites only the atoms from one of the two ground states. The result is the depopulation of this state and the atoms accumulate in a large number in the unpolarized state. Once they reach the polarized state they no longer absorb laser light since

the selection rules does not allow it. The nitrogen helps in quenching the alkali deexcitation radiation through the  $N_2$  molecule vibrational degrees of freedom. This prevents Rb depolarization through the absorption of emitted unpolarized radiation.  $^4He$  buffer gas is typically added to increase the total pressure inside the cell. The effect stands in broadening the D1 absorption line of the alkali vapor resulting in more absorbed light. This is not necessary if using narrow-frequency light sources such as solid-state Ti:Sapphire lasers or external-cavity frequency-narrowed laser diode arrays (LDAs). The limitation in power of the alkali vapor lamps or Ti:Sapphire lasers ceased with the appearance of the high-power diode laser arrays. Although their output spectrum is broader than the D1 absorption line, the overwhelming power of hundreds of watts currently available makes the diode lasers the normal choice for the latest projects involving Rb optical pumping.

The polarization transfer from the Rb valence electron to the noble-gas nucleus occurs through the Fermi-contact term in the dipole-dipole interaction. The result is a net increase with a large order of magnitude, typically 4-5, of the nuclear spin polarization from thermal Boltzmann distribution of the spins when placed into a magnetic field.

## 1.2 $^{129}Xe$ and $^3He$ : Properties and Applications

The initial purpose of the hyperpolarized gases was to serve as polarized targets in fundamental nuclear physics experiments. Hyperpolarized  $^3He$  has been used as a target in particle physics experiments leading to the discovery of the spin-structure function of the neutron[3]. Also, hyperpolarized  $^3He$  is presently used as a cold neutron spin filter and as a spin analyzer in the  $npd\gamma$  experiment at LANL for measurement of the parity violation in the weak interaction between proton and neutron [4, 5]. Both gases are used in searches

for an atomic electric dipole moment[6]. New applications can be found in the quantum computing research [7].

The most revolutionary use still is the implementation of the hyperpolarized gases as imaging agents in the medical magnetic resonance imaging (MRI). It was started by the Stony Brook/Princeton collaboration in 1994 [8] using hyperpolarized  $^{129}\text{Xe}$ .

The limitation in obtaining high xenon polarization moved the community attention towards  $^3\text{He}$ , with longer relaxation times and well-known polarization methods.  $^3\text{He}$  was used extensively in determining lung structure and functionality. The helium images resolution is typically above the ones acquired using hyperpolarized xenon because of the higher  $^3\text{He}$  polarization attained.

Hyperpolarized gases are background-free imaging agents. The lower proton density in the lung tissue, when compared with the rest of the body or organs, makes proton lung imaging very difficult, if not impossible. In the case of proton imaging there is a lack of signal over the lung region, as can be seen in see Figure 1-2a. The MRI images obtained with hyperpolarized gases offers superior resolution and information about the gas distribution inside the lung (Figure 1-2b). However, the noble-gas polarization is nonrenewable as it is for the proton. This translates into the disadvantage of limited resources in the case of an error, but offers the advantage of extremely short imaging times, since no recovery of the polarization is needed, as it is in the case of protons. Moreover, gas polarization can be destroyed intentionally in certain regions, offering the possibility of tracing its motion.

Physical properties important from the NMR and MRI point of view for  $^{129}\text{Xe}$  and  $^3\text{He}$  are listed in Table 1.1. Both have nuclear spin  $1/2$  and, because of their lack of quadrupole moment, they present long relaxation times. The high limit for the  $T_1$  spin-lattice relaxation times are given at one atm pressure of pure gas: 744 h for  $^3\text{He}$  and 4.1 h for



Parameter	Units	$^{129}\text{Xe}$	$^3\text{He}$
Nuclear spin, $K$	$\hbar$	$\frac{1}{2}$	$\frac{1}{2}$
Natural abundance	%	26.4	$1.37 \times 10^{-4}$
Gyromagnetic ratio, $\gamma$	kHz/Gauss	1.1778	3.2433
Normalized gyromg. ratio, $\gamma/\gamma_H$		0.276	0.762
$T_1$ relaxation time limit	hours/atm	4.1	744
Relaxation caused by $\text{O}_2$	$\text{s}^{-1}\text{torr}^{-1}$	$4.97 \times 10^{-4}$	$5.13 \times 10^{-4}$
Self-diffusion coefficient, $D_0$	$\text{cm}^2/\text{s}$	0.061	2.05
Diffusion coefficient in air, $D$	$\text{cm}^2/\text{s}$	0.14	0.86
Ostwald coefficient in blood, $L$		0.17	0.0085
Chemical shift range	ppm	7500	0.8

Table 1.1: MRI and NMR important physical properties of noble-gases  $^{129}\text{Xe}$  and  $^3\text{He}$ . Adapted from [9]

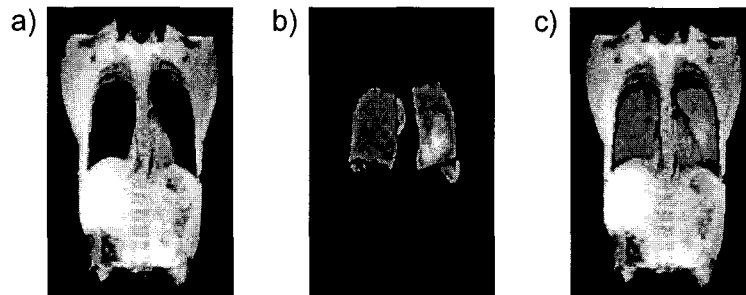


Figure 1-2: First human lungs image acquired with hyperpolarized xenon: a) Proton MRI images showing no signal over the lung space; b) Hyperpolarized  $^{129}\text{Xe}$  MRI image showing excellent resolution over the lung space filled with gas; c) The first two images superposed. Adapted from [12].

$^{129}\text{Xe}$ . Experimentally, relaxation times are typically much lower: up to 100 h for  $^3\text{He}$  and up to 3 h for  $^{129}\text{Xe}$ . The difference is believed to be mostly caused by interactions with the container walls. Recent measurements [10] for  $^{129}\text{Xe}$  showed Xe-Xe molecular interactions limiting  $T_1$  to 4.1 h from its previous predicted high limit of 56 h/amagat [11].

Both gases have relatively large gyromagnetic ratios:  $^3\text{He}$  presenting a factor of 2.76 over  $^{129}\text{Xe}$ , meaning that, for the same level of polarization, the NMR signal-to-noise ratio from  $^3\text{He}$  is 2.76 higher than for  $^{129}\text{Xe}$ .

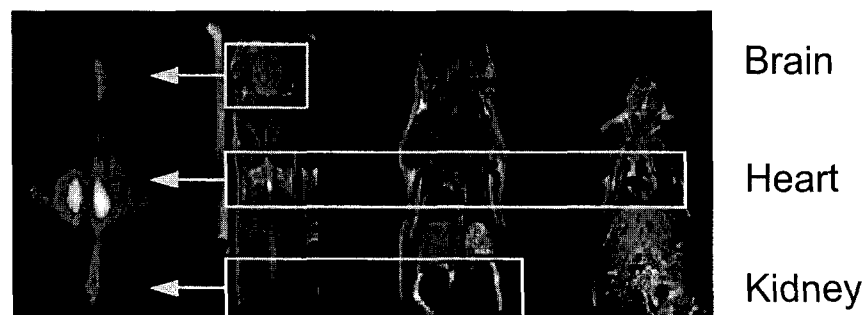


Figure 1-3: Dissolve-state images of brain, chest, and kidney in an anesthetized rat (left). On the right side are different proton MRI slices to help in locating the organs. Adapted from [14].

Helium is chemically inert and practically insoluble. Xenon is highly lipophilic<sup>1</sup> and therefore soluble in blood and tissue. It is well-known by the medical community [13] for its anesthetic properties when inhaled in large concentrations (over 70%). For MRI with hyperpolarized xenon this may set an ultimate limit of inhaled xenon in a single breath. Figure 1-2 shows the first spin-density human lung image, obtained at University of Virginia after a collaboration with the Princeton group, responsible with the production of hyperpolarized Xe. The image was acquired in a healthy volunteer using 71% enriched xenon

The large solubility of xenon in the blood and tissue makes it an excellent tool for dissolved-state imaging, as it was demonstrated by the group of T.E. Chupp at the University of Michigan in an anesthetized rat. Figure 1-3 shows the xenon dissolved in brain, heart, and kidney (right images are obtained by proton MRI and used for locating the organs).

A major advantage of  $^{129}\text{Xe}$  versus  $^3\text{He}$  is its large chemical shift which is strongly dependent on its surroundings. The large electron cloud of xenon leads to shifts of the

---

<sup>1</sup>lipophilic - having an affinity for lipids (e.g. fat).

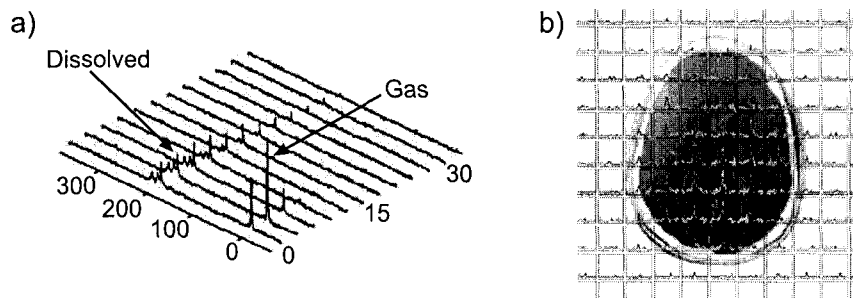


Figure 1-4: a) Wash-out dynamics in a rat lungs after the xenon inhalation is stopped. The central peak corresponds to the gas phase xenon in the lungs and the three peaks at 191, 199, and 213 ppm correspond to xenon in dissolved phase. Adapted from [15]. b) Human brain xenon dissolved-state 2D CSI spectra superposed over a brain proton image. Adapted from [16].

nucleus NMR frequency by interacting with surrounding atoms and molecules. The shift can be as high as 7500 ppm [17] for specific chemical compounds. This property is frequently used in probing chemical and biological environments. The chemical shift in dissolved-state MRI reaches up to 220 ppm in oxygenated red blood cells [18]. Novel MRI techniques, such as the chemical shift imaging (CSI), can separate images of dissolved xenon if the chemical shifts frequencies are clearly separated. Figure 1-4a shows the wash-out dynamics in a rat's lungs. The peak at 0 ppm corresponds to the hyperpolarized xenon in gas phase, and the three peaks in the region of 200 ppm correspond to xenon in dissolved phase. Recently, using a polarizer allowing production of more than 0.5 liters of xenon with polarization of  $\sim 14\%$ , Kilian *et al.* [16] were able to demonstrate for the first time a 2D CSI image in a human brain (shown in Figure 1-4b). The dissolved-state imaging is still under intense research and is limited mostly by the low xenon quantities and polarization.

Xenon has a high absorption energy ( $\sim 0.1$  eV) on most surfaces; in combination with its chemical shift properties, it results in the capability of surface studies using hyperpolarized xenon. Figure 1-5a presents the xenon chemical shift absorbed on powdered solids like

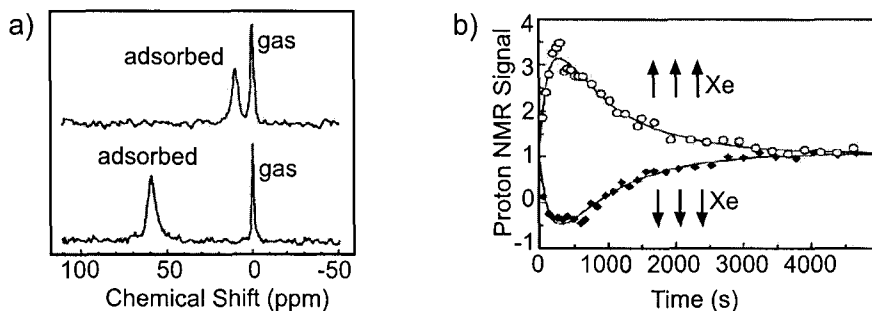


Figure 1-5: a) Chemical shift of hyperpolarized xenon signal adsorbed in graphitized carbon (top), showing a shift of 10 ppm, and Na-Y zeolite, with a shift of 59 ppm. Adapted from [19]. b) Proton signal enhancement in deuterated benzene solution containing dissolved hyperpolarized xenon. Adapted from [20].

graphitized carbon and Na-Y zeolites.

Numerous experiments are also related to the polarization transfer from  $^{129}\text{Xe}$  to other atoms, such as  $^{131}\text{Xe}$ ,  $^{13}\text{C}$ , or  $^1\text{H}$ . For transferring the polarization from  $^{129}\text{Xe}$  to other atoms, different methods are being used, such as low-field thermal mixing [21], high-field cross-polarization [22], and, the most common, SPINOE (spin polarization-induced nuclear Overhauser effect) [20]. Figure 1-5b shows the enhancement of the proton NMR signal in deuterated benzene solution containing dissolved hyperpolarized xenon. The fact that the enhancement is caused by xenon is demonstrated by inverting the xenon magnetization (bottom), with proton magnetization following the inversion. Many of these applications, such as the ones presented in Figure 1-5 involving xenon chemical shift sensitivity and xenon polarization transfer were performed by the group of A. Pines at Berkeley.

Due to oxygen paramagnetic properties both gases relax much faster in its presence. Oxygen dependence has been measured (see table) and  $^3\text{He}$  is used in obtaining perfusion maps for the lungs by measuring the local relaxation time for the hyperpolarized gas [23, 24].

Diffusion coefficient for xenon in air is  $\sim 6$  times smaller at one atmosphere than for helium, therefore restricted diffusion measurements have a better accuracy at small scales

if xenon is used instead of helium. Moreover, the difference between diffusion coefficients in mixtures with large self-concentrations is much higher. Multiple experiments using primarily  $^3\text{He}$  are reported as relating lung structure to the ADC (apparent diffusion coefficient) (e.g. [25, 26]). For qualitative studies of gas diffusion,  $^{129}\text{Xe}$  should be superior to  $^3\text{He}$ . Also, the imaging gradients cause a higher diffusive attenuation on helium than on xenon in the MRI signal. A helium atom, with a diffusion coefficient of  $0.86\text{ cm}^2/\text{s}$  in air [26], will traverse  $0.41\text{ mm}$  in one ms, compared with xenon which traverses only  $0.12\text{ mm}$  in one ms. Other diffusion measurements are related to xenon GD-NMR (gas diffusion nuclear magnetic resonance) to measure restriction sources of gas motion. In a series of experiments, the group of R. Walsworth [27] at the Harvard-Smithsonian Center for Astrophysics was able to measure the pore surface-to-volume ratio and tortuosity in random glass bead containers, limestone, and sandstone.

Xenon is naturally abundant and can be extracted from the atmosphere by fractional distillation of the air. Natural xenon contains only 26.4% of the  $^{129}\text{Xe}$  isotope, but it can be isotopically enriched.  $^3\text{He}$  has a limited supply and is presently extracted from the decay of tritium.  $^3\text{He}$  cost is at the same level with highly enriched xenon  $\sim\$200/\text{liter}$ . Natural xenon, however, has an extremely low cost, with the price below  $\$5/\text{liter}$  (SpecGas Inc., Ivyland, PA). From a financial point of view, natural xenon seems to be the best choice offering the lowest price per polarizable atom.

Detailed reviews for the use of hyperpolarized noble-gases are done by B.M. Goodson [28] for  $^{129}\text{Xe}$  and by Moller *et al.* [9] for  $^3\text{He}$ .

### 1.3 Polarizing Helium

The SEOP method for polarizing the  $^3\text{He}$  is well-known and characterized [29, 30].  $^3\text{He}$ , just like  $^{129}\text{Xe}$ , has no quadrupole moment, thus is characterized by a long  $T_1$  spin-lattice relaxation time. A major disadvantage of helium SEOP is that the spin-exchange rates between Rb and  $^3\text{He}$  are very small and it requires a long time for the spin transfer to take place (up to days). Recent studies involving also the UNH group have shown that using a second alkali metal, such potassium, with a higher spin-exchange efficiency with  $^3\text{He}$  can reduce the pump-up time as short as two hours [31].

A second method for polarizing  $^3\text{He}$  was developed soon after the discovery of hyperpolarized  $^3\text{He}$  via SEOP [32]. The method called Metastability Exchange Optical Pumping (MEOP) and is based on the metastable excited state  $2^3S_1$  of the  $^3\text{He}$  atom. An RF pulse excites part of the atoms from the ground state into the metastable state and a circular polarized laser light with 1083 nm wavelength, corresponding to the  $2^3S_1 \rightarrow 2^3P_1$ , pumps the  $^3\text{He}$  atom into a single level of the metastable  $2^3S_1$  state. The hyperfine interaction within the excited polarized  $^3\text{He}$  atom assures a fast mechanism for polarization transfer from the electron to the nucleus. Finally through binary collisions the polarization is transferred from the polarized metastable atoms to the disoriented ground state  $^3\text{He}$  atoms. The result is a polarized ground state  $^3\text{He}$  atom and an unpolarized atom in the metastable excited state, which will be pumped again by the laser. A low pressure below 10 Torr is required inside the cell for the metastable state to survive. Only small quantities can be polarized by MEOP at once, thus to accumulate large quantities of gas a compressor and a storage cell are needed. Special materials are required for these components in order to reduce

the relaxation of the hyperpolarized gas caused by the wall interactions. The advantage of the MEOP over the SEOP is the fast spin-exchange mechanism, about  $2 \times 10^4$  higher than SEOP [33]. To polarize a cell containing few Torr of  $^3\text{He}$  through MEOP one needs only one minute to reach 60% polarization, compared with hours to days for SEOP cells. The laser sources for MEOP (1083 nm) are not as commonly available as for SEOP (795 nm). Lasers typically used are the neodymium-doped lanthanum magnesium hexaluminate (LMA) pumped with an arc lamp or by an  $\text{Ar}^+$  or diode laser. Diode lasers have been implemented [34], but the power available is still very small (50 mW).

A state-of-the-art  $^3\text{He}$  polarizer running in the metastability exchange regime was developed at the University of Mainz [35, 36] and it is used in collaborations for MRI experiments using hyperpolarized  $^3\text{He}$ . The polarizer can produce up to 1 liter/hour of 50% polarized  $^3\text{He}$  and higher polarization can be obtained for lower flow rates. Recently a more compact and less-expensive design was demonstrated at NIST [37] being able to generate 1 liter/hour of 15% polarized helium.

## 1.4 Polarizing Xenon

Hyperpolarized  $^{129}\text{Xe}$  offers multiple advantages over  $^3\text{He}$  despite its lower gyromagnetic ratio or its lower spin-lattice relaxation time. It is natural abundant with no limitation on its supply, has a very low price, and has a high solubility offering dissolved MRI possibilities. Also, its chemical shift can be used in dissolved state imaging.

The methods for polarizing  $^{129}\text{Xe}$  are similar to the  $^3\text{He}$  SEOP to some degree. There are certain differences between the two. The spin-exchange rates with the alkali metal are an order of three higher for  $^{129}\text{Xe}$  requiring only tens of seconds for the pump-up time

compared with hours to days for  $^3\text{He}$ . Also,  $^{129}\text{Xe}$  presents additional mechanism for the spin-exchange, mainly at low pressures, coming from the long-lived Van der Waals Rb-Xe molecules.

Since present work will focus on the performances of a novel  $^{129}\text{Xe}$  polarizer, it calls for a short history of the research done in this field. Most of the initial studies on the optical pumping and spin transfer processes were done on closed cells. The first optical pumped hyperpolarized xenon was reported by B.C. Grover in 1978 [38]. Using a small amount of xenon gas, 0.5 Torr of 65% enriched xenon, and 500 Torr of  $^4\text{He}$  buffer gas in a 15 cc spherical Pyrex cell the author was able to measure 10%  $^{129}\text{Xe}$ . The cell was heated up to  $85^\circ\text{C}$  for the Rb vapor to reach a significant value for optical pumping.

The first MRI images with hyperpolarized  $^{129}\text{Xe}$  were acquired using closed cells provided with break seals for gas release after 75 ml of 70% enriched xenon was polarized to 35% [8]. The need for larger gas quantities resulted in the development of two distinct polarizing methods: the "batch" and the continuous-flow method.

#### 1.4.1 The "batch" method

The "batch" method is based on polarizing batches of xenon. An isolated cell provided with valves is regularly filled with fresh gas mixture. After the xenon is polarized the gas mixture is cooled down to eliminate Rb vapor and transferred. Furthermore, the xenon can be separated from the buffer gases by freezing it into a liquid nitrogen cryogenic trap. The frozen xenon has relaxation time in the order of hours up to days, depending strongly on the temperature and slightly on the holding field [39, 40, 21]. At liquid nitrogen temperature and a moderate magnetic field ( 500 Gauss)  $T_1$  is around 3 hours, which allows for xenon accumulation with acceptable loss in polarization.



The batch method was successfully implemented at Berkeley by the group of Alexander Pines [19]. Surface studies of adsorbed xenon were done using 0.5% optical pumped polarized xenon.

The Michigan group lead by T.E. Chupp has developed also a batch polarizing system [41]. The system was provided with a cryogenic accumulation system and was capable to produce batches of 157 cc of 7.5% polarized xenon every 5 minutes using two fiber coupled LDAs with a 30 W total laser power and an oven temperature between 80 and 120°C. The cell contained 1700 Torr of natural xenon and 150 Torr of nitrogen, placing the polarizer in the high pressure limit.

The highest  $^{129}\text{Xe}$  polarization of 70% reported so far in literature was achieved in a batch system [42] by the Marburg group in Germany using a Ti: Sapphire laser with a 2 W output power. They achieved this polarization in a low pressure regime with a gas mixture of natural xenon and nitrogen only, keeping the total pressure in the system constant at 75 Torr. The partial pressure of xenon was varied from 0.375 to 57 Torr and  $^{129}\text{Xe}$  polarization was highest at lowest concentration, decreasing to 20% for high xenon concentrations. Temperature ranged from 90 to 115°C. The polarization build-up time was measured between 7 and 30 seconds. Although not a continuous flow system, this work is important to us because it was the first low pressure polarizer reported.

#### 1.4.2 The continuous flow method

The continuous flow method takes advantage of the fast spin-exchange rates between Rb-Xe, and was developed in Happer's group at Princeton [43, 44]. Using a high power AlGaAs laser diode with an output of 140 Watts and a  $\sim 2$  nm FWHM centered on Rb D1 absorption line of 794.7 nm, the Princeton group was able to obtain 1 liter of xenon with 5% polarization

[44]. The gas mixture contained 98%  $^4\text{He}$ , 1% Xe, and 1%  $\text{N}_2$  and the cell was filled with 10 amagat<sup>2</sup> of gas mixture to take advantage of the Rb D1 resonant absorption broadening due to the high pressure. For 10 amagat of gas mixture in the cell the Rb absorption profile broadens to 0.3 nm at the FWHM. The authors claim an increase in laser absorption by a factor of 60 than without pressure broadening.

Based on this design, commercial polarizers became available through MITI (Magnetic Imaging Technologies Inc.), started in 1996 by members of the Princeton group. MITI was later bought by Amersham Health, recently acquired by GE. The commercial version of the polarizer works also in the high pressure regime (10 atm) and is capable to polarize both  $^{129}\text{Xe}$  and  $^3\text{He}$ . Xenon polarizations between 2 and 20% are attainable for flow rates as high as 1 liter/hour.

Recently the group of Clifford Bowers and co-workers from University of Florida reported a high capacity production system with numbers for polarization over 65% [45, 46]. Their design is similar with the Princeton group with a different geometry for the cell and a powerful Coherent seven bars diode laser with an output power of 210 Watts and a full width of 1.6 nm. The gas mixture was previously prepared with equal quantities of xenon and nitrogen of 1%, 2% and 5%. Several studies on polarization dependence on total pressure, gas mixture, and laser power were done and the results will be used for comparison with our work. The polarizer operates in the moderate-high pressure regime of 2.5-7 atm and the temperature used for the pumping cell ranged from 140 to 165°C. A maximum polarization of 67% was reported for a pressure of 3 atm, 165°C temperature, and a laser power of 150 Watts, for a gas mixture of 0.6% Xe (86% enriched  $^{129}\text{Xe}$ ), 1%  $\text{N}_2$ , and 98%  $^4\text{He}$ , and a

---

<sup>2</sup>1 amagat = density of an ideal gas at STP conditions and equal to  $2.69 \times 10^{19} \text{ cm}^{-3}$

Group [ref.]	Laser Power (W)	Pressure (atm)	$\beta_{129}$ (%)	$^{129}\text{Xe}$ Flow (sccm)	Polarization (%)
Princeton [44]	50	10	71.0	6.0	5
Princeton [47]	100	10	71.0	3.2	18
Washington [48]	40	7	26.4	0.6	10
Marburg [42]	2	0.1	26.4	0.1-0.8	70-20
U. Michigan [41]	30	2.4	26.4	8.3	7.5
U. Florida [46]	>150	2.4	26.4	0.65	67
U. Florida [46]	210	2.6	86.0		46
U. Florida [45]	210	2-5	86.0	4.13	40
U. Florida [45]	210	2-5	26.4	1.96	23
U. Florida [45]	210	2-5	26.4	4.91	12

Table 1.2:  $^{129}\text{Xe}$  reported polarization values obtained by other research groups.

flow rate of 2.45 sccm<sup>3</sup> xenon flow rate. The laser power dependence showed a saturation of the polarization after a certain level. Instabilities of the cell temperature could be observed due to the heat generated by the laser absorption. The polarization seemed to increase by going to low total pressures, but the authors didn't examine the very low pressures regime. Dependence of the polarization on the total flow rate for a constant total pressure was studied showing an increase of the polarization by going to higher flow rates (higher flow velocities). For a pressure of 4.5 atm the polarization reached saturation at  $\sim 150$  sccm and stayed constant for up to 540 sccm, the highest flow rate tested. Certainly there is a flow rate after which the polarization should decrease because of not sufficient contact time between the Rb and Xe. The polarization data points graphed versus the xenon concentration in the gas mixture point to the fact that low  $^{129}\text{Xe}$  concentration in the mixture leads to higher polarization. As a conclusion of these studies one would expect the highest polarization to occur for a low concentration of xenon, an optimum total flow rate, a moderate laser power, and a low to moderate pressure.

---

<sup>3</sup>sccm - Standard Cubic Centimeters per Minute

The UNH polarizer, main subject of this thesis, is a continuous flow polarizer presenting major differences regarding the design and physical operating parameters. The polarizer works in the low pressure regime, below atmospheric pressure, and with a novel concept of counterflowing the gas against the laser light. Innovative research was done in optimizing the laser beam shape and laser spectrum. In our system each gas component of the mixture can be independently controlled together with the total pressure, therefore an optimum operating regime could be searched and found. In Table 1.2 are presented the polarization numbers found in literature and obtained by different research group and will be a good comparison term with the UNH results.

## 1.5 Thesis Summary

The thesis contains six chapters, as follows:

- Chapter one, *Introduction*, reviews the hyperpolarized gases applications and polarizing methods.
- Chapter two, *Theoretical Background*, focuses the theory of the Rb optical pumping and the spin transfer to  $^{129}\text{Xe}$ . A 1D simulation program was developed based on the UNH polarizer physical parameters and optimum predicted parameters as well as theoretical results are shown.
- Chapter three, *Lasers and Optics*, concentrates on the lasers and optical arrangements developed in our group. Two different setups are presented: first is a novel optical arrangement for optimizing the shape of the output beam from fiber-coupled diode

lasers; the second is based on an external Littrow cavity used in narrowing the output spectrum from a stack of laser diode arrays.

- Chapter four, *UNH Xenon Polarizer*, makes a physical overview of the UNH polarizer and describes the  $^{129}\text{Xe}$  polarization determination method.
- Chapter five,  *$^{129}\text{Xe}$  Polarization: Results and Discussions*, presents the performance of the polarizer. Optimum experimental parameters, such as temperature, N<sub>2</sub> partial pressure, gas mixture and flow rate were found and they are compared with theoretical predictions.
- Chapter five, *Accumulation, Recovery and Delivery of Polarized Xenon*, describes a novel design for the accumulation freeze-out allowing full recovery of polarization after a freeze-thaw cycle. Two different delivery methods for the frozen and the gas state of the hyperpolarized xenon were also developed and are presented. Finally, the hyperpolarized xenon was delivered to Brigham and Women's Hospital in Boston for collaborative research and first MRI results are presented.
- Chapter six, *Orientational Low Field MRI*, describes a very low field imaging system built at UNH for orientational studies of human lungs. Using hyperpolarized  $^3\text{He}$  we acquired supine and upright 2D lung images of a human subject.
- Chapter seven, *Conclusions*, reviews the results of this work and underlines its relevance and implications on future hyperpolarized gas applications.

## Chapter 2

# THEORETICAL BACKGROUND

### 2.1 Rubidium Optical Pumping and Polarization

#### 2.1.1 Rubidium for Optical Pumping

Optical pumping relies on the valence electron of alkali metals, which is polarized through resonant absorption of circularly polarized light corresponding to the D1 transition energy (e.g. [49, 50]). Rubidium is very suitable and the most commonly alkali met in optical pumping experiments, especially because of its low melting point of 39°C, resulting in a high vapor density at relative moderate temperatures. Rubidium vapor density can be estimated from the equilibrium absolute temperature  $T$  using [51]:

$$[Rb] = \frac{10^{10.55 - \frac{4132}{T}}}{1.38 \times 10^{-16} T} \text{ (cm}^{-3}\text{)} \quad (2.1)$$

Typically temperatures in pumping mixtures are 80-200°C resulting in Rb vapor densities of  $10^{12}$ - $10^{15}$   $\text{cm}^{-3}$ . Another advantage is the large separation between the D1 (794.7 nm) and D2 (780.0 nm) lines, which allows the use of common diode lasers without restrictions regarding their spectrum, which is typically much narrower than the separation between the lines.

Natural rubidium comes in two stable isotopes:  $^{85}\text{Rb}$  with 72.2% and  $^{87}\text{Rb}$  with 27.8%. With  $Z=37$  the atomic structure is  $1s, 2s, 2p, 3s, 3p, 3d, 4s, 4p, 5s$ . The spin-orbit interaction lowers the  $5s$  energy level below  $4d$  and  $4f$  levels, therefore Rb atoms are characterized by the single electron in the  $5s$  state. The first excited states are the  $5p_{1/2}$  with the corresponding D1 line  $\lambda=794.7$  nm, and  $5p_{3/2}$  with the corresponding D2 line  $\lambda=780.0$  nm. The electron total angular momentum is  $\vec{J} = \vec{S} + \vec{L}$ , where  $S=1/2$  is the electron spin, and  $\vec{L}$  is the orbital angular momentum with  $L=0$  for the  $s$  state, and  $L=1$  for the  $p$  states. Both isotopes have nuclear spins:  $I=5/2$  for  $^{85}\text{Rb}$  and  $I=3/2$  for  $^{87}\text{Rb}$ , respectively. The atom total angular momentum is defined as  $\vec{F} = \vec{J} + \vec{I}$ .

When a magnetic field  $B_0$  is applied the Hamiltonian for an alkali atom can be written as:

$$H = A\mathbf{I} \cdot \mathbf{S} + g_s\mu_B S_z B_0 - \frac{\mu_I}{I} I_z B_0 \quad (2.2)$$

where the first term represents the hyperfine interaction between the electron and the nuclei and the last two terms characterize the interactions of the magnetic field with the electron and the nuclei, respectively. Typically magnetic field values used in optical pumping setups are small, such that the hyperfine interaction is dominant and the eigenstates for the Hamiltonian in Eq. 2.2 are also eigenstates of the total angular momentum  $\mathbf{F}$  and its projection  $F_z$ . A detailed calculation of the energy levels is given in [50].

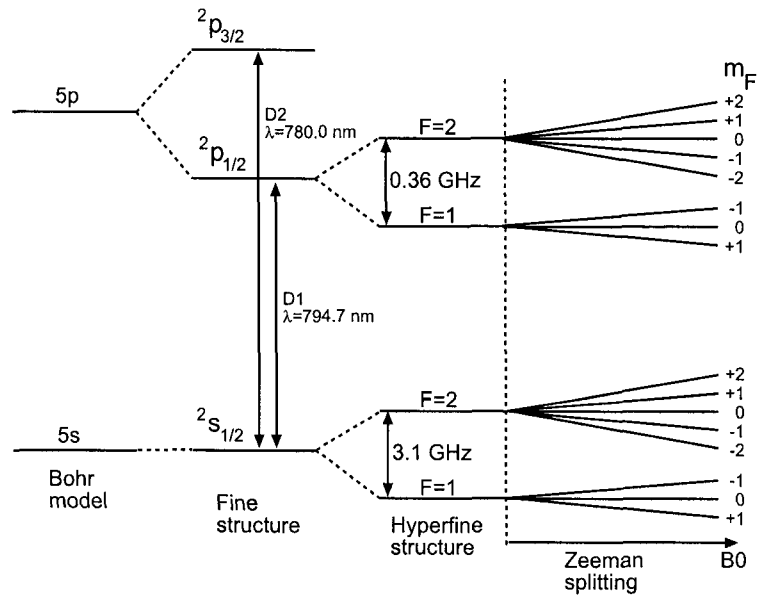


Figure 2-1:  $^{87}\text{Rb}$  energy levels when considering spin-orbit interaction, hyperfine interaction, and, finally, Zeeman splitting when placed into a weak magnetic field (not drawn to scale).

In Figure 2-1 are shown the  $^{87}\text{Rb}$  energy levels schematic as various interactions are added to the Bohr model. The separation between energy levels on the diagram are unscaled. A similar diagram can be drawn for the  $^{85}\text{Rb}$  isotope, with the difference being that the total angular momentum values are now  $F=2,3$  for the ground state  $5s_{1/2}$  and the first excited state  $5p_{1/2}$ . In the presence of a magnetic field Zeeman splitting of the atomic energy level is produced. The Bohr energy levels are separated by energies in the order of  $1 \text{ eV}$ , the fine structure substates, such as  $5p_{1/2}$  and  $5p_{3/2}$ , are separated by energies in the order of  $10^{-3} \text{ eV}$ , and the hyperfine states are separated by energies in the order of  $10^{-6} \text{ eV}$ . The Zeeman levels are separated by energies in the RF range and are proportional with the applied field. For  $^{85}\text{Rb}$  the separation between two consecutive Zeeman levels is  $\sim 0.5 \text{ MHz/Gauss}$  and  $\sim 0.7 \text{ MHz/Gauss}$  for  $^{87}\text{Rb}$ .



### 2.1.2 Optical Pumping Equations

The electron in one of the ground state levels can suffer transitions to higher energy level states by absorption of photons with matching wavelengths. The selection rules for the transition correspond to the incident photon polarization with respect to the magnetic field. By irradiating with a circularly polarized beam an ensemble of Rb atoms the allowed transitions are only  $\Delta m_F = \pm 1$ . If the incoming beam has positive helicity  $\sigma^+$  with respect to the magnetic field direction, then the electron can move only into the higher levels such that  $\Delta m_F = 1$ . The lifetime of the excited state is only  $10^{-8} - 10^{-9}$  s and the electron decays back into one of the ground state following the selection rule of:  $\Delta m_F = 0, \pm 1$ . The net result of continuous pumping with  $\Delta m_F = 1$  is a strong depopulation of the low  $m_F$  number states towards the highest  $m_F$  ground state. For  $\sigma^+$  incident light the Rb atoms will end in  $m_F = 2$  state for  $^{87}\text{Rb}$  and  $m_F = 3$  for  $^{85}\text{Rb}$ . This can be seen from the optical pumping schematic for the two isotopes in Figure 2-2. If the polarized light helicity is negative,  $\sigma^-$ , with respect to the magnetic field the process is reversed, with the lowest  $m_F$  numbers being populated (polarized).

A simplified schematic of Rb atomic levels which neglects the nuclear spin and the hyperfine structure is shown in Figure 2-3. Neglecting the nuclear spin is generally accepted as the nuclear spin is just a reservoir of angular momentum, and, eventually, just slows down the pumping process by the extra number of photons required to reach the final  $m_F$  polarized state [30, 52]. The Doppler broadening effect on the D1 absorption line makes also the hyperfine structure unresolved, and, to a good approximation, we can consider Rb as a zero nuclear spin atom from the absorbed energy point of view.

This zero-nuclear spin approximation is not acceptable in regions such as the vicinity of the cell walls, where the Rb depolarization rate is very high and a steady-state is not

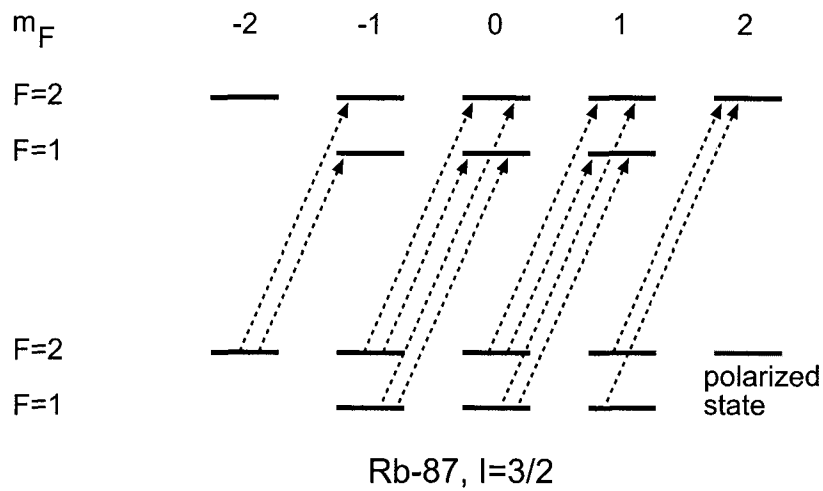
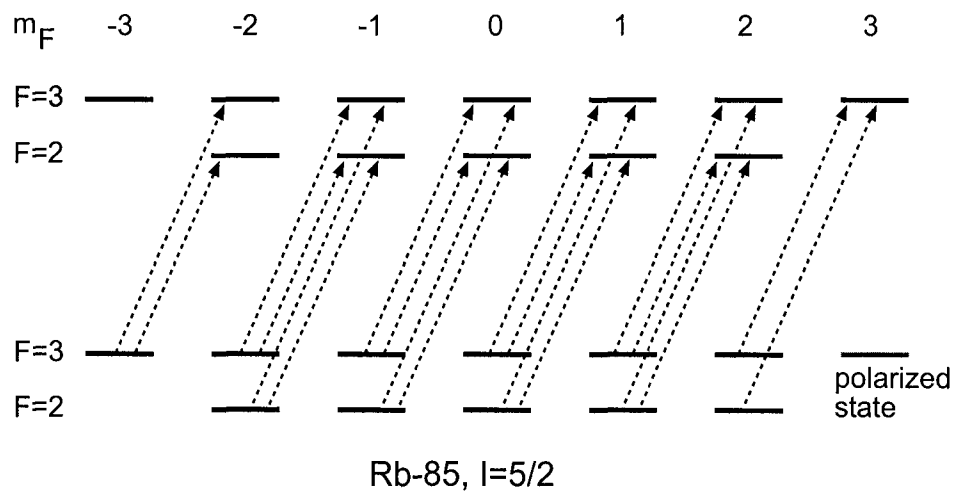


Figure 2-2: Rb optical pumping schematic for incident positive helicity circularly polarized light.

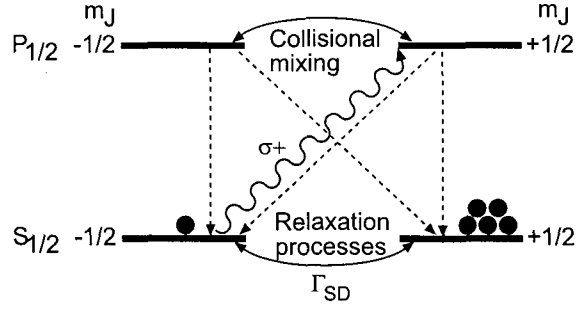


Figure 2-3: Simplified schematic of optical pumping for polarizing the valence electron of an alkali atom. In this schematic the spin of the Rb nucleus is neglected.

reached. The nuclear spin will act as an angular momentum reservoir and its effect on the optical pumping will be discussed later.

In the simplified form ( Figure 2-3), the electron is pumped following the selection rule  $\Delta m_J=1$  given by the light polarization  $\sigma^+$  and only the atoms  $m_J=-1/2$  will absorb the laser light and move into the excited state  $5p_{1/2}$  state with  $m_J=+1/2$ . The atom will de-excite into either of the two ground states with probabilities given by the Clebsch-Gordan coefficients. The probability decay from  $5p_{1/2} m_J=+1/2$  to  $5s_{1/2} m_J=-1/2$  is  $2/3$  and to  $5s_{1/2} m_J=+1/2$  is  $1/3$ . Statistically, three photons are needed in average to pump one atom into the final polarized state. The photon efficiency increases to 50% in the presence of buffer gases, which collisionally mix the excited  $5p_{1/2}$  levels.

A Rb atom that reached the final polarized ground state can be depolarized. The ground levels are mixed by mechanisms such as: absorption of photons resulted after Rb radiative decay from the excited state, collisions between alkali-metal atoms, wall collisions, and interactions with the gases present in the mixture, including the noble-gas to be polarized and which has the largest contribution to this process. All the processes mixing the ground levels  $5s m_J=-1/2$  with  $m_J=+1/2$  are summed up by a spin-destruction rate  $\Gamma_{SD}$ . Considering an optical pumping rate,  $\gamma_{opt}$ , which gives the number of Rb atoms pumped in one

second from  $m_J=-1/2$  to the final state  $m_J=+1/2$ , we can write the equation describing the populations of atoms in each of the two ground states:

$$\frac{d\rho_{\pm\frac{1}{2}}}{dt} = \pm \left( \gamma_{opt} + \frac{\Gamma_{SD}}{2} \right) \rho_{-\frac{1}{2}} \mp \frac{\Gamma_{SD}}{2} \rho_{+\frac{1}{2}} \quad (2.3)$$

Populations of the atoms in the two states are normalized:

$$\rho_{+\frac{1}{2}} + \rho_{-\frac{1}{2}} = 1 \quad (2.4)$$

and the Rb polarization for this particular case is defined as:

$$P_{Rb} = \rho_{+\frac{1}{2}} - \rho_{-\frac{1}{2}} \quad (2.5)$$

It is easily calculated from 2.3, 2.4, and 2.5 that:

$$\frac{dP_{Rb}}{dt} = \gamma_{opt}(1 - P_{Rb}) - \Gamma_{SD} \quad (2.6)$$

The solution for this equation gives the time dependence for the Rb polarization:

$$P_{Rb}(t) = \frac{\gamma_{opt}}{\gamma_{opt} + \Gamma_{SD}} \left[ 1 - e^{-(\gamma_{opt} + \Gamma_{SD})t} \right] \quad (2.7)$$

This shows an exponential build-up of polarization. Typical values for the time needed to reach saturation for Rb is in the order of 10-20 ms. When compared with the time scale for the other processes in a SEOP experiment, one can consider the steady-state solution for

the Rb polarization over the cell volume:

$$P_{Rb} = \frac{\gamma_{opt}}{\gamma_{opt} + \Gamma_{SD}} \quad (2.8)$$

From this relation it is straightforward that minimizing relaxation mechanisms maximizes Rb polarization.

### 2.1.3 Nuclear Spin Effect and Slowing-Down Factor

For the situations where the interactions time-scales are comparable with Rb pump-up time of 10-20 ms, the nuclear spin of Rb can not be neglected anymore. If the nuclear spin of Rb is to be considered, then there are 20 coupled equations [30] describing the population in each hyperfine  $m_F$  ground level presented in Fig. 2-2:

$$\left[ \frac{d\rho_{F,m_F}}{dt} \right]_{O.P.} = -\alpha_{F,m_F} \rho_{F,m_F} + \frac{1}{2(2I+1)} \sum_{F',m'} \alpha_{F',m'} \rho_{F',m'} \quad (2.9)$$

and

$$\left[ \frac{d\rho_{F,m_F}}{dt} \right]_{E.R.} = -\frac{3}{4} \Gamma_{ER} \rho_{F,m_F} + \Gamma_{ER} \langle F m_F | \mathbf{S} \cdot \rho \mathbf{S} | F m \rangle \quad (2.10)$$

where  $\rho_{F,m_F}$  are the population densities for hyperfine levels defined by the quantum numbers  $F$  and  $m_F$ ,  $\alpha_{F,m_F}$  are the absorption coefficients, and  $\Gamma_{ER}$  is the electron randomization rate. The time scale for electronic collisions is typically much shorter than the hyperfine interaction time, therefore the electron is considered to be decoupled from the nucleus during the collisions. In between collisions the hyperfine coupling leads to partial decay of the nuclear polarization.

With the population densities calculated from 2.9 and 2.10, one can determine the

hyperfine polarization and the electron-spin polarization defined as [30]:

$$P_F \equiv \langle F_z \rangle = \frac{\sum_{F,m_F} m_F \rho_{F,m_F}}{\sum_{F,m_F} \rho_{F,m_F}} \quad (2.11)$$

and

$$P_S \equiv \langle S_z \rangle = \frac{1}{2I+1} (P_{I+1/2} - P_{I-1/2}) \quad (2.12)$$

where  $P_{I+1/2}$  and  $P_{I-1/2}$  are calculated as the polarization in the upper and lower hyperfine multiplets, that is  $P_F$  for  $F = I + 1/2$  and  $F = I - 1/2$ , respectively. Rubidium polarization is determined from  $P_{Rb} = 2 \langle S_z \rangle$ .

The collisions and the spin-exchange between Rb atoms lead to a spin distribution on the hyperfine levels. Anderson *et al.* [53] have shown that for an ensemble of atoms with a high spin-exchange rate the population distribution on the hyperfine levels can be completely described by a single parameter called spin-temperature,  $\beta$ . Rb-Rb spin-exchange rates were measured for  $^{87}\text{Rb}$ - $^{87}\text{Rb}$  to  $8 \times 10^{-10} \text{ cm}^3/\text{s}$  [54], and similar rates are expected for  $^{87}\text{Rb}$ - $^{87}\text{Rb}$  and  $^{85}\text{Rb}$ - $^{85}\text{Rb}$ . This translates into  $\sim 10^5$  collisions in a second for a Rb vapor density of  $10^{14} \text{ cm}^{-3}$ . Figure 2-4a shows the schematic for a  $^{87}\text{Rb}$ - $^{87}\text{Rb}$  collision with both atoms in initial states  $|2, 1 \rangle$  and the probabilities to end in a certain hyperfine level after the collision for each of the two atoms. The Rb-Rb spin-exchange interactions conserve the total spin  $\mathbf{S} = \mathbf{S}_1 + \mathbf{S}_2$ , therefore this type of interaction does not contribute to the Rb depolarization and only to redistribution of atoms in the hyperfine levels.

When a spin-temperature equilibrium is reached the population density on a hyperfine level can be written as:

$$\rho_{F,m_F} = N(\beta) e^{\beta m} \quad (2.13)$$

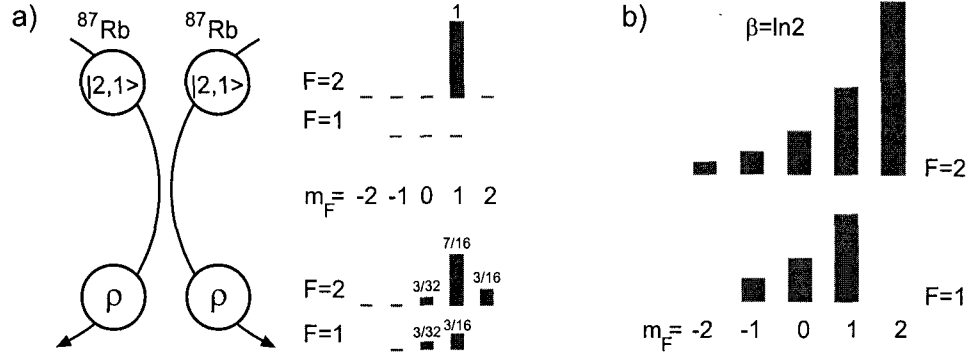


Figure 2-4: Rb-Rb spin-exchange: a) An example of interaction between two  $^{87}\text{Rb}$  atoms and the probabilities for the final state after the collision; b) Spin distribution on the hyperfine levels for a spin temperature  $\beta = \ln 2$ . Adapted from [55].

where  $\beta$  is the ensemble spin-temperature and  $N(\beta)$  is a normalization constant. Figure 2-4b shows the distribution for an ensemble of  $^{87}\text{Rb}$  with a spin-temperature  $\beta = \ln 2$

As previously said, the nuclear spin factor becomes important only in regions where the relaxation sources are high, such as the cell walls. It acts as a reservoir for momentum and slows down the electron polarization. Walker and Happer show in [55] the influence of the nuclear spin on the electron polarization as a function of the distance from the wall. The diffusion length is defined as  $\lambda_D = \sqrt{2D_a/\gamma_{opt}}$ . The electron polarization is saturated faster for a smaller nuclear spin since less photon momentum is wasted on the nuclear spin.

If an ensemble can be described by a spin-temperature distribution a slowing-down factor can be defined [30]:

$$S = \frac{P_F}{P_S} \quad (2.14)$$

where  $P_F$  and  $P_S$  are defined by Eqs. 2.11 and 2.12. The slowing-down factor depends on the spin-temperature and for natural Rb (0.72%  $^{85}\text{Rb}$ , 0.28%  $^{87}\text{Rb}$ ) can be calculated from

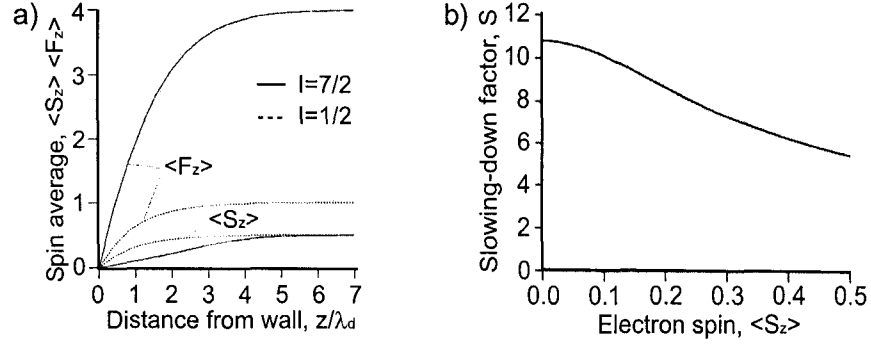


Figure 2-5: Nuclear spin effect on the electron polarization: a) Electron spin average for two different nuclear spins,  $I=1/2$  and  $I=7/2$ , as a function of the atom position from the wall. Adapted from [55].; b) Slowing-down factor as a function of electron polarization. Adapted from [30].

the relations:

$$P_F = 0.28N_3(\beta)[4 \sinh 2\beta + 4 \sinh \beta] + 0.72N_5(\beta)[6 \sinh 3\beta + 8 \sinh 2\beta + 4 \sinh \beta] \quad (2.15)$$

$$P_S = 0.28N_3(\beta) \sinh 2\beta + 0.72N_5(\beta) \sinh 3\beta \quad (2.16)$$

where  $N(\beta)$  are normalization factors. A graph for the slowing-down factor,  $S$ , as a function of the electron polarization,  $P_S$  is presented in Figure 2-5b. As expected, the nuclear spin influence is maximum for low electron polarization ( $S = 10.8$  for  $P_S = 0$ ), and is minimum for maximum electron polarization ( $S = 5.4$  for  $P_S = 1/2$ ).

For atoms with low nuclear spin value the optical pumping equations given by 2.9 and 2.10 can be analytically solved to give the time dependence of the nuclear polarization [30]:

$$\frac{dP_F(\beta, t)}{dt} = -\Gamma_{ER}P_S(\beta) = -\frac{\Gamma_{ER}}{S(\beta)}P_F(\beta) \quad (2.17)$$

Since the slowing-down factor is dependent on the electron polarization and on the spin-



temperature, the time dependence of the nuclear polarization is not exponential. Also, Wagshul and Chupp [30] demonstrated that the slowing-down factor has an effect on the polarization build-up and decay time constants, but not on the final achievable polarization:

$$P_{Rb}(t) = \frac{\gamma_{opt}}{\gamma_{opt} + \Gamma_{ER}} \left( 1 - e^{-\frac{(\gamma_{opt} + \Gamma_{ER})}{S} t} \right) \quad (2.18)$$

The saturated polarization is unchanged from the simplified derivation of Eq. 2.8, and depends only on the optical pumping rate and the spin-destruction rate.

#### 2.1.4 Buffer Gases in Optical Pumping

Buffer gases are added to the Rb vapor to increase the efficiency the pumping process. There are multiple reasons for the presence of buffer gases in the optical pumping mixture: quenching of the excited state energy, excited state collisional mixing, D1 absorption line pressure broadening, and reducing the Rb diffusion. Buffer gases are also critical in the spin-exchange as the van der Waals molecule formation and destruction requires the presence of a third body, usually nitrogen.

Radiative emissions from the Rb excited  $5p_{1/2}$  levels lead to uncontrolled circular polarized  $\sigma^{\pm}$  ( $\Delta m_J = \pm 1$ ) or linear polarized  $\pi$  ( $\Delta m_J = 0$ ) photons. Since they correspond to the D1 energy, can be reabsorbed by polarized Rb atoms. Radiative decay can be a major depolarization effect as the unpolarized photons propagate inside the cell.

Nitrogen is almost always used in the mixture to quench the Rb excited state energy into its vibrational levels [29]. The N2 quenching cross-section on Rb excited state  $5^2p_{1/2}$  was measured to  $58 \text{ \AA}^2$  [56]. Using this value Wagshul and Chupp [57] calculated a branching

ratio for the radiative decay:

$$P_{rad} \approx \frac{3}{3 + p_{N_2}} \quad (2.19)$$

where  $p_{N_2}$  is the nitrogen partial pressure in the mixture expressed in torr. A minimum quantity of  $N_2$  is required in the mixture such that the radiative de-excitation is insignificant. Nitrogen partial pressure of 100 T reduces the radiative decay below 3 %, which generally is considered acceptable. Another side advantage of  $N_2$  as buffer gas is that the Rb excited state lifetime is reduced from 28 ns to  $\sim 1$  ns [58].

Collisions of Rb atoms with buffer gases, especially He, result in a mixing of the atomic sublevels. This randomization is essential for the atoms in the excited state, because it increases the optical pumping efficiency from 1/3 to 1/2, as previously mentioned. Collisional mixing affects also the ground state levels also, but with a much smaller probability. Mixing of ground levels contribute to the spin-destruction rate. The cross-section for randomization after collisions with helium buffer gas is  $\sim 10^{-25}$  cm<sup>2</sup> for the ground state, and  $\sim 10^{-15}$  cm<sup>2</sup> for the excited  $5p_{1/2}$  level [59]. In the presence of nitrogen the Rb excited state reduces its lifetime to 1 ns compared with natural lifetime of 28 ns [60].

Another major motivation for using large quantities of buffer gas in the optical pumping systems is the pressure broadening of the spectral lines of Rb. Pressure broadening is a consequence of interaction between Rb electronic cloud and the gases in the pumping mixture, resulting in a distortion of the Rb atomic energy levels. Detailed measurements of the broadening effects were done by Romalis *et al.* [61] for all gases involved typically in the optical pumping. Besides broadening, buffer gases produce also a shift of the central D1 line. Table 2.1 shows a summary of the values measured by Romalis. Heavier gases such as  $N_2$  and Xe have a stronger van der Waals interaction with Rb and the result is an

Gas	D1 FWHM broadening, $\Gamma_{abs}$		D1 central line shift	
	(GHz/amg)	(nm/amg)	(GHz/amg)	(nm/amg)
$^3\text{He}$	18.7	0.039	5.6	0.012
$^4\text{He}$	18.0	0.038	4.3	0.009
$\text{N}_2$	17.8	0.038	-8.3	-0.017
$\text{Xe}$	18.9	0.040	-5.1	-0.011

Table 2.1: Pressure broadening and shifting of the D1 line induced by optical pumping gases. Values reported by [61].

asymmetry of the absorption lines, leading sometimes to satellite D1 lines. Measurement of the broadening and shifting effects are sometimes used in determining the gas density inside the cell. With very few exception, all previous reported polarizers were designed to work in the high pressure regime in order to increase the laser absorption efficiency when using broad high-power diode lasers. Typical pressure ranged between 3 and 10 atmospheres. The pressure broadening is much larger than Doppler broadening of 250 MHz or natural width of 5.7 MHz [62].

### 2.1.5 Laser Light Absorption and Optical Pumping Rate

The laser light absorption defines the optical pumping rate and the Rb polarization over the cell volume. After a Rb atom is polarized it becomes transparent to the polarized laser light. This causes an equilibrium of Rb polarization over the cell volume. Full Rb polarization over the cell volume, with the exception of the wall vicinity, can be achieved, especially in polarizing  $^3\text{He}$  which has a very small spin-exchange cross-section with Rb.

To calculate the pumping rate at a certain point and, implicitly, the Rb polarization given by Eq. 2.8, we need to calculate the laser attenuation and to map the photon flux across the cell:

$$\gamma_{opt}(\vec{r}) = \int_0^{\text{inf}} \Phi(\vec{r}, \nu) \sigma(\nu) d\nu \quad (2.20)$$

where  $[Rb]$  is the vapor density,  $\sigma(\nu)$  is the absorption cross-section, and  $\Phi(\nu, \vec{r})$  is the flux of photons (number of photons per  $\text{cm}^2$  and per second). The relation between the photon flux and the intensity,  $I$ , and the laser power,  $P$ , is given by:

$$I(\vec{r}) = \int_0^{\text{inf}} \Phi(\vec{r}, \nu) d\nu$$

$$P = \int_S dS \int_0^{\text{inf}} \Phi(\vec{r}, \nu) d\nu$$

The absorption cross-section is defined in [63]:

$$\sigma(\nu) = \frac{\Lambda_0^2}{2\pi} \Gamma_{nat} \left[ \frac{\Gamma_{abs}}{4(\nu - \nu_0)^2 + \Gamma_{abs}^2} + \frac{b(\nu - \nu_0)}{\Gamma_{abs}} e^{-\frac{|\nu - \nu_0|}{\Gamma_a}} \right]$$

where the first term is dominant presenting a Lorentzian shape centered around  $\nu_0$  and the FWHM,  $\Gamma_{abs}$ , is dominated by the pressure broadening. The second term parameterizes the asymmetry of the peak through parameters  $b$  and  $\Gamma_a$ , but for low pressures it can be neglected. We simplify the cross-section to a pure Lorentzian:

$$\sigma(\nu) = \sigma_0 \frac{\Gamma_{abs}^2}{4(\nu - \nu_0)^2 + \Gamma_{abs}^2} \quad (2.21)$$

where the peak amplitude,  $\sigma_0$ , is calculated from the sum rule:

$$\int_0^{\text{inf}} \sigma(\nu) d\nu = \pi r_e c f \quad (2.22)$$

where  $r_e$  is the classical electron radius,  $c$  is the speed of light, and  $f$  is the D1 transition

oscillator strength given in [63] as  $f=0.337$ . Integrating Eq. 2.21 leads to:

$$\int_0^{\text{inf}} \sigma(\nu) d\nu = \frac{\pi}{2} \sigma_0 \Gamma_{abs}$$

and further to a relation between the peak amplitude and the FWHM from Eq. 2.4:

$$\sigma_0 \Gamma_{abs} = 5.7 \times 10^{-3} \text{ cm}^2 \quad (2.23)$$

This relation is confirmed by the value of  $\sigma_0 = 3.2 \times 10^{-13} \text{ cm}^2/\text{Hz}$  for  $\Gamma_{abs} = 18 \text{ GHz}$  reported by Wagshul and Chupp [30].

Considering a laser beam oriented along the  $z$  axis parallel with the  $B_0$  field, and no wall relaxation involved in the pumping, the beam flux dependence with position  $z$  is:

$$\frac{d\Phi(z, \nu)}{dz} = -\lambda^{-1}(z, \nu) \Phi(z, \nu) \quad (2.24)$$

where  $\lambda$  is the absorption length expressed by:

$$\lambda^{-1}(\vec{r}, \nu) = 3[Rb]\sigma(\nu) \left( \left| \langle \frac{1}{2}, -\frac{1}{2}, 1, m_\gamma | \frac{1}{2}, m_S^* \rangle \right|^2 \rho_{-1/2} + \left| \langle \frac{1}{2}, \frac{1}{2}, 1, m_\gamma | \frac{1}{2}, m_S^* \rangle \right|^2 \rho_{1/2} \right) \quad (2.25)$$

where  $[Rb]$  is the Rb density,  $m_\gamma$  is the projection of the photon angular momentum on the quantification axis  $z$ , and  $m_S^*$  is the electron angular momentum projection in the  $5p_{1/2}$  excited state after photon absorption.

A linear or unpolarized beam incident on the cell with  $m_\gamma = 0$  results in equal Clebsch-Gordon coefficients and equal probabilities of pumping both ground levels. In this case the absorption length becomes  $\lambda^{-1} = [Rb]\sigma(\nu)$ .

For a circular polarized beam with positive helicity,  $\sigma^+$ , illuminating the cell, the second coefficient in Eq. 2.25 cancels and the absorption length becomes  $\lambda^{-1} = 2\sigma(\nu)[Rb]\rho_{-1/2}(z)$ . Using also Eqs. 2.4 and 2.5 we get:

$$\lambda^{-1} = \sigma(\nu)[Rb](1 - P_{Rb}(z)) \quad (2.26)$$

Therefore the photon flux absorption is dictated by:

$$\frac{d\Phi(z, \nu)}{dz} = -\sigma(\nu)\Phi(z, \nu)[Rb](1 - P_{Rb}(z)) \quad (2.27)$$

This can be used for mapping the photon flux inside the cell, optical pumping rate, and Rb polarization if considering a steady state solution. Integrating over frequency we get the laser intensity reduction as it travels through the cell:

$$\frac{dI(z)}{dz} = -[Rb](1 - P_{Rb}(z))\gamma_{opt}(z) = -[Rb]\Gamma_{SD}P_{Rb} \quad (2.28)$$

and which suggests that the photon absorption rate per Rb atom is equal to  $\Gamma_{SD}P_{Rb}$ .

Rb wall relaxation by diffusion towards the walls can be included in the optical pumping equations (2.3) through a diffusion term together with the slowing-down term:

$$\frac{d\rho_{\pm\frac{1}{2}}}{dt} = \pm\frac{1}{S}\left(\gamma_{opt} + \frac{\Gamma_{SD}}{2}\right)\rho_{-\frac{1}{2}} \mp \frac{1}{S}\frac{\Gamma_{SD}}{2}\rho_{+\frac{1}{2}} + D\nabla^2\rho_{\pm\frac{1}{2}}$$

This more complex equation and its solutions are discussed in detail by Wagshul and Chupp [30]. Similar solutions are also described by Larson *et al.* [63] and Walker and Happer [55].

### 2.1.6 Skew Light Effects

Rb relaxation mechanisms inherently exist during optical pumping and they are overwhelmed with high-power diode lasers. To fully utilize the laser power one needs a perfect parallelism of the laser beam with the magnetic field. B. Chann and the Wisconsin group of T.G. Walker demonstrated severe skew-light effects on the light absorption efficiency even at very small angles [64]. The mechanism of inefficiently light absorption is explained by the fact that the Rb polarization is never saturated from the laser point of view. Rb electron precess rapidly around the magnetic field resulting in a time-average of the electron spin smaller than 1/2. This results in extra light absorption of the Rb vapor:

$$\frac{d\Phi(z, \nu)}{dz} = -\sigma(\nu)\Phi(z, \nu)[Rb](1 - P_{Rb}(z) \cos \theta) \quad (2.29)$$

where  $\theta$  is the angle made by the laser beam and the magnetic field.

Also, Chann *et al.* showed that a positive helicity  $\sigma^+$  circular polarized incident beam, which makes an angle  $\theta$  with the magnetic field, can be decomposed in fractions of positive helicity "+", negative helicity "-", and linear " $\pi$ " polarized light with respect to the magnetic field direction:

$$f_+ = \cos^4(\theta/2); \quad f_- = \sin^4(\theta/2); \quad f_\pi = 2 \sin^2(\theta/2) \cos^2(\theta/2);$$

In these conditions the Rb optical pumping equations needs to be modified to take into consideration the absorption of wrong polarization light. Eq. 2.3 becomes:

$$\frac{d\rho_{\frac{1}{2}}}{dt} = \left[ \gamma_{opt} \left( f_+ + \frac{f_\pi}{2} \right) + \frac{\Gamma_{SD}}{2} \right] \rho_{-\frac{1}{2}} - \left[ \gamma_{opt} \left( f_- + \frac{f_\pi}{2} \right) + \frac{\Gamma_{SD}}{2} \right] \rho_{-\frac{1}{2}} \quad (2.30)$$

and the equation for Rb polarization build-up is:

$$P_{Rb}(t) = \frac{\gamma_{opt}(f_+ - f_-)}{\gamma_{opt} + \Gamma_{SD}} \left[ 1 - e^{-(\gamma_{opt} + \Gamma_{SD})t} \right] \quad (2.31)$$

Simple calculation gives  $(f_+ - f_-) = \cos \theta$ . In conclusion, Rb polarization will reach its saturation value with the same time constant. Nevertheless, its saturation value has now changed:

$$P_{Rb} = \frac{\gamma_{opt}}{\gamma_{opt} + \Gamma_{SD}} \cos \theta \quad (2.32)$$

Equation 2.32 together with 2.29 will be used in calculation of flux absorption and Rb polarization calculations when considering the skew light effect.

Chann *et al.* [64] estimated a doubling in laser flux absorption for a  $^3\text{He}$  cell, pumped by a 50 W, 2 nm FWHM laser, and  $\theta = 6^\circ$ . Angles in this range are common in optical pumping, since the  $B_0$  field ranges in gauss values and the Earth's magnetic field can be a significant transversal component of the resulted field.

### 2.1.7 Light Absorption Heating Effects

For large spin-destruction rates of Rb polarization, especially in  $^{129}\text{Xe}$  SEOP, most of the laser light, if not all, is absorbed by the Rb vapor and further transmitted through collisional quenching towards the  $\text{N}_2$  molecules. As a result of a quenching collision the  $\text{N}_2$  jumps into a highly excited vibrational state ( $\nu=5, 6$ ). Subsequent collisions with other buffer gases atoms thermalize the nitrogen molecules energy. Typically measurements of cell temperature with a temperature sensor in the vicinity of the cell is not sensitive to temperature gradients inside the cell. One can measure the temperature inside the cell locally using Raman scattering of a probe beam on nitrogen molecules [65].



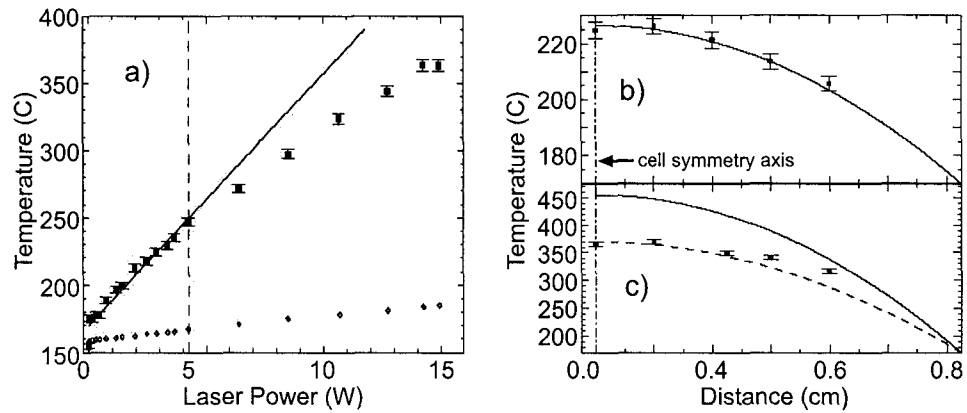


Figure 2-6: a) Temperature in the center of the cell as function of the pumping laser power. The diamond points show the temperature reading of a thermocouple on the cell surface. b) Temperature distribution inside the cell for 2.9 W laser power. c) Temperature distribution inside the cell for 15 W laser power; the solid curve shows the curve resulted by scaling b) with the laser power. Figures are adapted from [66].

Walter *et al.* used this method to measure local temperature inside optical pumped cells with a spatial resolution of 1 mm [66]. Figure 2-6 shows different experimental results obtained with this method for a closed optical pumping cell of 40 cc, containing 2 atm of  $^4\text{He}$ , 0.33 atm of  $\text{N}_2$ , and located inside an oven assuring a constant ambient temperature of  $170^\circ$ . Fig. 2-6a describes the temperature inside the cell dependence as a function of pumping laser power. The temperature varies linearly until a point where convection phenomena in the heat transfer interfere with the conduction transfer. The convection-conduction overlapping results also from Fig. 2-6 b) and c), where the temperature was mapped as a function of the position inside the cell. For a low input power of 2.9 W the temperature distribution is in agreement with a 3D diffusion equation with a constant heating source. If the laser power goes to 15 W convection develops and temperature distribution deviates towards unstable heat transfer regimes. Also, from Fig. 2-6c the heat transfer towards the walls is done faster, and the temperature doesn't scale with the absorbed power anymore. Large temperature

differences between the ambient and the center of the cell were also reported for  $^{129}\text{Xe}$  and  $^3\text{He}$  SEOP, in the range of  $100^\circ$  for moderate laser powers of 15-20 W.

The heating process of the optical pumping mixture can become crucial at high laser power of hundreds of watts. In a continuous flow  $^{129}\text{Xe}$  polarizer the Rb spin-destruction rate is very large for high xenon concentrations and all the laser power can be absorbed. Simple calculation shows temperature elevations of thousands of degrees of the gases inside the cell. The Reynolds numbers at high laser power will be well above the critical point and convection and mass-transfer phenomena should be expected. In regions of maximum laser absorption the gas flow will not be anymore laminar and turbulences in the gas flow will dominate. For high Reynolds numbers the heat transfer is done in a small layer close to the surface and the temperature inside the cell is much higher than the ambient. In this case it will be very difficult to estimate the gas mixture density since is strongly temperature dependent. Especially for optical pumping cell containing the Rb within the laser illumination region the Rb density can reach very high value and can not be considered to be in equilibrium with the oven temperature. An improved polarizer design needs to consider the location of Rb vapor source outside the laser illuminated region as will be discussed later.

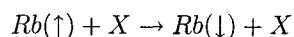
## 2.2 Rubidium Spin-Destruction Rate

### 2.2.1 Rb Atom Interactions

The Rb spin-destruction rate  $\Gamma_{SD}$  from Eq. 2.6, or the Rb electron-randomization rate  $\Gamma_{ER}$  from Eq. 2.18 account for all relaxation mechanisms. The causes for electron depolarization are various and some of them are still under debate: wall collisions, unpolarized photons

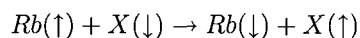
(radiation trapping), interactions of Rb with other Rb, N<sub>2</sub>, He, and Xe atoms. Some can be neglected because of their very small contribution, few orders of magnitude lower when compared with the others. For example wall collisions and radiation trapping can be minimized with the right choice of the system geometry and by saturating the mixture with N<sub>2</sub>.

From the point of view of the effect on the colliding atom the processes can be divided in two major categories: spin-destruction (SD) and spin-exchange (SE). In a spin-destruction process the electron polarization is lost typically to the motion degrees of freedom of the colliding pair. Rb spin-relaxation can be described generally by the next schematic:



where X is the collision atom.

In a spin-exchange collision the Rb electron is flipped by coupling with either the electron or the nucleus spin of the colliding atom. A spin-exchange is described schematically as:



The colliding atom arrow refers to its electron or nucleus spin. This process is very important because causes the spin-temperature distribution through Rb-Rb spin-exchange binary collisions and the spin transfer to the noble-gas nucleus through binary collisions or van der Waals molecules.

From the time scale point of view, the interactions are described as "fast" or "sudden", such are the binary collisions on a time scale of 1 ps, and as "slow" or "long-lived", such are molecular formations ( $10^{-7} - 10^{-11}$  s), characterizing the Rb<sub>2</sub> dimers and Rb-Xe interac-

tions. The dominant type is dictated by the total pressure inside the system. Interactions inside high-pressure systems are dominated mostly by the binary collisions and vice-versa.

Binary collisions are characterized by a relaxation coefficient defined as a velocity-averaged cross-section:  $\kappa \equiv \langle \sigma v \rangle$ . The relaxation term  $\kappa$  is not pressure nor field dependent. The temperature dependence is expected to correspond to thermal-velocity dependence, that is  $T^{1/2}$ . The relaxation rate caused through binary collision on a Rb atom by one of the components  $X$  from the SEOP mixture is:

$$\Gamma_{SD}^X = [X]k_{Rb-X} \quad (2.33)$$

where  $[X]$  is the density of  $X$  component expressed in  $\text{cm}^{-3}$ . Total spin-destruction rate caused by binary collisions for an optical pumping mixture containing N2, He, and Xe is written as:

$$\Gamma_{SD}^{bc} = [Rb]k_{Rb-Rb} + [He]k_{Rb-He} + [N2]k_{Rb-N2} + [Xe]k_{Rb-Xe} \quad (2.34)$$

The interactions happening during the molecules lifetime of Rb with Xe or other Rb atoms are strongly pressure and gas mixture dependent and the relaxation rate needs to take into account molecule formation and destruction rates, lifetimes, etc. They have also a field dependence and some of the interactions can be decoupled using relatively large magnetic fields.

In between the collision the free Rb atom Hamiltonian is:

$$H_{Rb} = A\mathbf{I} \cdot \mathbf{S} + g_s\mu_B S_z B_z - \frac{\mu_I}{I} I_z B_z \quad (2.35)$$

where  $\mathbf{I} \cdot \mathbf{S}$  is the Rb atom hyperfine interaction, and the last two terms are the interaction of the spin with the magnetic field  $B_z$  for the electron and the nucleus, respectively. For a free noble-gas atom the Hamiltonian just describes the nucleus spin precession about the applied magnetic field:

$$H_{NG} = -\frac{\mu_K}{K} K_z B_z \quad (2.36)$$

The interaction Hamiltonian during a collision of a Rb atom with another atom, such as noble-gas, buffer gases, and other Rb atoms, contributing either to the spin-destruction or spin-exchange is:

$$H_{int} = \gamma(R)\mathbf{N} \cdot \mathbf{S} + \alpha(R)\mathbf{K} \cdot \mathbf{S} + J(R)\mathbf{S}_i \cdot \mathbf{S}_j + A\mathbf{I} \cdot \mathbf{S} + \frac{2}{3}\lambda(R)\mathbf{S} \cdot (3\hat{\zeta}\hat{\zeta} - 2) \cdot \mathbf{S} + c\mathbf{I} \cdot (3\hat{\mathbf{n}}\hat{\mathbf{n}} - 1) \cdot \mathbf{I} \quad (2.37)$$

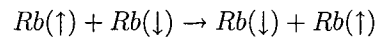
The first two terms are specific to interactions between Rb and all other components of the OP mixture. The last four terms are specific only to the alkali-alkali (Rb-Rb) atoms interactions, with last three expressing the hyperfine interactions [55].

The term  $V_{NS} \equiv \gamma(R)\mathbf{N} \cdot \mathbf{S}$  represents the spin-rotation interaction between the electron spin  $\mathbf{S}$  and the rotational angular momentum of the colliding pair of atoms  $\mathbf{N}$ . It transfers the electron spin polarization to the translational degrees of freedom of the atoms. Can be interpreted as the interaction of the Rb electron with the magnetic fields resulted by the relative motion of the atoms charges. This is the major term in Rb relaxation as order of magnitude. The spin-rotation relaxation acts during both: sudden binary collisions and long-lived van der Waals molecules.

The term  $V_{NS} \equiv \alpha(R)\mathbf{K} \cdot \mathbf{S}$  represents the hyperfine coupling between the alkali electron and the noble-gas nucleus. This is the interaction responsible for the spin-exchange and noble-gas nucleus polarization. The coupling is done during binary and molecular interac-

tions. Both coefficients  $\gamma(R)$  and  $\alpha(R)$  for the spin-rotation and Fermi-contact interactions are strongly dependent on the internuclear separation distance  $R$ .

The spin-exchange term  $V_{EX} \equiv J(R)\mathbf{S}_i \cdot \mathbf{S}_j$  express the dipole-dipole interaction between two alkali electrons during binary collisions between two Rb atoms. This interaction was mentioned previously as Rb-Rb spin-exchange and has large importance in establishing a spin-temperature within the Rb ensemble. The collision can be written schematically as:



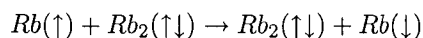
and has no net depolarization effect, so typically is not included in polarization calculations.

The hyperfine coupling inside the Rb atom present also in the free atom Hamiltonian and expressed as  $V_{HF} = \mathbf{A}\mathbf{I} \cdot \mathbf{S}$  has to be considered in xenon SEOP during the long time interactions like van der Waals molecules. Together with the spin-rotation interaction can define specific time-scale regimes of optical pumping processes, as it was shown by Happer *et al.* [67].

The term  $V_{SS} \equiv \frac{2}{3}\lambda(R)\mathbf{S} \cdot (3\hat{\zeta}\hat{\zeta} - 2) \cdot \mathbf{S}$  is called the spin-axis interaction and is similar to the spin-rotation term. The unit vector  $\hat{\zeta}$  lies along the direction of the internuclear axis. Experimental evidence [68, 69] suggests that the spin-axis arises mostly as a second order of the spin-orbit interaction. The spin-axis interactions happens through triplet Rb<sub>2</sub> molecules [68] and through the binary collisions [70].

Last term  $V_Q \equiv c\mathbf{I} \cdot (3\hat{\mathbf{n}}\hat{\mathbf{n}} - 1) \cdot \mathbf{I}$  represents a simplified form for the electric-quadrupole interaction for a single nucleus of spin  $\mathbf{I}$  in a rotating singlet Rb<sub>2</sub> dimers. The unit vector  $\hat{\mathbf{n}}$  defines the direction for the rotational angular momentum of the molecule. The constant  $c$  has the value of  $c = -\frac{eqQ}{8I(2I-1)}$  and depends on the quadrupole-electric moment  $Q$  of

the Rb nucleus and on the electric-field gradient at the nucleus in the stretched rotational state  $q$  [71]. This interaction relaxes the Rb nucleus (F-damping) compared with the other interactions which destroy just the electron polarization (S-damping). About 1% of the Rb atoms are found in singlet dimers molecules in typical optical pumping conditions. The binding energy of  $\sim 0.5$  eV is much larger than  $k_B T$  and only collisions with other gases in the SEOP mixture can break the dimers apart. A second mechanism, the chemical-exchange, can exceed the molecule formation in certain conditions:



In this case a polarized atom replaces an atom into the dimer, possibly already depolarized through the electric-quadrupole interaction.

In Rb dimers a term with a small influence is the coupling of the nucleus spin to the rotational angular momentum  $V_{NR} \equiv c' \mathbf{I} \cdot \mathbf{N}$  [71]. This term is much less influential than the quadrupole interaction for Rb, but it becomes dominant for other alkali metals such as Cs.

### 2.2.2 Rb-Rb Spin-Destruction

Although the molecule formation (dimers) between alkali atoms was indicated as a possible source of interactions [72, 73], experimental results taken at low magnetic fields didn't show a strong pressure dependence expected if the relaxation was caused inside Rb dimers. Bhaskar *et al.* [74] concluded that the dominant relaxation occurred during the binary collisions between alkali atoms, with insignificant contribution from dimers interaction. Few years ago Kadlecik and the group of Thad Walker observed a reduction of the relaxation rate with a factor of three if the  $B_0$  field was increased to  $\sim 6$  kGauss [75]. This behavior

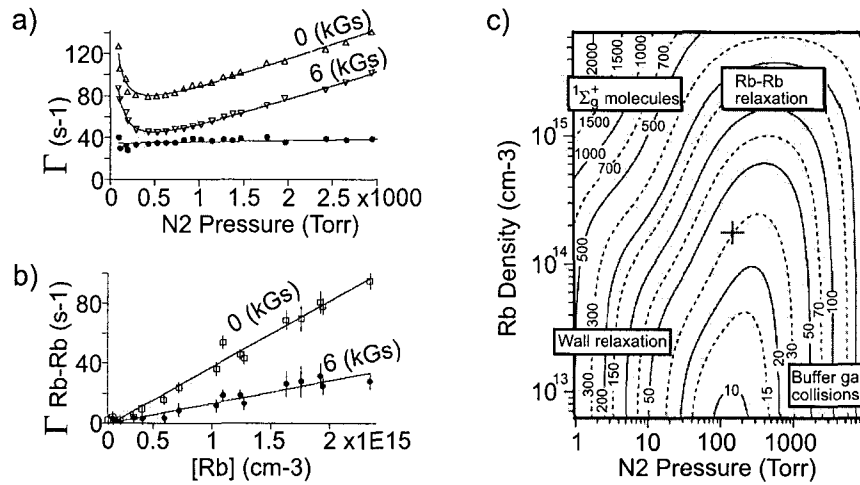


Figure 2-7: a) Nitrogen pressure dependence for two different field values. b) Rb-Rb spin relaxation rate showing a linear dependence for both, low field and high field limits, with the Rb density. c) Rb relaxation mapping at low field as a function of N2 pressure, defining different relaxation regions; the red cross shows the running parameters of UNH polarizer. Graphs a) & b) taken from [75] and c) from [71].

couldn't be explained by the simple theory of binary collisions and subsequent studies tried to develop a theory based on Rb<sub>2</sub> dimers interactions. In a series of publications Wisconsin and Princeton groups analyzed the experimental data on the premises that an important part of the relaxation at low fields and low pressures is caused by the spin-axis interactions in binary collisions [70] and in triplet dimers [68], and by the electric-quadrupole interactions in singlet dimers [73, 71].

Figure 2-7a shows the measurements of relaxation as a function of the N2 buffer gas pressure at low field (0 kG) and high-field (6 kG) done by the Wisconsin group members [75]. From the graph it is clear the decoupling of certain relaxation mechanism. However, the independence of the difference between the two curves (the full circles on the graph) on the buffer gas is difficult to be explained by the dimers theories. Furthermore, Fig. 2-7b shows a linear dependence, observed in previous experiments also, of the relaxation rate



with Rb density, leading to the conclusion that binary collisions is still the major factor in the Rb-Rb relaxation. Although numerous studies has been done, there is still not a good understanding of the contributions from each interaction to the final relaxation rate as the pressure increases. At very low pressures the dominant mechanism is the quadrupole interaction through the singlet dimers [68, 71]. At moderate and high pressures and for moderate Rb vapor densities most of the relaxation is caused during binary collisions, probably through the spin-axis coupling. Figure 2-7c presents a relaxation rates mapping done by the Wisconsin group. The dominant relaxation mechanisms, without considering the polarizing noble-gas, are presented on the map.

Rb-Rb spin-destruction rates were measured in typical optical pumping conditions several times [76, 30] to a value of  $\kappa_{SD}^{Rb-Rb} \sim 8 \times 10^{-14} \text{ cm}^3/\text{s}$ . A more recent measurement by Baranga *et al.* [77] at 31 Gauss magnetic field showed a value smaller by a factor of two:  $\kappa_{SD}^{Rb-Rb} = 3.9 \times 10^{-14} \text{ cm}^3/\text{s}$ . The field dependence study of Kadlecik *et al.* resulted to a more complex formula:

$$\kappa_{SD}^{Rb-Rb} = \left( 1.5 + \frac{2.88}{1 + (B(kG)/1.15)^2} \right) \times 10^{-14} \text{ cm}^3/\text{s} \quad (2.38)$$

where we neglected the Rb-N<sub>2</sub> relaxation to be discussed at a later point and the Rb dimer relaxation which is insignificant in our range of temperatures and pressures. At low magnetic fields it translates into  $\kappa_{SD}^{Rb-Rb} = 4.38 \times 10^{-14} \text{ cm}^3/\text{s}$  in relatively close agreement with Baranga's. At 150°C the Rb density is  $[\text{Rb}] = 1.04 \times 10^{14} \text{ cm}^{-3}$  and the spin-destruction rate is  $\Gamma_{SD}^{Rb-Rb} = 4.5 \text{ Hz}$ .

The spin-exchange rate in the Rb-Rb binary collisions, discussed before, greatly exceeds the spin-destruction rate. This is extremely important for optical pumping in establishing

a spin-temperature distribution within the Rb atoms. Last reported value for Rb-Rb spin-exchange value is  $\kappa_{SE}^{Rb-Rb} = 8.8 \times 10^{-10} \text{ cm}^3/\text{s}$  measured at 150°C, leading to more than  $9 \times 10^4$  spin-exchange interactions in one second.

### 2.2.3 Buffer-Gases Spin-Destruction

Rb relaxation after collisions with buffer gases atoms occurs mostly from spin-rotation interactions during the short time of  $\tau \sim 1 \text{ ps}$  characteristic to binary collisions. The relaxation happens only at the electronic level. That means that in between the collisions the electron can get repolarized from the nucleus through the hyperfine coupling. A large magnetic field is needed to reduce the relaxation rate by splitting the electron sublevels by  $\hbar/\tau$  [78].

The relaxation coefficient was measured by Wagshul and Chupp [30] and again, recently, by Walter *et al.* [78]. At a temperature of 150°C Wagshul found a value of  $\kappa_{SD}^{N_2} = 9.38 \times 10^{-18} \text{ cm}^3/\text{s}$ . A more detailed formula including a temperature dependence for the range of 90-150°C was deduced by Walter:

$$\kappa_{SD}^{N_2} = 6.33 \left( 1 + \frac{T(^{\circ}\text{C}) - 90}{194.3} \right) \times 10^{-18} \text{ cm}^3/\text{s} \quad (2.39)$$

When compared with Wagshul's for a temperature of 150°C this becomes  $\kappa_{SD}^{N_2} = 8.28 \times 10^{-18} \text{ cm}^3/\text{s}$  showing good agreement. For a system containing 130 T of N<sub>2</sub> at a temperature of 150°C the spin-destruction rate caused by N<sub>2</sub> on Rb is  $\Gamma_{SD}^{Rb-N_2} = 38 \text{ Hz}$ .

The Rb-<sup>4</sup>He spin-destruction rates are expected to be similar to Rb-<sup>3</sup>He measured by the community in the view of <sup>3</sup>He SEOP. For <sup>3</sup>He Baranga *et al.* [77] demonstrated a strong

temperature dependence of the spin-destruction rate:

$$\kappa_{SD}^{He} = T^{4.26} \times 10^{-29} - 6.7 \times 10^{-20} \text{ cm}^3/\text{s} \quad (2.40)$$

where T is the temperature in Kelvin and the term subtracted is the Rb-<sup>3</sup>He spin-exchange cross-section  $\kappa_{SE}^{Rb-3He} = 6.7 \times 10^{-20} \text{ cm}^3/\text{s}$ . Walter did a similar measurement extracting a linear dependence on temperature for a range of 90-150°C and the measurement comes in very close agreement with Eq. 2.39. Typical running parameters of our system is a total pressure of 500 T with ~75% of the mixture <sup>4</sup>He corresponding to a helium density of 0.5 amagat. This leads to a relaxation caused by He of  $\Gamma_{SD}^{Rb-He} = 19 \text{ Hz}$  at 150°C.

### 2.3 Rubidium-Xenon Spin-Exchange and Spin-Destruction

Far more complex than Rb-<sup>3</sup>He binary only collisions, Rb-Xe is characterized also by van der Waals molecular interactions. W. Happer and the Princeton group have done most of the research on characterizing the spin-exchange processes. For detailed theoretical derivations the reader should approach some of their Letters: [67, 55, 52]. Experimental work was done extensively also by the same group [79, 80, 44, 81], with recent major contributions for the low pressure regime by the Wisconsin group [82]. Previous work of Bouchiat *et al.* was important in predicting and demonstrating the van der Waals molecule existence between alkali vapor and heavy noble gases and measuring basic constants of the interactions [83, 84].

### 2.3.1 Spin-Exchange Equations

In a simplified representation where the Rb nuclear effects are neglected, the equation for noble-gas polarizing rate can be deduced in a similar manner as the ones for the Rb polarization. With  $\rho_{Xe(+\frac{1}{2})}$  and  $\rho_{Xe(-\frac{1}{2})}$  defining the densities of Xe atoms with nuclear spin projection  $K_z = \pm\frac{1}{2}$ , we can write:

$$1 = \rho_{Xe(+\frac{1}{2})} + \rho_{Xe(-\frac{1}{2})}$$

$$P_{Xe} = \rho_{Xe(+\frac{1}{2})} - \rho_{Xe(-\frac{1}{2})}$$

An unpolarized xenon nucleus is polarized after a spin-exchange interaction with a polarized Rb atom, therefore we can define the spin-exchange rate with  $\gamma_{SE}$ . The process is reversible leading to xenon depolarization. Several other mechanisms depolarizing the noble-gas nucleus are: interactions with other Xe atoms, interactions with the buffer gases, chemical shift anisotropy (CSA), interactions with the walls, inhomogeneities of the magnetic field, paramagnetic impurities in the gas mixture, etc. The total relaxation rate for  $^{129}\text{Xe}$  is:

$$\Gamma = \Gamma_{Xe-Xe} + \Gamma_{Xe-N_2} + \Gamma_{Xe-He} + \Gamma_{CSA} + \Gamma_{wall} + \Gamma_{inh}$$

The Xe-Rb spin-exchange is not considered because is taken into account separately in the build-up polarization equation. Major relaxation components at low pressure are Xe-Xe spin-rotation relaxation in van der Waals molecules and Xe wall relaxation. Recently B. Chann *et al.* [10] showed that interactions with buffer gases such as N<sub>2</sub> and He are insignificant and that Xe-Xe van der Waals molecular relaxation dominates at low and moderate pressure. Neglecting small relaxation rates, the xenon spin-relaxation rate can be

written as:

$$\Gamma = 6.7 \times 10^{-5} + 5.0 \times 10^{-6} \frac{[Xe]}{(1 \text{ atm})} + \Gamma_{wall} \quad (s^{-1}) \quad (2.41)$$

where the first term represents the molecular Xe-Xe spin-rotation and the second is the binary Xe-Xe spin-rotation. The spin-rotation interaction between two xenon atoms couples the nuclear spin to the rotational angular momentum. The wall relaxation rate  $\Gamma_{wall}$  is pressure independent and depends only on the cell geometry (surface/volume) and its surface properties (paramagnetic impurities).

The evolution of  $^{129}\text{Xe}$  nuclear spin-up density is described by:

$$\frac{d\rho_{Xe(+\frac{1}{2})}}{dt} = \left[ \gamma_{SE}\rho_{Rb(+\frac{1}{2})} + \frac{\Gamma}{2} \right] \rho_{Xe(-\frac{1}{2})} - \left[ \gamma_{SE}\rho_{Rb(-\frac{1}{2})} + \frac{\Gamma}{2} \right] \rho_{Xe(+\frac{1}{2})} \quad (2.42)$$

from which we deduce the polarization build-up equation:

$$\frac{dP_{Xe}(t)}{dt} = \gamma_{SE} [P_{Rb}(t) - P_{Xe}(t)] - \Gamma P_{Xe}(t) \quad (2.43)$$

Typically a steady state is achieved for the Rb polarization and the above equation can be solved analytically:

$$P_{Xe} = \frac{\gamma_{SE}}{\gamma_{SE} + \Gamma} P_{Rb} \left[ 1 - e^{-(\gamma_{SE} + \Gamma)t} \right] \quad (2.44)$$

The steady-state polarization for the noble-gas is achieved at:

$$P_{Xe} = \frac{\gamma_{SE}}{\gamma_{SE} + \Gamma} P_{Rb} \quad (2.45)$$

a value similar to the Rb saturation polarization from Eq. 2.7. High Xe polarization numbers are obtained by minimizing the spin-destruction and maximizing the spin-exchange rates.

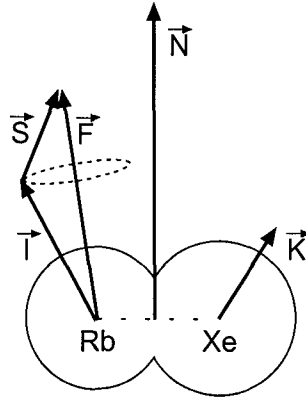


Figure 2-8: Xe-Rb angular momentums schematic.

To calculate the polarization for a steady-state system we need an overview of Rb-Xe interactions and the spin-exchange and spin-destruction rates.

### 2.3.2 Rb-Xe Interactions

The spin-destruction caused by the noble-gas atoms to the Rb includes also the spin-exchange. The interaction Hamiltonian between the Rb and the noble-gas is described by:

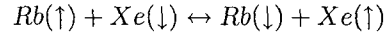
$$H_{Rb-Xe} = \gamma(R)N \cdot S + \alpha(R)K \cdot S + AI \cdot S \quad (2.46)$$

where the spin-rotation, hyperfine couplings between the Rb electron and Xe nucleus, and hyperfine coupling inside Rb atom can be recognized. The first term, spin-rotation, leads only to relaxation of Rb electron polarization, with no influence on Xe nucleus polarization.

The last term corresponds to hyperfine interaction inside the Rb atom and is neglected during the fast binary collisions, but has to be considered during the long time of the van der Waals molecules.

The second term is the isotropic term of the hyperfine interaction between the Rb

electron and the Xe nucleus and is responsible for transferring the polarization from the Rb electron to the noble-gas nucleus. Schematically is written as:



It originates from the Fermi-contact interaction and the strength coefficient is given by:

$$\alpha(R) = \frac{8\pi}{3} \frac{g_S \mu_B \mu_K}{K} |\psi(R)|^2 \quad (2.47)$$

where  $\psi(R)$  is the Rb electron wave function in the presence of the noble-gas nucleus evaluated at the noble-gas nucleus. Herman [85] showed that for alkali-noble-gas interactions there is an enhancement factor  $\eta$ , such  $\psi(r) = \eta\phi(r)$ , where  $\phi(r)$  is the electron wave function in the absence of the noble-gas. The enhancement factor means an increment factor in the probability for finding the Rb electron at the noble-gas nucleus position. It is believed to be the result of exchanging the Rb valence electron with another of the noble-gas of the same spin state. Evaluation of  $\eta$  shows a value of 50 for Rb-Xe interaction [55] resulting in a 2500 increase in the Fermi-contact strength coefficient. For  ${}^3\text{He}$  this factor is only 9.5 and partially explains the much smaller spin-exchange cross-section for Rb-He spin-exchange.

Although generally neglected, the long-range anisotropic terms in the Rb-Xe hyperfine interaction were predicted [86] to have some influence on the final polarization of the noble-gas. The full dipole potential created by the noble-gas nucleus at distance  $r$  is:

$$V_K(\vec{r}) = \frac{8\pi\mu_K}{K} \delta(\vec{r}) \mathbf{K} + \frac{\mu_K}{k} \mathbf{K} \cdot \frac{3\mathbf{r}\mathbf{r} - r^2 \mathbf{1}}{r^5} \quad (2.48)$$

which, besides the Fermi-contact interaction responsible for the spin-exchange, produces

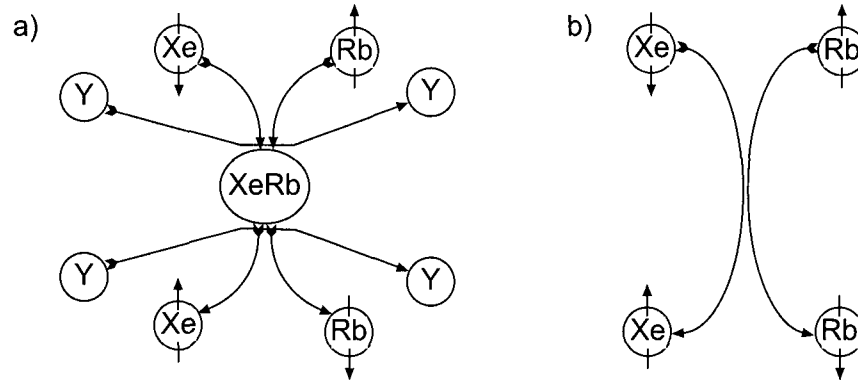


Figure 2-9: Spin-exchange schematic for: a) Xe-Rb van der Waals molecule formation after a third body collision; b) Xe-Rb binary collision.

also a second term in the Hamiltonian on the form:

$$H_{Rb-Xe,hf}^{anisotropic} = \beta(R)\mathbf{K} \cdot (3\hat{\mathbf{R}}\hat{\mathbf{R}} - \mathbf{1}) \cdot \mathbf{S} \quad (2.49)$$

This is called the anisotropic hyperfine interaction and tends to align the noble-gas nucleus spin antiparallel to Rb electron spin, resulting in depolarization of the noble-gas. Walter *et al.* [86] evaluated this term to be insignificantly small for heavier noble gases. Thus for Rb-Xe the evaluated anisotropic interaction is only 0.6% from the isotropic Fermi-contact interaction. For Rb-He this ratio is evaluated at 3%. That means that even for no relaxation acting on  $^3\text{He}$  full polarization can not be reached. Although no clear evidence exists, the anisotropic interaction is expected to be larger than evaluated, in the view of reported polarization numbers obtained for He and Xe. For the SEOP method maximum reported polarizations are  $\sim 75\%$  for  $^3\text{He}$  [31] and  $\sim 70\%$  for  $^{129}\text{Xe}$  [42]. The anisotropic interaction can be an upper limit for final noble-gas polarization.

The spin-exchange interactions happens during close contact of two Rb-Xe atoms: sudden binary collisions and long-lived van der Waals molecules. The former is less efficient



and dominates at high pressures, the latter is more efficient and dominates at low pressures. Figure 2-9 shows a schematic of the two processes with the Rb-Xe van der Waals molecule formation requiring the presence of a third body  $Y$  (Xe, N<sub>2</sub>, or He) and the sudden two-body collision.

### 2.3.3 Rb-Xe Binary Collisions

The binary collisions, dominant in the high pressure regime, are characterized by two cross-sections: one describing the Rb-Xe spin-rotation  $\sigma_{SR}$  and the second describing the Rb-Xe spin-exchange  $\sigma_{SE}$ . Recent measurements for the binary cross-section were reported by the Princeton group for the binary spin-exchange [81, 87]:

$$\kappa_{SE}^{Rb-Xe} = 2.10 \times 10^{-16} \text{ cm}^3/\text{s} \quad (2.50)$$

and the Wisconsin group [88] for the total binary spin-destruction rate:

$$\kappa_{SD}^{Rb-Xe} = 9.07 \times 10^{-16} \text{ cm}^3/\text{s} \quad (2.51)$$

The difference should be assigned to the binary collisions spin-rotation interactions:  $\kappa_{SR}^{Rb-Xe} = 6.97 \times 10^{-16} \text{ cm}^3/\text{s}$ . The spin-exchange due to binary collision is less efficient than the spin-rotation. In calculating Rb polarization we will use the total Rb-Xe spin-destruction rate as contribution to  $\Gamma_{SD}$  and for Xe polarization calculations we need the spin-exchange rate:

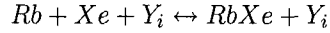
$$\Gamma_{SD}^{Rb-Xe,bin} = \kappa_{SD}^{Rb-Xe}[Xe]; \quad \gamma_{SE,bin} = \kappa_{SE}^{Rb-Xe}[Rb]$$

For 3 torr of Xe pressure corresponding to a density of  $1 \times 10^{17} \text{ cm}^{-3}$  the contribution

from binary collisions to Rb total spin-destruction rate is  $\Gamma_{SD}^{Rb-Xe,bin}=91 \text{ s}^{-1}$ . For a temperature of  $150^\circ\text{C}$  corresponding to Rb density of  $1 \times 10^{14} \text{ cm}^{-3}$  the spin-exchange rate due to binary collision is  $\gamma_{SE,bin}=0.02 \text{ s}^{-1}$ .

### 2.3.4 Rb-Xe van der Waals Molecules

The van der Waals interactions are more complex because of the long interaction times between the two atoms. The Rb electron spin spends more time in the vicinity of the noble-gas atom and the spin-destruction and spin-exchange rates are much larger than for binary collisions. Rb-Xe van der Waals molecules have lifetimes estimated at  $10^{-7} - 10^{-11} \text{ s}$  and a bounding energy of roughly  $20 \text{ meV}$  [89]. A single collision usually breaks the molecule and an inverse proportionality with the pressure of the molecule lifetime is expected. A van der Waals molecule is created or destroyed after a three body collision:



where the third body  $Y_i$  can be He, N<sub>2</sub>, or Xe ( $i=1:3$ ) and is needed for energy conservation. To describe the molecular formation specific parameters are defined:  $1/T_{Rb}$  and  $1/T_{Xe}$  are the Rb-Xe van der Waals molecule formation rates per Rb atom and per Xe atom, respectively.

$$\frac{1}{T_{Rb}} = \sum_i Z_i[Y_i][Xe]; \quad \frac{1}{T_{Xe}} = \sum_i Z_i[Y_i][Rb]$$

where  $Z_i$  are the formation rate coefficients. A van der Waals molecule will survive in average a time  $\tau$ :

$$\frac{1}{\tau} \equiv \sum_i \langle v\sigma_{vW} \rangle_i [Y_i] \equiv \sum_i k_{vW,i}[Y_i]$$

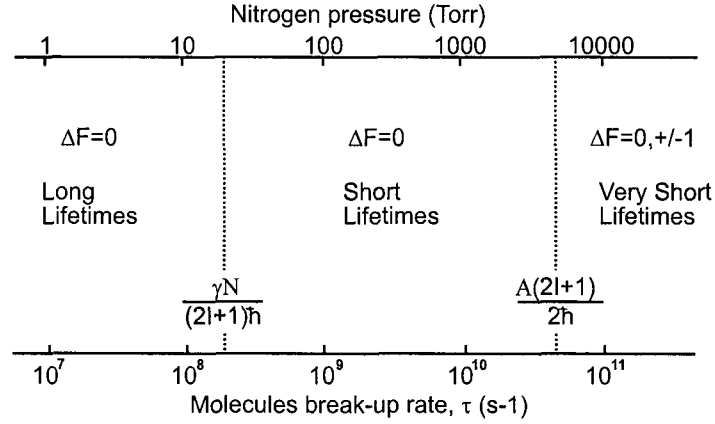


Figure 2-10: Molecular lifetime regimes as a function of the buffer gas pressure. Adapted from [67].

where  $k_{vW,i}$  are the break-up coefficients for the three gases. The chemical coefficient  $K$ , characterizing the chemical equilibrium, depends on the formation and break-up coefficients:

$$K \equiv \frac{[RbXe]}{[Rb][Xe]} = \frac{Z_i}{k_{vW,i}} = \frac{\tau}{T_{Rb}[Xe]} = \frac{\tau}{T_{Xe}[Rb]}$$

Happer *et al.* [67] divided the Rb-Xe van der Waals molecules lifetimes in three distinct regions. Figure 2-10 shows these three regions together with the molecular lifetime dependence on the buffer gas pressure (in their example N<sub>2</sub>).

The "very short" limit is characterized by molecules lifetimes very short compared with the spin-rotation or the hyperfine interaction:

$$\frac{A\tau(2I+1)}{2\hbar} \ll 1$$

The interactions are sudden with respect to Rb hyperfine coupling and the selection rule for the total angular momentum is  $\Delta F = 0, \pm 1$ . This regime is characteristic to high-pressure systems (over few amagats) and binary collisions are dominant for the Rb-Xe interactions.

For the "long lifetime" limit described by:

$$\left(\frac{\gamma\tau}{(2I+1)\hbar}\right)^2 \gg 1$$

the molecules survive very long and the molecular contribution to spin-exchange and spin-destruction is dominant. The electron has enough time to precess with a large angle around the total angular momentum  $\mathbf{N}$  of the molecules, resulting in the very large spin-rotation effect. Nevertheless, the Rb electron is strongly coupled to the nucleus and the only transitions allowed are the ones conserving the total angular momentum of the atom:  $\Delta F = 0$ .

For the intermediate regime or the "short" limit the molecules have a long lifetime compared to the Rb hyperfine interaction, but sudden with respect to the spin-rotation interaction. Since the Rb electron is still strongly coupled to the nuclear spin, only  $\Delta F = 0$  transitions are allowed.

Equations for the noble-gas nucleus and Rb time-dependent polarizations were deduced by Happer and co-workers depending on the molecular lifetime regime. The xenon polarization build-up equation presented in this thesis is much simpler by neglecting the Rb nuclear spin. To calculate xenon polarization for the steady state we need the van der Waals contributions to the Rb spin-destruction rate and to Rb-Xe spin-exchange rate.

### 2.3.5 Rb-Xe Molecular Spin-Exchange Rate

At low magnetic fields and in the short molecular lifetime limit, Cates and co-workers [80] calculated from Happer *et al.* [67] theory a simple relation for the van der Waals molecules contribution to the Rb-Xe spin-exchange rate. To consider the large quantities of buffer

gases in our system, we modified the formula of Cates into:

$$\gamma_{SE,vdW} = \frac{1}{\left(\frac{[Xe]}{\gamma_{Xe}} + \frac{[N_2]}{\gamma_{N_2}} + \frac{[He]}{\gamma_{He}}\right)} [Rb] \quad (2.52)$$

The parameters  $\gamma_{Xe}$ ,  $\gamma_{N_2}$ ,  $\gamma_{He}$  are the van der Waals specific spin-exchange rates for Xe, N<sub>2</sub>, and He, respectively. Together with the binary collisions contribution the total spin exchange becomes:

$$\gamma_{SE} = \left( \frac{1}{\frac{[Xe]}{\gamma_{Xe}} + \frac{[N_2]}{\gamma_{N_2}} + \frac{[He]}{\gamma_{He}}} + \kappa_{SE}^{Rb-Xe} \right) [Rb] \equiv \gamma'_{SE}[Rb] \quad (2.53)$$

The van der Waals specific rates have been measured or indirectly evaluated from existing experimental data and the values are:  $\gamma_{Xe}=5230 \text{ s}^{-1}$  [80];  $\gamma_{N_2}=5700 \text{ s}^{-1}$  calculated by [90] from [79]; and  $\gamma_{He}=17000 \text{ s}^{-1}$  calculated by [44] from [80]. A review of measurements for Rb-Xe spin-exchange rates through van der Waals molecules was done by Rice and Raftery [90].

### 2.3.6 Rb Molecular Spin-Destruction Rate

Rubidium spin-destruction rate caused by Rb-Xe van der Waals molecules at low pressures was studied in some extent by Nelson and Walker [82] for two different temperatures: 80 and 150°C. The parametrization of the van der Waals spin-destruction rate in the short time limit is [82]:

$$\Gamma_{SD,vdW}^{Rb-Xe} = \frac{\frac{2}{3}\phi_\gamma^2 + \frac{\beta_{129}}{2}\phi_\alpha^2}{T_{Rb}} \quad (2.54)$$

where  $T_{Rb}$  is the molecule formation rate per Rb atom mentioned before,  $\beta_{129}$  is the <sup>129</sup> isotopic abundance,  $\phi_\gamma$  and  $\phi_\alpha$  are the rms precession angles for the Rb electron around the

molecular spin  $\mathbf{N}$  and around the Rb nuclear spin  $\mathbf{I}$ , respectively:

$$\phi_\gamma = \frac{\gamma N \tau}{\hbar}; \quad \phi_\alpha = \frac{\alpha \tau}{\hbar}$$

Besides the Wisconsin group studies, there are no other reports on Rb spin-destruction at low pressure. The Rb spin-destruction measurements were done for a fixed gas mixture of 1% Xe, 1% N<sub>2</sub>, and 98% He, specific to the commercial high-pressure polarizers based on Princeton design [44].

The values obtained are  $\Gamma_{SD}^{Rb-Xe,vdW} = 2049 \text{ s}^{-1}$  and  $3240 \text{ s}^{-1}$  at 150°C and 80°C, respectively [82]. These numbers are pressure independent, but they are characteristic to the gas mixture used in measurements. In our system the gas mixture changes during our studies, since every gas component is individually controlled. Using the efficiencies in creating and breaking-up Rb-Xe van der Waals specific to Xe, N<sub>2</sub>, and He, and measured or calculated for the spin-exchange measurements, I extracted an approximate formula for the Rb molecular spin-destruction at 150°C:

$$\Gamma_{SD} = \frac{6469}{f_{Xe} + 1.1f_{N_2} + 3.2f_{He}} \text{ s}^{-1} \quad (2.55)$$

where  $f_{Xe}$ ,  $f_{N_2}$ , and  $f_{He}$  are the volumetric fractions.

For a typical gas mixture of 20:350:1000 sccm flow rates of Xe:N<sub>2</sub>:He used in our system, we obtain at 150°C  $\Gamma_{SD}^{Rb-Xe,vdW} = 2458 \text{ s}^{-1}$ . It is well-known that N<sub>2</sub> and Xe have a higher efficiency in the formation or destruction of the van der Waals molecules than He. Since we use a higher concentration of N<sub>2</sub> than the 1:1:98 mixture, commonly used by other people, the molecular Rb-Xe spin-destruction in our case is higher.

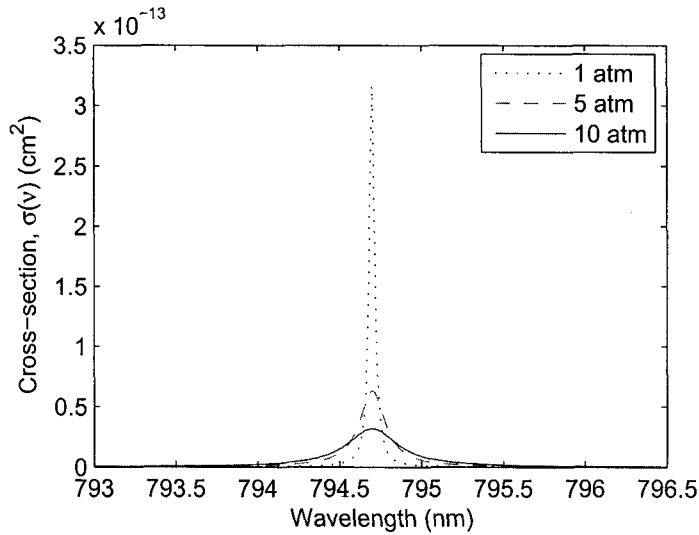


Figure 2-11: Laser absorption cross-section for different total pressure of the system considering an average D1 line broadening of 18 GHz/atm.

## 2.4 UNH Polarizer Concept

UNH polarizer concept presented in this thesis is different from anything reported previously and it combines several novel ideas resulted as this system and previous generation were built and tested. As mentioned in the introduction, xenon polarizers are separated in two main categories: "batch" production mode the continuous-flow production mode.

Figure 2-11 presents the Rb absorption profile at different total pressures of the OP mixtures and considering an average D1 broadening of 18 GHz/atm. It shows the advantage of using high pressure buffer gases, which results in a high optical pumping rate, even for lasers with a broad spectrum such are the diode lasers. Most of the reported polarizers were build following the Princeton group design [44], working at high pressure regimes ( $\sim 10$  atm) for an efficient absorption of the laser light.

The only known exception was reported by Ruth *et al.* [42] and their work involved very

low concentration of Xe combined with a very low total pressure of the pumping mixture of only 75 torr. Their number of 70% is still the largest  $^{129}\text{Xe}$  reported polarization and was obtained at only 10% Xe concentration in the mixture (the rest was N<sub>2</sub>). The polarization build-up time constant  $\tau_{SE}$  varied between 7 and 30 s, depending on temperature, 7 s corresponding to the highest temperature used of 150°C. Although the Xe polarization was extremely high compared with anything reported at that moment, the production rates were still insignificant for MRI applications.

Recently, the group of C. Bowers from the University of Florida built a continuous flow polarizers working at moderate pressure regime of 2-5 atmospheres and having a 210 W laser power available, probably the highest laser power ever used in an optical pumping experiment. Zook *et al.* [46] tested the system for different operating parameters and they observed increased of polarization numbers as they reduced the total pressure, hence reducing the xenon concentration in the OP mixture. Also, they observed polarization saturation after a certain flow rate for constant total pressure. Their largest number reported was 67% polarization for low Xe concentrations and at optimum running parameters found.

Low xenon concentration in the optical pumping mixture results in high polarization of Rb and high Xe polarization. Another alternative for a high Rb polarization is to use very high power diode lasers, resulting in high optical pumping rates. The inconvenience stands in the low absorption of the "wings" of the laser spectrum at low pressure. One way to increase the laser absorption is to increase the hot optical pumping region length and volume, such more Rb atom are available for laser absorption.

For high spin-exchange rates and low residence times for the pumping mixture (necessary for high flow and production rates) the normal choice is to use a low pressure regime.

Starting from these basic ideas we developed a new system and presented in Figure 2-12.



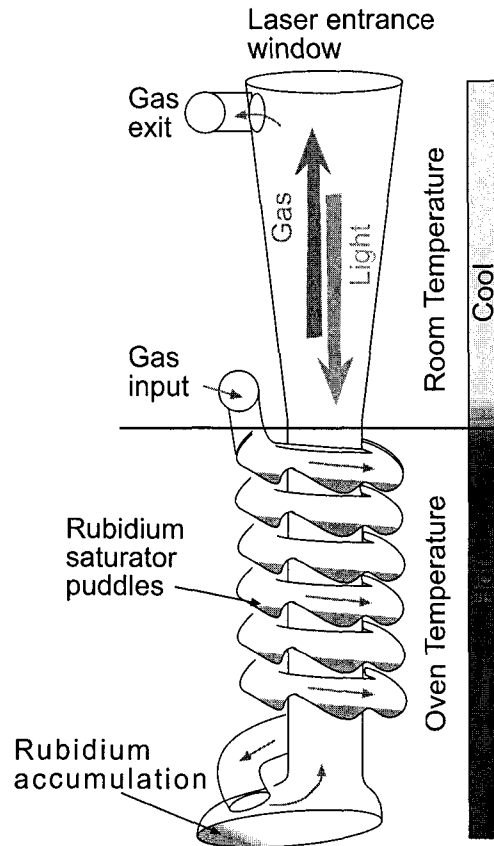


Figure 2-12: UNH polarizer concept. The Rb pre-saturator spiral saturates the gas mixture with Rb vapor before entering the optical pumping region. The very long high-temperature OP region assure an efficient absorption of the laser. Finally, the Rb is extracted from the gas mixture when is still illuminated by the laser and fully polarized, hence no Xe polarization is lost by spin-exchange with unpolarized Rb.

The main characteristics of the UNH design are:

- *Low-pressure regime.* Working at low total pressure results in a high spin-exchange rate because of the molecular contribution, about five times larger than high-pressure systems. A larger spin-exchange rate leads to a shorter time for the Xe polarization to reach saturation and the time-constant  $\tau_{SE}$  at low pressure and 160°C temperature is  $\sim 5$  s. This short spin-exchange time allows higher gas flow rates to be used, resulting

finally in higher hyperpolarized xenon production rates.

- *Long optical pumping region.* A large-volume high-temperature optical pumping region results in a higher absorption of the laser. By using a large diameter the surface-to-volume ratio is increased and the Rb and Xe surface relations are reduced. Nevertheless, an optimum diameter exists. For a too large diameter difficulties arise in shaping the laser beam to uniformly illuminate the whole region. Also, lower flow velocity which affects the final Xe polarization by a long residence time inside the optical pumping region. Small diameter results in a high gas flow velocity and there is insufficient time to reach steady-state for Xe polarization.
- *"Counterflow" of laser with the optical pumping mixture.* This novel idea, implemented only in the UNH polarizer, places the laser entrance window on top of the polarizer (see Fig. 2-12) and the gas input mixture on the bottom of the column. As a consequence, both Rb and Xe start being polarized as they move upwards towards the exit. We expect the highest Xe polarization to be achieved at the exit from the optical pumping region. After that, Rb density drops and Rb atoms are trapped on the glass surface. Laser intensity and the optical pumping rate are highest in the cold region, therefore we should expect full Rb polarization and minimum Xe polarization loss.
- *Rb pre-saturator.* Another new idea implemented in UNH polarizer was to pre-saturate the gas mixture with Rb vapor before entering the optical pumping region. This way higher flow rates of the gas mixture could be used without worrying about a saturation with Rb vapor. Therefore, we decided to use a long spiral shaped glass tube placed before the optical pumping region and outside the laser heating effects. A large amount

of Rb metal is loaded in the special designed bumps of the spiral (see figure). The gas mixture is heated to the oven temperature as it travels downwards to the optical pumping region, carrying the Rb vapor with it.

A side advantage of the pre-saturator is that by separating the Rb vapor source from the optical pumping region we eliminate possible runaways of the Rb vapor pressure from its equilibrium value. As previously mentioned, measurements of the gas mixture temperature inside optical pumping cells indicated large deviations from the oven temperature [66]. Laser absorption could result in high temperature gradients inside the cell and the Rb vapor pressure can not be considered in equilibrium with the oven temperature anymore.

Figure 2-13 presents the logistic of these enumerated unique elements of the UNH polarizer with their advantages and disadvantages. From the schematic we observe the interconnections between different polarizer's characteristics and how a characteristic's advantage cancels another's disadvantage. In comparison, Figure 2-14 shows a similar schematic for the typical high-pressure regime polarizers, where the highest disadvantage stands in limitation of the gas total flow and Xe production rate. The flexibility of this type of system is reduced.

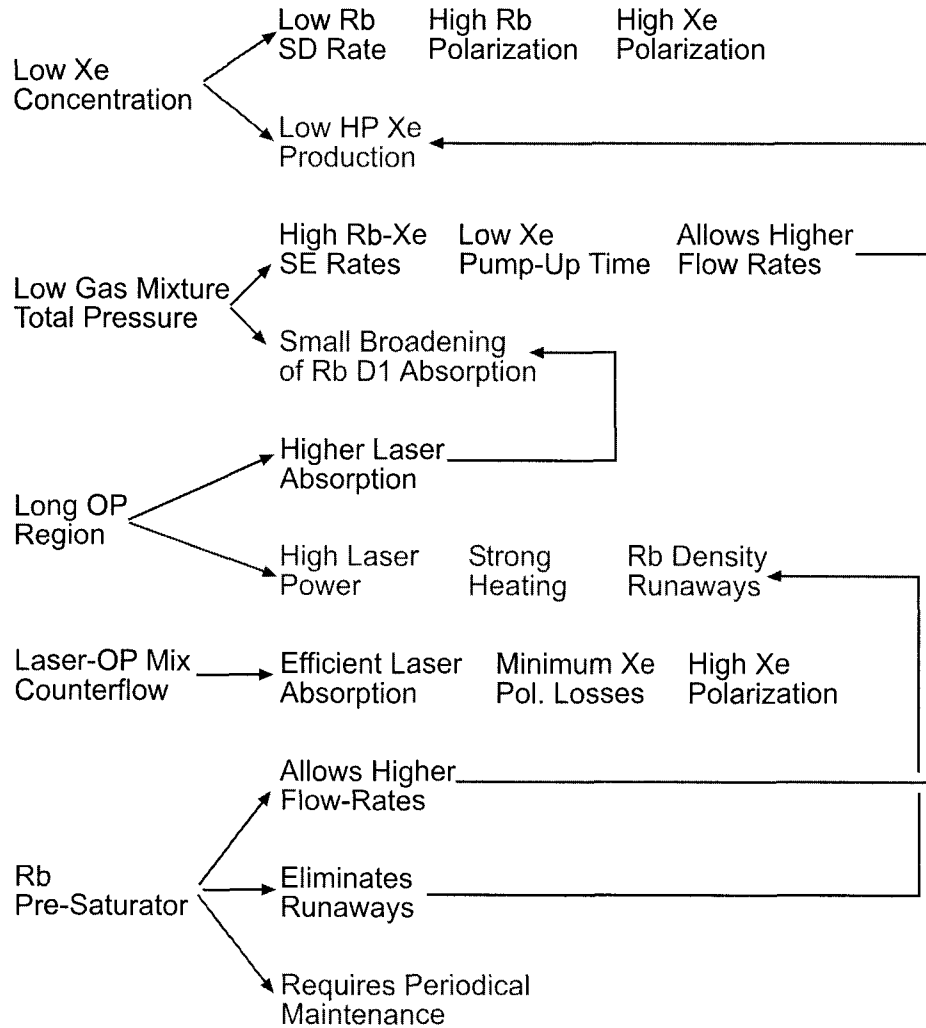


Figure 2-13: UNH polarizer logistic showing advantages (green) and disadvantages (red) of the main characteristics of our design. Most of the disadvantages are corrected by other implementations in the system. Low xenon production rate required to obtain high polarization output can be increased because of the low pressure regime and Rb pre-saturator. Lower laser absorption because of lower total pressure used is corrected by a long optical pumping cell. Rb density runaways from equilibrium in the optical pumping region because of the laser heating effects is greatly reduced by the pre-saturator.

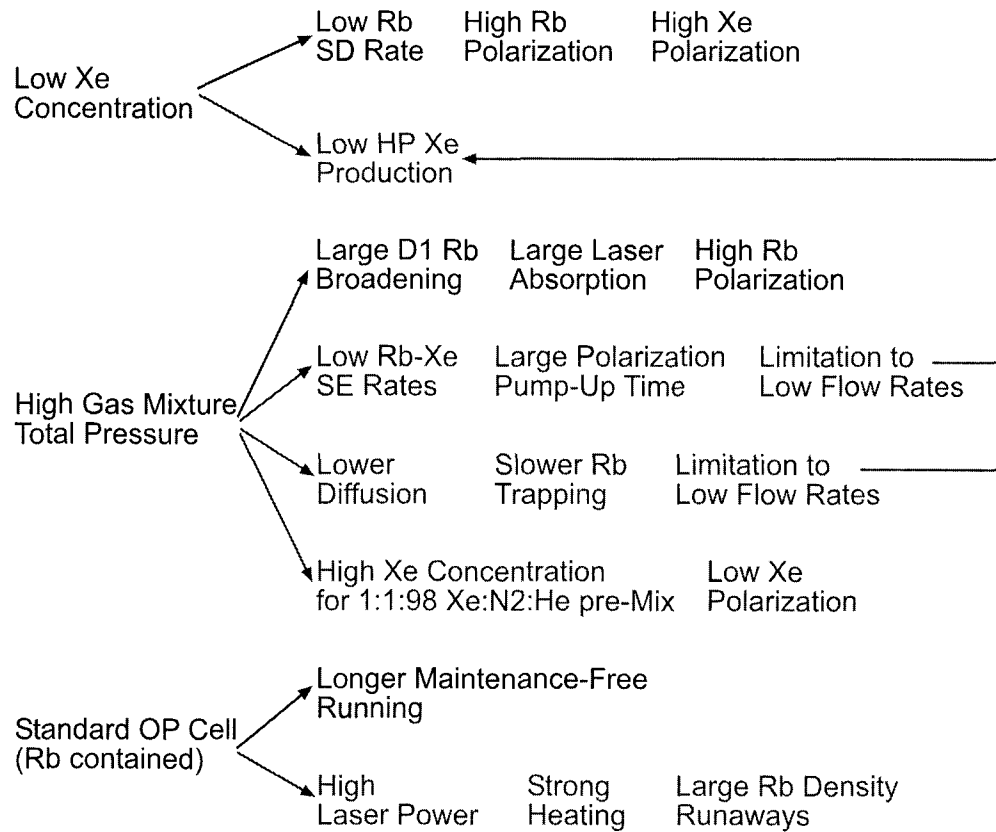


Figure 2-14: Logistic of the high-pressure regime polarizers showing limited advantages (green) compared with the multiple disadvantages (red), largest handicap being the limitation for the total flow rates and, implicitly, Xe production rate.

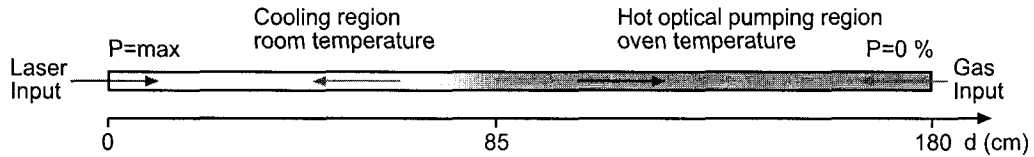


Figure 2-15: Simulation geometry: 4 cm diameter, 180 cm long cylinder, presenting a "hot" OP region and a Rb trapping cooling region.

## 2.5 Theoretical Modeling and Simulations

### 2.5.1 Modeling

After reviewing all reported spin-exchange and spin-destruction rates, we detain now all the information needed to trying simple calculations for the Xe output polarization. For this we implemented a 1D simulation which calculates the optical pumping rate, spin-destruction and spin-exchange rates, Rb polarization, and, finally, the Xe polarization build-up.

The SEOP cell is considered to be a 4 cm diameter cylinder, 180 cm long, corresponding to the physical size of our system. The column length is divided in 1 cm elements for calculations. There are two specific regions in defining the column: a "hot" high-temperature optical pumping region of 95 cm long and a cooling region of 85 cm length, where the gas temperature drops exponentially to the room temperature and the Rb is trapped out. Figure 2-15 shows the schematic of the cylinder as it is implemented in our simulation. The gas mixture loaded with Rb vapor starts flowing from the "hot" end and is considered already at the oven temperature. The temperature gradients are neglected, as well as heating effects by laser absorption. Rb density is given by Eq. 2.1.

The laser is shined from the other end of the column, against the gas mixture flow, and its flux is attenuated as it travels through. We modeled the laser spectrum as having

a Gaussian shape centered at 794.7 nm. For the laser spectrum we considered typically in our calculations two types of lasers: "broad" with FWHM=1.5 nm, corresponding to a standard diode laser; and "narrow" with FWHM=0.5 nm corresponding to an external-cavity frequency-narrowed laser. Laser power in our simulations is 100 W, corresponding to an initial flux of  $3.2 \times 10^{19}$  photons/s. We consider a perfectly uniform beam and parallel to the magnetic field (no skew light effect).

The Rb radiation trapping depolarization was neglected by considering a large amount of N2 at all times inside the gas mixture. Experimentally we observed a saturation pressure for N2 at  $\sim 125$  torr for our system. In all calculations shown the N2 flow rate is set such its partial pressure is  $\sim 130$  T.

The Rb reaches fast (ms) a steady-state polarization given by Eq. 2.8. In our calculations we neglect the nuclear spin effects and the slowing-down factor. We also ignore the Rb wall relaxation based on previous estimates and compared with other relaxations mechanisms (orders of magnitude difference). The optical pumping rate and Rb polarization are calculated from the laser absorption.

Xenon polarization is calculated by considering the gas flow towards the laser input. The gas enters with zero polarization in the hot region and it gains polarization as it moves towards the laser. Once it leaves the hot region Rb density drops drastically and the spin-exchange are minimal. For polarization build-up we consider a relation similar to Eq. 2.43, but modified to consider the gas propagation through the column to:

$$P_{Xe}(n) = P_{Xe}(n-1) + \left(1 - e^{-\Delta t(\gamma_{SE} + \Gamma)}\right) \left(\frac{\gamma_{SE}}{\gamma_{SE} + \Gamma} P_{Rb} - P_{Xe}(n-1)\right)$$

where the SE and SD rates notations follows previous ones and  $\Delta t$  is the time step for the

gas to move 1 cm. The Xe final polarization will be at distance  $d=0$  in our geometry or at step  $n=181$ .

For the gas mixture flowing through the cylinder we estimated low Reynolds numbers,  $R = v_0 l \rho / \nu$ , below 100. Therefore a Poiseuille flow is expected:

$$v(r) = v_{max} \left[ 1 - \left( \frac{r}{R} \right)^2 \right]$$

where  $v_{max}$  is the maximum flow on the symmetry axis of the cylinder and  $v_{max} = 2 \frac{\Phi}{[G]S}$  where  $\Phi$  is the total flow rate at STP,  $[G]$  is the total gas density expressed in amagat, and  $S = \pi R^2$ . A Poiseuille flow established in the cylinder results in a radial polarization distribution. The slow flowing gas towards the cylinder surface will spend more time inside the column compared with the mixture flowing in the center. We calculate xenon polarization as an average over the gas flow velocity.

We used the previously presented rates in the calculations. For xenon wall relaxation we used a value  $\Gamma_{wall} = 10^{-4}$ . This corresponds to a  $T_1$  of 100 min, which is relatively close to our measured relaxation time values in the down-tube.

The spin-destruction and spin-exchange rates are expected to be temperature dependent. For the binary collisions the rates should vary as  $T^{1/2}$  (from the thermal velocity term). Deviations from this simple dependence were observed. For the molecular rates the temperature dependence is not well-known. Nelson suggested [88] a  $T^{-2.64}$  dependence for the molecular spin-destruction and  $T^{-1.5}$  dependence for the molecular spin-exchange rates, but this is based on only two temperature points measurements. Therefore, the simulation does not include any temperature dependence and should perform best around 140-160° temperature, where most of the cited literature values were measured.



### 2.5.2 Simulation Results and Discussions

The Rb and Xe polarization build-up curves are presented in Fig. 2-16 for a temperature distribution inside the cylinder as shown on the graph. Once the gas mixture reaches the cooling region, Rb density drops to values where close to full polarization is reached. The narrow laser is absorbed much faster (in a shorter distance), which is reflected in a steeper Rb polarization build-up curve.

The faster narrow laser absorption is also shown in Figures 2-18, 2-19, 2-20, 2-21. A higher optical pumping rate is achieved with the narrow laser and higher final Rb and Xe polarizations. For all our calculations narrower spectrum lasers improve polarizer performances. Higher laser powers are preferred and we observe a theoretical saturation for Xe polarization at low Xe concentrations and very high laser powers (250 W) (Figure 2-23).

The only predicted disadvantage for using a narrow laser is caused by the skew light effect. The misalignment between the laser beam and the magnetic field has a stronger effect on the narrower spectrum lasers than on the broad lasers, as can be seen from Figure 2-22.

We also studied the output polarization dependence as a function of optical pumping region length (Figure 2-17). We observe a limit for low xenon concentrations. For our polarizer the OP region is 95 cm long, sufficient to saturate Xe polarization. Program predicts that even shorter columns should perform well. Also, by increasing the temperature the Rb density will be higher and the spin-exchange will occur faster resulting in a shorter needed optical pumping region.

Optimum temperature (Figure 2-24) seems to be in the range of 150-160°C, after which the polarization increases slightly. Temperatures much higher than 160°C are expected to give wrong results because no temperature dependence is included in the spin-exchange and spin-destruction rates. The molecular rates, crucial in our low pressure regime, are expected

Maximized Parameter	Laser Type	$\Phi_{Xe}$ (sccm)	$\Phi_{N2}$ (sccm)	$\Phi_{He}$ (sccm)	$\Phi_{tot}$ (sccm)	Pressure (torr)	Polarization (%)
$P \times M$	broad	52	334	858	1244	484	43.3
$P \times M^{1.5}$	broad	29	213	689	931	569	56.4
$P \times M^2$	broad	20	161	612	793	641	64.7
$P \times M$	narrow	68	275	260	603	286	52.8
$P \times M^{1.5}$	narrow	44	200	306	469	306	64.4
$P \times M^2$	narrow	33	165	322	408	322	71.4

Table 2.2: Optimum running parameters of the polarizer for maximizing different values of interest regarding output polarization and production rate.

to decrease as the temperature goes higher [82], therefore polarization will also decrease.

Optimum total pressure (Fig. 2-25) should occur in the range of 300-700 T for the broad laser, with a narrower peak at 400 T for the narrowed laser.

The total flow rate dependence (Fig. 2-26) shows a wide peak in the range of 300-800 sccm. Low flow rates corresponding to very slow gas velocities are not appropriate, as most of the He buffer gas has to be taken out, such there is still enough N2 for quenching. Nitrogen contributes drastically to Rb spin-destruction through Rb-Xe molecule formation, therefore Rb and Xe polarizations go down.

Summarizing, in order to obtain the highest Xe polarization numbers at low concentrations we were able to predict optimum theoretical running parameters for our polarizer: 150-160°C temperature, 300-700 T total pressure, and 300-800 sccm total flow rate.

With our program one can maximize or minimize a certain parameter by changing selected others. Using this feature we tried to optimize the gas components input flow rates and total pressure keeping the temperature fixed at 160°C, N2 partial pressure at 130 T, and lasers power at 100 W. When trying to maximize the Xe polarization its flow rate tends to go to zero, as expected. When maximizing the magnetization (polarization  $\times$  Xe flow) xenon flow goes to extremely high values and very small polarization, therefore is not a good

parameter to optimize. Table 2.2 shows the optimum flow rates and total pressure obtained when tried to maximize different combinations of polarization  $P$  and magnetization  $M$  products. The numbers are all, with one exception, in the range the optimum predicted parameters.

By "standard flow conditions" term that appears in most of the figures captions one should read: 10 sccm Xe, 350 sccm N<sub>2</sub>, 1000 sccm He, 500 torr total pressure, 160°C oven temperature. These are the optimum parameters found experimentally and used in most our calculations. Figure 2-27 shows plots of theoretical output polarization for two sets of input parameters: optimum empirical parameters, 1360 sccm total flow rate, 130 T N<sub>2</sub> (130 sccm), 500 T total pressure, 160°C temperature; and optimum theoretical parameters: 500 sccm total flow rate, 130 T N<sub>2</sub> (130 sccm), 500 T total pressure, 160°C temperature. The xenon flow rate was changed and counterbalanced with helium flow to keep total flow rate constant. The result shows that low flow rates are better for smaller xenon concentration, but at higher xenon flows the optimum empiric parameters are more suitable. Therefore we conclude that there should be different sets of optimum running parameters (such as total flow rate, total pressure, etc.) for different xenon concentrations, and the theoretical curves presented should be repeated for higher xenon concentrations also.

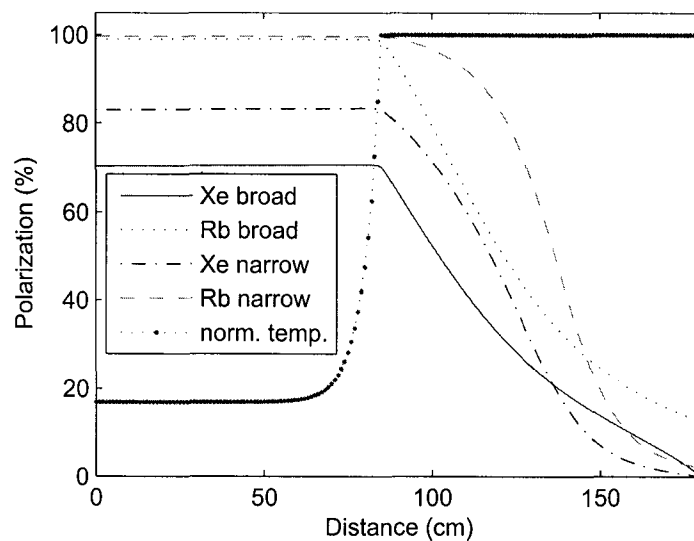


Figure 2-16: Polarization build-up for Xe and Rb as it travels from right to left inside the polarizer. The laser beam propagates from the left in the picture. Narrow laser is attenuated faster and Rb polarization is initially smaller than with the broad laser. Higher polarization is predicted for Xe with the narrow laser. Laser power is 100 W, flow conditions are "standard". Temperature is normalized to its maximum value of 160°C.

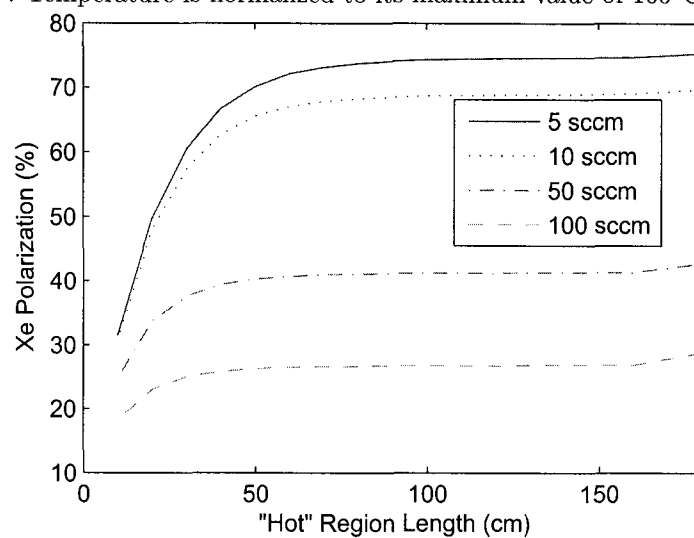


Figure 2-17: Output polarization as a function of high-temperature optical pumping region length. Our system has a 95 cm long optical pumping region, which should be sufficient for saturating Xe polarization. Shorter columns are predicted with the same performances. Flow conditions: "standard".

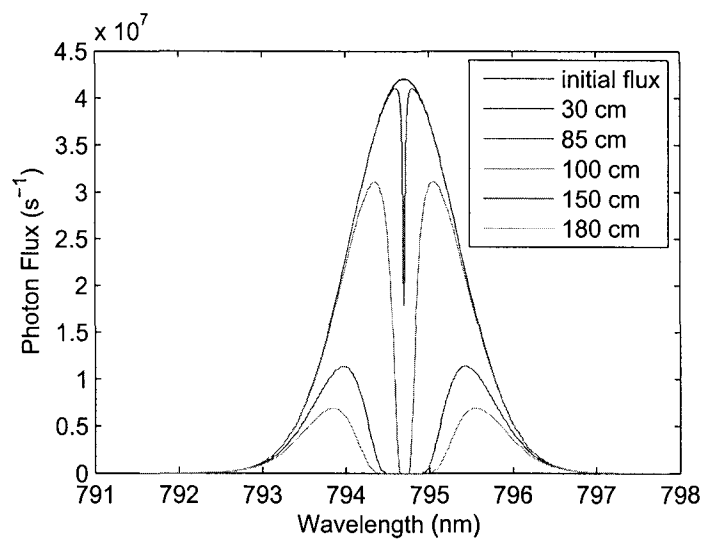


Figure 2-18: Broad Laser: flux attenuation as the laser travels through the column. After 85 cm the laser enters the "hot" 160°C optical pumping region. Laser power is 100 W, FWHM=1.5 nm. Flow conditions: "standard".

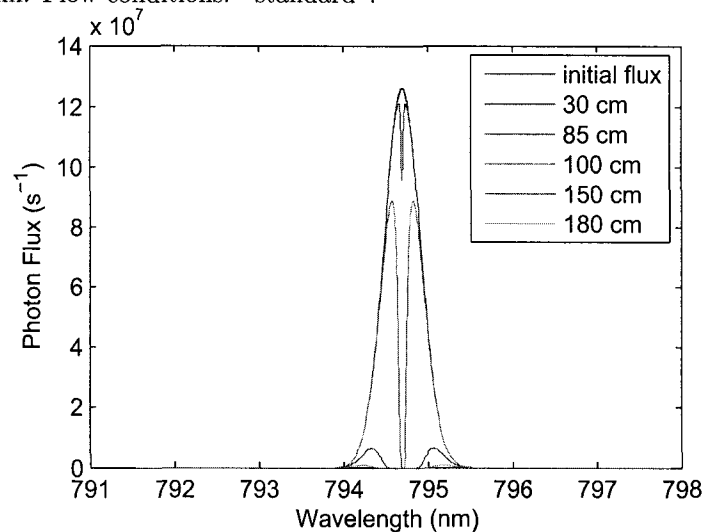


Figure 2-19: Narrow Laser: flux attenuation as the laser travels through the column. After 85 cm the laser enters the "hot" 160°C optical pumping region. Laser power is 100 W, FWHM=0.5 nm. Flow conditions: "standard".

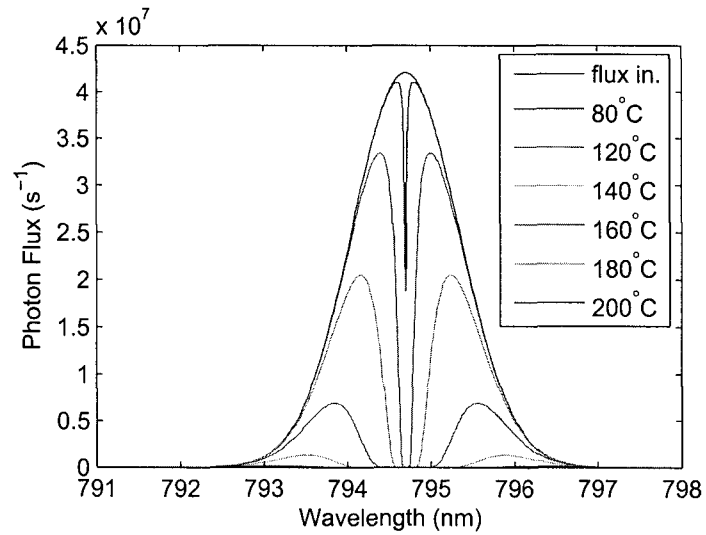


Figure 2-20: Broad Laser: total laser flux attenuation as a function of oven temperature. At 200°C most of the broad laser is absorbed. Laser power is 100 W, FWHM=1.5 nm. Flow conditions: 10:350:1000 sccm Xe:N2:He, 500 T total pressure.

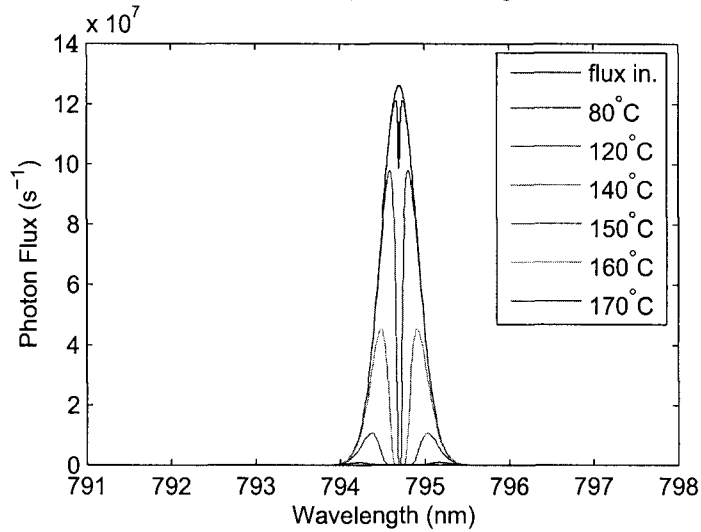


Figure 2-21: Narrow Laser: total laser flux attenuation as a function of oven temperature. At 160°C most of the broad laser is absorbed. Laser power is 100 W, FWHM=0.5 nm. Flow conditions: 10:350:1000 sccm Xe:N2:He, 500 T total pressure.

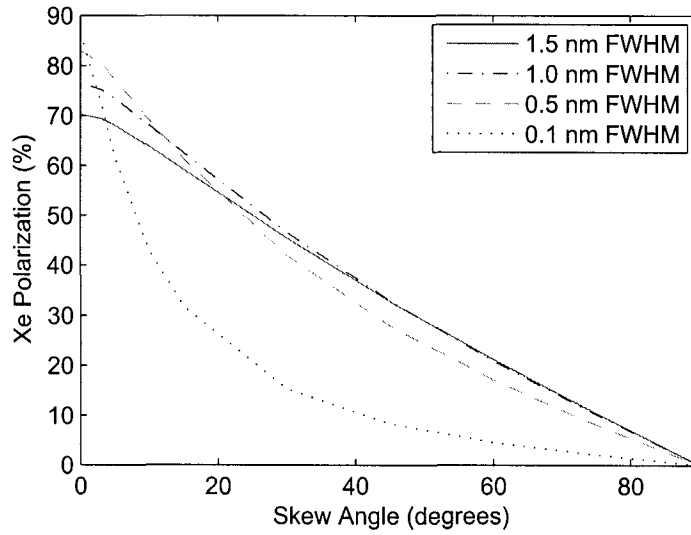


Figure 2-22: Skew light effect on the output polarization for the same 100 W laser power, but different spectrum widths. The effect is stronger on the narrower spectrum lasers. Flow conditions: "standard".

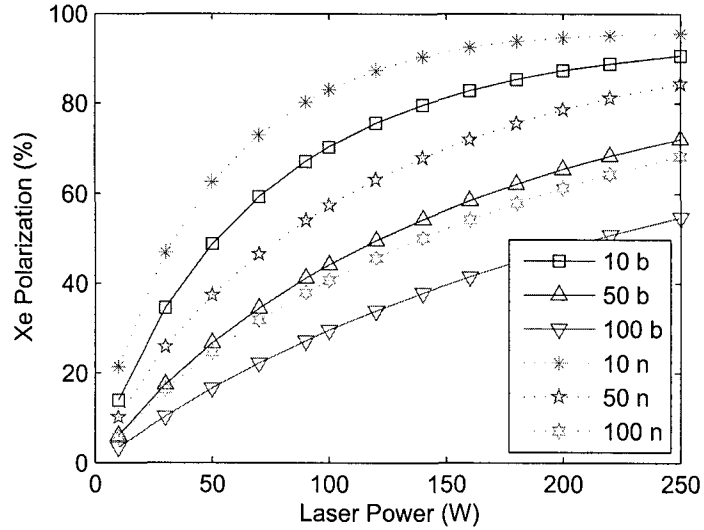


Figure 2-23: Laser power dependence for polarization: saturation is predicted for low Xe flow rates at very large laser powers. Numbers specify the Xe flow rate, "b" stands for broad laser, "n" stands for narrow laser. Flow conditions: "standard".

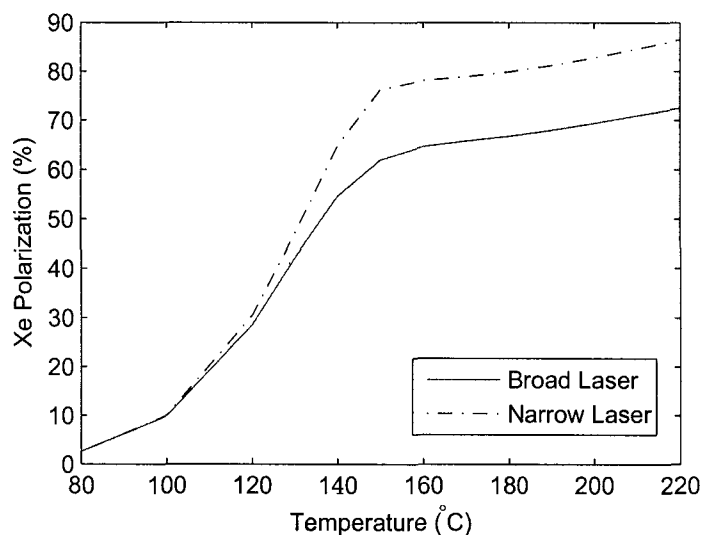


Figure 2-24: Temperature dependence for polarization showing a slight saturation at 150-160°C. The temperature dependence for the spin-destruction and spin-exchange rates are not included in the calculations and best estimate should be at 140-160°C. Flow conditions are 10:350:1000 sccm Xe:N<sub>2</sub>:He, 500 T total pressure.

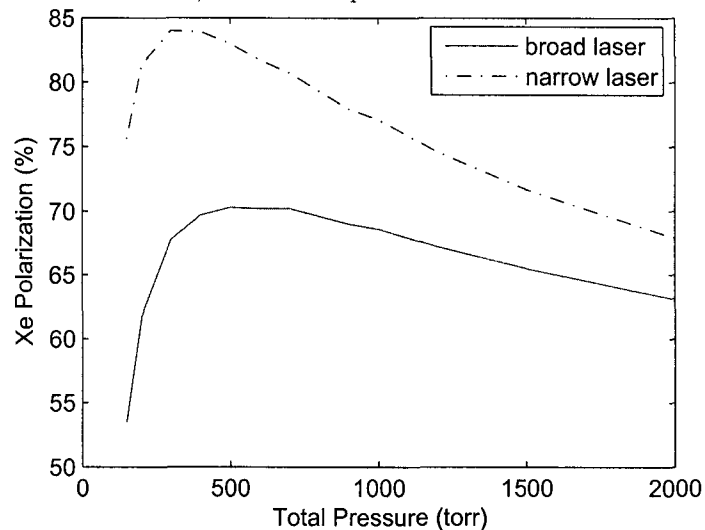


Figure 2-25: Total pressure dependence of the polarization. A maximum platform is predicted for 300-700 T with the broad laser. The narrow laser shows a peak at 400 T. Flow conditions: 3.7 T Xe (10 sccm), 130 T N<sub>2</sub> (350 sccm), He varied, 160°C, constant gas velocity.



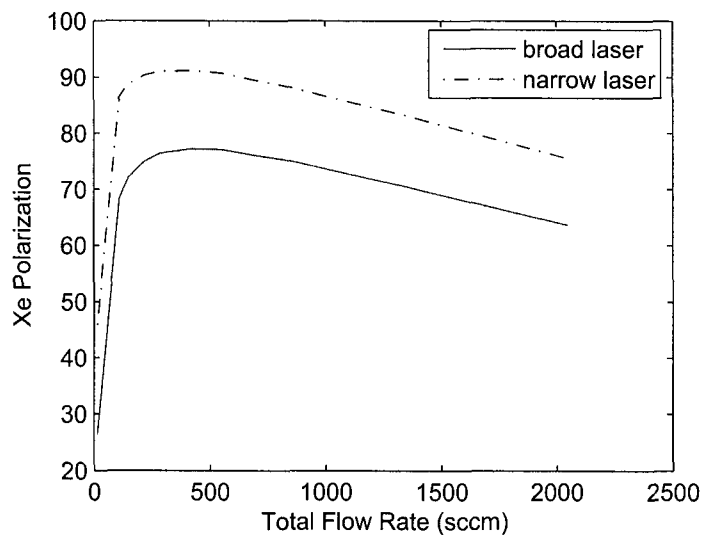


Figure 2-26: Total flow dependence of polarization shows a peak at  $\sim 500$  sccm, dropping fast for low flow rates. Flow conditions: 10 sccm Xe, 130 T N<sub>2</sub> (flow rate varied), He buffer (varied), 500 T total pressure, 160°C.

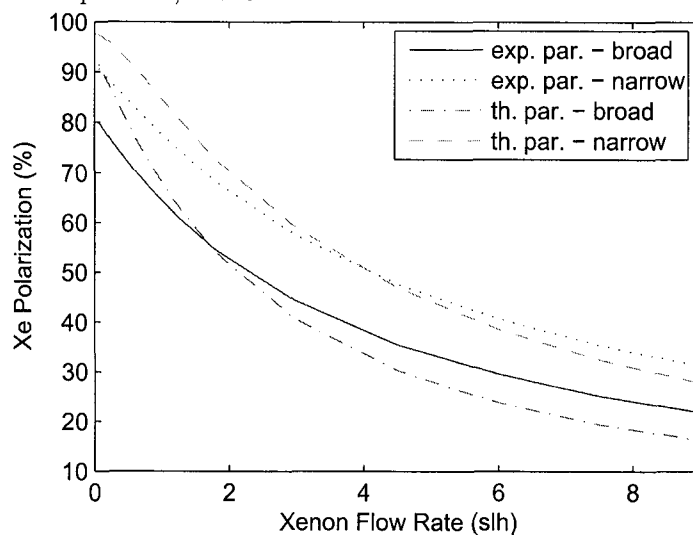


Figure 2-27: Map of the polarization as a function of Xe flow rate for optimum theoretical parameters (500 sccm total flow) and optimum experimental parameters (1360 sccm). Flow conditions: Xe flow varied, 130 T N<sub>2</sub>, He counterbalanced Xe flow, total flow rate constant, 500 T total pressure, 160°C.

## Chapter 3

# LASERS AND OPTICS

A component essential in an optical pumping setup is the angular momentum source. The high power diode lasers offer an excellent source of light for alkali optical pumping applications. Continuous-wave (CW) laser diode arrays (LDA) are commonly used in optical pumping because of their high power, compactness, and low cost. Wavelengths in the range of 800 nm were provided with AlGaAs active region lasers. Because of the Al oxidation and long term reliability problems a novel technology based on InGaAsP active region elements has been developed [91].

The laser wavelength corresponds to the D1 absorption line of the alkali metal, e.g. 794.7 nm for Rb. An LDA emission profile has typically a Lorentzian shape with a FWHM of 1.5-2 nm. The absorption profile for an alkali atom is characterized by the natural broadening overlapped by Doppler broadening with values below 1 GHz (0.02 nm) FWHM. Ti:Sapphire lasers have an emission smaller than Doppler broadening which makes this type of laser extremely efficient. The laser absorption is greatly enhanced by the Rb interactions with other atoms in the optical pumping mixture. Buffer gases are added to the optical pumping

mixtures to broaden the absorption line when using diode lasers. Pressure broadening is of  $\sim 18$  GHz/atm for He, N<sub>2</sub>, and Xe [61]. It results in 180 GHz or 0.37 nm FWHM absorption profile for a cell with 10 atmosphere of gas. Polarizers were designed to work at high pressure especially to absorb more laser power from the recently available diode lasers.

Commercial diode lasers are available in Fiber Array Packages (FAP) or bare diode arrays. The FAPs have a compact design and the output is coupled to a fiber optic. The bare LDA has a basic configuration with the light emitters directly exposed. We researched and implemented both type of lasers in our system: first, we optimized the beam shape output for a multi-FAP system; secondly, using an external feedback cavity we frequency narrowed for the first time the output spectrum of a stack of LDAs.

### 3.1 Multi-FAP Laser Beam Optimization

The FAP (Fiber Array Package) consists of an LDA bar with the necessary optics for collecting and symmetrizing the light within an environmentally sealed package. The optical output stands in a 19 fiber bundle contained within 800  $\mu$ m diameter aperture with a circular-symmetric multi-mode laser beam emission [92]. A standard fiber optic connector SMA-905 is provided for coupling and transport of the beam through fiber optics. The output nose is electrically insulated from the internal active package to protect the laser junction from external static charge. The heat generated inside the junction is transferred through the base side of the package to an external cooling source.

Figure 3-1 is showing the UNH multi-FAP setup. We used seven Coherent FAP-79-30c-800-B lasers with a maximum output power of 30 watt each [92]. The FAP units were mounted on a custom made cooling base. A Neslab HX-75 recirculating chiller provides

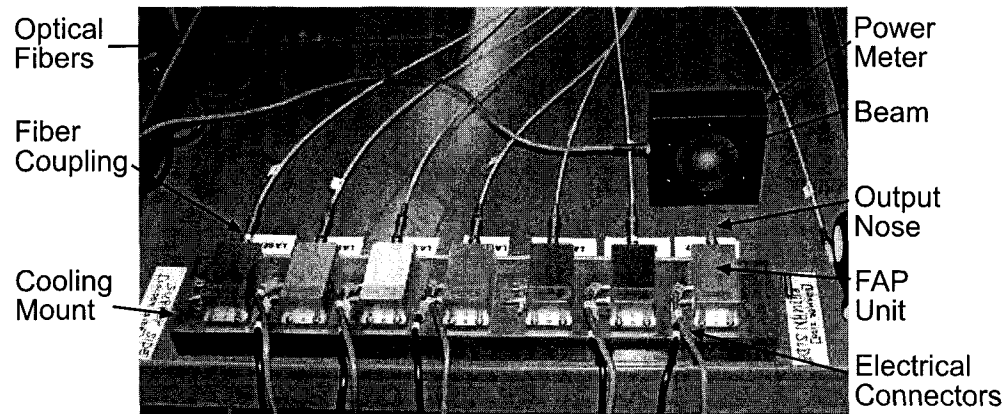


Figure 3-1: The UNH 7 FAP lasers setup (only 5 connected).

flow for the cooling fluid through the lasers mount base channel. The lasers are connected in parallel from a single DC power supply HP 6671A 8V/220A. Maximum laser power of 30 W per FAP occurs at 35 amps. The slope for the laser power is  $\sim 1$  W/amp per unit. Lasers are characterized individually by the manufacturer and delivered with specifications data sheets. Factory spectrums for the seven units show FWHMs between 1.3 and 1.6 nm at maximum power, with central wavelengths between 794.7 and 795.6 nm. The final beam wavelength changes with the internal temperature of the junctions. Changes in the temperature of the cooling fluid or in the laser operating current are reflected in the central wavelength. Our setup has a unique cooling source, therefore to optimize the position of the central wavelength for each individual unit we control small differences in currents. By using different lengths for the connecting electrical wires from the power supply to each individual lasers, the current in each unit is slightly different and optimized for a good match of the central wavelengths.

For combining the laser light from all seven units we used a 5 meter long Coherent 0632-198-01 7-to-1 fiber optic. The output configuration is circularly shaped with one laser in the centers and six surrounding it within 3 mm aperture. Optical transmission through

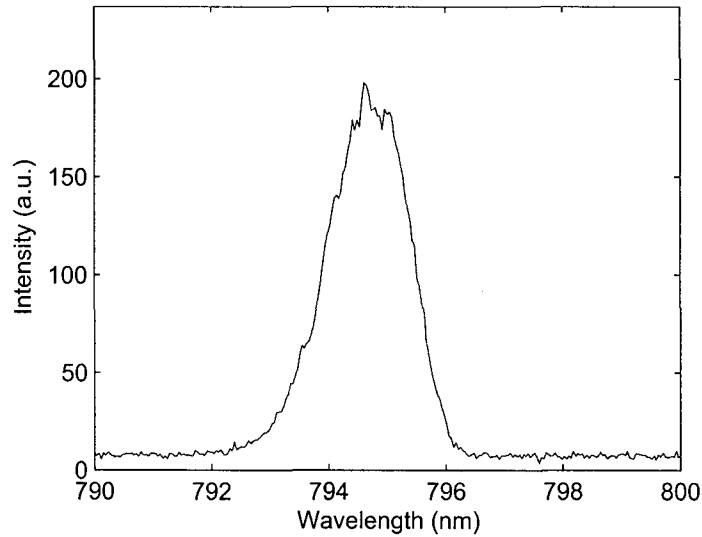


Figure 3-2: Multi-FAPs combined spectrum at 30 A and 25°C.

the fiber is specified to be smaller than 92%. The advantage of using fiber coupled lasers stands in the low divergence and the cylindrical symmetry of the output beam. Laser light transportation to the pumping cell is much eased also.

We measured the beam to diverge to be circularly symmetric within  $12.7^\circ$  when all 7 FPAs were connected to the fiber. The spectrum of the combined beam is shown in Figure 3-2. The spectrum has 1.65 nm FWHM centered at 794.7 nm for 30 A operating current and 25°C temperature. The spectrum is acquired using an Ocean Optics HR2000 high-resolution spectrometer.

The laser light that is coupled to a transport fiber optic becomes unpolarized. Therefore the optical setup must include light polarizing components. A typical optical setup used with lasers fiber-coupled is shown in figure 3-3. A polarizing cube splits an incoming beam into two linearly polarized halves offering the advantage of using the full laser power. It has the inconvenience of separating the beam into two components which need to be recombined. The linearly polarized components are transformed into circularly polarized

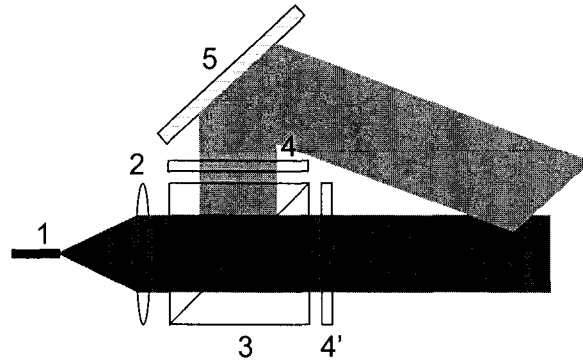


Figure 3-3: Typical optical setup for circular polarizing a fiber-coupled LDA: 1.fiber output; 2.collimating lens; 3.polarizing beam splitter cube; 4&4'.quarter-wave plates; 5.mirror.

light with optical retarders such as the linear birefringent quarter-wave plates shown in the schematic. For linear birefringent optics the index of refraction is different between the optical axis and the axis perpendicular to it. An incoming beam suffers a phase shift depending on its polarization state and its alignment with respect to the optical axis, e.g. a quarter-wave plate will produce a  $90^\circ$  phase shift between two components with electrical field vector parallel and perpendicular to the optical axis. If the incoming beam is linearly polarized and the plane of polarization makes a  $45^\circ$  angle with the optical axis the resulted beam has a circular polarization. In the same conditions a half-wave plate will just shift the polarization plane for the linear polarized incoming beam with  $90^\circ$ .

For small sized pumping cells the use of optical setups as shown in Figure 3-3 is commonly and successfully implemented. For long pumping cells this setup is not capable of producing a homogeneous well-aligned beam. As previously mentioned, skew light effects caused by misalignment between the laser and the magnetic field leads to very inefficient light absorption [93]. This fact required the development of a new optical setup which would optimize the beam shape for the long optical pumping region of our polarizer.

We found a solution for combining the two polarized halves into a final circularly shaped

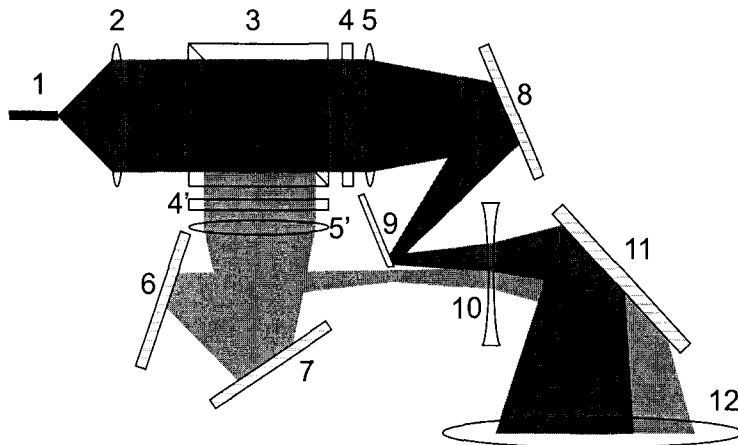


Figure 3-4: Novel optical setup for fiber coupled high-power lasers: 1) half-circle fiber output; 2) collimating lens; 3) polarizing beam splitter cube; 4&4') quarter-wave plates; 5&5') plano-convex lenses; 6&7&8) dielectric mirrors; 9) mirror at the focal point for beam combination; 10) biconcave lens; 11) dielectric-mirror in kinematic mount; 12) final 3" plano-convex lens.

beam. By starting with a half-circle configuration of the fiber output, we combined the two beams at an intermediate focal point to form a full-circle shaped beam. The optical setup is presented in Figure 3-4. The optical beam shaping components were chosen and positioned by implementation of a program to calculate and optimize the beam envelope size within the region of interest.

The half-circle input beam from the fiber is split into two components by the cube. Each of the halves travels the same distance until the focal point where they are recombined into a full circle. Half of a dielectric mirror (one inch diameter) is placed at the focus point to reflect one of the halves, with the other one passing very close to the mirror cut (see Figure 3-4).

Although initially we had seven FAP units available, we chose to decouple two of the lasers, such the output fiber configuration approached the half-circle shape. In consequence the maximum laser power available was 150 W. In Figure 3-5 are shown: a) the fiber output

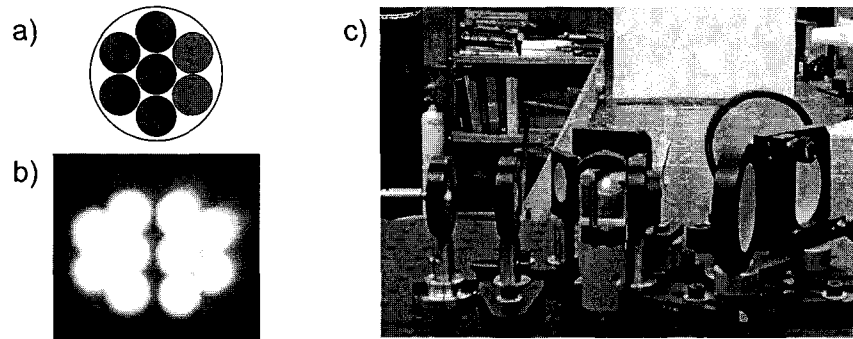


Figure 3-5: a) Fiber output configuration with only five FAPs connected.; b) Magnified image of the combined halves. c) Optics setup and the beam at one meter away.

configuration with only five FAPs connected; b) the photograph of the two beams combined together (also used in the optics alignment). Finally Figure 3-5c presents a general view of the breadboard with the optical components and the circular laser beam resulted at one meter away, fitting extremely well within the 4 cm diameter target. The shape of the final beam starts at 7.5 cm diameter at the entrance of the polarizing column ( $\sim 10$  cm away from the last lens), follows a conical shape arriving at 4 cm waist throughout most the straight tube. We found very helpful in positioning the optics and aligning the beam the use digital cameras. To use all seven FAPs we require a new fiber optic which has the seven outputs configuration in a semicircle shape.

Figure 3-6 presents three sets of measurements of laser power: at the fiber output (before any optical component), at 90 cm, and at 150 cm from the last lens in the setup. The power is measured with Molectron PM30 and PM150 thermal power meter heads. The 90 cm data set should be approximately equal with the power at the optical pumping region entrance (straight region of the column). For the five FAP lasers used we expect a nominal power of 150 W at 35 A coming out from the lasers. Power losses in the fiber are  $\sim 8\%$ , our measurements being in close agreement with factory specifications. These are combined



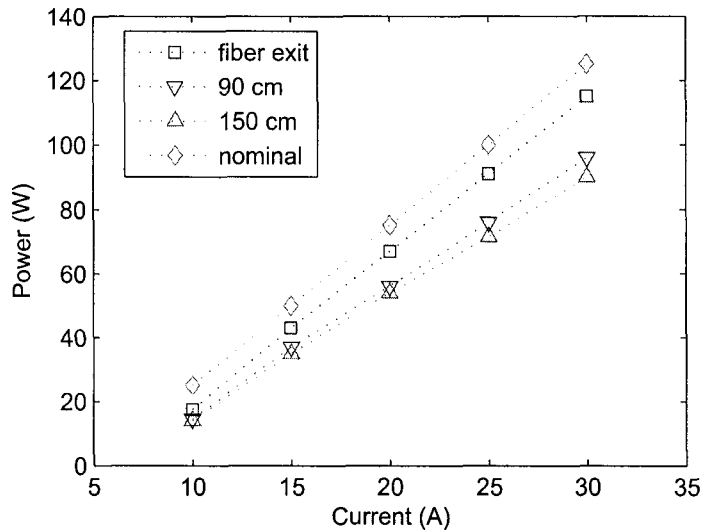


Figure 3-6: Laser power measurements done for the 5 FAP system at different points.

with losses from reflections on uncoated glass surfaces and restrictions in size of the optics, limiting the output power to  $\sim 76\%$  from the nominal power.

The diode lasers have predicted lifetime of thousands of hours if operated within the normal parameters. In time their power drops, wavelength shifts and the output spectrum becomes broader, thus regular check on their characteristics is required. We observed slight broadening of the output spectrum due to early aging of one of the FAPs. It was replaced it with one of the two spares left from the initial setup.

We observed inconsistencies in laser power measurements over time, with power varying from 90 to 115 W at 35 amps and 90 cm distance. One cause discovered was the dust deposited on optical components surface. Cleaning the optics showed an improvement in the output power of the setup. A second cause is the tight fitting of the beam inside the optics. The last convergent lens (# 12 in Fig. 3-4) has 3" diameter with the beam barely fitting inside. The position  $90^\circ$  mirror before the lens can be finely adjusted and was regularly used for final alignment of the beam inside the polarizer. Unfortunately, small

changes of the mirror send the beam side outside the final lens and some of the laser power was lost. This was probably the major reason for differences observed in the laser power.

This setup consisted the main laser in our experiments. We typically give 90 W as the power for the broad laser used. This is because we operated the laser at a lower current than maximum possible. During the optical pumping process the laser spectrum and Rb absorption profile are monitored continuously with the spectrometer. By small changes of the current and temperature we are able to shift the central wavelength of the laser in order to maximize the light absorption.

## **3.2 External-Cavity Narrowing of High Power LDA Stack**

### **3.2.1 External Cavities**

Laser diode arrays offer important advantages over the solid state laser regarding price, power, and compactness. Currently single bar LDA can produce up to hundred watts, but multiple LDA bars are commonly mounted into a stack to raise the power into the kilowatt range. The large spectral width of the laser diode arrays of typically about 2-4 nm limits the power that can be absorbed by the alkali atoms. The amount of power absorbed by the alkali atoms in optical pumping is increased by increasing the pressure in the pumping cell using buffer gases, such as  $^4\text{He}$ , and, thereby, broadening the atomic absorption lines [61]. Typical cell pressure of up to 10 atmospheres can broaden the atomic line to  $\sim 0.4$  nm at full width half maximum (FWHM). Previous xenon polarizers were designed to work in the pressure range where the laser absorption was increased by pressure broadening, such as the commercial MITI version, working at 10 atm pressure. The trade-off for more broad laser

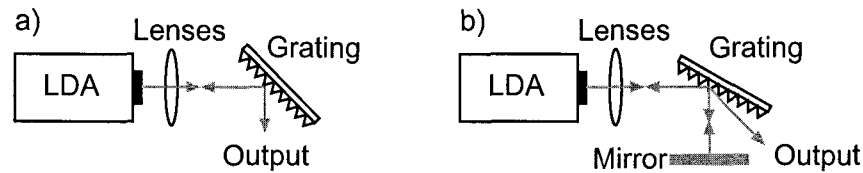


Figure 3-7: External cavities used in LDA frequency narrowing: a) Littrow cavity; b) Littman-Metcalf cavity.

absorption is a lower efficiency in Rb-Xe spin-exchange, which at high pressure is dominated by the binary collisions. To increase the laser efficiency in the low pressure regime it seems essential the development of frequency-narrowed emission high-power lasers.

It has been demonstrated that appropriately designed external cavities feedback can be used to lock the laser and force it into a narrow emission [94, 95, 96, 97]. In Figure 3-7 are shown two different external cavities used in narrowing an LDA output. The principle of an external cavity is that light from each emitter needs to be collimated, reflected off a diffraction grating at the first-order diffraction angle, and imaged back onto the emitter with high efficiency. For the Littrow cavity the output beam is taken from the specular reflection, known also as the zeroth-order of the diffraction. By slightly changing the grating angle the first-order feedback will correspond to a different wavelength, and the laser can be locked at a certain frequency. The tuning of the wavelength is limited to few nanometers and centered around the free running spectrum of the laser diode. Various experiments such as absorption measurements, Faraday rotation, etc., require a narrow-frequency low-power laser. The possibility of tuning the central wavelength makes external-cavity narrowed lasers extremely useful as probe beams. A system for such measurements is described in [98].

The Littrow cavity was successfully implemented by the Princeton group and their collaborators for narrowing an InGaAs diode laser [94] used in Xe optical pumping using Cs. They were able to narrow the laser from its free running mode of 2 nm FWHM,

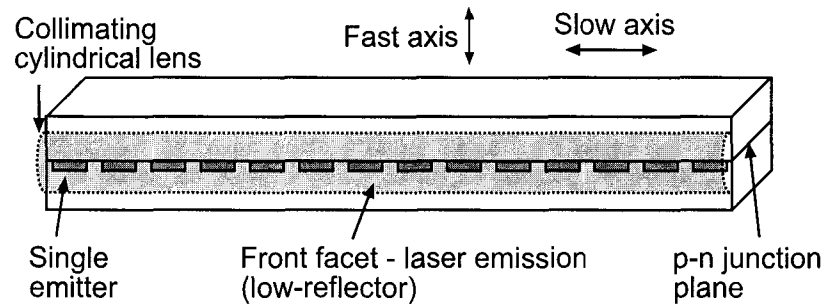


Figure 3-8: Single bar laser diode array schematic.

centered at 894.5 nm, and 1 watt CW output, to 0.12 nm and 0.4 watt. Michigan [95] and Wisconsin [96] groups reported also studies of xenon optical pumping using narrowed diode lasers. Low power laser diodes of 2-4 watt output were locked and narrowed at the Rb D1 absorption line. Although the differences in power were an order of magnitude different, both groups concluded that a narrow laser can have the same pumping effect as a broad laser. For example a narrow laser with 1.4 W and 0.08 nm FWHM gives the same  $^{129}\text{Xe}$  polarization as a 15 W broad diode laser.

A commercially LDA bar consists of a large number of emitters rectangularly shaped with the size in the micron range, usually aligned along the long axis. Figure 3-8 shows a schematic of such a bar. Each emitter operates in a single transverse mode (the fast axis - perpendicular to the plane of the active junction) and in a multitude of lateral and longitudinal modes (the slow axis - along the junction plane) [99]. The individual emitters are incoherent. The output light is strongly linearly polarized in the TM mode, where the electric field vector is parallel with the plane of the p-n junction. There is a large diffraction-limited divergence of  $\sim 40^\circ$  along the fast axis, and  $\sim 10^\circ$  along the slow axis. Typically the manufacturer attaches a small cylindrical lens, as shown in Figure 3-8 to eliminate the divergence of the beam on the fast axis, but the slow axis remains uncollimated.

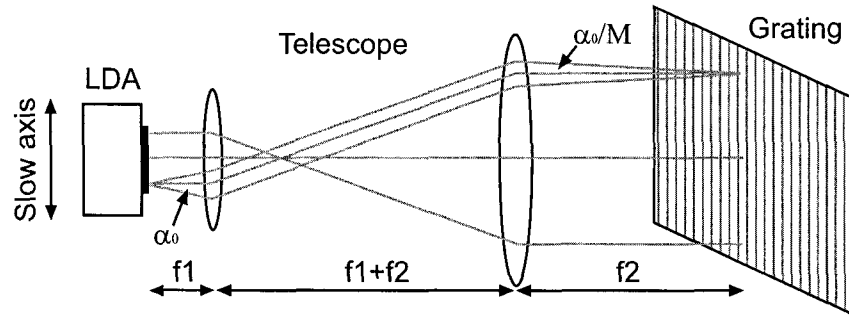


Figure 3-9: Schematic of a Littrow cavity showing LDA, telescope with magnification  $M$ , and grating. Adapted from [97].

A detailed study of an external Littrow cavity applied to a high-power LDA bar was done by the Wisconsin group. Using a 20 W commercial LDA bar, they were able to produce 14 W of narrowed beam, with a linewidth of 0.12 nm FWHM. Figure 3-9 was adapted from their Letter [97], where they discussed some of the difficulties in narrowing high-power LDA bars. Besides the divergence on the slow axis, a major problem for a commercial LDA is the deviation of the emitters positioning from a straight line along the slow axis. If there is a misalignment, then the LDA is called to have a "smile". As previously said, it is essential that the feedback from the grating is focused precisely back into the LDA emitters. For this a telescope with the magnification  $M$  is employed. Chann *et al.* [97] showed that, for an incoming beam on the grating, the Littrow condition for the first order of diffraction can be written as:

$$\lambda = 2d \sin(\theta - \phi) \cos(\alpha) \quad (3.1)$$

where  $\alpha$  characterizes the divergence on slow axis (vertical),  $\phi$  characterizes the divergence on the fast axis (horizontal) combined with the "smile" of the LDA emitters alignment, and  $\theta$  is the angle of the incidence angle of the beam on the grating. The influence of all these

parameters on the frequency narrowing will be described by:

$$\frac{\delta\lambda}{\lambda_0} = -\tan\alpha - \cot(\theta - \phi) \approx -\frac{\alpha^2}{2} - \phi \cot\theta \quad (3.2)$$

where  $\lambda_0 = 2d\sin\theta$  is the central feedback wavelength. The divergence angle on the slow axis, represented by the angle  $\alpha_0$  in Figure 3-9, is reduced by the the telescope. We have a  $1/M^2$  reduction factor in the spread of the spectrum width due to the divergence on the slow axis:

$$\frac{\delta\lambda}{\lambda_0} \sim \frac{1}{M^2}.$$

The telescope also reduces the "smile" influence on the emission linewidth by reducing the spread of the curvature angle. If  $s$  is the curvature of the "smile" (deviation of the emitters alignment along the slow axis) and  $f_c$  is the focal length of the micro lens, then:

$$\phi = \frac{s}{Mf_c}$$

and

$$\frac{\delta\lambda}{\lambda_0} \sim \frac{s \cot\theta}{Mf_c}.$$

In conclusion, to improve the narrowing of the output beam one needs a low divergence of the output beam, a good physical alignment of the emitters (no smile), large telescope magnification, and a large first order diffraction angle.

### 3.2.2 UNH External-Cavity Five-Bar Stack Setup

We describe a similar technique that we implemented to frequency-narrow a multi-array stack of LDAs. We used a high power LDA stack Nuvonyx PA-332 (Nuvonyx Inc., Bridgeton-

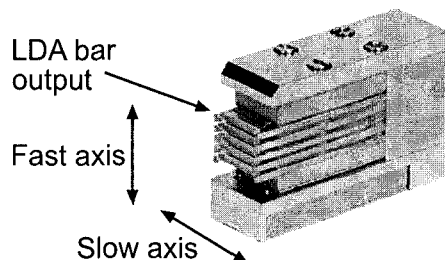


Figure 3-10: Picture of the commercial Nuvonyx 5 bar stack laser.

MO), shown in Figure 3-10, consisting of 5 LDA bars with 2.2 mm array pitch distance. Each bar has 49 optically independent emitters spaced  $\sim$ linearly across a 1 cm wide array (similar to Fig. 3-8). The stack is capable of delivering full power of 308 watt at a current of 65 A or 279 W at 60 A. The free running mode of the laser has the central wavelength at 796.5 nm for 20°C and 65 A operating current. The five bars are connected in parallel and they require a forward turn-on voltage of 1.65V, after which they exhibit approximately 0.003  $\Omega$  resistance each. Special precautions are needed for powering the diode lasers since they cannot sustain significant reverse bias voltage or current. We used a standard HP 6672A 20V-100A power supply provided with a short-circuit switch, to prevent bias currents or voltage spikes when supply is turned on. The laser efficiency has a maximum value of  $\sim$ 50% at full power. The internal generated heat needs to be dissipated and the LDA stack is provided with cooling channels for water circulation. A Neslab RTE-111 chiller recirculator sustains the laser cooling. Laser diode bars operate in a wide range of temperature and the free-running mode wavelength changes with 0.25 nm/°C. Changing the current will change the wavelength together with the internal temperature of the junction. To match the D1 Rb line of 794.7 nm sometimes the laser requires to be operated below room temperature. Condensation of water vapor from the atmosphere can endanger the LDA emitters surface. To prevent condensation we enclosed the laser module into a sealed

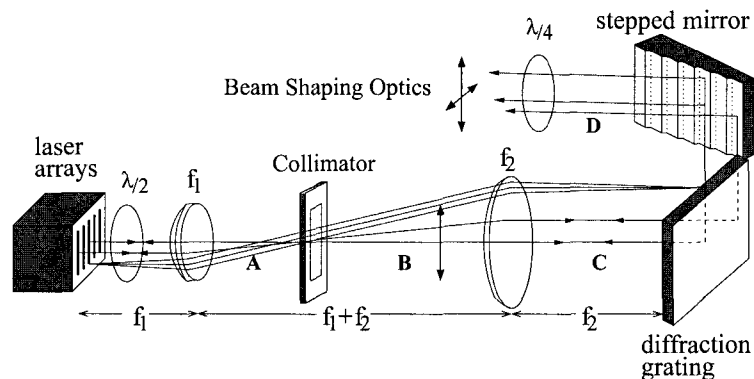


Figure 3-11: Schematic of the UNH external Littrow cavity for the 5 bars stack.

aluminum box, provided with optical window for the laser beam, electrical feedthroughs, and water-line feedthroughs. When the laser is running the aluminum box is also purged with dry air to assure a dry-clean atmosphere.

The beam divergence angles given by the manufacturer are  $38^\circ$  on the fast axis and  $10^\circ$  parallel to the array (slow axis). Cylindrical microlenses with 0.91 mm focal length were glued by manufacturer in front of each LDA bar to collimate the rapidly diverging light along the fast axis. This reduces the divergence angle to below  $0.10^\circ$  [99]. The slow axis divergence remains uncollimated. At full power the output beam has a parallel polarization to its laser junction with an extinction ratio of better than 20 dB.

A schematic of our external cavity arrangement is shown in Figure 3-11. We assembled a telescope with magnification  $M=2$  using a 250 mm focal length achromat lens and a 500 mm focal length plano-convex lens. The aberration is negligible in this case and both achromat and singlet lenses give similar results. A 75 mm by 140 mm copper-substrate gold-coated Richardson holographic diffraction grating (Spectra-Physics, Newport Corp.) with 1800 lines/mm provided the optical feedback to the laser arrays. The grooves orientation is parallel to the slow axis of the LDAs. The grating has the first order diffraction



Littrow angle at  $45.7^\circ$  for 795 nm. A temperature controller Newport 3040 drives a high-power TEC module attached to the backside copper substrate of the grating. A small fan dissipates the heat from the TEC backside. It is important to cool and keep the grating at a constant temperature since  $\sim 10\%$  laser absorption is typically lost inside the grating. Previous experience with common glass substrate holographic gratings showed instabilities in wavelength locking due to grating heating. Moreover, the glass gratings shattered when exposed at high laser power for longer periods of time.

### 3.2.3 Stepped-Mirror and Collimator Innovations

Two innovations were tested with this optical arrangement. First, we implemented a rectangular collimator in the intermediate focal point of the external cavity. The purpose of the collimator is to reduce the beam divergence on the slow axis by concentrating the laser feedback only into the spatial modes that pass through the collimator. The size of the collimator aperture is determined by the slow axis beam divergence and the fraction of the power that it blocks. The rectangular aperture is 0.5 cm along the fast axis and 3.5 cm along the slow axis. The divergence of the beam on the fast axis is minimal and no additional fast axis collimation is needed. The beam divergence is significantly reduced by the collimator while only  $\sim 10\%$  of laser power in the cavity is blocked.

Secondly, we designed and fabricated a gold plated stepped mirror for increasing intensity and beam uniformity. The stepped mirror provides individual reflective elements for each of the LDAs, such that the dark areas due to array pitch distance, magnified by the telescope, are substantially removed after the  $90^\circ$  reflection. The step width and step height were determined to first order by the light and dark band width of the incident beam measured at the location of the stepped mirror. The step in width is fixed once the mirror

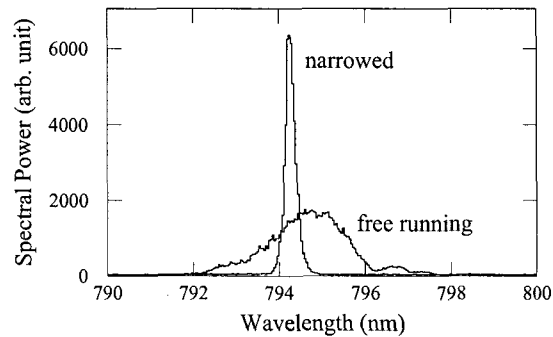


Figure 3-12: Comparison between free running and spectrally narrowed external cavity laser linewidth.

is sliced, but the steps in height can be finely adjusted through the custom designed mirror mount.

### 3.2.4 Laser Narrowing

The spectral output of the external cavity laser is measured by an Ocean Optics HR2000 high-resolution miniature fiber optic spectrometer with 0.07 nm resolution. The output laser beam could be analyzed for each of the 5 arrays individually or for the all combined after the beam was focused onto a glass diffuser and fed into the spectrometer fiber. Figure 3-12 shows a comparison between the free-running laser spectrum and the external cavity narrowed laser spectrum at 20 A. The narrowed linewidth for the combined beam from all 5 arrays is 0.31 nm FWHM. The spectral power of the narrowed laser is 3.5 times higher than of the free running laser.

The linewidth of the narrowed light for each individual array varies from 0.22 nm to 0.47 nm FWHM, as shown in Figure 3-13. The linewidth of all 5 arrays combined increases to 0.40 nm FWHM at 60 A, compared with 2.5 nm when free running.

The laser stack was not selected by the manufacturer on strict requirements for the

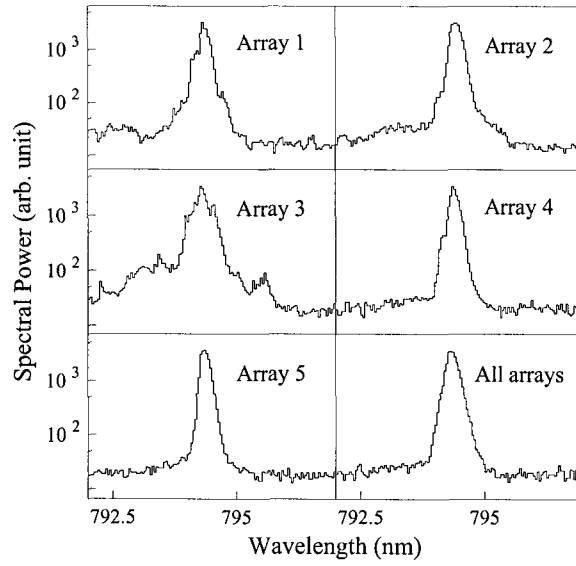


Figure 3-13: Spectral linewidth for each array and all five arrays combined.

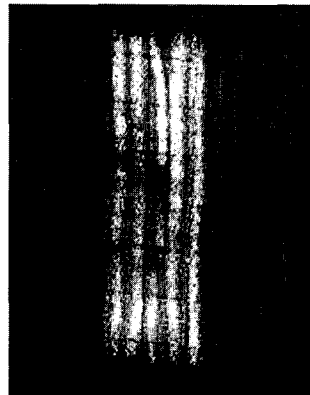


Figure 3-14: Image of the 5 LDA bars confirming the middle bar with the largest "smile".

LDAs' smiles or for the parallelism of the 5 LDAs along the slow axis. Figure 3-13 indicates that the linewidth varies significantly from array to array, with the middle LDA #3 having the largest linewidth. We photographed the smiles using a 15 cm focal length cylindrical lens to focus the slow axis onto a screen at a distance of 76 cm from the LDAs. The image captured on a digital camera for a low 10 A operating current is shown in Figure 3-14. It confirms that the LDA #3 in the middle has the largest smile. The parallelism of the 5 collimated beams is adequate, so the contribution to the linewidth of all 5 arrays combined is expected to be insignificant.

The difference in path length for arrays imaged at the near edge and arrays imaged at the far edge of the grating, defined as the grating depth of field, for our setup is 19.4 mm. The results indicate that the depth of field has very small contribution to the linewidth of all 5 arrays combined.

### 3.2.5 Output Power Optimization

The power coupled out from the cavity is maximized by rotation of the half-wave plate in the external cavity and shown in Figure 3-11. As previously mentioned, a half-wave plate just rotates the polarization plane for a linear polarized beam going through it. The LDA bars emit strong linear polarized light in TM mode, with the electric field vector lying along the long axis of the bar (vertical in Figure 3-11). The grating efficiency for the S-plane (electric vector perpendicular to the grating grooves) is typically much higher than that of the P-plane. From our measurements, the feedback is sufficient for frequency-narrowing even for the lowest grating efficiency. The maximum output power from the cavity occurs when the specular reflection from the grating is linearly polarized in the P-plane.

Holographic (interference) gratings are generated by recording an interference pattern

Power	Richardson Grating	Edmund Grating
Stimulated at A	42.9	40.6
Feedback at A	9.8	2.9
Output at D	23.0	23.5

Table 3.1: Comparison of stimulated and feedback power in the cavity with high and low modulation gratings at 20 A laser current.

onto a photoresistant coated substrate. They normally have a sinusoidal profile of the grooves, and their efficiency for a specific wavelength can be improved by changing the modulation depth<sup>1</sup> [100]. A maximum of 115 watt linearly polarized laser light is coupled out from the external cavity at a current of 60 A when using the Richardson high modulation (43% modulation depth) grating. The external cavity power output increases to 132 watt at 60 A for an off-shelf Edmund low modulation (12% modulation depth) grating. We couldn't use the Edmund glass grating for normal operation of the laser, since it shatters for laser currents larger than 30 A.

The laser power output was measured by a water-cooled thermal-head power meter Molelectron PM150-50C. Using a 2" diameter beamsampler, and after calibrating it to 5% reflectivity, we measured the power inside the cavity at different points to check for the power loss and verify the difference for gratings efficiencies. Table 3.1 shows the stimulated power and power feedback at position A (focused point after the first lens of telescope - see Figure 3-11 and the power output at position D (after the stepped mirror) for a Richardson high modulation grating and an Edmund low modulation grating at 20 A. The measured feedback efficiency is 22.8% for Richardson grating and 7.1% for Edmund grating, respectively. The power output at position D (after stepped mirror) with the low modulation grating is 52 watt at 30 A, significantly increased as compared to 46 watt with the high

<sup>1</sup>grating modulation depth - the ratio between the groove depth and the groove spacing

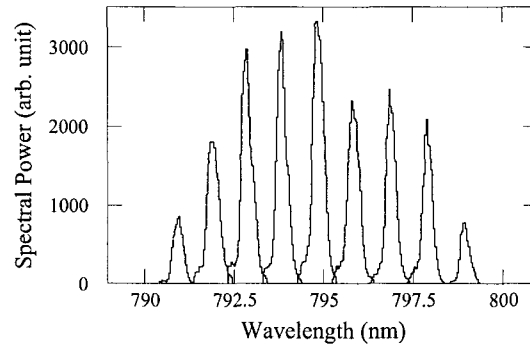


Figure 3-15: External cavity tuning range and the spectral power of the narrowed laser beam.

modulation grating. The power absorption in both gratings is  $\sim 10\%$ . As a conclusion of this study is that for high power lasers one needs to use gratings with a low modulation, with a good thermal conductivity substrate (e.g. copper) in order to dissipate the heat generated by laser absorption.

### 3.2.6 Laser Tuning

The Nuvonyx PA-332 LDA stack has free running central wavelength of 796.5 nm with FWHM of  $\sim 2.5$  nm at 20°Celsius. The free running central wavelength changes with laser operating temperature at a rate of 0.25 nm/°C. One of the most attractive features of the external cavity lasers is their wavelength tunability and stability over time. A large variation of the wavelength results by diffracting beams back to the laser with a slightly different first order Littrow angle. The external cavity in our application allows as much as 10 nm tuning. As the laser is tuned away from its free running central wavelength, the narrowed spectral power decreases, as shown in Figure 3-15.

### 3.2.7 Beam Shaping

The large polarizing cell, close to 2 meter in length, requires an optical setup for the beam shaping after the narrowing stage. Although the stepped mirror and the collimator inside the cavity reduce the divergence of the beam, the skew light effect due to the slow axis beam divergence could reduce the efficiency of the optical pumping process [64]. A combination of optical elements is implemented to control the beam size and divergence on both axis. The slow axis beam divergence is determined by measuring the beam size at various locations within 3 meters downstream. The measured divergence angle is  $2^\circ$  with the 3.5 cm collimator aperture in place. With the initial beam size after the stepped mirror known, a convex-concave lens combination can be constructed for both slow and fast axes. The focal lengths are chosen from the beam envelope calculations, and with beam divergence and initial size measured. After the shaping optics, the slow axis beam divergence angle is reduced to  $0.2^\circ$ . If wanted, the laser beam can be further homogenized in addition to the stepped mirror with an additional holographic diffuser, to be uniformly distributed across the xenon polarization column. Finally, for safety reasons, the laser is enclosed in a large custom made aluminum box. A combination of two final mirrors directs the beam down the polarizing column.

About 80 watts of narrowed laser power were measured to result after the beam shaping optics at 60 amps operating current. Due to the late development in respect with the work presented in this thesis, the laser was used mostly for demonstration purposes on the UNH polarizer. Very few studies were performed with it.

This is an extremely important development, which can substantially increase the utilization of laser power, particularly for SEOP applications at low pressure.

## Chapter 4

# UNH XENON POLARIZER

### 4.1 Polarizer Implementation

The UNH polarizer is a large scale unique system, and implements for the first time the idea of counterflowing the optical pumping mixture against the laser light. The system is vertically orientated and a schematic of its components is presented in Figure 4-1 and described in detail in what follows.

#### 4.1.1 $B_0$ Magnetic Field

The magnetic field required for Rb optical pumping and for NMR measurements is generated by a seven coil tower configuration. Coils have a diameter of  $\sim 51$  cm, the distance between the top and the bottom coils being 190 cm. Positioning of the coils was done optimizing the homogeneity of the field on the central axis. This configuration produces a magnetic field of  $\sim 6$  Gauss/amp. The coils are driven by two HP 6655A 120V-4A power supplies connected in parallel. The current through the coils is monitored by measuring the voltage



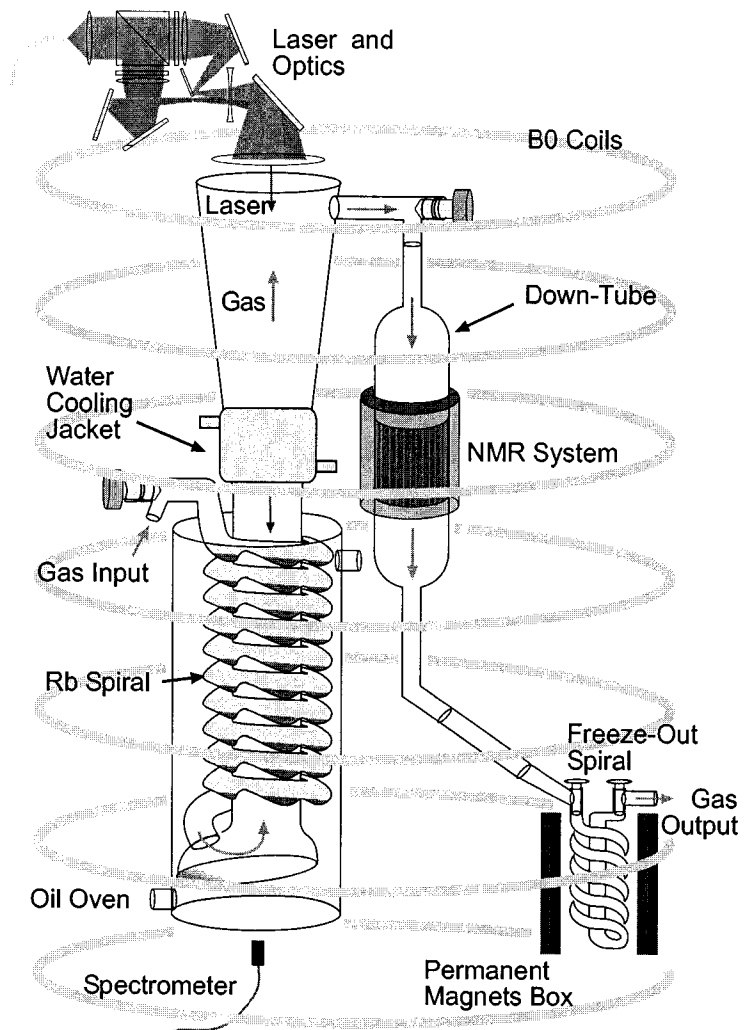


Figure 4-1: UNH polarizer schematic. Main components are pointed in the figure.

across a shunt resistor on a 6.5 digit HP 34401A multimeter. The warmup time of the coils and power supplies is about half-hour, changes in current afterwards being less than 10 ppm. The NMR frequency is 33.7 kHz corresponding to a field of 28.6 G for  $^{129}\text{Xe}$  and 10.7 G for protons. The frequency was chosen arbitrary to a low value such the effect on van der Waals molecule interaction is small. The field homogeneity in the NMR region was deduced from the xenon signal to be  $\sim 200$  ppm.

#### 4.1.2 Lasers and Optics

The lasers and the optics being used are described in detail in a previous chapter. We use mostly the 5 FAPs laser, capable of outputting  $\sim 90$ - $115$  W of polarized light with a 1.5 nm FWHM spectrum. The optics board is placed above the column on a swing pipe arm. Careful alignment is required every time the optics or the column are moved. For this we use a digital camera able to see small part of the infrared laser light. The alignment procedure stands in centering the beam on the top of the column and, by fine adjustments, in minimizing the reflections on the column side walls all the way to the bottom. Due to the length of the column we found numerous times that the laser alignment was very important in reproducing the polarization numbers.

For initial testing we attached to the polarizer the new high-power frequency-narrowed 5-bar stack laser. Since this laser is not fiber coupled and the narrowing optical setup is physically too large to be mounted on top of the column, the beam needs to travel across the polarizer in order to reach the top window entrance. The laser optical table is attached to the side of the polarizer and the beam is deviated by two  $90^\circ$  reflections down the column. The last mirror located above the column has a mount with fine adjustment screws for beam alignment.

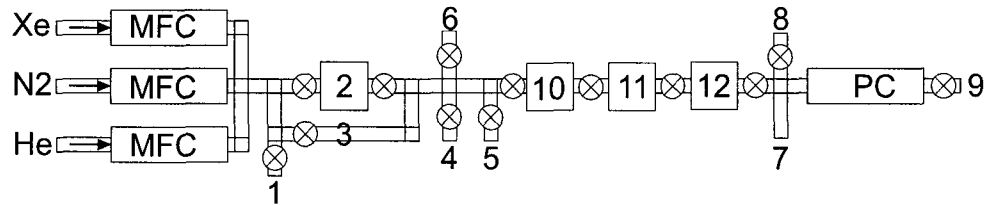


Figure 4-2: Gas flow panels schematic. Input panel: MFC-mass flow controller; 1-connection to calibration volume; 2-purifier; 3-bypass loop; 4-pressure Baratron gauge; 5-secondary vacuum pump; 6-Pirani gauge. Output panel: PC-pressure controller; 7-Pirani gauge; 8-ballast nitrogen input; 9-exhaust vacuum pump. Polarizer components: 10-polarizer; 11-down-tube; 12-freeze-out. A  $\otimes$  refers to a valve. System not drawn to scale.

#### 4.1.3 Gas Flow System

A schematic of the flow system is shown in Figure 4-2. Two different panels are present in the system: one for the gas input control which includes the mass flow controllers, and one for the gas output (exhaust) where the pressure controller is located.

The flow rates are controlled for xenon, nitrogen, and helium, individually by MKS 1479A series mass flow controllers (MKS, Wilmington-MA). Maximum flow rates are 150 sccm for Xe, 500 sccm for N<sub>2</sub>, and 5000 sccm for He. The manufacturer calibration for the instruments is done for a specific gas, typically nitrogen. In order to use them for a different gas the instruments require re-calibration. The flow panel was designed with multiple connections, one of them being attached to a small stainless steel gas bottle. The volume of the cylinder was measured with distilled water and used as the "calibrated" volume in our system. Using this known volume we measured the volumes of the other components of the flow system. Finally these volumes can be used together with a Baratron pressure gauge in calibrating the flow rates for each mass flow controller. This is done by comparing the calculated pressure value from the gas volume measured by the mass flow controller to the Baratron read pressure. We were able to calibrate all three instruments

with errors below 3% for the flow rates of interest.

To trap eventual gas impurities the input panel is provided with a NuPure 200 XL purifier (NuPure, Ottawa-ON).

The pressure in the system is monitored and controlled upstream using an MKS 640 series pressure controller placed on the output panel before the exhaust vacuum pump. It is capable of controlling up to 1000 Torr maximum pressure and allows up to 20 liters/minute of gas flow through it. The glassware connectors of the polarizer are ball-joint type and the system can not be used above the atmospheric pressure.

For vacuuming we have two Alcatel two-stage rotary vane vacuum pumps, one connected to the input panel (normally off during the polarizer operation) and one on the output, after the pressure controller, which is the main exhaust pump of the system. The lower limit for the vacuum reached in the system is  $\sim 10^{-4}$ . Two vacuum convection type pressure gauges Pirani PG105 from SRS (Stanford Research System Inc., Sunnyvale-CA) controlled by an IGC100 Ion Gauge Controller are mounted on both panels for very low pressure measurements.

All flow and pressure controllers are computer regulated through an MKS 247D four-channel controller with the addition of a Keithley four-channel DC power supply. A Lab-View program supervises the electronics, monitors, and records the gas flow rates, pressures and temperatures.

#### 4.1.4 Polarizing Column

The novelty and improvement of our system derives mainly from the design of the polarizing cell. The cell is a long piece of glass with a total length of  $\sim 1.8$  m and can be described in terms of three different operational regions: a) rubidium saturation region (spiral), b) laser

absorption and polarizing region (straight-tube), and c) rubidium condensing region (top conical tube).

The lower part of the column,  $\sim 94$  cm long, includes two of the above mentioned regions: the Rb saturation and the polarizing region. In order to have a large Rb vapor density this part of the polarizer needs to be immersed inside of an oven and kept at a high temperature. A large cylindrical glass oven encloses this lower part.

Initial setup of our system included an air heated oven. The inefficient single-pass system exhausted considerable heat into the room. In addition, thermocouple measurements indicated large temperature gradients, as high as  $20^{\circ}\text{C}$  between the bottom (input) and top (output), at  $160^{\circ}\text{C}$  nominal working temperature. To reduce heat dissipation, homogenize temperature, and allow removal of local generated heat caused by high-power laser absorption, we designed a new oven to work with liquid agent. The oven is a Pyrex cylinder with 14 cm diameter and 89 cm length. It has an oil input very close to the top and two outputs for the hot oil, one close to the bottom, and a secondary overflow output just above the input level, but on the opposite side. For heating and circulation of the thermal agent we use a Neslab Exacal EX-252HT (Neslab, Portsmouth-NH) large volume bath-recirculator capable to reach temperatures up to  $300^{\circ}\text{C}$ . For the heating fluid we use high-temperature silicone-based oil Dynalene 600 (Dynalene, Whitehall-PA). The time needed to reach  $160^{\circ}\text{C}$  from room temperature is less than one hour with a temperature gradient below  $5^{\circ}\text{C}$  between top and bottom. The oven is insulated with a double-layer of fiberglass insulation.

The Rb saturator is a spiral glass tube connecting to the central column on the bottom. The spiral has close to 6 m in length, 21 loops, and is made from 2.5 cm diameter glass tube, presenting periodic bumps blown to hold the rubidium pools. Its purpose is to offer a long path for the entering gas mixture to reach the oven temperature and to saturate the

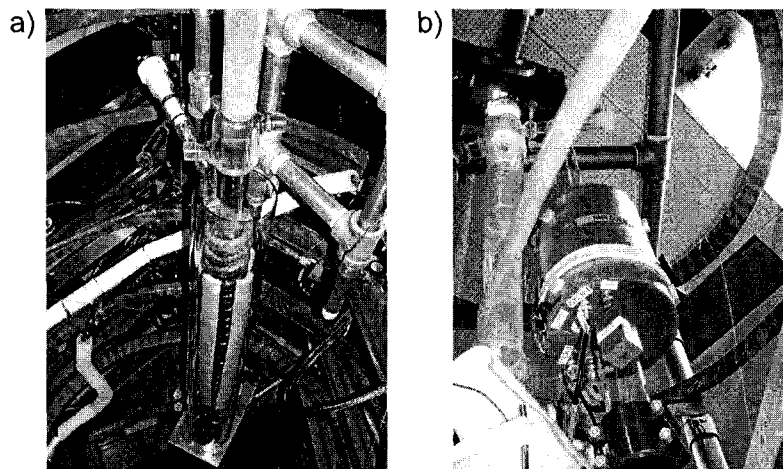


Figure 4-3: a) Lower half of the main column inside the oven (not insulated at the moment). The spiral Rb saturator is visible with the optical pumping straight inner tube. b) Top half of the main column (left) and the down-tube (right). The laser is turned on and the optics box is visible over the top of the column. The NMR coils are placed in position around the down-tube.

gas mixture with Rb vapor before entering the main column.

The spiral is provided with bumps to hold the Rb puddles. It is periodically loaded, at large time intervals, with Rb. A small side arm is located at the very top of the spiral where a break-seal Rb ampoule (Alfa Aesar, Ward Hill-MA) is attached. After the column is washed, cleaned, and dried, the seal of the ampoule is broken and, using a heat gun, the Rb is chased from the ampoule into the spiral and into the lower half spiral bumps. Initially we used to fill with Rb all the bumps inside the spiral, from top to bottom, but we observed that only Rb in the lower half of the spiral was carried away by the gas mixture. Typically we load the spiral with 25 g of Rb. Figure 4-3a shows the lower half of the polarizer placed inside the oven (normally insulated). The side arm with the stopcock is the gas mixture input.

The gas mixture, saturated now with Rb vapor, moves from the spiral into the vertical optical pumping region. The OP region is a straight cylinder, 4 cm diameter and  $\sim 95$

cm long. The mixture starts flowing upwards, against the laser beam coming from the top of the column (counterflowing). The polarization process begins at the bottom of the column, with the optical pumping mixture being illuminated with attenuated laser light, and progresses as it moves towards the highly illuminated region of the cell. The highest polarization level is expected to be attained in the top few centimeters of the hot region, where most of the laser light is absorbed.

The top half of the column is for cooling of the gas mixture, resulting in Rb condensation on the walls while still being illuminated by the laser. In order to allow the laser beam to converge to the optical pumping region size, this part was designed with a conical shape (baseball bat). It starts with 7.5 cm diameter on top and connects with the 4 cm diameter optical pumping tube on the bottom. Its length is 84 cm. To improve the cooling of the gas mixture, we implemented a 10 cm long cooling jacket above the oven (see Fig. 4-1). The water inside the cooling jacket is typically maintained at 10°C by a Neslab CFT-25 chiller. Visual observations confirm that most of the rubidium is trapped on the walls at this spot leaving the region above much cleaner when compared with no cooling jacket situation. A photo of the top half of the column is shown in Figure 4-3b. The laser optics box is seen on top illuminating the column.

After the Rb vapor is removed, the remaining gas mixture, including the hyperpolarized xenon, exits the polarizer column through the top stopcock into the down-tube. The down-tube is a long tube (122 cm) and drives the gas mixture from the polarizing column to the base of the polarizer where the freeze-out system for xenon accumulation is located. We found this tube extremely useful in measuring the Xe polarization. We implemented an NMR set of coils around the 5 cm diameter region of the tube, as shown in Figure 4-1 and Figure 4-3b. This allows NMR signal measurements at room temperature.

Finally, the xenon can be frozen and separated from the He and N<sub>2</sub> using the freeze-out system. The freeze-out system and freeze-thaw results will be discussed in detail in a next chapter.

In time, after long periods of use, the Rb vapor starts depositing in a visible layer on the top column walls, especially around the cooling jacket. We visually observed dripping of Rb from that region towards the bottom of the column, resulting in low output Xe polarization numbers. The explanation is that Rb drops inside the optical pumping region generate uncontrolled Rb vapor because of the laser heating. The xenon polarization numbers showed much lower number when compared with a clean system for the same running conditions.

When the system becomes contaminated with Rb it needs to be taken apart, cleaned, and refilled with fresh Rb. Cleaning the main column requires precaution, since it can be extremely dangerous. Rubidium is highly explosive in the presence of water and burns easily in contact with air. We developed a special procedure for washing the system. Since it can not be open to the atmosphere, we continuously flush the system with nitrogen through one of the stopcocks. At the same time we start filling the column with isopropyl alcohol from the other side (stopcock). The Rb reacts slowly with the alcohol and is "eaten" away. When the Rb puddles have disappeared we add water to clean possible small remains. Large amount of hydrogen can result when reacting with water, therefore nitrogen flushing is essential. Thereafter, we start a normal cleaning procedure with Alcanox and acid (Piranha solution) wash. Only trained personnel should attempt the cleaning procedure and team work is required. The column is dried under vacuum and leak tested under a ultra-high vacuum system. A new Rb ampoule is attached and the spiral is refilled with fresh Rb. From the experience accumulated so far, this procedure is required every three to six months, depending on the polarizer utilization.



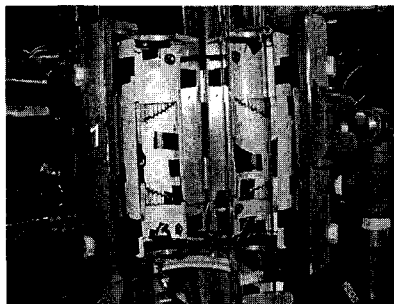


Figure 4-4: 1-aluminum enclosure Faraday cage; 2-drive coil; 3-receive coil. The setup can be halfway open for easy access (as shown).

## 4.2 Polarization Measurement

### 4.2.1 NMR Hardware

Xenon polarization is measured using a standard NMR free induction decay (FID) technique. A Surrey Medical Imaging Systems (SMIS) MRI console is used for RF drive and acquisition of the FID NMR signal. The commercial console was not designed to standardly support low kHz range frequencies. Therefore we implemented a mix-down stage for the transmit signal and a mix-up stage for the receive signal using an external 20 MHz reference signal and two frequency mixers ZAD-3 (Mini-Circuits, Brooklyn-NY). A more detailed description and schematic of the console is given in a next chapter.

We use separate drive and receive coils for a better match of their impedances at resonance with the electronics. Both coils have a "bird-cage" configuration as shown in Figure 4-4, with wires winded vertically. They are enclosed by a large diameter aluminum pipe, acting as a Faraday cage. The cage and the coils were designed to be open for easy access and removal of the enclosed down-tube (see Fig. 4-4). The coils were both tuned

with resonance capacitors to the NMR frequency of 33.7 kHz.

The RF drive signal is fed into a two stage amplifying system: a homebuilt amplifier allowing gate conditioning, followed by one channel of a home-theater amplifier (Outlaw Audio, Durham-NH). The output impedance of the amplifier needs to match a speaker impedance, 4-8  $\Omega$ , thereby the LCR resonance circuitry used for the drive coil has to be the series type. The drive coil has 16 windings (8 on each side) on a PVC pipe form with 8.6 cm outside diameter and 21.7 cm height. The coil inductance is 21.3  $\mu\text{H}$ . After tuning it with a high-voltage 1.1  $\mu\text{F}$  capacitor, we measured a resonance Q factor of 3.4 and a AC impedance at the resonance of 1.4  $\Omega$ . A small 0.1  $\Omega$  shunt resistor is present in the circuit to monitor the current for flip angle calibration purposes.

The free induction decay signal from the transverse magnetization of the polarized nuclei is picked-up by the receive coil and pre-amplified with a Stanford Research System SR560 low-noise voltage preamplifier. The signal-to-noise ratios (SNR) characteristic to the SR560 preamplifier increases with the input impedances. High impedance requires a parallel resonance for the receive coil. The receive or "pick-up" coil has 80 windings (40 on each side) on a PVC pipe form with 6.2 cm outside diameter and  $\sim 7.2$  cm height. The resulting inductance is 89.4  $\mu\text{H}$ . After tuning the coil with a low-loss 0.26  $\mu\text{F}$  capacitor we obtained a resonance Q factor of 19.6 and 387.4  $\Omega$  AC impedance at the resonance.

The down-tube, designed to drive the gas mixture after it leaves the polarizer column, has an outside diameter of 5 cm in the region where gas NMR signal is measured. Basic heat-transfer calculations shows that the gas has enough time to reach room temperature before the NMR coils region.

A cylindrical cell with an outside diameter of 5 cm (similar to the down-tube) and 30 cm in length is filled with distilled water and used instead of the down-tube for proton

calibration signal. This way we cancel geometric coil factors and errors that could interfere when comparing hyperpolarized  $^{129}\text{Xe}$  versus proton signals.

#### 4.2.2 Polarization Calculation

The polarization of  $^{129}\text{Xe}$  is measured by calibrating the NMR signal against the thermally polarized proton from a water sample. The ratio of the NMR signals is:

$$\frac{S_{Xe}}{S_H} = \frac{P_{Xe}}{P_H} \cdot \frac{N_{Xe} \cdot \beta_{129}}{N_H} \cdot \frac{\gamma_{Xe}}{\gamma_H} \cdot \frac{\sin(\alpha_{Xe})}{\sin(\alpha_H)} \cdot \frac{f(\nu_{Xe})}{f(\nu_H)} \cdot \frac{e^{-\frac{t_d \nu_{Xe}}{T_2^{*Xe}}}}{e^{-\frac{t_d \nu_H}{T_2^{*H}}}} \quad (4.1)$$

where:  $S$  is the signal strength equal with the free induction decay amplitude (FID) or the integral of the fourier transform (FFT) of the FID;  $P$  is the polarization;  $N$  is the number of the nuclei;  $\beta_{129}$  is the isotopic abundance of the  $^{129}\text{Xe}$ ;  $\gamma$  is the gyromagnetic ratio of the nuclei;  $\alpha$  is the flip angle used, typically  $90^\circ$ ;  $f(\nu)$  is a correction factor due to the receive coil resonance frequency response;  $e^{-\frac{t_d}{T_2^*}}$  is the  $T_2^*$  decay of the signal during the delay time  $t_d$  before acquiring the signal.

The polarization for proton is given by the Boltzmann spin equilibrium when place inside a static  $B_0$  field:

$$P = \tanh\left(\frac{\mu B_0}{k_B T}\right) \approx \frac{\mu B_0}{k_B T} \quad (4.2)$$

Our working frequency is at 33.7 kHz and the corresponding magnetic field is 7.9 Gauss. Boltzmann polarization for the protons at this field is  $P \approx 2.6 \cdot 10^{-9}$  at room temperature. Although this is an extremely small number when compared with gas hyperpolarization, it is compensated by the high density of the protons in water and can still be detected. To increase the SNR for the proton signal we typically acquire 1024 averages for the calibration files, using 15 s repetition time between the shots to allow full recovery of the longitudinal

magnetization.

The number of xenon atoms is calculated based on the ideal gas law:

$$N_{Xe} = \frac{P_{Xe}V}{k_B T_{Xe}} \beta_{129}$$

where  $P_{Xe}$  is the xenon partial pressure in the gas mixture,  $V$  is the sensitive volume of the pick-up coil,  $k_B$  is the Boltzmann constant, and  $T_{Xe}$  is the gas mixture temperature considered to be the room temperature. The isotopic abundance  $\beta_{129}$  is 26.4% for the natural xenon, but will change for isotopically enriched  $^{129}\text{Xe}$ .

The number of protons are calculated from:

$$N_H = \frac{2\rho_{water}V N_A}{18}$$

where  $\rho_{water}$  is the density for water,  $V$  is the same active volume of the pick-up coil,  $N_A$  is Avogadro's number, 18 is the molecular mass of water (in AMU), and 2 is the number of protons per water molecule.

We did flip angle calibrations for both xenon and proton to assure a full  $90^\circ$  flip of the magnetization. A standard SMIS NMR pulse sequence was modified to increase the RF drive amplitude in a specified number of steps for a specific power level of the SMIS machine. The program has the averaging capability needed especially for proton signal acquisition. The SMIS settings used for polarization measurements correspond typically to  $90^\circ$  flip angle and they were deduced from curves such as the ones shown in Figure 4-5.

The  $f(\nu)$  function has a Lorentzian shape describing the coils resonance response in frequency domain. The coil resonance is used to enhance the NMR signal, with the maximum signal resulting at the resonance frequency. The quality factor of an LCR resonance  $Q$  is

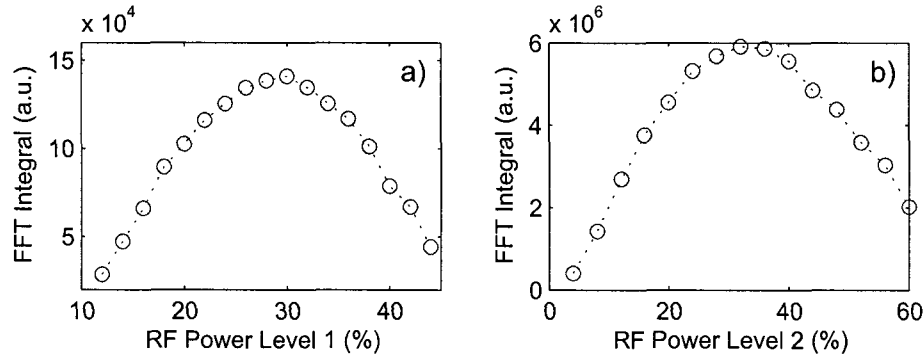


Figure 4-5: Flip angle calibration for: a) proton, b) xenon; obtained by amplitude increase in small steps. Proton  $90^\circ$  is reached at 30% on power level 1 and at 30% on power level 2 for xenon, respectively.

defined as:

$$Q = \frac{\omega_0 L}{R} = \frac{\Delta\nu}{\nu_0}$$

where  $\Delta\nu$  is the full-width at half-max (FWHM) of the spectrum and  $\nu_0$  is the central frequency. In the kHz frequency range the coil resonance can be very narrow, with Q quality factors of over 100. In consequence small differences in NMR frequencies can change the measured signal. To measure coils resonance characteristics we used a Network Analyzer. The Q for our pick-up coil is only  $\sim 20$ , relatively a small value. Xenon and water signals are acquired at the same frequency 33.7 kHz within differences of  $\pm 10$  Hz. The calculated corrections resulted from this differences are too small to be considered in our case.

The last correction factor in Equation 4.1 is to account for the  $T_2^*$  decay of the NMR signal during the delay times in acquisition. The large driving signal needed for rotating the magnetization into the transverse plane is picked-up by the receive coil if the coils are not completely decoupled (orthogonal). This parasite signal decays with a dumping factor characteristic to the receive coil resonance and typically superposes over the NMR signal for the first 1-3 ms. To prevent the preamplifier overloading and eliminate parasite signal

acquisition, we blank the pre-amplifier for the first 3 ms after the drive signal. Since xenon and proton have different  $T_2^*$  decay times, we found this correction factor to be significant (up to 10%). We extract the  $T_2^*$  values from the FWHM of the FFT spectrum. The delay times are in the range of 3-4 ms.

### 4.2.3 NMR Signal Analysis

The equations which describe the motion of the magnetization in the static magnetic field  $B_0$  are known as the "Bloch equations" [101, 102]. The detected NMR signal comes from the precession of the transverse magnetization at the Larmour frequency caused the  $B_0$  field. To rotate the magnetization from its initial alignment along the  $B_0$  field (generally considered along the  $z$  axis) an RF drive pulse with frequency corresponding to the Larmour frequency is required. The spins precession around  $B_0$  creates an oscillating magnetic flux and induces an emf into the the receive coil. Because of local field inhomogeneities at the nuclei level the spins rotates with slightly different frequencies. This results in time-increasing phase differences over the spins ensemble. The resulted signal from the whole spins ensemble decays as the difference in phases becomes larger, until a total disorder in spins phases is reached and the signal vanishes. The exponential decaying constant of the signal  $T_2^*$  is defined by the inherent spin-spin interactions of an individual spin with its neighbors ( $T_2$ ), plus other external causes such the  $B_0$  field inhomogeneities, local field gradients caused by susceptibilities, etc. Generally, the equation describing the transverse magnetization motion in the laboratory frame is:

$$M_{xy}(t) = M_{xy}^0 e^{-i\omega_0 t} e^{-\frac{t}{T_2^*}} \quad (4.3)$$

where  $M_{xy}^0$  is the initial transverse magnetization,  $\omega_0$  is the Larmour precession frequency around  $B_0$ , and the last term gives the signal exponential decay caused by spins phase differences ( $T_2^*$ ).

The time Fourier transform of the free induction decay has a real and an imaginary part:

$$S(\nu) = FT(M_{xy}(t)) = \frac{M_{xy}^0 T_2^*}{1 + T_2^{*2}(\omega - \omega_0)^2} - i \frac{M_{xy}^0 T_2^{*2}(\omega - \omega_0)}{1 + T_2^{*2}(\omega - \omega_0)^2} \quad (4.4)$$

The real part is called the absorption-mode and the imaginary part is called the dispersion-mode. The absorption-mode has a Lorentzian shape and could be used in signal analysis, if the initial phase in the rotation term of Eq. 4.3 is always zero. Since this is not experimentally true, the real and the imaginary parts get always mixed after the Fourier transform is done and the analysis of the signal can only be attempted after the phase correction. Instead, we decided to use the magnitude of the FFT signal in our analysis, mostly because no phase correction is required and a fitting routine can be easily implemented. The FFT magnitude curve is a peak centered at the Larmour frequency,  $\nu_0$ , with a full-width at half-max (FWHM) equal to  $\Delta\nu$ . We introduced in the formula an offset from zero, which is the magnitude of the noise picked by the coil. The noise level  $S_{off}$  is decreased by taking multiple averages, with  $SNR \sim \sqrt{N}$ . We described the fitting function by:

$$S(\nu) = S_{off} + \frac{S_0}{\sqrt{3}} \cdot \frac{\Delta\nu}{[4(\nu - \nu_0)^2 + \frac{\Delta\nu^2}{3}]^{\frac{1}{2}}} \quad (4.5)$$

The relation between the  $T_2^*$  and  $\Delta\nu$  is given by:

$$T_2^* = \frac{\sqrt{3}}{\pi} \frac{1}{\Delta\nu} \quad (4.6)$$

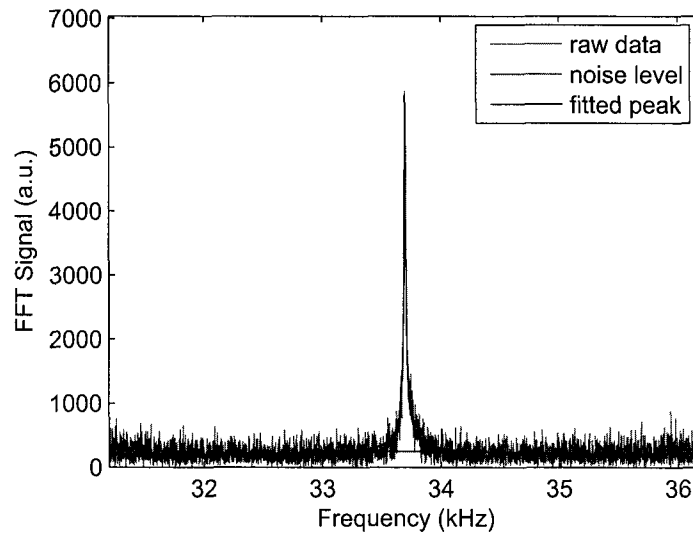


Figure 4-6: Example of NMR signal from a proton calibration file shows SNR=30, FWHM=19.3 Hz, and  $T_2^*=45$  ms. File was acquired with  $90^\circ$  flip angle, 1024 averages, and TR=15 s.

We determine all the parameters of the NMR spectrum by fitting and integrating the peak. The final value of the signal is the integral of the peak minus the noise background. Field inhomogeneities in the NMR region caused sometimes asymmetries in the FFT peak. The fitted integral was typically smaller than the integral of the experimental peak. Therefore we chose to use in our calculation the sum of experimental data points between the two extreme points where the peak reaches the noise level. The noise level intersections are found after the spectrum is smoothed with an average of 3 consecutive points.

Proton calibration files were acquired using 1024 averages with 15 s repetition time between the shots, time measured to be enough for the full longitudinal polarization to recover ( $T_1 \approx 2.5$  s). Figure 4.2 shows an example for the proton calibration file taken at 33.7 kHz. The SNR is  $\sim 30$  with a FWHM=19.3 Hz resulting in a  $T_2^*$  value of 45 ms.

Xenon files were acquired also in average mode, with 4 averages and a 20 s between the shots, to allow fully polarized xenon to flow in the NMR region. After a  $90^\circ$  flip angle the



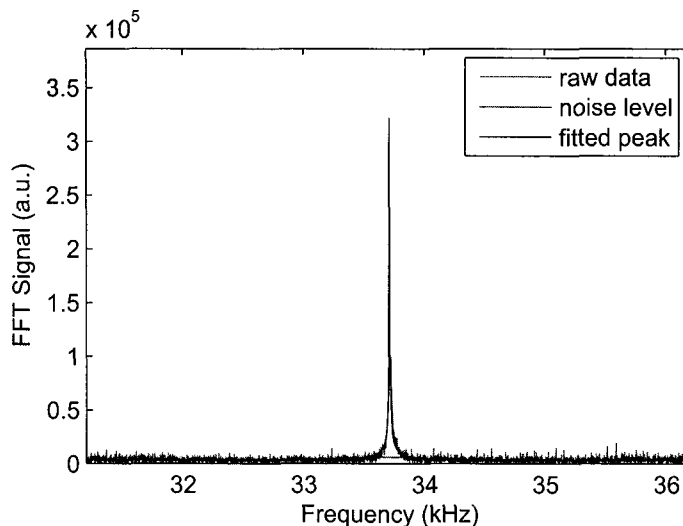


Figure 4-7: Example of NMR signal from the hyperpolarized xenon shows SNR=104, FWHM=7.3 Hz, and  $T_2^* = 120$  ms. File was acquired with  $90^\circ$  flip angle, 4 averages, TR=20 s, and polarizer flow conditions of: 10:350:1000 sccm Xe:N<sub>2</sub>:He, total pressure 500 T.

xenon hyperpolarization is completely lost and we need to wait about 15-20 s for the whole volume of gas in the NMR region to be replaced by a gas fresh mixture coming from the polarizer. Figure 4-7 shows the signal from such a file for xenon flow rate of 10 sccm, a total mixture flow of 1360 sccm, and a total pressure of 500 T. The FFT spectrum indicates SNR $\approx$ 104, FWHM of 7.3 Hz, and  $T_2^* \approx 120$  ms.

#### 4.2.4 Error Calculation

All the errors presented are systematic. The largest contribution in the final error is given by the proton calibration file. We acquired multiple calibration files and finally took the average of the main parameters needed to calculate xenon polarization. The relative error of the proton signal is  $\sim 10\%$ . This surprisingly large variations were due to magnetic field homogeneity variations and NMR coils positioning in the same place every time.

Mass flow controllers instrumental errors are defined at very large values by the factory

manuals. MKS Instruments gives for the 1479A series mass flow controllers the absolute error as being 1% from the maximum flow rate of the instrument. Using a measured volume, we performed calibration on each MFC within 3% of our values of interest. We measured for the He MFC 1% error at 1000 sccm flow rate, 1% for the N<sub>2</sub> MFC at 350 sccm, and 3% for the Xe MFC at 10 sccm. For the pressure readings we accepted the factory error of 0.2% from the full scale. Gas temperature values were considered to vary within 3° from their nominal value. To the sinus of the xenon flip angle was allowed a variation of 1%.

## Chapter 5

# $^{129}\text{Xe}$ POLARIZATION: RESULTS AND DISCUSSIONS

### 5.1 General Results

First results from this high-flow low-pressure polarizer showed the capability of producing highly polarized xenon in large quantities. The system underwent improvements over time as we reached a better understanding of its components. We implemented a cooling jacket on the main column to improve the gas cooling after the hot pumping region and the oven thermal agent was changed from air to oil in order to decrease the temperature gradient and to improve the heat exchange capacity. More improvements were done on the xenon accumulation and transportation systems which will be presented in a next chapter.

From the theoretical simulations we established a working regime for the polarizer which was finally optimized through experimental results. Initial experimental tests of polarization dependence on total gas mixture pressure showed slight dependence in the range 300-700

torr. We decided to run the system at a medium pressure of 500 torr. A lower value will increase the gas flow and rush the Rb depletion and column contamination with it, a higher value will be too close to the atmospheric pressure, making the ball-joint vacuum connections unsafe.

Generally we mapped the polarization for a specific set of parameters as a function of xenon flow rate. The total flow rate of the gas mixture was kept constant by counterbalancing the flow of xenon with the flow of the buffer gas helium. For example, we started mapping xenon polarization for 10 sccm Xe, 350 sccm N<sub>2</sub>, 1000 sccm He, for a total flow rate of 1360 sccm; the next point on the map was 20 sccm Xe, 350 sccm N<sub>2</sub>, 990 sccm He.

The nitrogen partial pressure is kept constant at a value  $\sim 130$  torr during the polarization mapping. We found this N<sub>2</sub> saturation pressure for effectively quenching the Rb excited states empirically.

During our polarization studies gas mixture components are changed. With the polarizer components volumes measured previously, we calculated the time needed for a new gas mixture to be polarized in the new conditions. The waiting time was  $\sim 5$  minutes for our typical running parameters (1.36 liters/minute total flow, 500 torr total pressure).

We found polarization numbers to be decaying over large periods of time (months). They strongly depend on the "polarizer state". By the "polarizer state" one should understand a convolution of physical parameters characterizing the polarizer, such as the laser alignment and column contamination with Rb. Largest effect is given by the polarizer contamination with Rb.

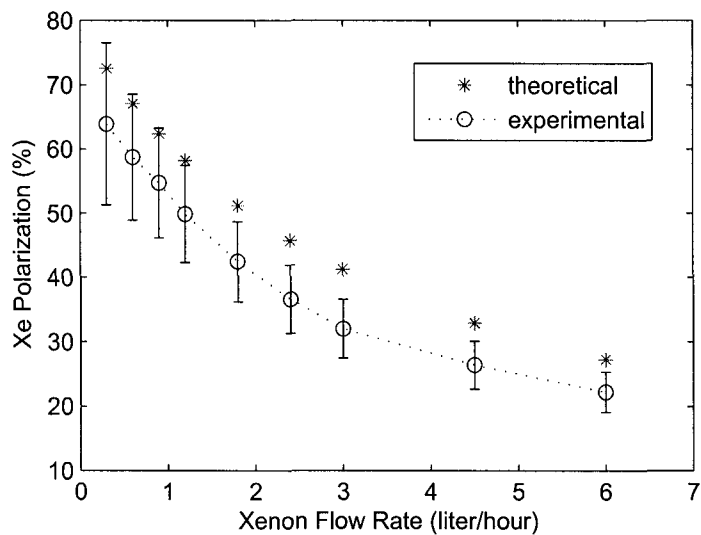


Figure 5-1:  $^{129}\text{Xe}$  polarization at optimum found running conditions. For comparison the theoretical numbers corresponding to the same flowing conditions and for 90 W broad laser power are also plotted.

## 5.2 Polarizer Performance

The polarization map shown in Figure 5-1 presents the highest numbers obtained at optimum polarizing parameters found experimentally. The oven temperature was set at  $160^\circ\text{C}$  and the total flow was kept at 1360 sccm, for a nitrogen constant flow rate of 350 sccm. The maximum polarization obtained with our system was  $63.9 \pm 12.6\%$  for a xenon flow rate of 0.3 liters/hour (5 sccm). We were unable to see a saturation for polarization for very low xenon flow rates, although we were limited by the instrumental errors of the xenon mass flow controller. A saturation should occur when the laser power is high enough to keep a 100% Rb polarization, and where  $^{129}\text{Xe}$  polarization will be influenced only by a minimized spin-destruction rate.

Theoretical numbers predicted for the same flow rates and for a broad laser power of

90 W are plotted for comparison on the graph. Predicted polarization are larger than the experimental obtained values, but they follow closely the dependence on the xenon flow rate. The theory-experiment differences can have multiple causes, and, without diagnostic instrumentation to measure Rb density and polarization inside the column it is very difficult to make any supposition. We also neglected some relaxation mechanism, such is the surface relaxation for Rb. Rb-Xe molecular spin-destruction, the largest mechanism, was approximated from the only source of literature existent [82]. We observed visually turbulence of Rb flow for higher xenon flow rates, certainly caused by gas mixture heating after laser absorption. Our 1D simulation considers a perfect uniform temperature distribution, with no laser heating effects. Taking into account all these factors, we consider that the predicted numbers are still in close agreement with the experiment.

### 5.3 Temperature Dependence

Polarization as a function of temperature was mapped to locate the optimum running temperature for the polarizer. Rubidium vapor density changes drastically with temperature [51]. By controlling the temperature of the oil inside the oven, we control the Rb vapor density in the hot spin-exchange region of the column. Theoretically, there should be an optimum Rb density for which a maximum polarization is attained. A low Rb density will not be sufficient for efficient laser absorption and fast Rb-Xe spin-exchange. Rb in excess will become opaque to the laser in a very short distance and, again, polarization transfer will not have enough time to reach saturation. Theoretical simulations showed polarization saturation for temperatures 150-160°C. The theoretical numbers after 160°C are probably incorrect since no temperature dependence was included in the optical pumping and spin-

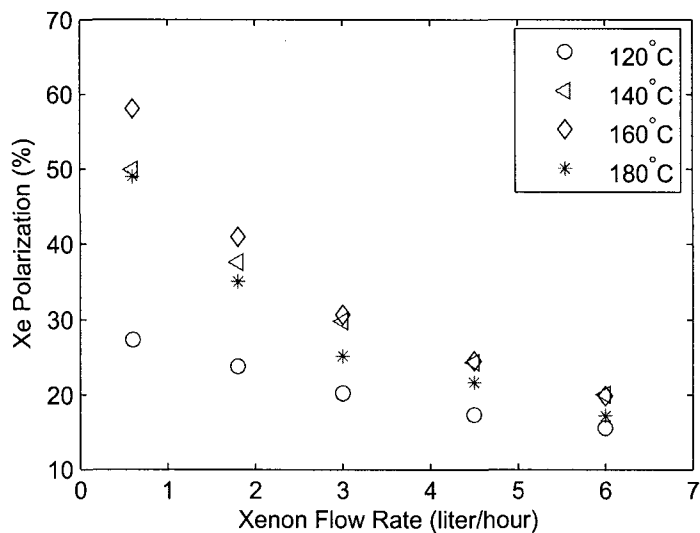


Figure 5-2: Polarization dependence on xenon flow rate at different oven temperatures showing an optimum at 160°C. Flow conditions: total flow rate constant at 1360 sccm, total pressure constant at 500 T, N2 flow rate 350 sccm.

exchange rates. Moreover, the molecular spin-exchange rates are expected to decrease at higher temperatures [88].

Temperatures reported in literature for xenon polarizer range between 80 and 180°C. We did several mappings of the polarization for different oven temperatures. Figure 5-2 shows one of these studies. The total flow rate and the nitrogen partial pressure were kept constant during the study. We started with 10 sccm of Xe, 350 sccm of N2 and 1000 sccm He, and increased the xenon flow rate, counterbalancing with helium for a constant total flow of 1360 sccm. The total pressure was constant at 500 torr for all experiments. Due to the size of oven and the hot polarizing region, there is a temperature gradient of 5°C between the top entrance of the hot oil, and the bottom exit. We considered the nominal temperature to be the one shown by the top thermocouple.

The optimum temperature for our system was found to be at 160°C, corresponding to a Rb vapor density of  $1.7 \times 10^{14} \text{ cm}^{-3}$ . This is in good agreement with our theoretical

predictions, although the drop of polarization at 180°C is not seen in Fig. 2-24. At higher xenon flow rates, corresponding in our case to higher xenon concentrations, the polarization curves overlap for temperatures between 140 and 180°C. Probably polarization numbers at higher concentrations of xenon in the mixture are dominated by the insufficient laser power instead of Rb density effect.

As previously mentioned, observation of the polarizer for long periods of time demonstrated that contamination of the main column with Rb resulted in low xenon polarization numbers. Although we don't have quantitative measurements for Rb density inside the polarizer or local OP mixture temperature, we strongly believe that the low numbers resulted after prolonged utilization of the polarizer.

The high-power laser absorption leads to high temperatures of the gas-vapor mixture, evaporating eventual pools of Rb created on the side walls of the column. Although Rb is trapped on the upper side of the column, we observed dripping of Rb liquid into the lower optical pumping region.

In a system like ours, where the Rb metal pools are designed to be outside the pumping region, one could test the contamination by doing regularly temperature maps of polarization. We observed severe changes in temperature dependence of xenon polarization when contamination was too high. When this was the case, the system needed cleaning of existent Rb, followed by a refill of the spiral with fresh Rb pools.

## 5.4 Nitrogen Dependence

Nitrogen has the major role of quenching the Rb excited states fluorescence when relaxing to lower states. The lack of nitrogen will lead to emission of unpolarized light by



the excited Rb atoms, photons which could be further absorbed and lead to depolarization of the polarized ground state. As one would expect, there should be a saturation point for nitrogen in the gas mixture where most of the Rb fluorescence is quenched by nitrogen.

In Figure 5-3 we present polarization dependence on the nitrogen partial pressure in the gas mixture. The system was run at 160°C, for a total flow rate of 1070 sccm and xenon flow rate constant of 20 sccm (1.2 slh). The variation of nitrogen flow and pressure was counterbalanced with helium.

The saturation with nitrogen was found at  $\sim 125$  torr partial pressure. Past this value the polarization is constant within the error bars. The nitrogen maximum flow rate was limited to a maximum of 500 sccm by the mass flow controller, hence we were unable to test higher partial pressures for an eventual decay of polarization.

For all our measurements the nitrogen flow was chosen such its partial pressure was larger than 125 T. An estimation from Eq. 2.19 gives at 125 torr N<sub>2</sub> partial pressure a radiative decay probability of 2.3%.

In Figure 5-4 the polarization numbers from Figure 5-3 are normalized and plotted together with the quenching probability calculated from Eq. 2.19. The two plots are not matching at lower values of N<sub>2</sub> partial pressure. Based on previous measurements [56], Wagshul and Chupp [57] advised pressures larger than 60 T to be used, such N<sub>2</sub> will assure sufficient quenching. The fact that we observed a much larger number for our system and a slower saturation with N<sub>2</sub> can be caused by the higher power of the laser in our case. After a quenching collision the N<sub>2</sub> molecule jumps to a highly excited vibrational state ( $\nu=5, 6$ ). This energy is thermalized after multiple collisions with other buffer atoms. Walter *et al.* [66] claimed that the vibrational relaxation times can be extremely long compared with rotational or translational relaxations (which are at a scale of 1 ns). For high optical

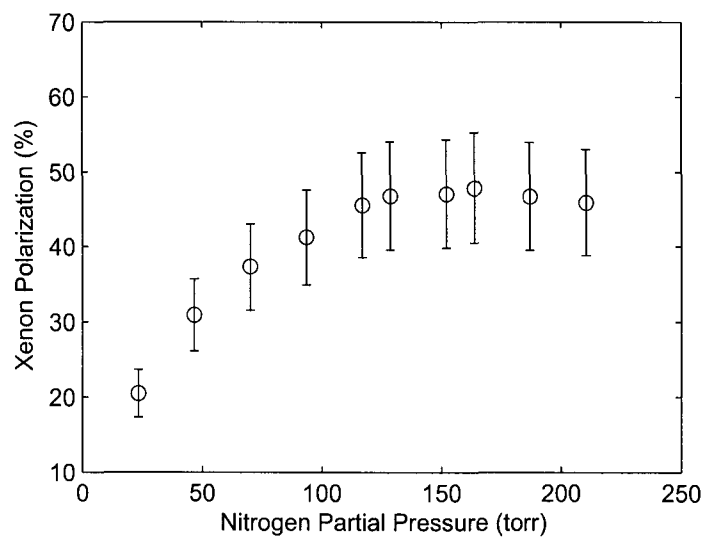


Figure 5-3: Polarization dependence on nitrogen partial pressure: saturation is obtained above 125 torr. Flow conditions: Xe flow rate constant at 20 sccm, total flow rate constant at 1070 sccm, total pressure constant at 500 T, temperature 160°C.

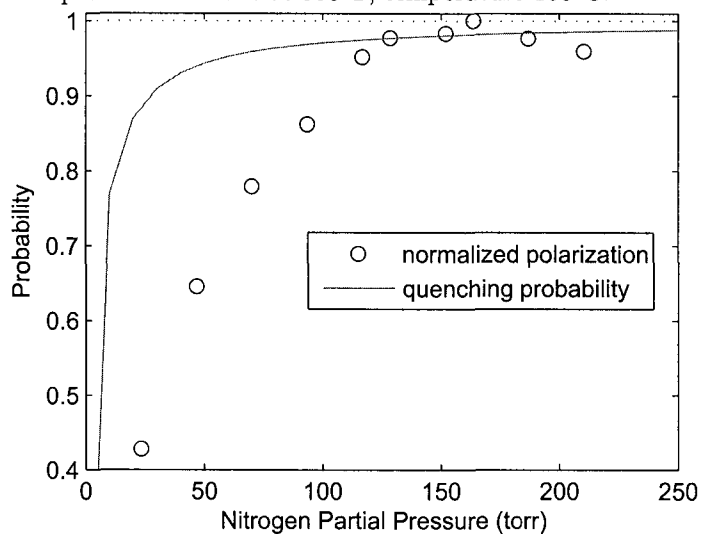


Figure 5-4: Nitrogen quenching probability, reported by Wagshul *et al.* [57], plotted together with the normalized Xe polarization numbers from Fig. 5-3 show that for our system saturation with N<sub>2</sub> appears at a higher value than 60-100 T, considered sufficient in previous reports.

pumping rates, high Rb densities, and high Rb spin-destruction rates there will be more quenching required, therefore more N2 will be needed.

Theoretical simulation doesn't include the quenching process. Increasing the N2 pressure in our program shows actually a decrease of polarization because of a higher Rb spin-destruction rate. Therefore, we believe that the predicted numbers for N2 saturation are underestimated when using high power lasers in Xe optical pumping.

## 5.5 Flow Velocity Dependence

Xenon polarization process is dependent on the gas velocity or total flow rate. The spin-exchange process requires a minimum amount of time for the  $^{129}\text{Xe}$  to be in contact with Rb vapor to reach polarization saturation. A flow too slow will reduce the output polarization due to longer acting spin-destruction mechanisms. There should be an intermediate range of flow rates and gas flow velocities where the xenon polarization is maximized. Our simulation predicted an optimum flow rate in the range of 300-800 sccm.

Three different total flow rates were tested by mapping xenon polarization as a function of its flow rate and the results are presented in Figure 5-5. The maps were done at 160°C temperature, with the N2 pressure of  $\sim 130$  T, and following the same procedure of counterbalancing the amount of xenon with helium to keep the total flow constant. For the 685 sccm total flow we started with 10 sccm Xe, 175 sccm N2, and 500 sccm He; for the 1360 sccm total flow we started with 10 sccm Xe, 350 sccm N2, and 1000 sccm He; for the 1910 sccm total flow we started with 10 sccm Xe, 500 sccm N2, and 1400 sccm He. Although the step taken in the flow rate variation was large, from the graph we observe the existence of an optimum flow velocity for low xenon concentrations. We conclude that the optimum

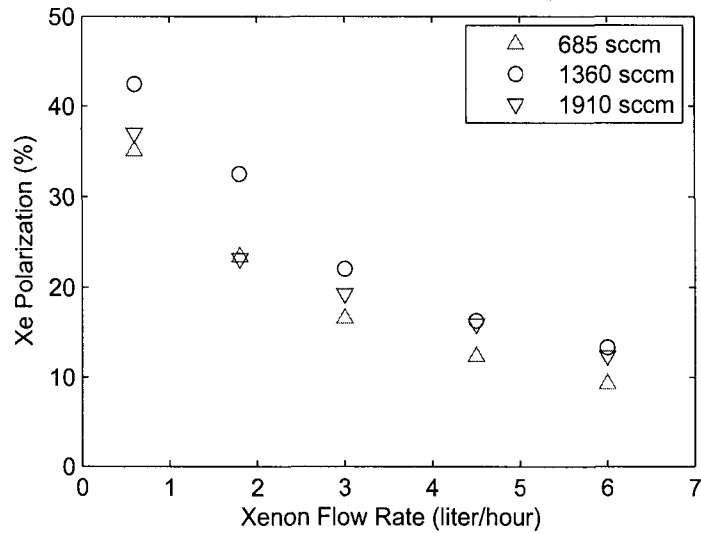


Figure 5-5: Polarization dependence on the xenon flow rate for three different total flow rates. Flow conditions: total flow rate constant for each set of data, total pressure constant at 500 T, N<sub>2</sub> partial pressure ~130 T, 160°C temperature.

total flow rate value is 1360 sccm at 160°C temperature.

The difference between theoretical and experimental optimum gas flow velocity is probably due to local flow turbulences inside the optical pumping region. For the predicted numbers we considered a Poiseuille flow distribution inside the cylinder.

## 5.6 Broad Laser versus Narrow Laser

The main source of angular momentum for the experiments presented in this work was the fiber-coupled beam-optimized broad laser. The laser is capable to output typically 90-115 W of broad-spectrum uniform beam, with a spectrum characterized by 1.5 nm FWHM.

As described in a previous chapter, one of our later developments was the spectrum narrowing of a 5 LDAs stack using an external Littrow cavity. We implemented and tested

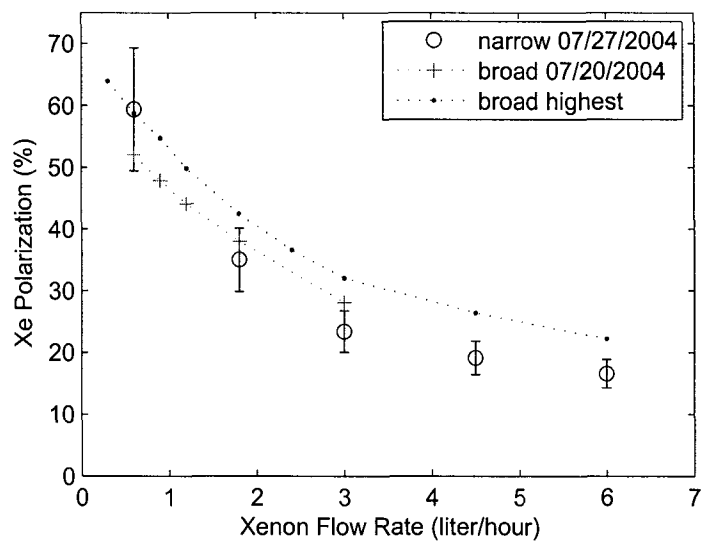


Figure 5-6: Polarization map using the frequency-narrowed LDA stack and two set of polarization numbers obtained with the broad laser for comparison. Flowing conditions are the optimum found for the broad laser with 1360 sccm total flow, 500 T total pressure, 130 T N<sub>2</sub>, and 160°C temperature.

the narrow laser on the polarizer at a moment where the gas deliveries to Brigham and Women’s Hospital were of high priority. Therefore very few detailed studies of the polarizer using the narrow laser were attempted. Still, we accomplished basic studies such as polarization mapping and polarization dependence on the laser power.

We usually operated the narrow laser at full current of 60 A, for an output power of 115 W after the stepped mirror and ~80 W after the beam shaping optics (entering the polarizer). The narrow laser was totally absorbed inside the column during the polarizing process.

In Figure 5-6 are plotted the highest polarization numbers obtained with the narrow laser together with two different maps taken with the broad laser for comparison.

The largest polarization resulted was 59±10% for 10 sccm Xe flow rate (0.6 slh). Flowing conditions were similar to the optimum found for the broad laser: 160° oven temperature,

1360 sccm total flow, and 500 torr total pressure, from which 130 torr is the N<sub>2</sub> partial pressure.

Comparing the two sets of data taken with the broad laser, "highest" and "broad 07/20/2004", we observe that for the later experiment the polarizer "state" was of lower quality, the column being contaminated with Rb. Therefore, we should expect higher Xe polarizations for the narrow laser than the ones presented for a clean system. We still remark that the polarization numbers attained with the narrow laser are higher than the broad laser at low xenon concentration, but they fall below at higher concentrations (flow rates).

All theoretical simulations predicted higher polarization numbers for the narrow laser, even with the small difference of 10 W between the two lasers. The beam for the narrow laser is not uniformly spread, although we implemented the stepped mirror to eliminate the dark spots between the 5 LDA bars. Also, the narrow beam has a square shape and doesn't fill uniformly the polarizer column.

The result of lower polarization numbers for the narrow laser at high xenon concentrations was completely unexpected and we need more studies to conclude what is the cause.

## 5.7 Laser Power Dependence

Our theoretical calculations presented in Fig. 2-23 didn't anticipate any saturation in our available range of laser power of up to 115 W.

In Figure 5-7 we show a detailed study of polarization dependence on the broad laser power for three different Xe concentrations in the gas mixture. The system was operated at 155°C temperature, 500 T total pressure, and three different flow rates settings described

in the figure caption. We observe a linear dependence with the laser power for the 10 and 20 sccm Xe flow rates. For the 50 sccm Xe flow rate we are missing one important data point for 35 A laser current, but the polarization shows the beginning of a saturation curve at 30-32.5 A. In a similar manner we mapped the polarization dependence on the narrow laser power, which clearly presents, not only a saturation, but even a drop in the polarization at higher currents. The linear curve ends at 52.5 A, corresponding to  $\sim 70$  W, thereafter polarization drops to a lower unstable level. In the case of the narrow laser we took only a single set of data for Xe flow rate of 30 sccm. More information for the low xenon concentration could show a non-saturating behavior.

High xenon concentrations in the system results in large flow instabilities because of very short distances in the laser absorption. We base our affirmation on visual observations of the Rb flow inside the column for different xenon flow rates (total flow rate constant). Rb fluorescence was used in recording gas mixture flow movies with digital cameras. Large flow turbulences were seen when Xe concentration was increased.

We defined our optimum empirical conditions based on low Xe concentrations polarization values. For our findings we used the broad laser, which is not absorbed as quickly (in a short distance) as the narrow laser is. We typically observed that for higher Xe flow rates the polarization numbers were converging to the same values, although the running conditions, such as temperature or total flow rate, were different (see Figures 5-2, 5-5).

In conclusion, in certain conditions we observed experimentally a high limit for the total laser power, thereafter the polarization is decreasing. More detailed studies in a clean system are required for both type of lasers to reach a better understanding.

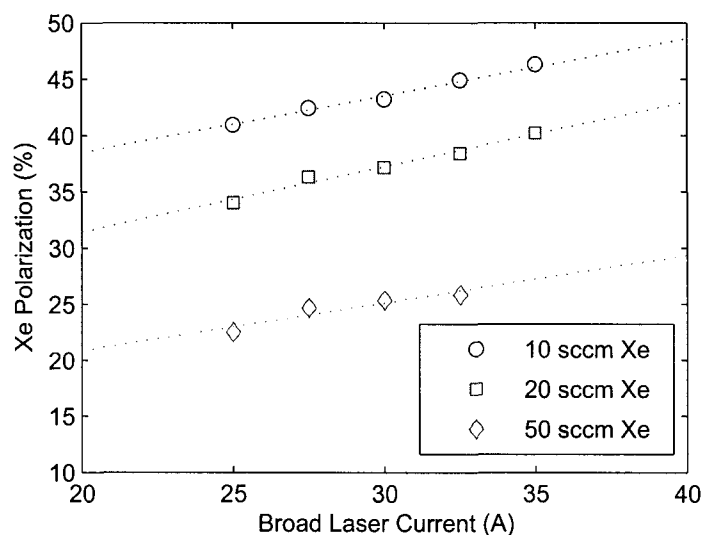


Figure 5-7: Polarization dependence on the broad laser power for three different Xe flow rates. No saturation is observed for the 10 and 20 sccm Xe flow rates. For 50 sccm Xe flow rate is difficult to conclude. The flow conditions are: 10:350:1000 sccm Xe:N<sub>2</sub>:He for the 10 sccm Xe set, 20:350:1000 for the 20 sccm Xe set, respectively 50:960:350 for the 50 sccm Xe set. Total pressure was constant at 500 T total pressure, 155°C temperature.

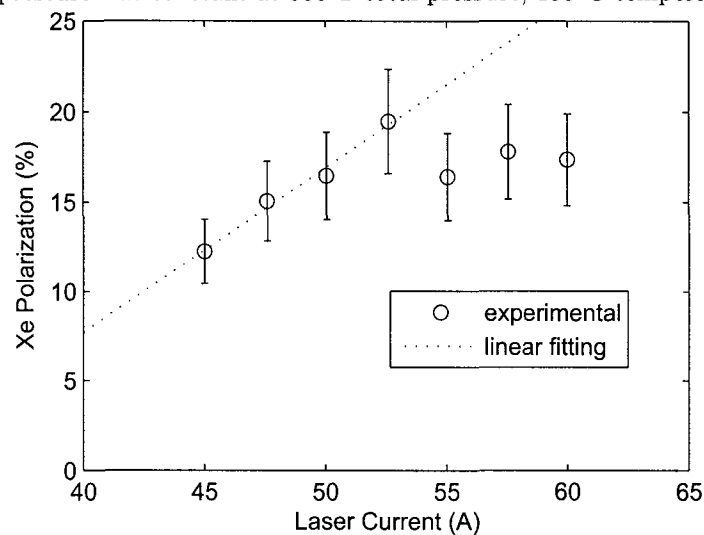


Figure 5-8: Polarization dependence on the narrowed laser power showing a fast saturation at 52.5 A, a value much lower than expected. The flow conditions are: 30:350:1000 sccm Xe:N<sub>2</sub>:He, 500 T total pressure, 160°C temperature.



## 5.8 Enriched versus Natural Xenon

There are situations where the MRI signal has to be maximized and using  $^{129}\text{Xe}$  isotopically enriched xenon is one way of doing it. For a specific set of MRI experiments at BWH we used 86% enriched xenon, which has 3.25 more  $^{129}\text{Xe}$  atoms than natural xenon.

The map of polarization in Figure 5-9 was obtained using the broad laser and standard flowing conditions. Besides the point corresponding to the lowest Xe flow rate of 5 sccm, the enriched xenon follows the same dependence on the xenon flow rate as the natural xenon. On the same graph we plotted also the highest polarization numbers resulted with natural xenon and presented in Figure 5-1.

The polarizer was contaminated with Rb at the time the enriched xenon was used, therefore the two sets of polarization numbers can not be compared. We believe numbers for enriched xenon should be similar to the natural xenon for the same operating conditions. Unfortunately, we don't have any data points acquired with natural xenon for the same polarizer state as when the mapping for enriched xenon was done.

The magnetization of  $^{129}\text{Xe}$ , defined as polarization multiplied by the Xe flow rate multiplied by the isotopically abundance, is more important than polarization itself for MRI applications. We plotted in Figure 5-10 the magnetization for the two sets of data presented in Fig. 5-9. Although the largest numbers for natural xenon recorded are much higher than for enriched xenon, magnetization maps shows a clear advantage of using enriched xenon over natural xenon. Of course, the difference in price (of at least a factor of 30), brings the unitary cost of hyperpolarized xenon signal towards the utilization of natural xenon.

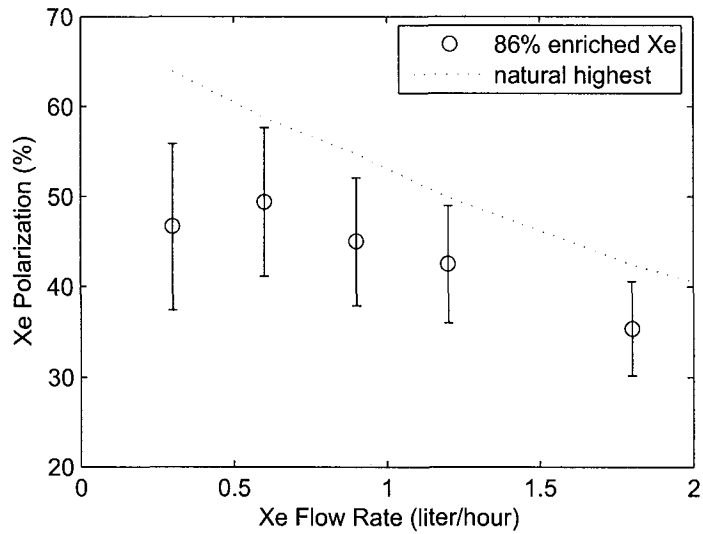


Figure 5-9: Enriched 86%-<sup>129</sup>Xe polarization map plotted together with the highest obtained polarization number for natural xenon. Flow conditions: 1360 sccm total flow rate, 500 T total pressure, 130 T N<sub>2</sub> pressure, and 160°C temperature. Xe flow was counterbalanced with He.

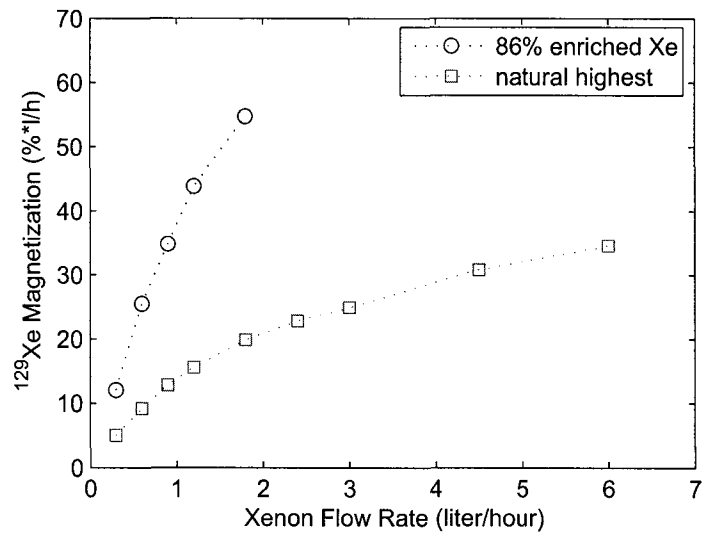


Figure 5-10: Xenon magnetization (flow x polarization) - comparison between 86% enriched Xe and natural. The enriched xenon shows a much higher magnetization.

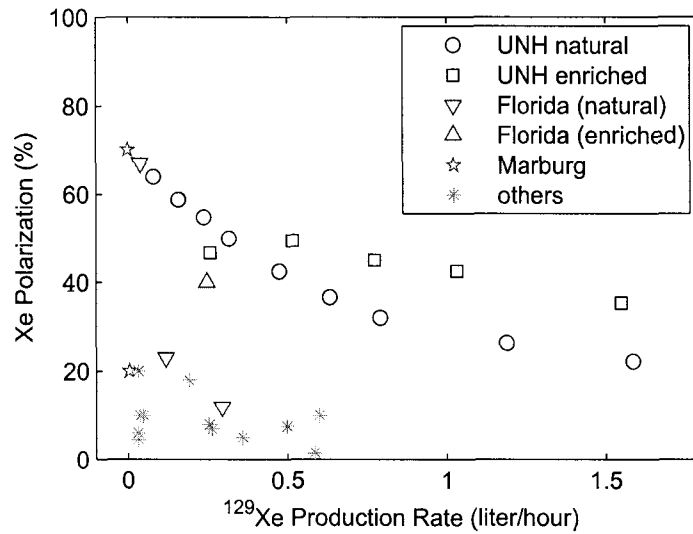


Figure 5-11: Overall comparison of the UNH polarizer performance with reported results of other research groups around the world.

## 5.9 Overall Results of the UNH Polarizer

In Figure 5-11 we show a comparison of the UNH polarizer results with the performances reported in literature by other research groups (developing or using xenon polarizer). The graph shows the production rate capabilities, plotting the polarization versus  $^{129}\text{Xe}$  production rate.

The UNH polarizer is by far the most productive polarizer. We plotted two series of numbers produced by our polarizer, one corresponding to the highest polarization numbers obtained for natural xenon, and the data obtained with 86% enriched xenon. Similar studies of the polarization dependence on the running parameters were performed and reported by the Bowers group from the University of Florida [46] for natural and enriched xenon, but at a different pressure regime. The Marburg group [42] still has the highest reported  $^{129}\text{Xe}$  polarization of 70%, result produced at low pressure and very low Xe concentrations.

Other polarization numbers plotted were reported by the Princeton group [44, 47] and other research groups around the world (see Table 1.2).

It is interesting to observe the "continuity" of the UNH natural xenon polarization map with the two higher polarization values obtained by the Florida and Marburg groups. Although taken at different conditions of pressure, temperature, and laser power, it is surprising the proximity of our results at very low xenon concentrations. Also, the enriched xenon polarization number from Florida comes in close agreement with the UNH number.

Limitation of maximum polarization by other interactions than experimentally demonstrated, such is the Rb-Xe anisotropic term in the dipole-dipole interactions, can be the cause of this "continuity". Maximum reported polarizations are  $\sim 80\%$  for  $^3\text{He}$  and  $70\%$  for  $^{129}\text{Xe}$  and these are possible high limits for the SEOP method using Rb.

## Chapter 6

# ACCUMULATION AND DELIVERY OF POLARIZED XENON

### 6.1 Accumulation and Recovery of Hyperpolarized Xenon

The hyperpolarized xenon is just a small fraction of the high-flow low-pressure gas mixture in the optical pumping process in order to achieve high polarization numbers. Nitrogen and helium are added to the gas mixture as buffer gases for well-known reasons. To efficiently use the hyperpolarized xenon one has to separate it from the gas mixture. Typically this is done with a liquid nitrogen trap which freezes and separates the xenon from helium and nitrogen.

Figure 6-1 shows the phase diagram for xenon. Xenon liquefies at 166°K and freezes at 161°K at standard atmospheric pressure. For systems working in the high pressure regime it is necessary to expand first the gas mixture, such the N<sub>2</sub> is not frozen or liquefied together with Xe. Since our system runs below atmospheric pressure (500 torr), xenon is the only

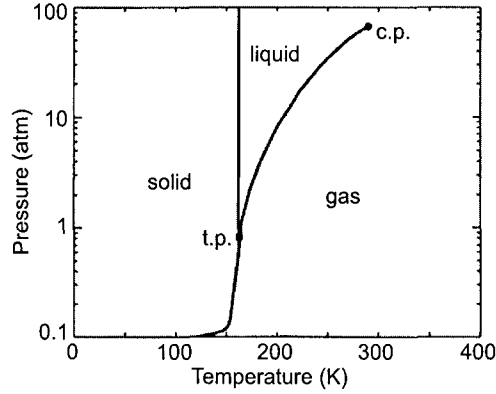


Figure 6-1: Xenon phase diagram. Adapted from [103].

gas trapped at liquid nitrogen temperature in the freeze-out.

### 6.1.1 Frozen Xenon Relaxation Mechanisms

It is well-known [43, 21, 39] that xenon in the frozen state has long spin-lattice relaxation times. For example, at 77°K and moderate magnetic field values solid  $^{129}\text{Xe}$  has a relaxation time of  $\sim 2.5$  hours. This can reach hundreds of hours at very low temperatures. The relaxation mechanisms for the spin-lattice relaxation are still under debate [40, 39, 104]. It is believed that there are three distinct temperature regimes with different relaxation mechanisms for the frozen state [39].

For the very low temperatures, below 50°K, the dipole-dipole interaction between  $^{129}\text{Xe}$  and  $^{131}\text{Xe}$  mediate the  $^{129}\text{Xe}$  relaxation:

$$V_{dd} = \frac{\mu_{\alpha}\mu_{\beta}}{I_{\alpha}I_{\beta}r_{\alpha\beta}^3} \left[ \mathbf{I}_{\alpha} \cdot \mathbf{I}_{\beta} - 3 \frac{(\mathbf{I}_{\alpha} \cdot \mathbf{r}_{\alpha\beta})(\mathbf{r}_{\alpha\beta} \cdot \mathbf{I}_{\beta})}{r_{\alpha\beta}^2} \right] \quad (6.1)$$

For temperatures between 50 and 120°K the spin-rotation interaction describes best the

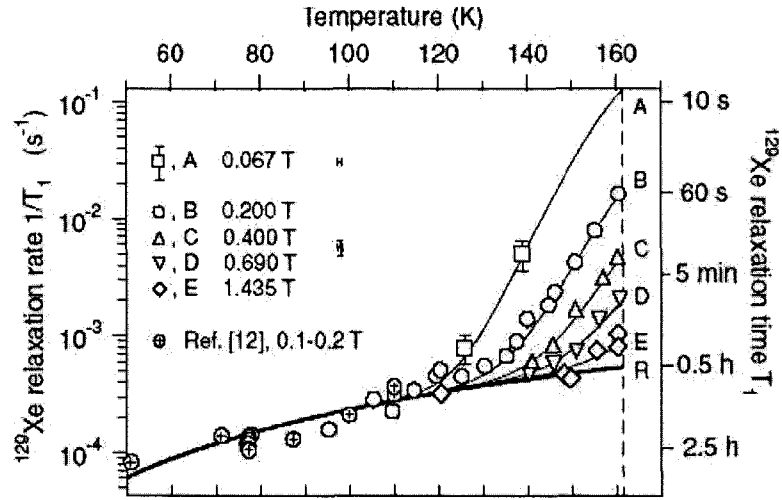


Figure 6-2: Natural xenon relaxation rates in frozen state as a function of temperature and magnetic field. Adapted from [39].

lattice relaxation:

$$V_{sr} = \alpha(r_{\alpha\beta})\mathbf{I}_{\alpha} \cdot \mathbf{N}_{\alpha\beta} \quad (6.2)$$

where  $\mathbf{I}_{\alpha}$  is the nuclear spin of  $^{129}\text{Xe}$  and  $\mathbf{N}_{\alpha\beta}$  is the angular momentum of the pair formed by the  $^{129}\text{Xe}$  and a second atom  $\beta$  separated by the distance  $r_{\alpha\beta}$ . This also characterizes the spin-lattice relaxation mechanisms for the gas and liquid states. Until recently it was believed that this mechanism dominated also the frozen state regime for temperatures above 120°K, but experimental evidence [39] showed relaxation time values several order of magnitude smaller than predicted by the spin-rotation interaction.

Figure 6-2 shows recent results of the Princeton group where Kuzma *et al.* [39] did a systematic study on the relaxation mechanisms and the accumulation process of frozen process. The spin-rotation interaction leads to Raman scattering of photons in the xenon crystals. The relaxation rate by spin-rotation is proportional to the temperature squared and very little dependent on the field.

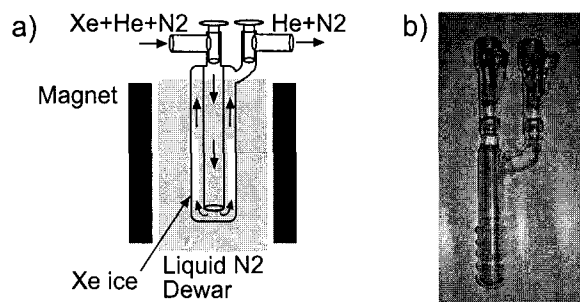


Figure 6-3: a) Typical design of a "cold-finger" or straight-tube xenon trap. b) Photo.

The dipole-dipole interaction between  $^{129}\text{Xe}$  and its nearest neighbors is modulated by vacancy diffusion and has a strong temperature and field dependence. This can be seen on the graph in Figure 6-2 for the two regimes of temperatures: 50-120°K (modulated by spin-rotation interactions) and transition temperatures over 120°K (modulated by dipole-dipole interactions). The transition regime of temperature larger than 120°K agree very well with the dipole-dipole interaction modulated by vacancy diffusion.

### 6.1.2 Xenon Accumulation

As mentioned, the relaxation at liquid nitrogen temperature of 77°K is known to be  $\sim 2.5$  hours, a relatively large value. For the transition from and to the gas state the relaxation depends strongly on temperature and on the holding magnetic field. A major issue in recovering the xenon polarization from its frozen state is the time spent near the phase transition, where relaxation times are of the order of seconds. Despite reported recovery ratios of over 90 % for small quantities [42, 21], losses as high as 30-50 % were routinely observed.

The typical xenon trap is the coaxial double-tube condenser ("cold-finger") sketched in Figure 6-3a. The initial gas mixture comes through the inner glass tube, starts to



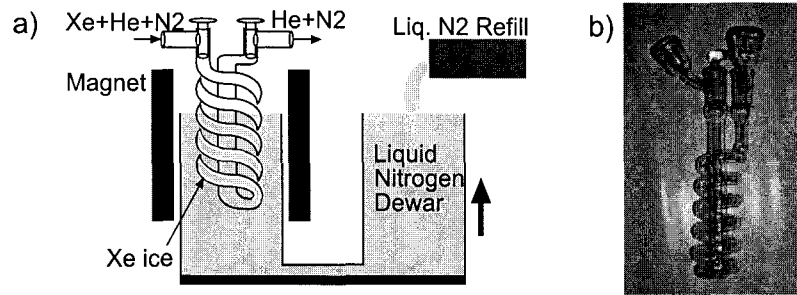


Figure 6-4: a) Novel design of spiral freeze-out xenon trap. The dewar is kept filled with liquid nitrogen, and can be easily lifted such the freeze-out is gradually inserted in the liquid nitrogen. b) Photo.

cool down, and freezes in a thick layer on the outer tube walls. Hypotheses exist for loss mechanisms during both accumulation and thawing [39]. During accumulation warm gas mixture passing over already frozen xenon could maintain the top layer of frozen xenon at a higher temperature, particularly for large quantities of frozen xenon. The relaxation time of the inner layers of xenon could be much smaller if its temperature falls into a region where dipole-dipole interaction dominates. Recent studies of the Princeton group [104] concluded that relaxation during thawing dominated, at least in their system. They observed that when xenon thawed and passed through liquid phase, it could drop at the bottom of the freeze-out and spend long time in the liquid phase, where relaxation times is in the order of seconds. We started our initial freeze-thaw measurements by using this type of freeze-out, which can be seen in Figure 6-3b. The recovery ratios measured with this freeze-out were below 50%.

Starting from these hypotheses we designed a new freeze-out system which would eliminate the fast relaxation mechanisms during phase transitions. The schematic of the implemented freeze-out system with the UNH high-flow low-pressure polarizer is shown in Figure 6-4a. Made from a glass helix with five turns of 1 cm diameter and 15 cm height,

the "spiral" freeze-out offers a large surface for xenon trapping. For the liquid nitrogen dewar we built an "U"-shaped aluminum container insulated with foam walls. The U-shape gives multiple advantages such as a large buffer quantity of liquid nitrogen, level control capabilities, etc. The magnet box was built in-house using NdFeB rare-earth permanent magnets. It generates a field of 0.31 T inside a region of 7.5 cm x 10 cm and 15 cm height. Iron field clamps were added to the top side of the box to reduce the field gradients for the incoming hyperpolarized xenon.

The working principle of our freeze-out is quite simple. Gas mixture containing hyperpolarized  $^{129}\text{Xe}$  comes from the polarizer main column through the down-tube, where  $^{129}\text{Xe}$  polarization can be measured using an NMR coil setup (previously presented). It enters the freeze-out and flows downwards through the spiral partially or fully immersed in the U-shaped liquid nitrogen dewar. The dewar is fully filled with liquid nitrogen and its vertical position can change in rapport with the freeze-out which is fixed and attached to the magnet box. We arrange the dewar such that initially it covers just the bottom spiral of the freeze-out. Depending on xenon quantity to be accumulated, we periodically raise the liquid nitrogen level by raising the dewar. The mount sustaining the dewar can be attached to a motorized linear actuator and the whole process becomes computer controlled.

Xenon forms a thin layer of ice distributed over the spiral wall surface with a minimum gradient temperature between the glass surface and the inner layer of frozen xenon. At the end of accumulation process the xenon snow is uniformly spread inside the spiral in a layer proportional with the quantity of xenon frozen. Thawing this thin uniform layer proceeds quickly when immersed in hot water, such the relaxation is minimized.

Presently, the only flaw of this system is the limitation to xenon quantities of  $\sim 1.5$  liters, thereafter we observed clogging of the spiral and a pressure gradient between the input and

the output gas panels. This can be easily surpassed by building a larger freeze-out and magnet box.

### 6.1.3 Single Freeze-Thaw Polarization Recovery Ratio

Using this system we measured systematically recovery ratios of the polarization as a function of the production rate. The initial polarization was measured during production of polarized xenon in the down-tube. The "recovered" final polarization after the freeze-thaw cycle was measured in the same conditions after thawing the accumulated xenon back into the down-tube. This way we minimized uncertainties for measured recovery ratios by eliminating the intermediate step of proton signal calibration. Natural xenon was used for all these studies.

After the xenon is frozen in a manner as previously described, the top valve of the polarizer is closed and the polarizer main column is isolated. The down-tube, freeze-out and the output panel is vacuumed for helium and nitrogen (see polarizer schematic, Figure 4-1). Using a second foam dewar filled with hot water, we quickly immerse the freeze-out in it for fast thawing of the polarized xenon from the freeze-out back into the down-tube. The pressure is measured with the pressure controller Baratron from the output gas panel. The calculated errors are large for small quantities of xenon because of the instrumental limitations. Using flow meters with the right range we can substantially reduce the errors.

The results of our study are presented in Table 6.1. We demonstrated full recovery of 100% for xenon polarization after freeze-thaw cycles for quantities up to 500 cc. Once the quantities were increased, the layer of xenon ice starts to grow leading to a slower thawing process, thus increasing the relaxation. A correction for xenon relaxation in the frozen state during the 10 minutes accumulation time was done on the thawed signal, considering a 2.5

Xenon Flow (sccm)	Accumulated Volume (cm <sup>3</sup> )	Recovery Ratio (%)	Absolute Error (%)
10	100	100.0	-14.9
50	507	100.0	-1.8
75	746	95.1	±3.5
100	1000	91.5	±2.9

Table 6.1: Polarization recovery ratios after a freeze-thaw cycle using the spiral freeze-out.

hours relaxation time.

This is an extremely important result in the view of transferring the hyperpolarized xenon from the polarizer. Xenon can be accumulated in large quantities and transported, with losses dictated just by the spin-lattice relaxation times.

#### 6.1.4 Multiple Freeze-Thaw Recovery Ratio

We attempted more measurements on the frozen hyperpolarized xenon. One of the experiments stood in measuring an average recovery ratio for multiple fast consecutive freeze-thaw cycles.

After freezing ~500 cc of polarized xenon into the freeze-out, we thawed the gas back into the down-tube and acquired an NMR signal using a small flip angle (4.5°). Next we quickly froze the gas back into the freeze-out. We repeated this freeze-thaw-acquire routine for 12 consecutive times in about one hour.

The purpose was to determine the recovery ratio for a system where the thawing process is produced from a static system, such as the "batch-mode" polarizer. Since there is no fast flow, the xenon gas will freeze into the closest nitrogen temperature surface. In our case this means the first top spiral of the freeze-out. This is also a similar situation to the "cold finger" method, because xenon accumulates locally in a thick layer.

The freezing and accumulation of xenon happens very fast from our experience (pressure

monitoring). We observed large quantities of xenon in the range of liters collapsing into the freeze-out in less than 30 seconds. No liquid nitrogen level control was utilized for this experiment. One complete freeze-thaw cycle took  $\sim 5$  min, such all 12 cycles happened in  $\sim 1$  hour. Since one hour is significant time for xenon relaxation for both, frozen and gas states, we corrected the acquired signals for  $T_1$  decay considering  $T_1 \approx 2.5$  h for both phases. As later will be shown, gas phase measurements have relatively close values to the mentioned one.

The signal decay for this particular case is given by:

$$S(n) = S_0 R^{n-1} e^{-\frac{(n-1)T_{cyc}}{T_1}} \quad (6.3)$$

where  $S_0$  is the initial signal,  $R$  is the recovery ratio to be determined,  $n$  is the number of the freeze-thaw cycle,  $T_{cyc}$  is the time needed for a complete cycle, considered to be 5 min.

After correcting the signals for the  $T_1$  decay, we finally fit the data with a power function of the type:

$$S(n) = A + B \cdot R^{n-1}$$

Figure 6-5 present the plot of resulted raw experimental data, the time corrected data, and the fitted curve. The resulted recovery ratio from the fit is 82.8%. This value clearly shows the difference between the two different methods for freezing and thawing the hyperpolarized xenon. A thin layer along a large contact surface resulted in full recovery of polarization, compared with this method of freezing the xenon in a thick layer, similar to a cold finger trap.

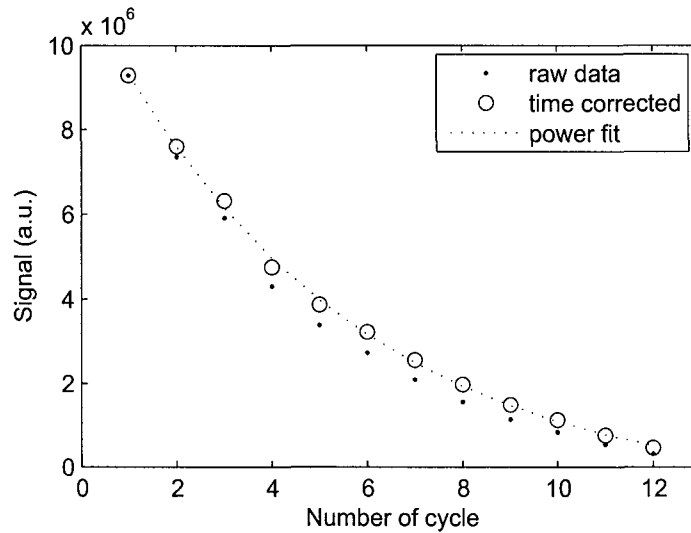


Figure 6-5: Multiple freeze-thaw cycles decay of the signal and recovery ratio measurement.

### 6.1.5 T<sub>1</sub> Measurement in Frozen State

Knowing the recovery ration of 82.8% in our system for a freeze-thaw "static" cycle we attempted a T<sub>1</sub> measurement of xenon in the frozen state. In a similar manner as for the multiple freeze-thaw cycle experiment, we measured the signal of the thawed gas every half hour. The 500 cc gas was kept frozen at liquid nitrogen temperature and 0.3 Tesla magnetic field between the measurements. This time we corrected the raw data for the losses caused by the freeze-thaw cycles, using the recovery ratio of 82.8% determined previously.

The fitted T<sub>1</sub> from the time exponential decay is 2 hours, which is smaller than other reports of 2.5 hours [39], but within the error limits. For example, if we considered a correction for the freeze-thaw losses of 80% instead of 82.8%, the resulted T<sub>1</sub> matched exactly 2.5 hours.

With more careful and repetitive measurements the precision for this value can be improved, but ideally will be a direct measurement of the signal from the frozen xenon.

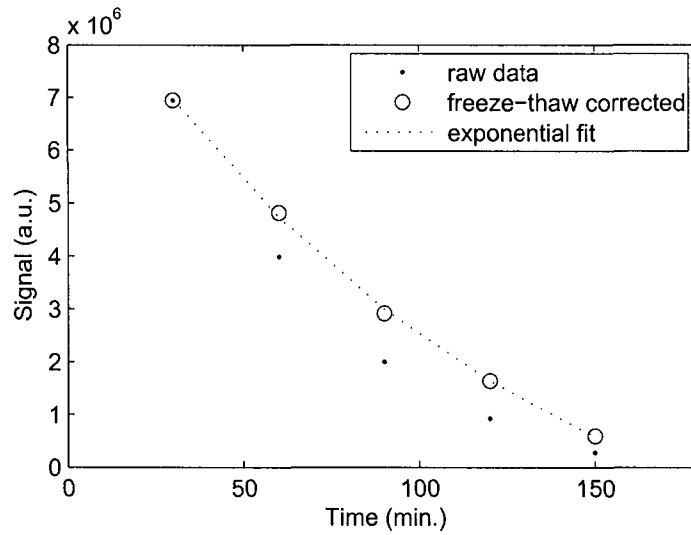


Figure 6-6: Frozen state relaxation and  $T_1$  measurement.

The fact that  $T_1$  measured this way falls in relatively close agreement with other reported values confirms the multiple freeze-thaw recovery ratio.

## 6.2 Optimum Production Rates

In the view of gas deliveries for collaborative purposes we focused towards optimization of gas production in the frozen state. Depending on the final desired quantity and polarization, one can optimize the running parameters of the polarizer to achieve this. Low xenon flow rates result in high-polarization numbers, but the frozen xenon relaxes more during the time required to accumulate the rest of the quantity.

For an accumulation time  $T_a$ , a constant relaxation time  $T_1$ , and an initial Xe polarization  $P_0$ , it can be easily calculated an averaged final polarization of accumulated xenon

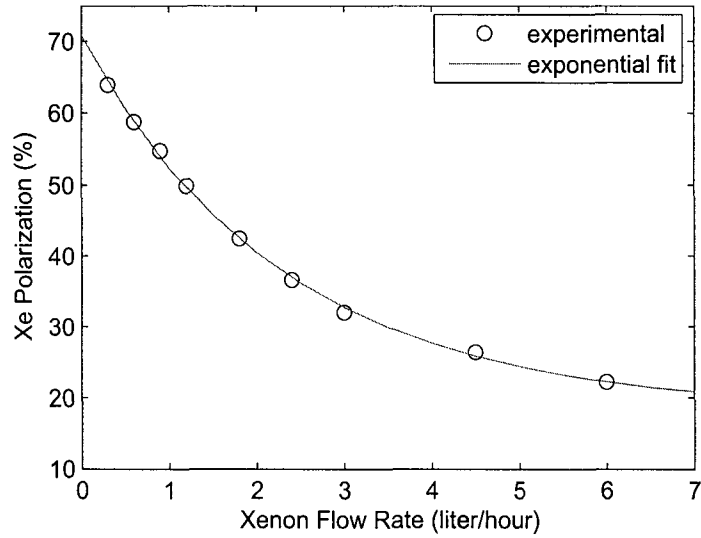


Figure 6-7: Empirical exponential fit for the highest xenon polarization numbers as a function of its flow rate.

is:

$$P = P_0 \frac{T_1}{T_a} (1 - e^{-\frac{T_a}{T_1}}) \quad (6.4)$$

This result is based on constant xenon flow rate, polarization, and  $T_1$  relaxation rate.

If a relation between the xenon flow rate and its polarization can be established, then optimization curves for the production rate can be generated. For this we used an empirical exponential-decay fit for the xenon polarization dependence on its flow rate. Typically, the exponential-decay fit is excellent and an example is shown in Figure 6-7. The empirical formula resulted is:

$$P_0(\Phi) = 18.25 + 52.5e^{-\frac{\Phi(\text{slh})}{2.32}} (\%)$$

where  $\Phi$  is the xenon flow rate expressed in standard liter per hour (slh) and  $P_0$  is the polarization during production. This empirical formula changes easily with the polarizer state, therefore periodical mappings of the polarization are required in order to update it.



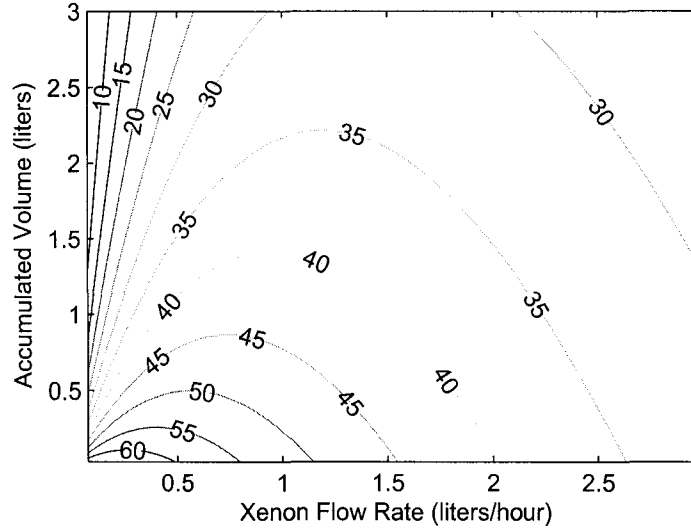


Figure 6-8: Polarized xenon production map considering a relaxation time in frozen state of 2.5 hours and a known initial xenon polarization dependence on its flow rate. Optimum xenon flow rate can be found for a final accumulated volume and final wanted polarization.

Implementing this relation into Eq. 6.4 results:

$$P = \left( 18.25 + 52.5e^{-\frac{\Phi(sth)}{2.32}} \right) \frac{T_1}{T_a} \left( 1 - e^{-\frac{T_a}{T_1}} \right) \quad (6.5)$$

We have now an estimate for the final polarization of the accumulated xenon for a known xenon flow rate  $\Phi$  and accumulation time  $T_a$ . Since there is a direct proportionality between the accumulation time, accumulated quantity of xenon, and xenon flow rate, production maps can be generated in a contour format, such is the one presented in Figure 6-8. Optimum running conditions are found this way for a desired final polarization, final xenon volume, or accumulation time. The contours are labeled with polarization values expressed in percents.

From this map is readable that high polarization numbers are obtained for small xenon flow rates and small accumulated quantities of xenon. For delivery purposes we typically

wanted around one liter volume of accumulated xenon. Following the production map it results that maximum achievable polarization is  $\sim 42\%$  for a flow rate of 1 liter/hour. In most of the cases we ran the system at 1.2 liter/hour (20 sccm), which doesn't change significantly the final polarization and reduces the accumulation time.

### 6.3 Frozen State Deliveries

Based on reported relaxation times of hours [21, 39] for the frozen xenon, we first concentrated our efforts in designing a transportation method of hyperpolarized xenon in a liquid nitrogen dewar. The purpose for hyperpolarized xenon deliveries was for collaborative research with the group of Sam Patz at the Brigham and Women's Hospital (BWH) (Boston-MA). The delivery time was typically more than two hours, thus we expected less than 50% of the polarization to survive the trip to BWH.

We demonstrated full recovery of the polarization after a freeze-thaw cycle and this encouraged the frozen state delivery. We used a 50 liter volume Thermolyne Jr Locator III biological cryogenic dewar. The advantage of this dewar, besides its very low liquid loss (less than a liter/day), is the large diameter of the top opening (20 cm). This allows the immersion of a large permanent magnet box providing  $\sim 0.1$  T holding field necessary for delivery.

After the xenon is accumulated, the spiral freeze-out is vacuumed from the remaining nitrogen and helium, closed, and transferred into the delivery magnet box. The magnet box is then transferred inside the large Thermolyne dewar previously filled with liquid nitrogen. The dewar is loaded into a pick-up truck and transported to BWH-Boston. Once the frozen xenon reaches the destination, it is thawed under the highest field available (typically the

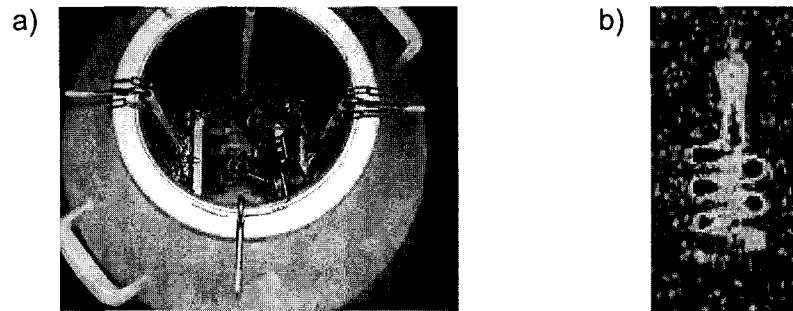


Figure 6-9: a) Frozen xenon delivery system: large cryogenic dewar, permanent magnet box, and the freeze-out ready for delivery. b) First hyperpolarized xenon image of the spiral freeze-out acquired at BWH after a frozen state delivery.

MRI magnet) in order to reduce relaxation. A photo of this delivery system is shown in Figure 6-9a.

We demonstrated and practiced initially the frozen state delivery of hyperpolarized xenon. Figure 6-9b shows the first image acquired using hyperpolarized xenon produced at UNH and delivered to BWH. The image is of the spiral freeze-out after the xenon was thawed and was acquired in a 1.5 T MRI scanner, modified to work at xenon Larmour frequency.

We found the frozen delivery method to present inconveniences. The large size and weight of the dewar requires team work for handling and transportation. After the destination is reached, the thawing is done at once, since thawing in multiple stages is not possible. Special attention is required when the thawing is done because the glassware components and the connections involved (including the freeze-out) are not rated to work above atmospheric pressure, therefore the risk of an error is very high.

Further development of the frozen delivery system to include a final stage of liquid helium could increase drastically the relaxation time to days [21], although this method will be limited by the high cost of liquid helium.

## 6.4 Xenon Gas State Relaxation Studies

### 6.4.1 Gas Relaxation Mechanisms

Relaxation time for xenon gas was believed initially to be constrained only by the spin-rotation interactions during the binary collisions with a limit given by [11]:

$$T_1^{sr} \approx \frac{56}{\rho} \text{ (h)} \quad (6.6)$$

where  $\rho$  is the xenon density inside the expressed in amagat. This expression resulted after a set of initial measurements done at very high pressures (above 50 atm) and where the binary collisions are dominant. Although the predicted relaxation times given by the above relation are very long at low pressures, experimental values fall usually in the range of tens of minutes to few hours. Maximum  $^{129}\text{Xe}$   $T_1$  reported is of 3.7 h [105]. Large relaxation times of  $\sim 3$  h were also reported by Breeze *et al.* [106, 107].

The major relaxation mechanism believed initially to be causing the large difference at low pressures between the measured relaxation times and predicted by Eq. 6.6 was the dipole-dipole interaction of  $^{129}\text{Xe}$  atoms with container wall impurities presenting large magnetic moments. Xenon has a large adsorption energy and attaches easily and for long times to the cell walls, thus losing completely its polarization. Proposed and demonstrated solutions are focused on inert coatings deposited on the cell walls. Wall coatings have been studied for reducing spin-destruction rates for alkali vapor [108] and hyperpolarized gases such as  $^1\text{H}$  [109],  $^3\text{He}$  [110],  $^{131}\text{Xe}$  [111], and  $^{129}\text{Xe}$  [112, 113, 106, 107, 114]. Coatings are typically silicone based compounds and some examples already demonstrated to reduce wall

relaxation are: Dry-Film (General Electric Co.), octadecyldimethylchlorosilane (OTS), and Surfasil (Pierce Chemical Lab.). A systematic study on different silane based coatings and their effect on wall interaction was done by the Carleton University group [106, 107, 115]. Even with the surfaces coated, the relaxation times didn't approach the limit predicted by binary collisions, therefore additional mechanism acting at low pressure should count for the difference.

Previous studies showed typically a linear dependence of xenon relaxation rate as a function of its density at high gas densities (over 20 amagat) [11, 107]. This dependence is expected to be given by relaxation mechanisms happening during binary collision. For low and intermediate pressure ranges it was unclear until recently what caused the xenon to deviate from the binary predictions. In a recent study of xenon relaxation at low pressures Chann *et al.* [10] showed an important contribution coming from the spin-rotation interactions through Xe-Xe van der Waals molecules.

For hyperpolarized xenon in the gas state the major relaxation mechanisms are described by:

$$\frac{1}{T_1} = \frac{1}{T_{1,bin}^{sr}} + \frac{1}{T_{1,vdW}^{sr}} + \frac{1}{T_1^{wall}} + \frac{1}{T_1^{CSA}} + \frac{1}{T_1^{inh}} \quad (6.7)$$

where the first term  $T_1^{sr}$  represents the spin-rotation losses and can be split into two terms: one coming from binary collisions and a second from van der Waals molecules,  $T_1^{wall}$  shows the wall interaction losses,  $T_1^{CSA}$  is the chemical shift anisotropy contribution, and  $T_1^{inh}$  results from the field inhomogeneities.

The spin-rotation interaction couples the Xe nuclear spin to the rotation angular momentum of a Xe-Xe pair during binary collisions or van der Waals molecules. As binary collision rate is directly proportional to the pressure, its contribution becomes minimal at

low pressures. The van der Waals contribution to the relaxation rate is pressure independent, as the pressure dependencies for number of collisions ( $\sim[\text{Xe}]$ ) and molecule lifetime ( $\sim[\text{Xe}]^{-1}$ ) cancel each other. The major contribution of Xe-Xe van der Waals molecule was demonstrated by the Wisconsin group recently [10]. They showed a new limitation for the  $T_1$  relaxation time to 4.1 hours caused by this type of interaction.

The wall relaxation is a constant of the container and can be reduced by coatings applied to the vessel. A study of the wall relaxation dependence on diameter of cylindrical cells was done at low pressures [114]. The results show a clear proportionality of  $T_1$  with the square of the cell diameter. This concludes that vessel with larger surface/volume ratios will keep the xenon polarized longer.

The  $T_1^{CSA}$  was demonstrated by Moudrakovski *et al.* [115] to give a field dependence of the relaxation at very high pressures. Chemical shift anisotropy characterizes specially atoms with large chemical shift as xenon and is caused by an anisotropy in the nucleus shielding by the large electron cloud [116]. It is also the only mechanism that could explain the higher relaxation time for lower magnetic fields [115]. The chemical shift interaction happens during binary collisions, thus its contribution for densities below 20 amagats should be minimal. This is confirmed also from the experimental data of Moudrakovski *et al.*

The inhomogeneity of the field is another relaxation factor and was studied initially for the  $^3\text{He}$  atom [117, 118], where this mechanism becomes important due to its fast diffusion inside the cell. The gas diffusion is inversely proportional to the cell pressure. The general expression used when referring to the relaxation rate caused by field inhomogeneities is [117]:

$$\frac{1}{T_1} = D \frac{|\vec{\nabla} \mathbf{B}_x|^2 + |\vec{\nabla} \mathbf{B}_y|^2}{B_0^2} \quad (6.8)$$

where  $D$  is the diffusion coefficient of the noble gas,  $B_0$  is the main field considered to be along the  $z$  axis, and  $B_x, B_y$  are field components on  $x$  and  $y$  axis defining the inhomogeneities. The relaxation for xenon at low pressure and low magnetic fields was studied in detailed by Cates and coworkers at Princeton [119].

Using a self-diffusion coefficient  $D=0.0565 \text{ cm}^2/\text{s}$  for xenon at one atmosphere [120] and considering different field gradients as the input values for  $|\vec{\nabla}\mathbf{B}_{xy}|$  for a main magnetic field of  $B_0=28 \text{ G}$ , we estimated the relaxation caused by field inhomogeneities. Thus for a contribution of  $T_1^{inh}$  of  $\sim 1$  hour the field gradients should be  $1.4 \text{ G/cm}$  for  $28 \text{ G}$  main field. The field homogeneity in our systems is much better ( $\sim 10^{-3}$ ), at least in the NMR region, and the relaxation rate caused by the field inhomogeneity is generally too small to be considered.

Our interest is for the low pressure regime (0.1-1 amagat), where we expect most of the polarization loss to be caused by spin-rotation through van der Waals molecules and wall interactions, if the condition of a homogeneous field is met. A general numeric formula was given by Chann *et al.* [10] for spin-rotation relaxation rate given by van der Waals molecules and binary collisions:

$$\frac{1}{T_1} = \left[ 6.7 \times 10^{-5} + 5.0 \times 10^{-6} \frac{[Xe]}{(1 \text{ amg})} \right] (s^{-1})$$

The pressure dependent term characterizes the binary collisions. This formula shows that molecular relaxation exceeds the binary collisions below 14 amagat xenon density.

Adding also the wall relaxation term we obtain a formula which should describe closely

the relaxation rate in our pressure range:

$$\frac{1}{T_1} = \frac{1}{(4.1 \text{ h})} + \frac{1}{(55.6 \text{ h})} \frac{[Xe]}{(1 \text{ amg})} + \Gamma_{wall} \quad (6.9)$$

where  $\Gamma_{wall,0}$  is the wall relaxation rate at one amagat of gas density. The wall relaxation,  $\Gamma_{wall}$ , is specific to the xenon container.

#### 6.4.2 T1 Measurements in Gas State

We performed multiple measurements on the relaxation of the hyperpolarized xenon in our system at different pressures in the down-tube. After accumulating the hyperpolarized xenon in the freeze-out, we vacuumed the down-tube and the freeze-out, and thawed the xenon back into the down-tube. First results confirmed the potential of delivering the hyperpolarized xenon in the gas state, since relaxation times measurements showed comparable values to the ones in the frozen state.

For relaxation time measurements we used the same NMR coils system surrounding the down-tube, as for measuring polarization numbers. Therefore, almost all the studies were done with the down-tube as the gas vessel. To observe the exponential time-decay given by  $T_1$  relaxation we implemented pulse sequences with multiple repetitive shots having small flip angles and separated by a specified repetition time. For hyperpolarized gas each shot destroys the transverse polarization, therefore the flip angle has to be small in order to allow the acquisition of a large number of shots. The signal time-decay is defined by:

$$S(n, \alpha) = S_0 e^{-\frac{(n-1)T_R}{T_1}} \cos^{n-1}(\alpha) \quad (6.10)$$

where  $S_0$  is the initial signal (or initial polarization),  $n$  is the number of the shot,  $T_R$  is the



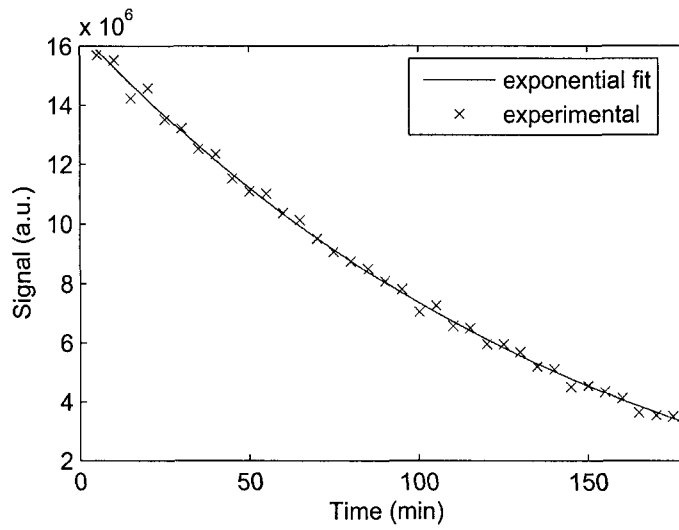


Figure 6-10:  $T_1$  signal decay data points and fitted curve.

repetition time between two consecutive shots, and  $\alpha$  is the flip angle in each shot.

By using the same multi-pulse sequence, but with extreme repetition times, one differentiates between the decay caused by the flip angle and the decay caused by the spin relaxation,  $T_1$ . If the repetition time is chosen such that  $T_R \ll T_1$ , the time-decay of the signal is insignificant and the resulted decay is caused only by the small flips of the magnetization destroyed in every shot. This way the flip angle can be measured. After the flip angle is determined the repetition time is increased to values comparable to  $T_1$  and the data points resulted are fitted using a curve described by Eq. 6.10.

We calibrated our system to give a flip angle of  $4.5^\circ$  for a specific RF power settings of the SMIS console. For  $T_1$  measurements we typically acquired 36 repetitive shots, with a repetition time of 5 min, resulting in an acquisition time of 3 hours. Figure 6-10 shows the signal time-decay of the hyperpolarized xenon at 600 torr, the measurement that gave us the highest relaxation time of 159 minutes (2.5 hours) in the down-tube.

In Figure 6-11 we present an overview of all our  $T_1$  measurements in the down-tube

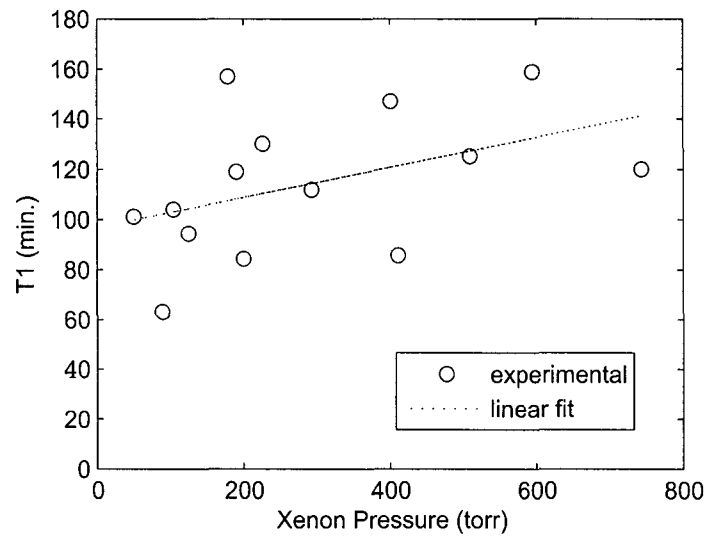


Figure 6-11: Xenon relaxation time overview measurements in the down-tube.

taken for different xenon pressures. The numbers are hardly reproducible for the same pressure. The inconsistency in measuring  $T_1$  for the same experimental conditions was observed also by other groups [106]. One explanation for the  $T_1$  variations at the same pressure could be different down-tube contamination levels with Rb or other impurities. Although we implemented the cooling jacket for a faster Rb trapping inside the polarizing column, we still observed deposition of Rb on the walls of the polarizing column above the cooling jacket and in the down-tube.

The experimental points tend to follow a linear fit and show a slight pressure dependence. The relaxation rate increases slightly as the pressure drops and this comes probably from a diffusion related effect. It could be generated by field inhomogeneities along the down-tube. Lower xenon densities leads to a higher diffusion coefficient in Eq. 6.8 and small gradient fields participate in xenon relaxation.

A large part of the relaxation is caused the wall relaxation. The limit of 4.1 h predicted by molecular relaxation is far from being reached. The average value of 1.9 h in our mea-

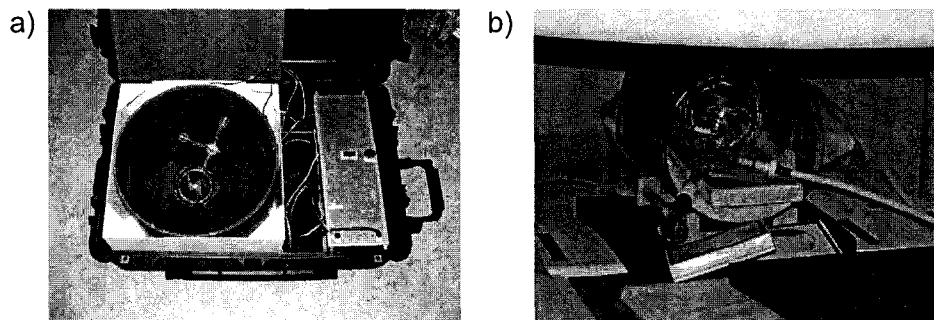


Figure 6-12: a) Gas delivery system with the transporting case, metal box enclosing the coil, and the delivery cell. b) Delivery cell inside the coil at 0.2 T magnet at BWH.

measurements concludes to a wall relaxation rate of  $7.84 \times 10^{-5} \text{ s}^{-1}$ . No coatings were applied to the down-tube, although a careful cleaning with Piranha solution is always performed when the system is refilled with fresh Rb.

## 6.5 Gas State Deliveries

For gas state delivering purposes we built a large solenoid coil with 40 cm diameter and 25 cm height, enclosed in a ferromagnetic steel box to improve field homogeneity and reduce external noise. The holding field inside the coils is  $\sim 28$  Gauss, matching the polarizer field. The whole setup fitted inside of a large wheeled case, as shown in Figure 6-12a. The coil is powered from the wall outlet or from the car 12 V plug. To power the coil for short periods of time, necessary when moving the case from lab to the car and vice-versa, a large capacity rechargeable battery was added.

After the xenon is polarized and accumulated in the freeze-out, it is thawed into the delivery cell. The pressure inside the cell is monitored with a Baratron pressure gauge and has typical values of 600-700 torr. The cell is finally transferred into the transport case with

precaution, such as the field gradients are minimized. The case fits easily into the trunk of a car to be delivered to BWH. The delivery is handled routinely by a single person. Once the gas reached destination, it can be transferred in small amounts from delivery cell to the study cells.

Multiple large spherical cells with volumes ranging from one to five liters were acquired and provided with three-way glassware stopcocks. Because the final accumulated xenon quantity is limited to 1.5 liters by the freeze-out capacity, we used only the one liter cells for deliveries. The cells were previously washed following a standard lab cleaning procedure [58]: Alcanox soapy water, 3x distilled water rinse, Piranha acid wash, 3x distilled water rinse.

For two of the one liter cells we tried a Surfasil (Pierce Chemical Lab.) coating. We filled them with 10% Surfasil, 90% hexane solution and let them stand for a half-hour. Finally, the cells were emptied and rinsed with toluene. We used two different procedures for curing the Surfasil coating solution: one of the cells was placed inside a vacuum oven and left under rough vacuum at 200° for 24 hours, the second cell was dried at room temperature under ultra high vacuum ( $10^{-6}$  torr) for 24 hours.

Constrained by the tight time schedule of gas deliveries, the priority for detailed studies of xenon relaxation times inside the delivery cells or during transportation was very low. Because of their large volume, cells didn't fit in our polarizer NMR coils for quick measurements. Nevertheless, two measurements were attempted in the human scale low field imager at UNH. The field used in the low field imager was 46 Gauss corresponding to 54 kHz Larmour frequency. Following the flip angle calibration we measured the relaxation time for two Surfasil coated cells using the multi-shot technique described previously. Both cells showed relaxation times of  $\sim 3$  h, after flip angle corrections, at pressures of  $\sim 600$  T of natural xenon. No clear evidence of improvement in delivered polarization at BWH

was observed for the coated cells when compared to uncoated. Therefore it is unclear how important the coatings are in our delivery conditions. Extreme cleaning solutions, such as Piranha, could be sufficient for decreasing the wall relaxations at a level where other relaxation mechanisms become dominant. We observed certain differences between uncleaned and Piranha washed cells with a low surface/volume.

## 6.6 Hyperpolarized Xenon MRI at BWH

To demonstrate the capability of our polarizer and the arisen possibilities from its use, we entered into a collaboration with the group of Sam Patz from Brigham and Women's Hospital and Harvard Medical School. The purpose of the collaboration was medical imaging studies using hyperpolarized  $^{129}\text{Xe}$ . The collaborators have an excellent background and a large interest in working with hyperpolarized gases [121, 27, 122], especially  $^{129}\text{Xe}$ .

Based on xenon unique properties, such its high-solubility in tissues and blood, its large chemical frequency shift depending on the surrounding, and its low diffusion coefficient, we focused our studies on two main parameters related to lung structure and functionality.

First, the solubility of xenon in blood and the difference in frequency between the gas phase and the dissolved phase can be an excellent tool for measuring the gas exchange efficiency. It was first demonstrated by our collaborators [122] in porous media materials and it should be relatively unproblematic to adapt this method to gas exchange studies in lungs. The gas exchange efficiency is directly related to the local surface-to-volume ratio.

Secondly, we planned detailed measurements for the diffusion coefficient  $D(t)$  of  $^{129}\text{Xe}$  at the pulmonary acinar level as a function of time. Measurements of xenon diffusion as a function of time could give detailed description about the lung microstructure. Xenon low diffusion coefficient allows to probe structures much smaller than possible with helium. All

the experiments were proposed on animals first, followed by human subjects.

For MRI experiments we used the 0.2 Tesla GE scanner accessible to our collaborators in the Brigham and Women's Hospital. The low field value presents certain advantages regarding the attainable SNR for the hyperpolarized gases. At high magnetic fields of 1.5 T or higher local gradients arise due to the susceptibility of the tissue in the lungs, limiting the transverse relaxation time  $T_2^*$  to 7 ms. Low field imaging at 0.1 T using hyperpolarized gases was demonstrated to increase the SNR up to a factor of 30 when compared with 1.5 T [123, 124, 125], due to smaller background magnetic fields and larger  $T_2^*$  values.

UNH responsibility for this project is to provide the hyperpolarized xenon, initially delivering the gas from UNH to the hospital, and later to build a second polarizer and relocate it at the scanner site. As described before, we developed two different methods for gas delivery from UNH to BWH. We performed initially frozen state hyperpolarized xenon deliveries, switching to deliveries in the gas state once we realized its advantages.

In order to calibrate polarization numbers of the delivered xenon, we built a large "thermal" cell. A xenon "thermal" cell is typically a high pressure cell from which the NMR signal is measured based on Boltzmann thermal equilibrium polarization, in the same way as described for proton calibration signal. To reduce xenon T1, which dictates the recovery of the thermal polarization after an NMR signal measurement, oxygen is typically added to the thermal cell. Oxygen reduces drastically xenon T1 due to its paramagnetism [126]. We calculated an optimum ratio of xenon to oxygen of 2:1 for maximizing the SNR from the thermal cell. Finally a large spherical three liter cell was filled with 4 atm of 75 % enriched xenon and 2 atm of oxygen. The SNR ratio obtained with this cell was  $\sim 10$  in a single shot, extremely high taking into account the low 0.2 T  $B_0$  magnetic field. The hyperpolarization of delivered xenon was calibrated against the thermal signal.

Maximum polarization delivered to BWH Hospital was estimated at 13.8% for a measured polarization at UNH of 40.1%. We observed inconsistencies in the final delivered polarization numbers and we find difficult to explain the differences without further investigations. Thawing the xenon under various vacuum conditions could lead to small amounts of oxygen inside the cell, hence decreasing the relaxation time uncontrollably. Large magnetic field gradients resulted when moving the cell from the polarizer to the transporting case, or caused by large current variation in the delivery coil (powered by car battery during transportation), can be also causing inconsistent relaxation. With a more accurate pressure monitoring when thawing the gas and a polarization monitor inside the transportation case the causes for polarization losses and inconsistent relaxations can be tracked down.

The project is still ongoing at the time this thesis is written, therefore only first results are presented. We delivered hyperpolarized xenon on a regular basis for initial studies, which included coils and gradients calibration. The scanner is a commercial GE medical imager designed to work at proton frequency and required changes in order to function with hyperpolarized xenon. A Tecmag imaging console capable of multiple nuclei frequencies, such as  $^3\text{He}$  and  $^{129}\text{Xe}$ , was acquired and installed for the 0.2 T scanner. The imaging coils were calibrated for the flip angle. First images were acquired in order to adjust gradient coils settings. Pulse sequences were developed and optimized to work with hyperpolarized xenon. For example, when doing hyperpolarized gas imaging, one major improvement in pulse sequencing design is the central phase encoding, where the image is scanned from the center towards the sides, such the gas polarization is efficiently used within the interest region. The spiral image presented in Fig. 6-9b is taken with a standard pulse sequence which starts the scanning from top to the bottom of the image. The signal in the images is very strong for the top half of the image, but starts decaying in the lower half, the

polarization being destroyed by the multiple small flip angle shots necessary in scanning the k-space. The bottom two spirals of the freeze-out helix do not appear in the image as the polarization is already too small for the signal to be visible.

### 6.6.1 Xenon Dissolved-State Imaging

Measurements of surface-to-volume (S/V) ratios for soft porous media using hyperpolarized xenon were done by a collaboration including members in our present collaboration. They demonstrated this new non-destructive method based on xenon chemical shift and large solubility. The results were in relatively good agreement with measurements from destructive microscopy. After destroying the polarization of the hyperpolarized xenon dissolved in the porous media with selected RF pulses, they monitored the exchange of polarized xenon from the gas-phase into the dissolved-state.

Xenon dissolves well in tissue and blood. For short times after the xenon is inhaled, the dissolved state signal into the lung parenchyma will be proportional to the surface area of the lung. By monitoring the signal in the gas-state and in the dissolved-state one can obtain information on lung functionality, such as regional ventilation and lung surface area available for gas exchange. Previous measurements of dissolved xenon in lung tissue and blood showed chemical shifts in the range of  $\sim 200$  ppm, sufficient for a clear separation of the gas and dissolved phases.

As a first stage of our proposed dissolved-state imaging we demonstrated the capability of separating the gas state image from the chemical shifted image of dissolved xenon in corn oil.

For this we used two cylindrical cells, one of  $\sim 10$  cm length and 2.5 cm diameter, and a second one which is  $\sim 5$  cm long and 5 cm in diameter. The cells were placed in the same



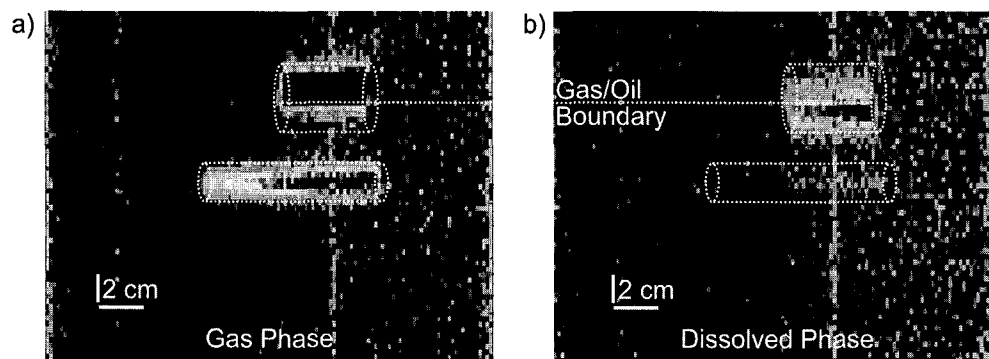


Figure 6-13: Separation of xenon in gas state and xenon dissolved in oil images. Bottom cell contains only xenon. The top cell is half filled with oil and half with xenon. Cells physical positioning are indicated by the dotted drawings. By taking two consecutive scans with TE values such in the first scan the gas and dissolved states are in phase (both have  $0^\circ$  phase) and in the second scan there is a difference of  $180^\circ$  between them (gas has  $0^\circ$  phase and dissolved has  $180^\circ$  phase), we can separate the images for the gas and dissolved states: a) image of the gas phase only; b) image of the dissolve in oil xenon only (lower half of the top cell). Imaging parameters:  $128 \times 64$ ,  $FOV=20$  cm,  $SW=16.6$  kHz,  $TR=25$  ms,  $TE=6.36$  and  $7.41$  ms.

vertical plane. The long empty cell was filled first with hyperpolarized xenon and placed in the scanner because of xenon larger relaxation time (minutes). The second wider cell, half filled with corn oil, was filled with xenon right before the experiment and shaken for  $\sim 8$  s before the scanning was started. This is necessary because of the very short relaxation time of xenon in dissolved state ( $T_1 \sim 10$  s).

The chemical shift of xenon in oil was previously measured to be 472 Hz at 0.2 T (200 ppm). For the separation of the images corresponding to gas and dissolved state a minimum of two scans are required. We approached a technique known to the MRI community as the two-point Dixon method [127]. Two consecutive gradient-echo centric-encoded scans were acquired, first scan having  $TE=6.36$  ms and second  $TE=7.41$  ms, respectively. Therefore for the first scan both states, gas and dissolved, presented  $0^\circ$  phase. For the second scan a difference of  $180^\circ$  results in the phase of the dissolved state signal, due to the 1.1 ms

difference in TE. The chemical shift of 472 Hz for the xenon leads to this phase difference. Finally, by adding and subtracting the signals obtained for the two scans we get the images for the gas state and for the oil state, respectively.

A small "bleeding" of the gas-phase signal into the dissolved signal can still be observed, resulting in an imperfect separation of the dissolved phase. The cause is believed to be an imperfect centering of the gas phase and its non-zero frequency in the rotation frame. This "bleeding" could be corrected for a 1D projection of the two cells by a first order phase correction for the chemical shift displacements prior to the Fourier transforms. For the 2D imaging it can be problematic to correct the "bleeding" for each line of the spectrum.

The 3-point Dixon technique [128] require a third set of data with the dissolved phase at  $-180^\circ$  phase difference from the gas phase. We acquired also this necessary scan and the results with the analysis description will be published in the close future.

### 6.6.2 *In vitro* Rabbit Lung Imaging

In the view of lung structure studies using hyperpolarized xenon, we attempted *in vitro* rabbit lung imaging and  $T_1$  measurements of hyperpolarized xenon inside the lungs. This experiment was performed using enriched xenon because of low polarization numbers obtained at UNH, caused by a contaminated system. Although the delivered xenon polarization was only very low (less than 5%), we obtained relatively good results.

Figure 6-14 shows two rabbit lung images acquired. SNR ratio is small because of very low polarization, but the lungs profiles are clearly visible with a uniform signal distribution.

We measured relaxation times larger than 43 s in the rabbit lungs, as shown in Figure 6-15. First four points show the gas injection (from syringes filled with xenon), with the signal increasing to a maximum value. Thereafter the signal starts the exponential

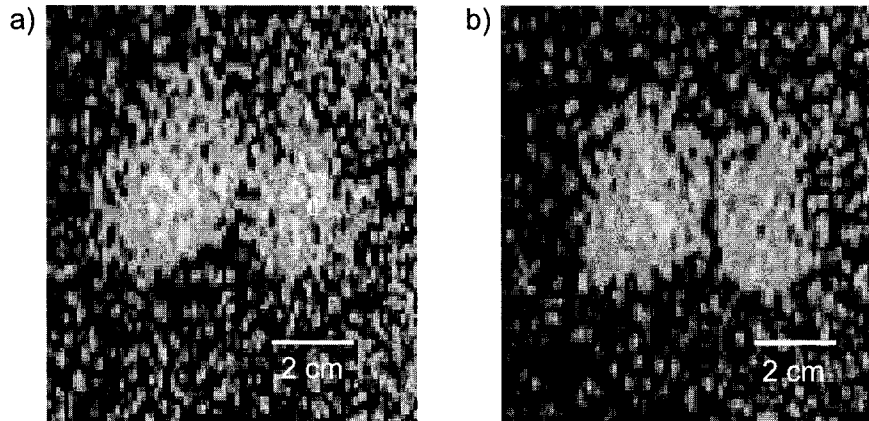


Figure 6-14: *In vitro* rabbit lungs images at 0.2 T obtained with hyperpolarized xenon: a) 55 cc xenon injected; b) 75 cc xenon injected. We used a gradient-echo centric pulse sequence, 128x64 overfilled to 256x256, FOV=20 cm, TR=8.7 ms, TE=40 ms.

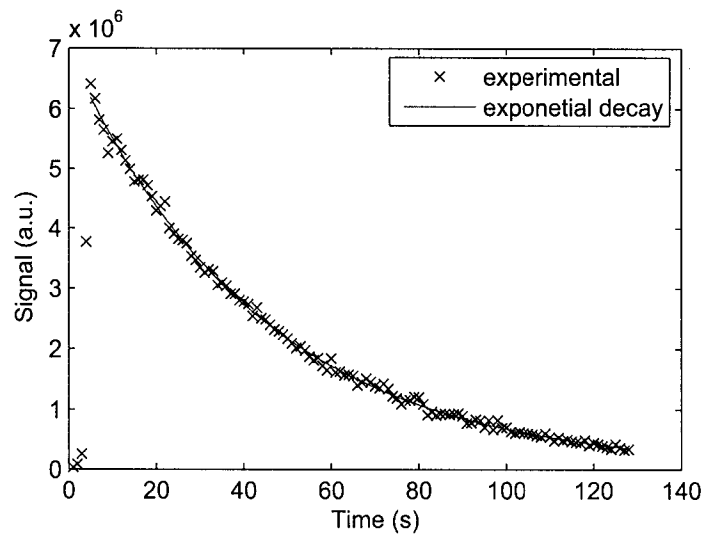


Figure 6-15:  $T_1$  measurement in rabbit lungs: first four data points correspond to the injection of the xenon inside the lungs, followed by the exponential decay of the signal.

decay characterized by the spin-lattice relaxation of xenon inside the lungs. The data were acquired using a new coil, without a previous flip angle calibration performed, therefore the data presented on the graph are the raw data, and  $T_1=43$  s resulted from the fit should be considered the low limit for the relaxation time.

## Chapter 7

# ORIENTATIONAL LOW FIELD MRI

### 7.1 Low Field MRI

The signal-to-noise ratio of the hyperpolarized gases in animal or human lungs is, to a first approximation, only weakly dependent on the applied magnetic field, unlike in the traditional case of thermal equilibration where the SNR of a sample essentially scales with  $B_0^2$  [124, 125]. Therefore, laser-polarized  $^3\text{He}$  MRI can be performed at applied magnetic fields substantially lower to those found in clinical scanners, potentially  $< 100$  G. The impressive body of clinical laser-polarized  $^3\text{He}$  MRI work performed until now has generally been performed at applied fields of 1.5 T, not because of the field requirement, but rather because this is the standard equipment available to most MRI researchers in clinical settings.

Imaging of laser-polarized noble-gases at much lower applied fields offers a number of advantages because certain fundamental imaging constraints are diminished. Most notably, distortions, line broadening, and inherent loss of resolution that result from large background magnetic field gradients due to susceptibility mismatches in heterogeneous samples,

such as the lung tissue, are significantly, if not completely, reduced. T2 and T2\* are significantly longer, resulting in much higher SNR from echo experiments, and the ability to use single-shot, multi-echo experiments like RARE and EPI much more easily [129]. Additionally, the significantly lower (kHz range) Larmor frequencies used correspond to greater skin depths meaning the applied RF can penetrate thin conductors that would otherwise be shielded and could not be imaged.

A collaboration involving also the UNH group has previously demonstrated the feasibility of low-field  $^3\text{He}$  MRI using a solenoid magnet operating at approximately 20 G [124, 125]. They obtained images of sealed glass cells with  $^3\text{He}$  using this system, and achieved a resolution and SNR comparable to clinical scanners. It was also demonstrated the reduction of susceptibility-induced gradients for both sealed cells [124] and excised rat lungs [125]. The result was a  $^3\text{He}$  T2\* of  $\sim 100$  ms at 2 mT (20 G) in excised rat lungs, as opposed to  $\sim 5$  ms at 1.5 T.

It has been theorized that the non-uniform nature of pulmonary ventilation and perfusion is the result of gravity-dependent orientation [130, 131]. However, the details of gravitational effects on lung function are poorly understood and are currently under much debate [132, 133, 134]. A major limitation in these studies is the lack of a method to obtain quantitative, high-resolution regional ventilation maps in a non-invasive and repeatable manner. Much of the current knowledge of regional pulmonary dynamics has come from studies that use invasive probes, often on post-mortem samples. Pulmonary physiology would thus greatly benefit from the ability to quantitatively image ventilation and V/Q ratios as a function of orientation. A low field imager with open access for orientational studies would be an ideal instrument for this type of measurements, since in all MRI clinical scanners the subject is restricted to horizontal positioning.

From a practical standpoint, operation at lower applied fields allows for novel magnet systems. A low-field imager would be substantially lower in cost and easier to build and maintain because the field can be generated using resistive coils, as opposed to the traditional superconducting solenoid. The significant reduction of the stray fields also reduces the siting considerations. Furthermore, the lower field strength permits the use of novel magnet designs that can better accommodate certain subjects for basic physiology studies, or subjects in critical care.

## 7.2 UNH Imager Description

We report the design, construction and performance characteristics of a very low field MRI system that employs a set of resistive electromagnetic coils and planar gradients. The imaging region is completely unobstructed in all axes parallel to the coil plane. We include the operating details and specifications of this system, results of  $^3\text{He}$  and  $^1\text{H}$  NMR diagnostics during development, and our first  $^3\text{He}$  human lung MRI images.

### 7.2.1 The Magnet

The  $B_0$  field was produced by two pairs of coils. The larger pair consisted of 2 m diameter,  $0.91\ \Omega$  coils, with 120 turns each, separated by 73.6 cm. The second pair—used for field correction and homogeneity optimization—measured  $0.11\ \Omega$ , consisted of two 86 cm diameter coils with 100 turns each, and were separated by 120.0 cm. In Figure 7-1, two photographs show the layout of the four coils with dimensions indicated. The coil positions were optimized using a spreadsheet program to obtain the best field uniformity within a 30 cm-diameter spherical region. Field calculations were made by applying the Biot-Savart

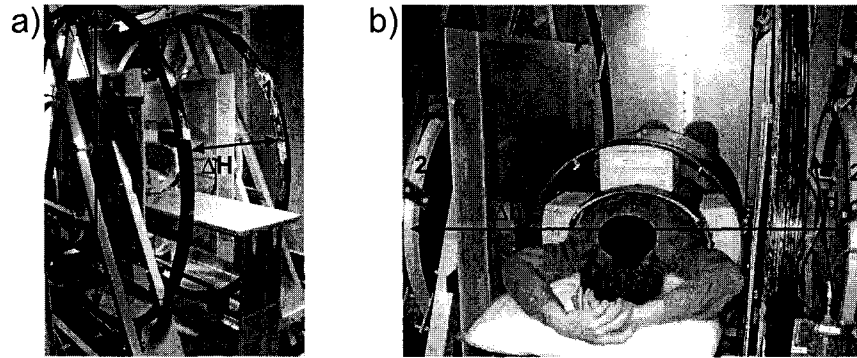


Figure 7-1: Photographs of the system showing the  $B_0$  coils: a) Large Coils:  $D=2\text{m}$ ,  $\Delta H=0.74\text{m}$ ; b) Small Coils:  $d=0.86\text{m}$ ,  $\Delta h=1.2\text{m}$ ; Human subject is shown in imaging position.

equation to small segments of the coils. A plot of the measured field uniformity in the horizontal  $yz$  plane of the system is shown in Figure 7-2. The  $B_0$  coils were powered by different current sources: the larger pair was driven by two Sorensen SRL 40-50 power supplies connected in series, and the smaller one by a Hewlett-Packard 6012A. Both pairs were vertically mounted on large triangular aluminum brackets inside a large steel RF-shielded Faraday cage (8 ft wide x 12 ft long x 8 ft high) with the coil axis across the width of the room. The DC current feeds to the coils were filtered to prevent transmission of broadband kHz frequency noise, using large capacitors connected in parallel at the output of the power supplies and LC filters mounted on the feed-through panel of the Faraday cage. The  $B_0$  field generated by this configuration was 1.38 G/A for the large pair of coils and 0.68 G/A for the small pair. No water cooling was used on these coils. The optimum current ratio between the large and small coils was  $\sim 5$  and was determined by FID SNR measurements from low-flip angle single-pulse excitations of laser-polarized  $^3\text{He}$  in small phantom glass cells, and by  $90^\circ$  pulses on water phantoms. The maximum resulting field, limited by the heat generated inside the Faraday cage, was 7 mT (70 Gauss). The field uniformity,



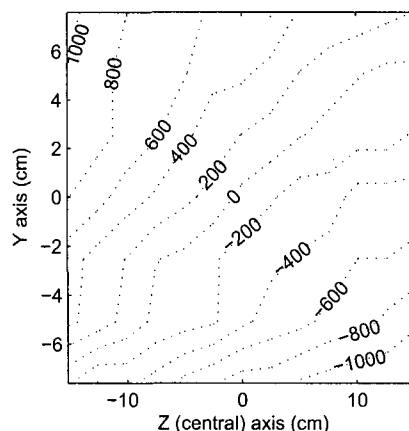


Figure 7-2: Measured  $B_0$  field deviation map (ppm). The plot was generated by moving a small water phantom along a 1 inch grid and recording the NMR frequency at each point.

as shown in Figure 7-2, differed slightly from the theoretically predicted distribution due mostly to small variations and imperfections in the coil shapes. Resistive heat from the coils and temperature changes inside the Faraday cage caused also instability problems for the field. The coils required a half to an hour to reach a stable temperature and current. A cooling fan was mounted in a separate room to vent the system through a pipe attached to one of the cage vents. Homogeneity adjustment was available by slightly modifying the current in the smaller pair of coils—often a factor of 2 improvement was possible with this method. In addition, shimming was possible via the use of a additive shim box that added current offsets to the gradient coils through the gradient amplifiers.

Planar gradient coils were built on 90 x 120 cm ( $x$  and  $y$ ) and 120 x 120 cm ( $z$ ), 3 mm thick G10 plastic sheets using three layers of 1.2 cm wide, 40  $\mu\text{m}$  thick copper tape as the conductive material. The design was created by implementing the Biot-Savart law in a Microsoft Excel program, where the field created by small elements of the gradients was summed and used to get the final 3D field distribution. The program finally optimized gradient shape and position to maximize strength and linearity across a 60 cm DSV. The  $x$

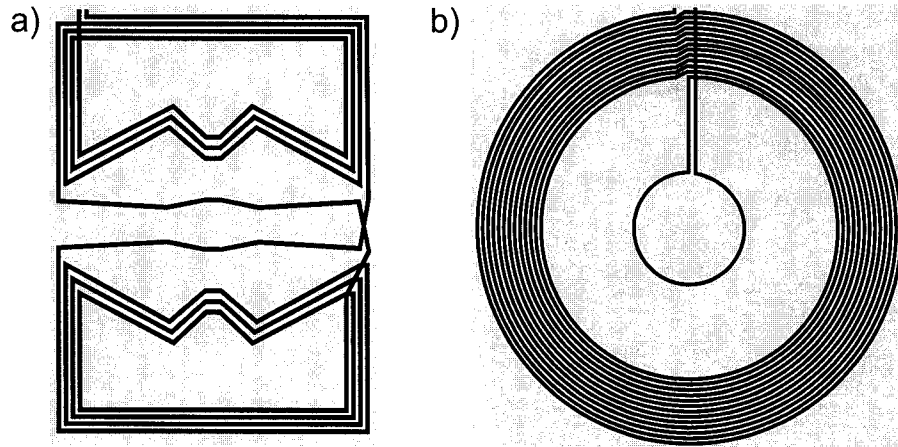


Figure 7-3: a)  $x,y$ -axis planar gradient conductor pattern; b)  $z$ -axis planar gradient conductor pattern.

and  $y$  gradients were wound as shown in Figure 7-3a, with a  $0.78 \Omega$  dc-resistance for each pair and  $92.2 \mu\text{H}$  inductance, and an output calibration of  $1.34 \times 10^{-3} \text{ G/cm/A}$ . The  $z$  gradient pair had a spiral form, as shown in Figure 7-3b, with a  $1.29 \Omega$  dc-resistance,  $368.8 \mu\text{H}$  inductance, and an output of  $4.82 \times 10^{-3} \text{ G/cm/A}$ . Calculated field plots indicated excellent uniformity of the gradients was expected over a 30 cm DSV. The gradients were attached to the same aluminum brackets as the main  $B_0$  coils, leaving a gap of 71 cm between them, a wide open space for the placement of a patient table and large human coils. The gradients were powered using standard Techron 8604 amplifiers from a GE Medical Systems human scanner. The maximum current supplied by the amplifiers was 130 A for the  $x$  and  $y$  gradients and 86 A for the  $z$  gradient, resulting in a maximum gradient field of 0.18, 0.18, and 0.41 G/cm for the  $x$ ,  $y$ , and  $z$  gradients, respectively. In Figure 7-4, a photograph shows the three planar gradients installed in the system, along with an experimental plot of the  $z$  gradient linearity. Due to the overlap of the gradient sheets, heating of the copper tape was an issue for our system. Initial tests indicated only a low duty cycle acceptable for

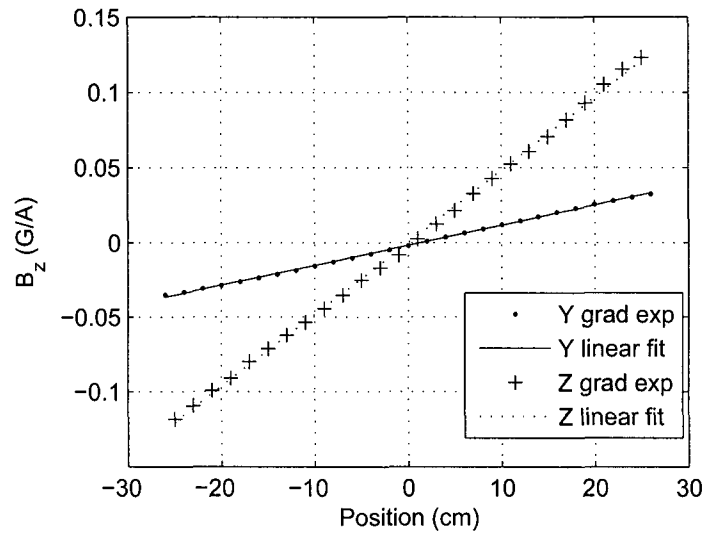


Figure 7-4: Gradient linearity plots for the  $y$  and  $z$  gradients, showing linearity for 50 cm along the central  $y$  and  $z$  axes, respectively. The gradient deviates no more than 0.4% from the linear fit showing slopes of  $1.342(6) \times 10^{-3}$  and  $4.824(7) \times 10^{-3}$  G/A/cm for  $y$  (same as  $x$ ) and  $z$ , respectively.

the gradients, so we were forced to use repetition times larger than 100 ms in our imaging sequences.

Numerous noise sources, including DC power supplies, oscilloscopes, computers and monitors, existed within our range of frequencies (50-200 kHz), requiring the use of the steel Faraday cage, which was designed to attenuate RF interference in the range of 10 kHz to 10 MHz by up to 100 dB. We used a low-noise power transformer for electrical power inside the room. A feed-through panel was made from thick aluminum and all the electrical connections were fed through using multiple passive filtering elements. We could measure lower noise attenuation at different points of the cage, mostly in the corners and in some places where the steel panels were mounted together. Where it was necessary, we added copper tape with conductive adhesive for a better electrical connection between cage panels, reducing the noise level.

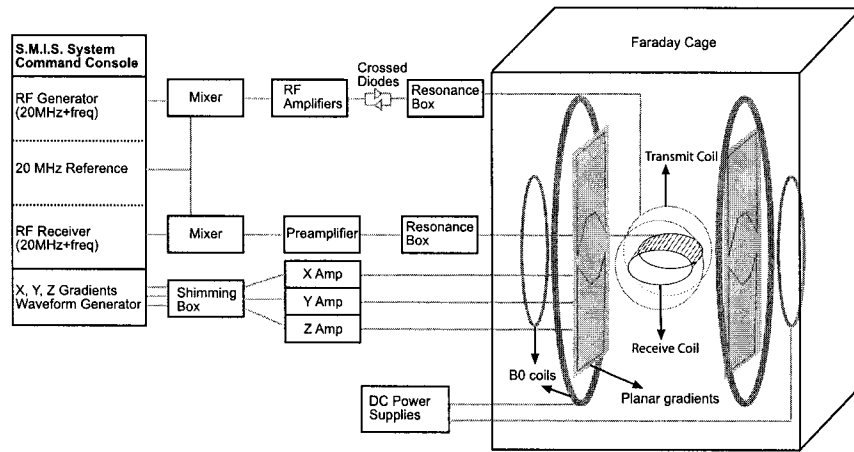


Figure 7-5: Schematic of the low field imager.

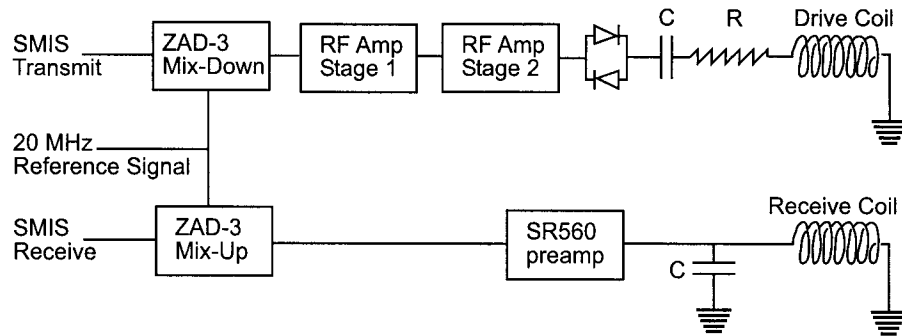


Figure 7-6: Receive and transmit coil circuitry.

### 7.2.2 Electronics

A schematic of the imaging system is shown in Figure 7-5. A commercial Surrey Medical Imaging Systems (SMIS) console was used for RF and gradient pulse control. The console did not have the hardware to produce the very low (kHz) imaging frequencies required for these low field strengths, so we implemented a heterodyne mix-down stage for the transmit signal and a mix-up for the receive signal using a reference signal of 20 MHz from the PTS synthesizer in the SMIS console, and ZAD-3 mixers [Mini-Circuits, Brooklyn, NY]. This circuitry is shown in more detail in Figure 7-6. We used separate coils to match their

resonance impedance of the RF amplifier to the drive coil and the input of the preamplifier to the receive coil.

The transmit  $B_1$  coil was built in a Helmholtz configuration with 5 windings on each side using 12 gauge copper wire on a 66 cm-diameter PVC pipe as a form. The RF drive signal was fed into a two stage amplifying system: a homebuilt amplifier allowing a gate conditioning for the output, followed by one of the five channels of a 5 x 165 W theater amplifier [Outlaw Audio, Durham, NH]. Aside from a cross-diode box after the RF amplifiers, there was no other filtering used for the drive signal. Tuning of the transmit coil was achieved by use of high-voltage resonance capacitors that were connected in series with the coil to establish a low output impedance on the audio amplifier ( $\sim 4 \Omega$ ). The quality factor  $Q$  of the transmit coil resonance was  $\sim 10$ . The receive coil, wound in a cosine pattern with  $4 \times 80$  turns, was designed to fit a medium sized human chest, with an ellipsoidal shape of 44 cm wide x 33 cm high x 38 cm long. The receive signal was pre-amplified with a Stanford Research System SR560 low-noise voltage preamplifier upstream of the frequency mixer and the imaging console. The receive coil had a parallel resonance resulting in a high impedance,  $\sim 100 \text{ k}\Omega$ . The high impedance on the input of the SR560 preamplifier matched the lowest internal noise coming out from the preamplifier. Using resonance boxes with multiple capacitor configurations, we were able to tune the coils to different frequencies ranging from 54-200 kHz. The  $Q$  of the receive coil was  $\sim 80$  to 120, depending on the operating frequency. Such high  $Q$  values at frequencies  $\sim 100$  kHz resulted in coil response bandwidths of  $\sim 1$ -2 kHz, significantly less than typical imaging spectral widths of 10-20 kHz. As a result, all images acquired from this system required post-processing to remove the convolved effect of the frequency response of the coil. We performed coil  $Q$  and AC impedance measurements on the resonance using a HP 3577A Network Analyzer. A benefit

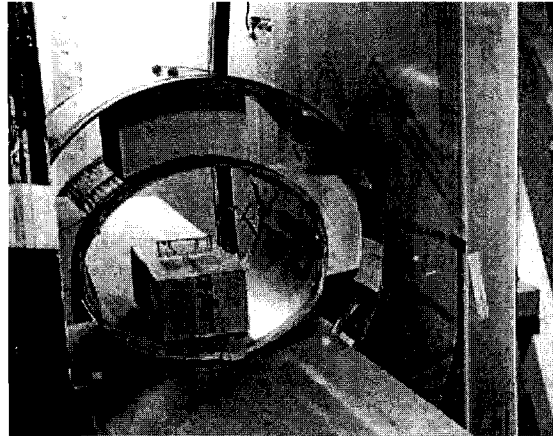


Figure 7-7: Photograph of the excite and receive coils: the large Helmholtz  $B_1$  coil was bolted into the table and the receive coil was attached to it using foam spacers and plastic bolts.

of working at such low frequencies is that sample noise is negligible, with Johnson noise being the only significant source.

The practical result of this effect is that the coils are not sample loaded—placing the coil over the head and shoulders of a test subject showed no variation in the coil resonance as displayed on the network analyzer. The only effect on the coil resonance as a result of the subject being in the coil was if their body weight caused the coil to flex while lying inside the coil in a horizontal orientation. Conversely, a significant problem was the electromagnetic coupling between transmit and receive coils and the resultant induction of noise in the receive coil by the transmit coil. With careful physical alignment and by blanking the preamplifier during transmit and a 3-4 ms dead-time after the transmit pulse, coupling between the coils was significantly reduced. In addition, precise positioning of the receive coil in the magnetic center of the gradients could eliminate the induced pulses from gradient switching and noise coupling. Once orthogonality was achieved, the human coils were bolted together to maintain their physical alignment, as is shown in detail in Figure 7-7. However

cross-coupling noise was often still present in some images, hurting the overall image SNR.

The gradient line filters consisted of simple passive inductors built with ferrite toroid cores [Ferroxcube TX63/28/25]. Both the output and sample common lines from each Techron amplifier were wound 20 times around these small toroids using a 10 gauge connection wire. These passive inductors blanked the gradient lines when the amplifier was not generating a pulse—effectively reducing their noise to that when placed in "stand-by", rather than "ready" mode. This method of filtering was applied to all three Techrons, but only reduced the noise during image acquisition from the slice select and phase encode amplifiers. An additional pair of filters, based on an active inductor concept, was implemented specifically for the read-out gradient during the image acquisition time. This consisted of two larger toroid ferrite cores (Ferroxcube T107/65/25), each double wound in a 1:1 transformer configuration (2×9 windings). One side of the transformer was made by winding the output wire of the read-out gradient amplifier. The wire from the second side was connected directly to a Sorensen SRL 10-50 DC power supply that matched the read out gradient current during the signal acquisition. These filters reduced the noise acquired during the image acquisition, in the presence of the read-out gradient pulse, to within a factor of 2 of that when the amplifier was in "stand-by" mode. To permit this filtering method to work effectively, however, the Techron amplifier assigned for the read-out gradient pulse was operated in constant-voltage mode, rather than the traditional constant-current mode, and the shape of the read-out gradient pulses suffered slightly as a result.

### 7.2.3 Gas polarization and delivery

The highly polarized  $^3\text{He}$  was produced using the well-established method of spin-exchange optically-pumping of a dense Rb vapor with the  $^3\text{He}$  gas [55]. For human imaging stud-

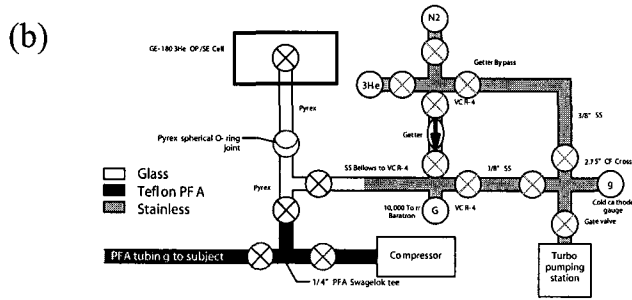
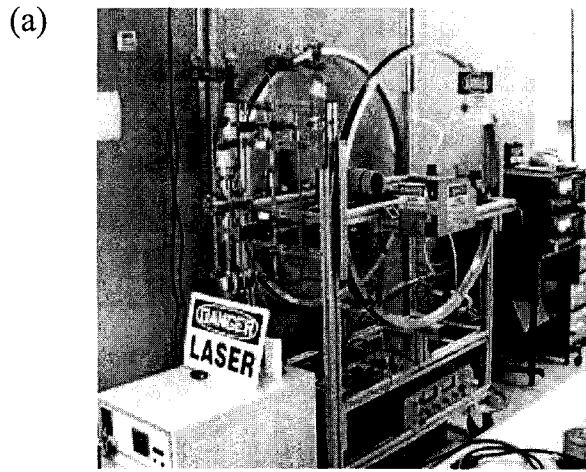


Figure 7-8: a) Photograph of  $^3\text{He}$  polarizer; b) Gas handling schematic (not drawn to scale). A  $\otimes$  refers to a valve.

ies which require large volumes of laser-polarized  $^3\text{He}$ , our collaborators from Harvard-Smithsonian Center for Astrophysics built a modular  $^3\text{He}$  polarization apparatus with gas storage, transport, and delivery stages similar to those previously implemented for  $^{129}\text{Xe}$  imaging [41]. A photograph of the apparatus is shown in Figure 7-8a. The glass optical pumping/spin-exchange cells on this polarizer were  $\sim 3.5$  cm in diameter and  $\sim 9$  cm long, and were constructed with GE-180 aluminosilicate cylinders ( $\sim 80$  cm $^3$  volume) with hemispherical end windows. Few milligrams of Rb were deposited in the cells before use, and then used a Pyrex high vacuum valve to mate to the center of the cell and attach the



cell to the polarizer. Each cell was enclosed in a dedicated Pyrex outer jacket that served as an oven. This construction enabled us to easily remove each polarization cell from the polarizer, and permitted diagnostic NMR to be performed directly on the cell, without loss of  $^3\text{He}$  gas. The cell could then be reattached to the polarizer and re-pumped.

The need to produce multiple batches of highly polarized  $^3\text{He}$  as quickly as possible and the small Rb- $^3\text{He}$  spin-exchange cross section required the polarizer to be operated at a very high Rb density in order to obtain a short Rb- $^3\text{He}$  spin-exchange time. Typically, we optically pumped the cells at 195-210° C ( $\sim 2$  hour spin exchange time). Operating at such a high Rb density ( $\sim 5 \times 10^{16}$  cm $^{-3}$ ) was feasible only because of the availability of relatively inexpensive high-power diode laser arrays (LDAs) that can provide enough resonant light to efficiently pump the vapor. For each experiment, the cell was filled with 5-6 bar of  $^3\text{He}$  and 0.1 bar of N $_2$ . Hot air flowing through the oven maintained the desired Rb density. Two fiber-coupled LDAs [Coherent, Inc., Santa Clara, CA] each provided 30 W of continuous wave laser light at 795 nm with a nominal 1 nm line width (FWHM). A pair of linear polarizing beam splitters and bi-refracting crystals converted this output into circularly polarized light in one orientation before reaching the cell. We used a simple 1 m diameter Helmholtz pair to create the magnetic field, typically  $\sim 10$  G, for optical pumping.

$^3\text{He}$  polarization reached  $\sim 20$ -40% after spin-exchange optical pumping for  $\sim 2$ -4 hours. The  $T_1$  of  $^3\text{He}$  in the cell was  $\sim 20$  hours. The cell was either removed from the polarizer for direct  $^3\text{He}$  NMR in-situ, or the  $^3\text{He}$  was allowed to expand from the pumping cell into a previously evacuated glass and Teflon compressor for storage and subsequent delivery. Transfer of the gas to compressor always occurred after the cell had cooled, to reduce loss of Rb vapor. As a safety precaution, we also passed the  $^3\text{He}$  gas through a Rb filter en-route to the compressor. We delivered  $^3\text{He}$  from the compressor via narrow Teflon tubing that

passed through a feed-through in the Faraday cage to the delivery manifold located adjacent to the human subject. The absence of large transverse magnetic gradients minimized  $^3\text{He}$  depolarization during the transfer, while the pneumatic control of the compressor with pressurized nitrogen ensured almost no  $^3\text{He}$  gas was lost to dead-space during this process. A schematic of the polarizer delivery stage is shown in Figure 4-1b. The delivery manifold for human subjects consists of a Tedlar bag, vacuum and inert gas ports, and a Teflon tube used as a mouthpiece. We measured the  $^3\text{He}$  gas  $T_1$  in both, the compressor and the Tedlar bag, to be  $\sim 20$  min.

In addition to polarization of large volumes of  $^3\text{He}$  via the dedicated polarizer described above, we also polarized small spherical and cylindrical sealed glass cells containing  $^3\text{He}$  for use as diagnostics during development of the imager. The cells, ranging in volume from  $\sim 20$ - $100$   $\text{cm}^3$  and pressure from 3-8 bar, were optically pumped in a small ceramic oven heated with hot air up to  $170^\circ$  C, and circularly-polarized 795 nm laser light was provided by a single 15 W LDA (Optopower, Tuscon, AZ) with a broad 2-3 nm FWHM line width. We optically-pumped these cells for at least 4 hours. The best of these cells achieved over 60% polarization, as independently verified by the Wisconsin group [31].

#### 7.2.4 MRI Techniques

During system development, we employed a wide variety of small solenoid RF coils tuned to frequencies between 54 and 200 kHz. Generally,  $^3\text{He}$  and  $^1\text{H}$  signals were acquired between 100 and 200 kHz, with the lower frequencies intended for parallel development of  $^{129}\text{Xe}$  laser-polarization systems. For NMR at these frequencies, we set the  $B_0$  field to between 31 and 62 G for  $^3\text{He}$ , and 23.5 and 47 G for  $^1\text{H}$ . We could easily use the same coil to acquire  $^3\text{He}$  or  $^1\text{H}$  signals simply varying  $B_0$  by adjusting the current output on the three power

supplies that powered the  $B_0$  coils. This manual  $B_0$  adjustment also made it very easy to center the  $^3\text{He}$  or  $^1\text{H}$  signal on the receive coil resonance without requiring adjustment of the transmitter or receiver offset via the software. Given the extremely narrow frequency bandwidth, especially of the receive coils (1-2 kHz), adjustment of the transmitter or receiver offsets were avoided once the spectrometer frequency had matched that of the two RF coils.

Initial diagnostics and SNR measurements were made using standard single hard-pulse-FID-acquire sequence. Generally, we set the pulse width from 100 to 500  $\mu\text{s}$  in order to provide for sufficient cycles of the Larmor frequency during the pulse, as well as time to allow the leading edge to reach a consistent value and approximate a square shape (the inductance of the  $B_1$  transmit coil yielded a finite rise time from 10 to 150  $\mu\text{s}$ , depending on the resonance, and also resulted in an exponential discharge of the LCR circuit). Spectral widths were optimized for a particular experiment, between 5 and 25 kHz, with number of data points ranging from 128 to 4096, and low-flip excitations for  $^3\text{He}$  or  $90^\circ$  pulse excitations for water were achieved by adjustment of the coarse power modulation setting and the fine RF transmitter amplitude settings in the SMIS software. A long delay time of 3-4 ms was usually allowed after the RF excitation pulse and before signal detection to allow for sufficient drive coil ring-down and to avoid acquiring the coils coupling response together with spectral information.

Laser-polarized  $^3\text{He}$   $T_1$  and flip-angle calibrations were measured using a multiple shots sequence, with repetition times of seconds for flip angle calibrations, and  $T_R$  of minutes for  $^3\text{He}$   $T_1$  measurements. With  $T_R \ll T_1$  we can determine the flip angle  $\alpha$ . Once  $\alpha$  is known, repeating the experiment with a longer  $T_R$  permits determination of  $T_1$ . A similar pulse sequence was implemented using a 1ms 5-lobe sinc pulse as preparation for imaging experiments. One-pulse FID's, as well as flip-angle calibrations were made with the soft

pulse sequence as well.

All  $^3\text{He}$  imaging experiments were conducted with standard spin-warp gradient-echo sequences based on the standard code supplied with the SMIS instrument. Imaging gradient calibration constants were set accurately in the SMIS software by comparison of known cell physical dimensions to image dimensions based on the desired FOV in initial images. We aimed to minimize the echo time  $T_E$  by using wider spectral widths (10-20 kHz) and smaller datasets (64 or 128 points); while  $T_R$  was limited by the heat dissipation of the gradient panels to 100-500 ms. Despite the narrow RF coil frequency response and its reduced effectiveness with off-resonance pulses, slice selection was tested by application of a gradient pulse during the shaped RF pulse and the phase-encode gradient. Generally, in order to optimize SNR, slice selection was not used, and the gradient current amplifier was switched off. Usually only one signal averaging scan was acquired for each  $^3\text{He}$  image. For  $^1\text{H}$ , a standard spin-echo sequence was used to optimize SNR at the very low frequency used.

Human imaging and spectroscopy was performed at 39 Gauss (3.9 mT) with  $B_1$  set to 127 kHz. The Q of the human transmit and receive resonance circuits were 9.7 and 83.3, respectively, with a receive coil frequency response FWHM of 1.5 kHz and an impedance of 75 k $\Omega$ . We employed a gradient-echo sequence with non-sequential (centric) phase encoding,  $T_E/T_R = 10/100$  ms and a flip angle of  $8^\circ$ . The RF pulses we used were nominally sinc-shaped and of 1 ms duration, and all images were acquired without slice selection. We set the field of view (FOV) to 50 cm, spectral width 16.67 kHz, the image matrix was 128 x 64, and no signal averaging. All raw data sets were zero-filled to 256 x 256 before the Fast Fourier Transform was applied, resulting in a final image resolution of 2 mm.

The high coil Q and resulting small frequency response bandwidth ( $\sim 1$ -2 kHz) of the

receive RF coils used resulted in a convolution of the coil response onto the image data in frequency-space, and thus led to a strong attenuation of signal away from the center frequency. Post-processing of the transformed image data removed this attenuation and non-uniform noise floor from the image [135]. We first acquired the true coil ring-down response from a hard RF pulse, using a one-pulse sequence and reducing the dead-time. However, during human imaging, slight flexing of the coil from the subject's body weight or movement would affect this response. We therefore obtained the coil response from the imaging experiment itself, by averaging the rows of the transformed data set where no true signal was present. The resulting acquired response function was then divided through the processed image data sets, restoring uniform signal intensity across the image space.

### 7.2.5 Human Imaging Protocols

All human experiments were performed according to a protocol approved by the Institutional Review Board at the University of New Hampshire. The subject for lung imaging was a healthy 47-year-old male. As the polarized gas was delivered to the Tedlar bag, we asked the subject to take three or four deep breaths, each lasting 1-2 seconds. After filling, the Tedlar bag was sealed off from the He polarizer. Once the subject completed the last deep breath and was at relaxed expiration, we opened the valve between the Tedlar bag and the mouthpiece and the subject was instructed to breathe in all the gas from the bag via the mouthpiece ( $\sim 500 \text{ cm}^3$  of polarized  $^3\text{He}$ ). This was followed by a small intake of room air to chase the  $^3\text{He}$  deeper into the lungs. MR imaging or spectroscopy sequences commenced immediately and the subject maintained this breath hold for 20-50 seconds. Once imaging was complete, we asked the subject to exhale and to follow with three or four deep breaths of room air.

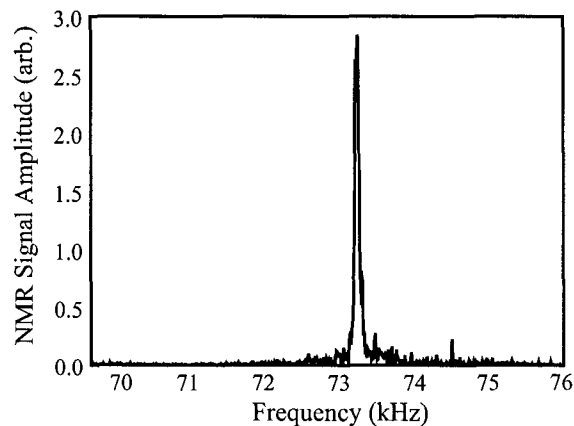


Figure 7-9: Single scan spectrum of a water sample showing a SNR of 30.

### 7.3 Results

Major steps in the development of the instrument preceded the goal of human lung imaging. The  $^1\text{H}$  spectrum of water from a  $140\text{ cm}^3$  sample, shown in Figure 7-9, was obtained initially as an indicator of the SNR that may be expected from the system, and was acquired using a small solenoid receive coil and an earlier generation for the transmit coil. The spectrum was obtained in a single scan without signal averaging, at 73 kHz (17 G), and yielded an SNR  $\sim$  30. This measurement served as a benchmark during installation of the Faraday cage and the addition of the Techron gradient amplifiers to the system, along with the implementation of the required passive and active inductor line filters. The narrow frequency response of the coil is apparent from the non-uniform noise floor across the spectral width.

Small laser-polarized  $^3\text{He}$  cells also yielded similar spectra with significantly higher SNR, despite the use of low flip angles, due to the increased SNR efficiency of laser-polarized noble-gas samples in comparison to thermally-polarized ones at lower field strengths [125]. After installation of the gradient panels and filtering on the gradient lines, we acquired the first  $^3\text{He}$  images, shown in Figure 7-10a, of the phantoms that had been used previously

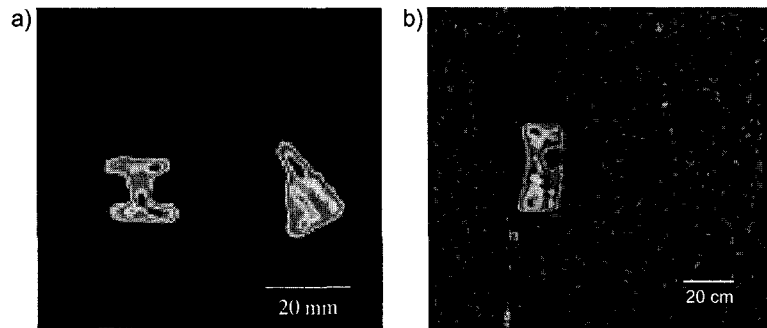


Figure 7-10: a) Images of <sup>3</sup>He cells; b) Longitudinal projection of a large water sample at 30 G.

in bench-top low-field MRI experiments [124]. The small solenoid receive coil used for this image had a significantly lower  $Q$  so the coil response was relatively uniform across the region of interest containing the cells. The images appeared undistorted, and after gradient calibration, their image dimensions matched their true dimensions in the two imaging axes, indicating true gradient linearity across this smaller FOV. This was expected from the linearity plot in Figure 7-4b, and the absence of concomitant gradient effects [136].

Once the large excite and pick-up coils for human imaging were designed and built, they were tuned for the imaging frequency, arbitrary chosen to be  $\sim 126$  kHz. Initial tests for SNR were run using a large tub (14.5 cm height x 25 cm wide x 38 cm long) filled with water. Plastic objects with different shapes and positions were placed inside for resolution check. We were able to acquire 2D projection of the water tub, shown in Figure 7-10b, using a spin echo sequence for a FOV of 125 cm and 5 kHz spectral width, 128x128 data points, and 48 averages with a repetition time  $T_R$  of 2.4 s and  $T_E$  of 36 ms. The image shows small field instabilities for this long run (over 4 hours), but a good resolution for the image and excellent SNR for the system, considering the low proton signal at this field ( $\sim 1000$  times lower than for a 3 T imager).

We then carefully calibrated excitation flip angles to determine appropriate pulse power levels for both 500  $\mu\text{s}$  hard pulses and 1 ms 5-lobes sinc pulses, covering a wide range of excitation flip angles. These measurements were carried out with repeated low-flip angle pulsing. Also, the helium polarizer was tested to determine polarization lifetime ( $T_1$ ) of  $^3\text{He}$  in each polarization cell, as well as the  $^3\text{He}$   $T_1$  in the glass and Teflon compressor unit.

We then placed the cells directly in the RF coils in the magnet and measured the  $^3\text{He}$   $T_1$  to be 6 to 20 hours. We also measured similar  $T_1$  for the helium compressor by disconnecting it from the polarizer and placing it directly inside the magnet. Finally, we transferred the polarized  $^3\text{He}$  gas from the polarization cell, via the compressor, to a Tedlar sample bag in the RF coils. Similar measurements yielded a  $^3\text{He}$   $T_1$  of  $\sim 20$  min. In some cases, we intentionally added  $\text{O}_2$  to the bag first in order to simulate the conditions found in the lungs. Imaging of the gas under such circumstances yielded images that indicated a reasonable  $B_1$  homogeneity over a 20 cm DSV region.

Three-D imaging with off-center slice selection is challenging to implement at very low frequencies. Slice selection requires the use of a frequency selective RF pulse that excites spins in a specific band determined by the application of a gradient pulse across the sample. In commercial imagers the  $B_1$  output of the RF coils across the imaging spectral width is constant. As discussed above, the RF coil response at these kHz frequencies is often narrower than the imaging spectral width, especially for the receive coils. However, one experiment was performed to confirm that we would have the ability to perform slice selection on-center. Two small cells of laser-polarized  $^3\text{He}$  were placed in the coils, but were offset from one another vertically by 4 cm. Figure 7-11a shows the image of the two cells, acquired without a slice selection gradient pulse. In Figure 7-11b, the image acquired with slice selection implemented is shown. The cell offset vertically from the center of the imager



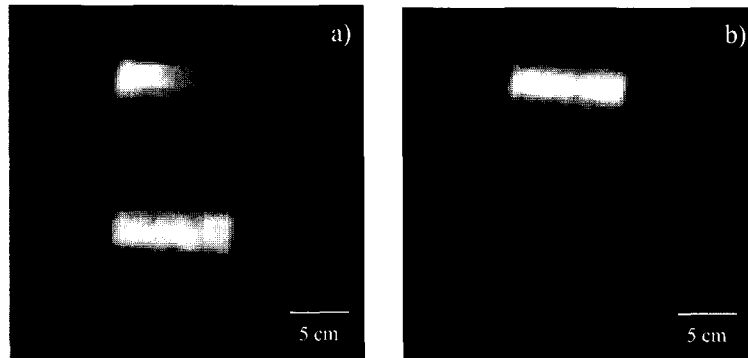


Figure 7-11: Slice selection test at low field: a) no slice gradient over the two  $^3\text{He}$  cells resulting in a 2D projection; b) with slice gradient on the lower cell is eliminated.

has now been removed from the image. The image of Figure 7-11b shows that an effective slice selection of  $\sim 4$  cm was feasible with this specific system. Narrower slice selection was precluded because of the limited gradient strength available in the transverse axes. The image of the upper cell in Figure 7-11a is incomplete due, we believe, to a region where  $B_0$  was varying from the nominal value. The addition of the slice selection gradient in Figure 7-11b remedies this problem by adding a small field shimming through the slice gradient from the shim box.

Nearly all the images underwent corrections due to the narrow width of the receive coil resonance. In Figure 7-12 we show the improvement in the final image quality using this method. The coil response from the FFT of the raw data which did not have  $^3\text{He}$  signal was used to correct the experimental data, resulting in recovery of low signals in the regions outside the resonance.

Our first human lung image was acquired with the subject lying horizontally on a non-conducting and non-magnetic patient table as shown in Figure 7-1b. After polarizing the  $^3\text{He}$  for a few hours, the gas was transferred via the compressor into the Tedlar bag, located inside the imaging room, next to the subject. The gas was delivered to the subject following

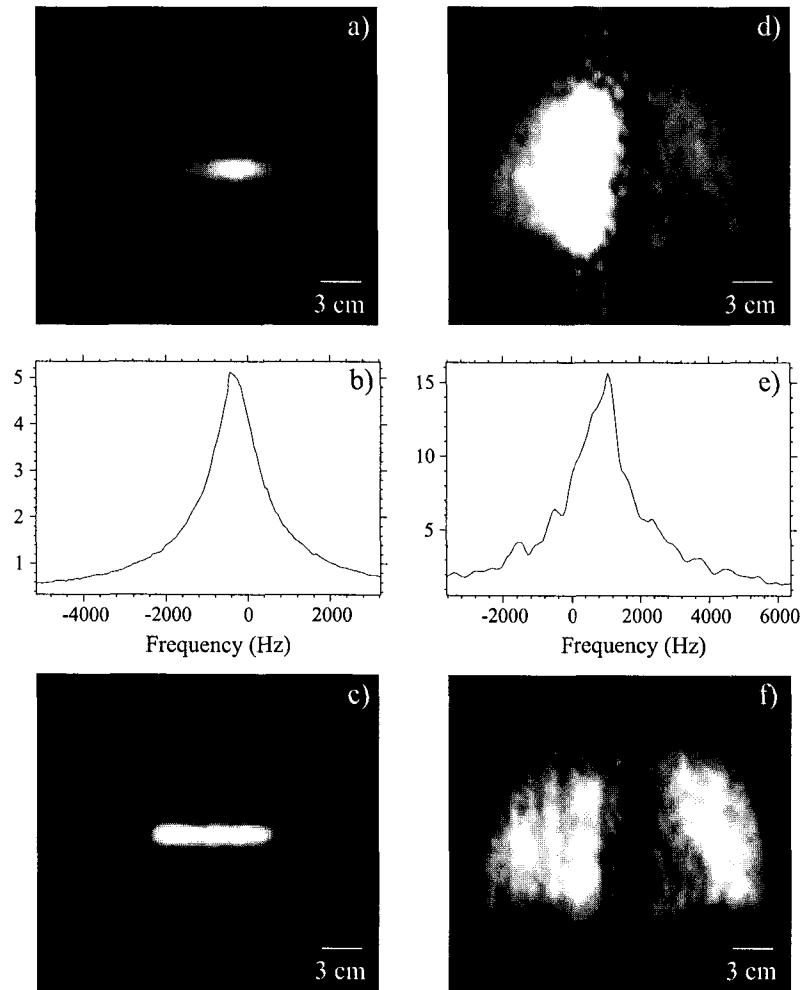


Figure 7-12: Coil response corrections for cell and lung images: a) and d) raw images; b) and e) coil resonance response obtained from the raw data without signal; c) and f) coil-response corrected images.

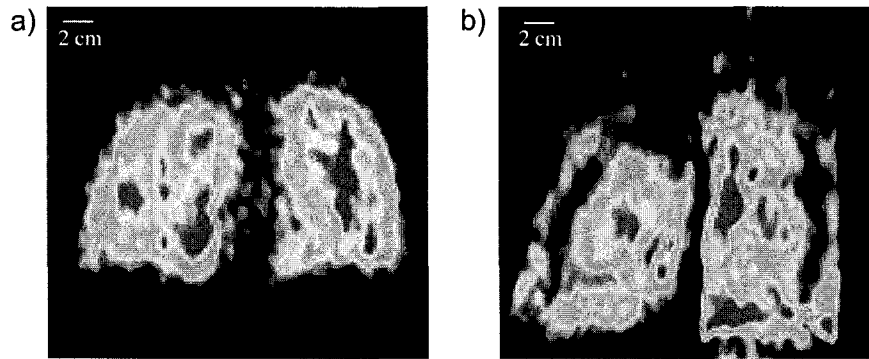


Figure 7-13: Human lungs image at 39 Gauss: FOV=50cm, SW=16.67 kHz,  $T_E/T_R=10/100$  ms, data scans 128x64 overfilled to 256x256: a) horizontal (supine) orientation, b) vertical orientation.

the human imaging protocol. The 2D projection images obtained is shown in Figure 7-13, with the subject's left lung at the right side of the image. The horizontal image from Figure 7-13a shows a very nice definition of the lobes, with a uniform  $^3\text{He}$  signal. The medial aspect of left lung has a lower intensity consistent with the location of the heart.

We also rotated the drive-receive coils for vertical orientation imaging, but the image is of lower quality. However, medical aspects of this first study are discussed in detail in the collaboration's recent published paper [121].

The xenon polarizer was developed after the end of low field imaging collaboration and no attempt to use hyperpolarized  $^{129}\text{Xe}$  was attempted.

## Chapter 8

# CONCLUSIONS

In this thesis I mainly described a novel polarizer design for producing large quantities of highly polarized  $^{129}\text{Xe}$  through Rb optical pumping. The advantage of working at low pressure allows a large spin-exchange rate between Rb and  $^{129}\text{Xe}$ . Large flow rates of the gas mixture are required in order to match optimum running condition of our apparatus. The idea of two separate regions for the main cell, a hot region where the optical pumping and spin-exchange occurs and a cold region where the Rb vapor is trapped from the gas mixture, was implemented into a large scale polarizer.

Simple theoretical modeling predicted extremely high numbers for the output polarization. Also, we were able to predict an optimum running regime for the polarizer, which later showed to be in close agreement with experimental values.

A novel design for the optics offered a circular output laser beam for a good coverage of the polarizing column. Around 90 W output of circular polarized laser power was typically used in the optical pumping process. Lately, we demonstrated for the first time the narrowing of the spectrum for a very high power stack of laser diode array bars. For this, we implemented an external Littrow cavity, improved with two novel components: a stepped

mirror for the output beam uniformity, and a collimator to reduce the emitted divergence of the beam.

Polarization numbers, such as 64% for 0.3 liter/hour xenon production, 50% for 1.2 l/h, and over 20% for 6 l/h, were achieved with our system. Xenon polarization dependencies on different parameters were determined. Polarization is maximized at 160° C temperature, ~125 torr nitrogen partial pressure, ~1.4 liters/minute total gas mixture flow, and 500 torr total pressure.

Using a novel design of the freeze-out system, which assures the accumulation of frozen polarized xenon in a thin layer at liquid nitrogen temperature, we observed full recovery of the polarized xenon. We confirmed by multiple a freeze-thaw cycles method that accumulating the xenon in a thick layer resulted in recovery ratios of only 82.3%.

Polarized xenon could be frozen and thawed back into the NMR measurement system for studies of relaxation times and recovery ratios. Large relaxation times of over 2.5 h were measured in the gas state and a value of 2 h was observed for the frozen state.

Delivery systems for both states, gas and frozen hyperpolarized xenon, were designed and implemented and they were successful tested. Collaborative MRI studies using hyperpolarized xenon are ongoing at Brigham and Women's Hospital.

First results of the collaboration, based on UNH delivered xenon, were included in this thesis. We were able to demonstrate the capability of separating the oil dissolved-phase from the gas-phase of hyperpolarized xenon. Also, we performed a first experiment of *in vitro* rabbit lung imaging and measure the relaxation time in the lungs.

An additional chapter presented the development of a very-low field MRI scanner working with hyperpolarized gas. We built on limited time and resources a human scale imager working at very low magnetic field strengths. The system, based on resistive coils and

planar gradients, allows full orientational access of human subjects for polarized gas lung imaging. During the progress towards human imaging, we have approached multiple low field imaging issues, such as noise reduction, off-resonance signal correction, and slice selection. Finally, first orientational  $^3\text{He}$  human lung images were obtained at 39 Gauss, with the subject in horizontal (supine) and vertical (upright) positions.

## Appendix A

# IRB HUMAN PROTOCOL APPROVAL

Institutional Review Board (IRB) approval page is required to be attached to PhD Theses presenting experiments involving human subjects. Attached is the human protocol IRB approval for the low field MRI using hyperpolarized  $^3\text{He}$ .

# UNIVERSITY OF NEW HAMPSHIRE

Office of Sponsored Research  
Service Building  
51 College Road  
Durham, New Hampshire  
03824-3585  
(603) 862-3564 FAX

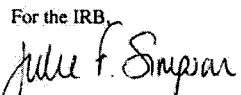
LAST NAME	Hersman	FIRST NAME	F. William
DEPT	Physics Department, DeMeritt Hall	APP'L DATE	5/9/2001
OFF-CAMPUS ADDRESS (if applicable)	Physics Department, DeMeritt Hall	IRB #	2544
		REVIEW LEVEL	EXP
		DATE OF NOTICE	1/29/2002
PROJECT TITLE	High Resolution Imaging of Lung Structure and Function/Advanced Technology Development of Laser-Polarized Noble Gas Magnetic Resonance		

The Institutional Review Board (IRB) for the Protection of Human Subjects in Research reviewed and approved the protocol for your project as Expedited as described in Federal Regulations 45 CFR 46, Subsection 46.110 (b) (1) category 4.

Approval is granted for one year from the approval date above. At the end of the approval period you will be asked to submit a project report with regard to the involvement of human subjects. If your project is still active, you may apply for extension of IRB approval through this office.

The protection of human subjects in your study is an ongoing process for which you hold primary responsibility. In receiving IRB approval for your protocol, you agree to conduct the project in accordance with the ethical principles and guidelines for the protection of human subjects in research, as described in the following three reports: Belmont Report; Title 45, Code of Federal Regulations, Part 46; and UNH's Multiple Project Assurance of Compliance. The full text of these documents is available on the Office of Sponsored Research (OSR) website at [http://www.unh.edu/osr/compliance/Regulatory\\_Compliance.html](http://www.unh.edu/osr/compliance/Regulatory_Compliance.html) and by request from OSR.

Changes in your protocol must be submitted to the IRB for review and approval prior to their implementation; you must receive written, unconditional approval from the IRB before implementing them. If you experience any unusual or unanticipated results with regard to the participation of human subjects, report such events to this office within one working day of occurrence. If you have questions or concerns about your project or this approval, please feel free to contact this office at 862-2003. Please refer to the IRB # above in all correspondence related to this project. The IRB wishes you success with your research.

For the IRB,  
  
Julie F. Simpson  
Regulatory Compliance Manager

cc: File



## Appendix B

# IACUC ANIMAL PROTOCOL APPROVAL

Institutional Animal Care and Use Committee (IACUC) approval for the experiments involving animals (rabbits) performed at Brigham and Women's Hospital by our collaborators is attached. The results of our first experiment involving *in vitro* rabbit lung imaging using hyperpolarized  $^{129}\text{Xe}$  is contained within this thesis.

JUL-14-2004 10:13  
 Harvard Medical School  
 Standing Committee On Animals  
 Gordon Hall, Room 411  
 25 Shattuck Street  
 Boston, MA 02115

HARVARD MEDICAL

617 432 3169 P. 01/01  
 Tel: (617) 432-4886  
 Fax: (617) 432-3169  
 Staff Asst.: (617) 432-3192  
 IACUC Coord.: CB Insp. Coord.: CLT



ANNUAL REVIEW FORM

RECEIVED  
 MAY 12 2004

Fax Number: (617-278-0610) Phone Number: (617-278-0610)  
 Protocol Number: 03654 Date Approved: 6/27/2004 Date Due: 6/1/2004  
 Principal Investigator: Dr. Samuel Patz  
 Title of Protocol: Applications of Hyperpolarized <sup>129</sup>Xe ← Note, should be 129Xe.

In order to comply with Federal, State and Harvard regulations governing the humane care and use of laboratory animals, the Harvard Medical Area Standing Committee on Animals must review and approve animal protocols at least annually. Please complete the information requested below and mail this form to Michelle A. Montplaisir, Staff Assistant, at the address given above, or send via fax to 432-3169. Thanks.

Please answer the following questions regarding your protocol:

A. What is the status of your animal protocol? PENDING  ACTIVE  CLOSED             
 If closed, please sign and date this form and return to this office immediately

B. Has the species, number of animals used, and/or activity relating to this animal protocol changed in any manner since the last approval?  YES  NO  
 If yes, please indicate the amendment approval date(s)           

C. Do you intend to change the species, number of animals and/or activity related to this animal protocol?  YES  NO If yes, you must submit a Protocol Amendment Form obtained from this Office

D. Where are your research animals housed? Bldg. To be determined Rm.           

E. Where are your animal procedures performed for this protocol? Bldg. To be determined Rm.           

F. Please list all current lab personnel, including new research fellows, who are working with each species, giving their name, title, phone/e-mail contact information and experience/training for each species related to this animal protocol. Use the 2nd page of this form for that information. Include departed personnel this past year.

G. Are you using the ascites method of monoclonal antibody production?  YES  NO  
 (If yes, please see attached memo regarding Ascites) Not

H. Who is funding your study? Funding Agency NHLBI Grant Number             
 Grant Title Introduction and Applications of Hyperpolarized <sup>129</sup>Xe           

Please sign below and return this form to the Office for Research Subject Protection by fax or mail.  
 PI Signature: [Signature] Date: 5-12-04

Based upon the information given above, this protocol has been found acceptable for renewal.

Signature of IACUC Chairman: [Signature] 6/27/04  
 Gerald B. Pier, Ph.D. Chairman Renewal Date

# Bibliography

- [1] A. Kastler. Optical methods for studying hertzian resonances. *Nobel Lecture*, page 186, 1966.
- [2] M.R. Bouchiat, T.R. Carver, and C.M. Varnum. Nuclear polarization in  $\text{he}^3$  gas induced by optical pumping in dipolar exchange. *Phys. Rev. Lett.*, 5(8):373–375, 1960.
- [3] P. L. Anthony, R. G. Arnold, H. R. Band, H. Borel, and P. E. Bosted. Determination of the neutron spin structure function. *Phys. Rev. Lett.*, 71(7):959–964, 1993.
- [4] K.P. Coulter, A.B. McDonald, W. Happer, T.E. Chupp, and M.E. Wagshul. Neutron polarization with polarized  $^3\text{he}$ . *Nucl. Instr. Meth. Phys. Res. Sect. A*, 270(1):90–94, 1998.
- [5] D.R. Rich and *et al.* A measurement of the absolute neutron beam polarization produced by an optically pumped  $^3\text{he}$  neutron spin filter. *Nucl. Instr. Meth. Phys. Res. Sect. A*, 481(1-3):431–453, 2002.
- [6] T. E. Chupp, R. J. Hoare, R. L. Walsorth, and B. Wu. Spin-exchange-pumped  $^3\text{he}$  and  $^{129}\text{xe}$  zeeman masers. *Phys. Rev. Lett.*, 72(15):2363–2367, 1998.
- [7] P. L. Anthony, R. G. Arnold, H. R. Band, H. Borel, and P. E. Bosted. An implementation of the deutschjozsa algorithm on a three-qubit nmr quantum computer. *Chem. Phys. Lett.*, 296(1-2):61–67, 1998.
- [8] M.S. Albert, G.D. Cates, B. Driehuys, W. Happer, B. Saam, C.S. Springer, and A. Wishnia. Biological magnetic resonance imaging using laser-polarized  $^{129}\text{xe}$ . *Nature*, 370:199–201, 1994.
- [9] H. E. Moller, X. J. Chen, B. Saam, K. D. Hagspiel, G. A. Johnson, T. A. Altes, E. E. de Lange, and H. U. Kauczor. Mri of the lungs using hyperpolarized noble gases. *Magn Reson Med*, 47(6):1029–51, 2002.
- [10] B. Chann, I.A. Nelson, L.W. Anderson, B. Driehuys, and T.G. Walker.  $^{129}\text{xe}$ - $^{129}\text{xe}$  molecular spin relaxation. *Phys. Rev. Lett.*, 88(11):113201, 2002.
- [11] E.R. Hunt and H.Y. Carr. Nuclear magnetic resonance of  $\text{xe}^{129}$  in natural xenon. *Phys. Rev.*, 130(6):2302–2305, 1963.

- [12] J.P. Mugler III and *et al.* Mr imaging and spectroscopy using hyperpolarized  $^{129}\text{Xe}$  gas: preliminary human results. *Mag. Res. Med.*, 37:809–815, 1997.
- [13] S.C. Cullen and E.G. Gross. The anesthetic properties of xenon in animals and human beings, with additional observations on krypton. *Science*, 113:580–582, 1951.
- [14] S.D. Swanson, M.S. Rosen, K.P. Coulter, R.C. Welsh, and T.E. Chupp. Distribution and dynamics of laser-polarized  $^{129}\text{Xe}$  magnetization in vivo. *Mag. Res. Med.*, 42:1137–1145, 1999.
- [15] K. Sakai, A.M. Bilek, E. Oteiza, R.L. Walsworth, D. Balamore, F.A. Jolesz, and M.S. Albert. Temporal dynamics of hyperpolarized  $^{129}\text{Xe}$  resonances in living rats. *J. Magn. Reson. B*, 111(3):300–304, 1996.
- [16] W. Kilian, F. Seifert, and H. Rinneberg. Chemical shift imaging of human brain after inhaling hyperpolarized  $^{129}\text{Xe}$ -gas. *Proc. Intl. Soc. Magn. Res. Med.*, 10:758, 2002.
- [17] T. Pietraiss and H.C. Gaede. Optically polarized  $^{129}\text{Xe}$  in nmr spectroscopy. *Adv. Mat.*, 7(10):826–838, 1995.
- [18] C.H. Tseng, S. Peled, L. Nascimben, E. Oteiza, R.L. Walsworth, and F.A. Jolesz. Nmr of laser-polarized  $^{129}\text{Xe}$  in blood foam. *J. Magn. Reson.*, 126(1):79–86, 1997.
- [19] D. Raftery, H. Long, T. Meersmann, P.J. Grandinetti, L. Reven, and A. Pines. High-field nmr of adsorbed xenon polarized by laser pumping. *Phys. Rev. Lett.*, 66(5):584–587, 1991.
- [20] G. Navon, Y.Q. Song, T. Rõõm, S. Appelt, R.E. Taylor, and A. Pines. Enhancement of solution nmr and mri with laser-polarized xenon. *Science*, 271:1848–1851, 1996.
- [21] M. Gatzke, G.D. Cates, B. Driehuys, D. Fox, W. Happer, and B. Saam. Extraordinarily slow nuclear spin relaxation in frozen laser-polarized  $^{129}\text{Xe}$ . *Phys. Rev. Lett.*, 70(5):690–693, 1993.
- [22] H.W. Long, H.C. Gaede, J. Shore, L. Reven, C.R. Bowers, J. Kritzenberger, T. Pietraiss, and A. Pines. High-field cross polarization nmr from laser-polarized xenon to a polymer surface. *J. Am. Chem. Soc.*, 115:8491–8492, 1993.
- [23] A. J. Deninger, B. Eberle, M. Ebert, T. Grossmann, G. Hanisch, W. Heil, H. U. Kauczor, K. Markstaller, E. Otten, W. Schreiber, R. Surkau, and N. Weiler. (3)he-mri-based measurements of intrapulmonary  $p(\text{o}_2)$  and its time course during apnea in healthy volunteers: first results, reproducibility, and technical limitations. *NMR Biomed*, 13(4):194–201, 2000.
- [24] R. R. Rizi, J. E. Baumgardner, M. Ishii, Z. Z. Spector, J. M. Edvinsson, A. Jalali, J. Yu, M. Itkin, D. A. Lipson, and W. Geffter. Determination of regional  $v_a/q$  by hyperpolarized 3he mri. *Magn Reson Med*, 52(1):65–72, 2004.
- [25] B. T. Saam, D. A. Yablonskiy, V. D. Kodibagkar, J. C. Leawoods, D. S. Gierada, J. D. Cooper, S. S. Lefrak, and M. S. Conradi. Mr imaging of diffusion of 3he gas in healthy and diseased lungs. *Magnetic Resonance in Medicine*, 44(2):174–179, 2000.

- [26] D.A. Yablonskiy, A.L. Sukstanskii, J.C. Leawoods, D.S. Gierada, G.L. Bretthorst, Lefrak. S.S., J.D. Copper, and M.S. Conradi. Quantitative in vivo assessment of lung microstructure at the alveolar level with hyperpolarized  $^3\text{He}$  diffusion mri. *Proc. Natl. Acad. Sci.*, 99(5):3111–3116, 2002.
- [27] R.W. Mair, G.P. Wong, D. Hoffmann, M.D. Hurlimann, S. Patz, L.M. Schwartz, and R.L. Walsworth. Probing porous media with gas diffusion nmr. *Phys. Rev. Lett.*, 83(16):3324–3327, 1999.
- [28] B. M. Goodson. Nuclear magnetic resonance of laser-polarized noble gases in molecules, materials, and organisms. *J. Mag. Res.*, 155:157–216, 2002.
- [29] W. Happer. Optical pumping. *Rev. Mod. Phys.*, 44(2):169–250, 1972.
- [30] M.E. Wagshul and T.E. Chupp. Laser optical pumping of high-density rb in polarized  $^3\text{He}$  targets. *Phys. Rev. A*, 49(5):3854–3869, 1994.
- [31] E. Babcock, I. Nelson, S. Kadlecik, B. Driehuys, L. W. Anderson, F. W. Hersman, and T.G. Walker. Hybrid spin-exchange optical pumping of  $^3\text{He}$ . *Phys Rev Lett*, 91(12):123003, 2003.
- [32] F.D. Colegrove, L.D. Schearer, and G.K. Walters. Polarization of  $\text{He}^3$  gas by optical pumping. *Phys. Rev.*, 132(6):2561–2572, 1963.
- [33] G. Eckert, W. Heil, M. Meyerhoff, E.W. Otten, R. Surkau, M. Werner, M. Leduc, P.J. Nacher, and L.D. Schearer. A dense polarized  $^3\text{He}$  target based on compression of optically pumped gas. *Nucl. Instrum. Methods Phys. Res. A*, 320(1-2):53–65, 1992.
- [34] E. Stolz, N. Meyerhoff, N. Bigelow, M. Leduc, P.J. Nacher, and G. Tastevin. High nuclear polarization in  $^3\text{He}$  and  $^3\text{He}$ - $^4\text{He}$  gas mixtures by optical pumping with a laser diode. *Appl. Phys. B*, 63(6):629–633, 1996.
- [35] J. Becker. Study of mechanical compression of spin-polarized  $^3\text{He}$  gas. *Nucl. Instrum. Methods Phys. Res. A*, 346(1-2):45–51, 1994.
- [36] J. Becker, J. Bermuth, M. Ebert, T. Grossmann, W. Heil, D. Hofmann, H. Humblot, M. Leduc, E.W. Otten, D. Rohe, and R. Surkau. Interdisciplinary experiments with polarized  $^3\text{He}$ . *Nucl. Instrum. Methods Phys. Res. A*, 402(2-3):327–336, 1998.
- [37] T.R. Gentile, G.L. Jones, A.K. Thompson, R.R. Rizi, D.A. Roberts, I.E. Dimitrov, R. Reddy, D.A. Lipson, W. Gefter, M.D. Schanll, and J.S. Leigh. Demonstration of a compact compressor for application of metastability-exchange optical pumping of  $^3\text{He}$  to human lung imaging. *Mag. Res. Med.*, 43(2):290–294, 2000.
- [38] B.C. Grover. Noble-gas nmr detection through noble-gas-rubidium hyperfine contact interaction. *Phys. Rev. Lett.*, 40(6):391–392, 1978.
- [39] N. N. Kuzma, N. Patton, K. Raman, and W. Happer. Fast nuclear spin relaxation in hyperpolarized solid  $^{129}\text{Xe}$ . *Phys. Rev. Lett.*, 88(14):147602–1, 2002.

- [40] N. N. Kuzman, D. Babich, and W. Happer. Anisotropic nuclear spin relaxation in single-crystal xenon. *Phys. Rev. B*, 65:134301, 2002.
- [41] M. S. Rosen, T. E. Chupp, K. P. Coulter, R. C. Welsh, and S. D. Swanson. Polarized xe-129 optical pumping/spin exchange and delivery system for magnetic resonance spectroscopy and imaging studies. *Rev. Scient. Instruments*, 70(2):1546–1552, 1999.
- [42] U. Ruth, T. Hof, J. Schmidh, D. Fick, and H. J. Jansch. Production of nitrogen-free, hyperpolarized  $^{129}\text{xe}$  gas. *Appl. Phys. B*, 68(1):93–97, 1999.
- [43] G.D. Cates, D.R. Benton, M. Gatzke, W. Happer, K.C. Hasson, and N.R. Newbury. Laser production of large nuclear-spin polarization in frozen xenon. *Phys Rev Lett*, 65(20):2591–4, 1990.
- [44] B. Driehuys, G.D. Cates, E. Miron, K. Sauer, D.K. Walter, and W. Happer. High-volume production of laser-polarized  $^{129}\text{xe}$ . *Appl. Phys. Lett.*, 69(12):1668–1670, 1996.
- [45] A.L. Zook and C.R. Bowers. High capacity production of  $\approx 40\%$  spin polarized xenon-129 for nmr and mri application at the nrmfl. *Nat. High Mag. Field Lab. Reports*, 8(4):20–23, 2001.
- [46] A.L. Zook, B.B. Adhyaru, and C.R. Bowers. High capacity production of  $\approx 65\%$  spin polarized xenon-129 for nmr spectroscopy and imaging. *J. Mag. Res.*, 159:175–182, 2002.
- [47] R.G. Fitzgerald, K.L. Sauer, and W. Happer. Magnetic resonance imaging with laser-polarized  $^{129}\text{xe}$ . *Chem. Phys. Lett.*, 284(1-2):87–92, 1998.
- [48] J. C. Leawoods, B. T. Saam, and M. S. Conradi. Polarization transfer using hyperpolarized, supercritical xenon. *Chem. Phys. Lett.*, 327(5-6):359–364, 2000.
- [49] R.L. de Zafra. Optical pumping. *Am. J. Phys.*, 28:646–654, 1960.
- [50] R. Benumof. Optical pumping theory and experiments. *Am. J. Phys.*, 33:151–160, 1965.
- [51] T.J. Killian. Thermionic phenomena caused by vapors of rubidium and potassium. *Phys. Rev.*, 27(5):578–587, 1936.
- [52] S. Appelt, A. Ben-Amar Barange, C.J. Erickson, M.V. Romalis, A.R. Young, and W. Happer. Theory of spin-exchange optical pumping of  $^3\text{he}$  and  $^{129}\text{xe}$ . *Phys. Rev. A*, 58(2):105–108, 1998.
- [53] L.W. Anderson, F.M. Pipkin, and J.C. Baird. Hyperfine structure of hydrogen, deuterium, and tritium. *Phys. Rev.*, 120(4):1279–1289, 1960.
- [54] H.M. Gibbs and R.J. Hull. Spin-exchange cross sections for  $\text{rb}^{87}\text{-rb}^{87}$  and  $\text{rb}^{87}\text{-rb}^{85}$  collisions. *Phys. Rev.*, 153(1):132–151, 1967.
- [55] T. G. Walker and W. Happer. Spin-exchange optical pumping of noble-gas nuclei. *Rev. Mod. Phys.*, 69(2):629–642, 1997.

- [56] E.S. Hrycyshyn and L. Krause. Inelastic collision between excited alkali atoms and molecules. vii. sensitized fluorescence and quenching in mixtures of rubidium with H<sub>2</sub>, HD, D<sub>2</sub>, N<sub>2</sub>, CH<sub>4</sub>, CD<sub>4</sub>, C<sub>2</sub>H<sub>4</sub>, and C<sub>2</sub>H<sub>6</sub>. *Can. J. Phys.*, 48:2761–2768, 1970.
- [57] M.E. Wagshul and T.E. Chupp. Optical pumping of high-density rb with a broadband dye laser and gaalas diode laser arrays: Application to <sup>3</sup>he polarization. *Phys. Rev. A*, 40(8):4447–4454, 1989.
- [58] M.S. Rosen. *Laser-polarized 129Xe magnetic resonance spectroscopy and imaging; the development of a method for in vivo perfusion measurement*. PhD thesis, University of Michigan, 2001.
- [59] V.R. Pomeroy. *Spin-exchange polarized <sup>3</sup>He using optically pumped alkali atoms for MRI and neutron spin-filters*. PhD thesis, University of New Hampshire, 1998.
- [60] A. Corney. *Atomic and laser spectroscopy*. Claredon Press, Oxford, 1977.
- [61] M.V. Romalis, E. Miron, and G.D. Cates. Pressure broadening of rb d1 and d2 lines by 3he, 4he, n2, and xe: Line cores and near wings. *Phys. Rev. A.*, 56(6):4569–4578, 1997.
- [62] M.E. Wagshul. *Polarization of <sup>3</sup>He by spin exchange with high density laser optically pumped Rb vapor*. PhD thesis, Harvard University, 1991.
- [63] B. Larson, O. Hausser, P.P.J. Delheij, D.M. Whittal, and D. Thiessen. Optical pumping of rb in the presence of high-pressure 3he buffer gas. *Phys. Rev. A*, 44(5):3108–3118, 1991.
- [64] B. Chann, E. Babcock, L.W. Anderson, and T.G. Walker. Skew light propagation in optically thick optical pumping cells. *Phys. Rev. A*, 66:033406, 2002.
- [65] A. Compaan, A. Wagoner, and A. Aydinli. Rotational raman scattering in the instructional laboratory. *Am. J. Phys.*, 62:639, 1994.
- [66] D.K. Walter, W.M. Griffith, and W. Happer. Energy transport in high-density spin-exchange optical pumping cells. *Phys. Rev. Lett.*, 86(15):3264–3267, 2001.
- [67] W. Happer, E. Miron, S. Schaefer, D. Schreiber, W.A. van Wijngaarden, and X. Zeng. Polarization of the nuclear spins of noble-gas atoms by spin exchange with optically pumped alkali-metal atoms. *Phys. Rev. A*, 29(6):3092–3110, 1984.
- [68] C.J. Erickson, D. Levron, D. Happer, S. Kadlecck, B. Chann, L.W. Anderson, and T.G. Walker. Spin relaxation resonances due to the spin-axis interaction in dense rubidium and cesium vapor. *Phys. Rev. Lett.*, 85(20):4237–4240, 2000.
- [69] P.J. Leo, E. Tiesinga, P.S. Julienne, D.K. Walter, S. Kadlecck, and T.G. Walker. Field dependence of spin relaxation in a dense rb vapor. *Phys. Rev. Lett.*, 81(7):1389–1392, 1998.

- [70] S. Kadlecěk, T. Walker, D.K. Walter, C.J. Erickson, and W. Happer. Spin-axis relaxation in spin-exchange collisions of alkali-metal atoms. *Phys. Rev. A*, 63(5):052717, 2001.
- [71] S. Kadlecěk, L.W. Anderson, C.J. Erickson, and T.G. Walker. Spin relaxation in alkali-metal  $1\sigma+g$  dimers. *Phys. Rev. A*, 64(5):052717, 2001.
- [72] R.A. Bernheim. Spin relaxation in optical pumping. *J. Chem. Phys.*, 36(1):135–140, 1962.
- [73] R. Gupta, W. Happer, G. Moe, and W. Park. Nuclear magnetic resonance of diatomic alkali molecules in optically pumped alkali vapors. *Phys. Rev. Lett.*, 32(11):574–577, 1974.
- [74] N.D. Bhaskar, J. Pietras, J. Camparo, W. Happer, and J. Liran. Spin destruction in collisions between cesium atoms. *Phys. Rev. Lett.*, 44(14):930–933, 1980.
- [75] S. Kadlecěk, L.W. Anderson, and T.G. Walker. Field dependence of spin relaxation in a dense rb vapor. *Phys. Rev. Lett.*, 80(25):5512–5515, 1998.
- [76] R.J. Knize. Spin destruction in rubidium-rubidium and potassium-potassium collisions. *Phys. Rev. A*, 40(11):6219–6222, 1989.
- [77] A.B. Ben-Amar Baranga, S. Appelt, M.V. Romalis, C.J. Erickson, A.R. Young, G.D. Cates, and W. Happer. Polarization of  $3\text{He}$  by spin exchange with optically pumped rb and k vapors. *Phys. Rev. Lett.*, 80(13):2801–2804, 1998.
- [78] D.K. Walter, W.M. Griffith, and W. Happer. Magnetic slowing down of spin relaxation due to binary collisions of alkali-metal atoms with buffer-gas atoms. *Phys. Rev. Lett.*, 88:093004, 2002.
- [79] X. Zeng, Z. Wu, T. Call, E. Miron, D. Schreiber, and W. Happer. Experimental determination of the rate constants for spin exchange between optically pumped k, rb, and cs atoms and  $^{129}\text{Xe}$  nuclei in alkali-metal-noble-gas van der Waals molecules. *Phys. Rev. A*, 31(1):260–278, 1985.
- [80] G.D. Cates, R.J. Fitzgerald, A.S. Barton, P. Bogorad, M. Gatzke, N.R. Newbury, and B. Saam. Rb- $^{129}\text{Xe}$  spin-exchange rates due to binary and three-body collisions at high Xe pressures. *Phys. Rev. A*, 45(7):4631–4639, 1985.
- [81] Y.Y. Jau, N.N. Kuzma, and W. Happer. High-field measurement of the  $^{129}\text{Xe}$ -rb spin-exchange rate due to binary collisions. *Phys. Rev. A*, 66(5):052710, 2002.
- [82] I.A. Nelson and T.G. Walker. Rb-xe spin relaxation in dilute Xe mixtures. *Phys. Rev. A*, 65:012712, 2002.
- [83] C.C. Bouchiat, M.A. Bouchiat, and L.C.L. Pottier. Evidence for rb-rare-gas molecules from the relaxation of polarized rb atoms in a rare gas. theory. *Phys. Rev.*, 181(1):144–165, 1969.



- [84] M.A. Bouchiat, J. Brossel, and L.C. Pottier. Evidence of rb-rare-gas molecules from the relaxation of polarized rb atoms in a rare gas. experimental results. *J. Chem. Phys.*, 56(7):3703–3714, 1972.
- [85] R.M. Herman. Theory of spin exchange between optically pumped rubidium and foreign gas nuclei. *Phys. Rev.*, 137(4A):A1062–A1065, 1965.
- [86] D.K. Walter, W. Happer, and T.G. Walker. Estimates of the relative magnitudes of the isotropic and anisotropic magnetic-dipole hyperfine interactions in alkali-metalnoble-gas systems. *Phys. Rev. A*, 58(5):3642–3653, 1998.
- [87] Y.Y. Jau, N.N. Kuzma, and W. Happer. Magnetic decoupling of  $^{129}\text{Xe}$ -rb and  $^{129}\text{Xe}$ -cs binary spin exchange. *Phys. Rev. A*, 67(2):022720, 2003.
- [88] I.A. Nelson. *Physics of practical spin-exchange optical pumping*. PhD thesis, University of Wisconsin-Madison, 2001.
- [89] J. Pascale and J. Vandeplanque. Excited molecular terms of the alkali-rare gas atom pairs. *J. Chem. Phys.*, 60(6):2278–2289, 1974.
- [90] C.V. Rice and D. Raftery. Rubidiumxenon spin exchange and relaxation rates measured at high pressure and high magnetic field. *J. Chem. Phys.*, 117(12):5632–5641, 2002.
- [91] M. Jansen *et al.* High performance laser diode bars with aluminum-free active regions. *Opt. Expr.* 3, 4(1), 1999.
- [92] Coherent Laser Group. *User's Manual Fiber Array Packaged (FAP) Laser Diode Bars*. Coherent Inc., 5100 Patrick Henry Drive, Santa Clara, CA 95054, www.coherent.com, 1997.
- [93] B. Chann, E. Babcock, L.W. Anderson, and T.G. Walker. Measurements of  $^3\text{He}$  spin-exchange rates. *Phys. Rev. A*, 66:032703, 2002.
- [94] D. Levron, D.K. Walter, S. Appelt, R.J. Fitzgerald, D. Kahn, S.E. Korbly, K.L. Sauer, W. Happer, T.L. Earles, L.J. Mawst, D. Botez, M. Harvey, L. DiMarco, J.C. Connolly, H.E. Möller, X.J. Chen, G.P. Cofer, and G.A. Johnson. Magnetic resonance imaging of hyperpolarized  $^{129}\text{Xe}$  produced by spin exchange with diode-laser pumped cs. *Appl. Phys. Lett.*, 73(18):2666–2668, 1998.
- [95] J.N. Zenger, M.J. Lim, K.P. Coulter, and T.E. Chupp. Polarization of  $^{129}\text{Xe}$  with high power external-cavity laser diode arrays. *Appl. Phys. Lett.*, 76(14):1798–1800, 2000.
- [96] I. Nelson, B. Chann, and T.G. Walker. Spin-exchange optical pumping using a frequency-narrowed high power diode laser. *Appl. Phys. Lett.*, 76(11):1356–1358, 2000.
- [97] B. Chann, I. Nelson, and T.G. Walker. Frequency-narrowed external-cavity diode-laser-array bar. *Opt. Lett.*, 25(18):1352–1355, 2000.

- [98] K.B. MacAdam, A. Steinbach, and C. Wieman. A narrow-band tunable diode laser system with grating feedback, and a saturated absorption spectrometer for cs and rb. *Am. J. Phys.*, 60(12):1098, 1992.
- [99] Nuvonix Inc. *Pump Array Users Manual*. 3753 Penridge Drive, Bridgeton, MO 63044, www.nuvonyx.com, 2003.
- [100] E.G. Loewen, M. Nevière, and D. Maystre. Grating efficiency theory as it applies to blazed and holographic gratings. *Appl. Opt.*, 16(10):2711–2722, 1997.
- [101] F. Bloch. Nuclear induction. *Phys. Rev.*, 70(7-8):460–474, 1946.
- [102] F. Bloch, W.W. Hansen, and M. Packard. The nuclear induction experiment. *Phys. Rev.*, 70(7-8):474–485, 1946.
- [103] D.R. Lide, editor. *CRC Handbook of Chemistry and Physics*. CRC Press, 1990.
- [104] B. Patton, N.N. Kuzma, and W. Happer. Reducing the relaxation of frozen hyperpolarized  $^{129}\text{Xe}$  during cryogenic separation. *Proceedings 45th E.N.C.*, page p174, 2004.
- [105] M. Pfeffer and O. Lutz.  $^{129}\text{Xe}$  gas nmr spectroscopy and imaging with a whole-body imager. *J. Magn. Reson., Series A*, 108(1):106–109, 1994.
- [106] S.R. Breeze, S. Lang, I. Moudrakovski, C.I. Ratcliffe, J.A. Ripmeester, and B. Simard. Coatings for optical pumping cells and extending the lifetime of hyperpolarized xenon. *J. Appl. Phys.*, 86(7):4040–4042, 1999.
- [107] S.R. Breeze, S. Lang, I. Moudrakovski, C.I. Ratcliffe, J.A. Ripmeester, G. Santyr, B. Simard, and I. Zuger. Coatings for optical pumping cells and short-term storage of hyperpolarized xenon. *J. Appl. Phys.*, 87(11):4040–4042, 2000.
- [108] M.A. Bouchiat and J Brossel. Relaxation of optically pumped rb atoms on paraffin-coated walls. *Phys. Rev.*, 147(1):41–54, 1966.
- [109] J.A. Fedchak, P. Cabauy, W.J. Cummings, C.E. Jones, and R.S. Kowalczyk. Silane coatings for laser-driven polarized hydrogen sources and targets. *Nucl. Instr. Meth. Phys. Res. Sect. A*, 391(3):405–416, 1999.
- [110] W.A. Fitzsimmons, L.L. Tankersley, and G.K. Walter. Nature of surface-induced nuclear-spin relaxation of gaseous  $\text{He}^3$ . *Phys. Rev.*, 179(1):156–165, 1968.
- [111] Z. Wu, W. Happer, M. Kitano, and J. Daniels. Experimental studies of wall interactions of adsorbed spin-polarized  $^{131}\text{Xe}$  nuclei. *Phys. Rev. A*, 42(5):2774–2784, 1999.
- [112] X. Zeng, E. Miron, W.A. Van Wijngaarden, D. Schreiber, and W. Happer. Wall relaxation of spin polarized  $^{129}\text{Xe}$  nuclei. *Phys. Lett. A*, 96(4):191–194, 1983.
- [113] B. Driehuys, G.D. Cates, and W. Happer. Surface relaxation mechanisms of laser-polarized  $^{129}\text{Xe}$ . *Phys. Rev. Lett.*, 76(24):4943–4946, 1999.

- [114] H. Fujiwara, A. Kimura, Y. Yanagawa, T. Kamiya, M. Hattori, and T. Hiraga. Relaxation behavior of laser-polarized  $^{129}\text{Xe}$  gas: Size dependency and wall effect of the  $t_1$  relaxation time in glass and gelatin bulbs. *J. Mag. Res.*, 150:156–160, 2001.
- [115] I. L. Moudrakovski, S.R. Breeze, B. Simard, C.I. Ratcliffe, J.A. Ripmeester, T. Seideman, J.S. Tse, G. Santyr, and I. Zuger. Coatings for optical pumping cells and short-term storage of hyperpolarized xenon. *J. Chem. Phys.*, 114(5):4040–4042, 2001.
- [116] Abragam A. *The Principles of Nuclear Magnetism*. Oxford University Press, 1961.
- [117] R.L. Gamblin and T.R. Carver. Polarization and relaxation processes in  $\text{He}^3$  gas. *Phys. Rev.*, 138(4A):A946–A960, 1965.
- [118] L.D. Schearer and G.K. Walters. Nuclear spin-lattice relaxation in the presence of magnetic-field gradients. *Phys. Rev.*, 139(5A):A1398–A1402, 1965.
- [119] G.D. Cates, S.R. Schaefer, and W. Happer. Relaxation of spins due to field inhomogeneities in gaseous samples at low magnetic fields and low pressures. *Phys. Rev. A*, 37(8):2877–2885, 1988.
- [120] P.W.E. Peereboom, H. Luigjes, and K.O. Prins. An nmr spin-echo study of self-diffusion in xenon. *Physica A*, 156(1):260–276, 1989.
- [121] R. W. Mair, M.I. Hrovat, S. Patz, M.S. Rosen, I.C. Ruset, G.P. Topulos, L.L. Tsai, J.P. Butler, F. W. Hersman, and R. L. Walsworth.  $^3\text{He}$  lung imaging in an open access, very-low-field human mri system. *Mag. Res. Med.*, 53:745–749, 2005.
- [122] J.P. Butler, R.W. Mair, D. Hoffmann, M.I. Hrovat, R.A. Rogers, G.P. Topulos, R.L. Walsworth, and S. Pats. Measuring surface-area-to-volume ratios in soft porous materials using laser-polarized xenon interphase exchange nuclear magnetic resonance. *J. Phys.: Condens. Matter*, 14:L297–L304, 2002.
- [123] L. Darrasse, G. Guillot, P.J. Nacher, and G. Tastevin. Lower field 3-helium nuclear magnetic resonance in human lungs. *C. R. Acad. Sci. Paris*, 324:691–700, 1997.
- [124] C. H. Tseng, G. P. Wong, V. R. Pomeroy, R. W. Mair, D. P. Hinton, D. Hoffmann, R. E. Stoner, F. W. Hersman, D. G. Cory, and R. L. Walsworth. Low-field mri of laser polarized noble gas. *Phys Rev Lett*, 81(17):3785–8, 1998.
- [125] G. P. Wong, C. H. Tseng, V. R. Pomeroy, R. W. Mair, D. P. Hinton, D. Hoffmann, R. E. Stoner, F. W. Hersman, D. G. Cory, and R. L. Walsworth. A system for low field imaging of laser-polarized noble gas. *J Magn Reson*, 141(2):217–27, 1999.
- [126] C.J. Jameson, A.K. Jameson, and J.K. Hwang. Nuclear spin relaxation by intermolecular magnetic dipole coupling in the gas phase.  $^{129}\text{Xe}$  in oxygen. *J. Chem. Phys.*, 89(7):4074–4081, 1988.
- [127] W.T. Dixon. Simple proton spectroscopic imaging. *Radiology*, 153:189–194, 1984.
- [128] G.H. Glover and E. Schneider. Three-point dixon technique for true water/fat decomposition with  $\text{B}_0$  inhomogeneity correction. *Mag. Reson. Med.*, 18:371–383, 1991.

- [129] E. Durand, G. Guillot, L. Darrasse, G. Tastevin, P. J. , A. Vignaud, D. Vattolo, and J. Bittoun. Cpmg measurements and ultrafast imaging in human lungs with hyperpolarized helium-3 at low field (0.1 t). *Magn Reson Med*, 47(1):75–81, 2002.
- [130] J. B. West, C. T. Dollery, and A. Naimark. Distribution of blood flow in isolated lung; relation to vascular and alveolar pressures. *J Appl Physiol*, 19:713–24, 1964.
- [131] J. B. West, A. R. Elliott, H. J. Guy, and G. K. Prisk. Pulmonary function in space. *Jama*, 277(24):1957–61, 1997.
- [132] R. W. Glenny, W. J. Lamm, R. K. Albert, and H. T. Robertson. Gravity is a minor determinant of pulmonary blood flow distribution. *J Appl Physiol*, 71(2):620–9, 1991.
- [133] J. B. West. Importance of gravity in determining the distribution of pulmonary blood flow. *J Appl Physiol*, 93(5):1888–9; author reply 1889–91, 2002.
- [134] H. Chang, S. J. Lai-Fook, K. B. Domino, C. Schimmel, J. Hildebrandt, H. T. Robertson, R. W. Glenny, and M. P. Hlastala. Spatial distribution of ventilation and perfusion in anesthetized dogs in lateral postures. *J Appl Physiol*, 92(2):745–62, 2002.
- [135] M. I. Hrovat, F. W. Hersman, S. Patz, R. W. Mair, and R. L. Walsorth. Signal correction for narrow-bandwidth coils. *Proceedings Intl. Soc. Mag. Reson. Med.*, 11:p1053, 2003.
- [136] A. Mohoric, J. Stepisnik, M. Kos, and G. Planinsic. Self-diffusion imaging by spin echo in earth’s magnetic field. *J. Mag. Res.*, 136(1):22–26, 1999.